Monte-Carlo event generation for the LHC

A thesis submitted for the
degree of Doctor of Philosophy

by

Frank Siegert

September 2010

Institute for Particle Physics Phenomenology
Department of Physics

Durham University

Contents

Abstract

This thesis discusses recent developments for the simulation of particle physics in the light of the start-up of the Large Hadron Collider. Simulation programs for fully exclusive events, dubbed Monte-Carlo event generators, are improved in areas related to the perturbative as well as non-perturbative regions of strong interactions. A short introduction to the main principles of event generation is given to serve as a basis for the following discussion. An existing algorithm for the correction of parton-shower emissions with the help of exact tree-level matrix elements is revisited and significantly improved as attested by first results. In a next step, an automated implementation of the POWHEG method is presented. It allows for the combination of parton showers with full next-to-leading order QCD calculations and has been tested in several processes. These two methods are then combined into a more powerful framework which allows to correct a parton shower with full next-to-leading order matrix elements and higher-order tree-level matrix elements at the same time. Turning to the non-perturbative aspects of event generation, a tuning of the PYTHIA event generator within the Monte-Carlo working group of the ATLAS experiment is presented. It is based on early ATLAS minimum bias measurements obtained with minimal model dependence. The parts of the detector relevant for these measurements are briefly explained. Throughout the thesis, results obtained with the improvements are compared to experimental measurements.

Declaration of Authorship

The work in this thesis is based on research carried out at the Institute for Particle Physics Phenomenology, Department of Physics, University of Durham, England, and the Department of Physics and Astronomy, University College London, England. No part of this thesis has been submitted elsewhere for any other degree or qualification.

The research was carried out in collaboration with Dr. S. Höche, Dr. F. Krauss, M. Schönherr and Dr. S. Schumann in the SHERPA collaboration and Prof. Dr. J. Butterworth, Dr. A. Buckley, Dr. J. Katzy, H. Schulz and Dr. M. Warsinsky in ATLAS.

It is based on the following works:

- Stefan Höche, Frank Krauss, Marek Schönherr, Frank Siegert
  NLO matrix elements and truncated showers
  arXiv:1009.1127 [hep-ph] (submitted to JHEP)

- Stefan Höche, Frank Krauss, Marek Schönherr, Frank Siegert
  Automating the POWHEG method in Sherpa
  arXiv:1008.5399 [hep-ph] (submitted to JHEP)

- Stefan Höche, Steffen Schumann, Frank Siegert
  Hard photon production and matrix-element parton-shower merging
  Phys. Rev. **D 81**, 034026 (2010); arXiv:0912.3501 [hep-ph]

- Stefan Höche, Frank Krauss, Steffen Schumann, Frank Siegert
  QCD matrix elements and truncated showers
  JHEP **05** (2009), 053; arXiv:0903.1219 [hep-ph]

- T. Gleisberg, S. Höche, F. Krauss, M. Schönherr, S. Schumann, F. Siegert, J. Winter
  Event generation with SHERPA 1.1
  JHEP **02** (2009), 007; arXiv:0811.4622 [hep-ph]

- A. Buckley, J. Katzy, O. Kepka, H. Schulz, F. Siegert, M. Warsinsky
  ATLAS Minimum Bias Tune 1 : Documentation to support tuning CONF note
  Internal ATLAS note `ATL-COM-PHYS-2010-267`

Acknowledgements

Many people have supported me during my studies and deserve gratitude:

My supervisors, Frank Krauss in Durham and Jon Butterworth in London, for making it possible to do excellent research in both a theoretical and experimental environment. Frank has fuelled my interest in particle physics and given many inspirations on the way. Jon passed on his great passion for making experimental measurements as truthful as possible;

The members of the SHERPA team for a very fruitful collaboration. Most notably I am indebted to Stefan Höche who has become not only a role model with his passion for particle physics but also a good friend. Thanks go also to my great collaborators Steffen Schumann, who got me involved with particle physics in first place, and Marek Schönherr;

My colleagues in the IPPP and elsewhere for making research enjoyable and at the same time broadening my scientific horizon. I am indebted to Thomas Binoth, who died too early. Special thanks go to Gudrun Heinrich, Daniel Maître, and my office mates. Thanks are also due to Linda Wilkinson, Trudy Forster and the system administrators in the IPPP for making the institute such an efficient place for research;

My collaborators in the ATLAS experiment, especially Claire Gwenlan, Markus Warsinsky, Andy Buckley and Tancredi Carli;

MCnet for funding my work through a Marie Curie studentship, and in particular Mike Seymour and Peter Richardson for being great network managers.

Finally I thank those closest to me, my wife and children, my parents, brother and grandparents for their endless love and support.

Dedicated to Ulrike, Edgar and Josefine.

Introduction

The subject of particle physics is the study of fundamental particles and their interactions. Currently and in the recent past, most measurements in this area have come from particle colliders. The four experiments at the electron-positron collider LEP and two collaborations at the electron-proton collider HERA have finished their data taking in the last years, while the Tevatron experiments are continuing to deliver precise results from proton-antiproton collisions. A new frontier has been reached this year when the Large Hadron Collider (LHC) at CERN started colliding proton beams at a new highest energy of 7 TeV and first measurements from several of its experiments were published.

At the four interaction points of the LHC ring one can find detectors built by the ALICE, ATLAS, CMS and LHCb collaborations. While LHCb is a specialised detector for measurements related to CP violations in hadron decays, and ALICE is designed to study heavy ion collisions, the two most versatile experiments are ATLAS and CMS. ATLAS is a multi-purpose detector built by an international community of physicists, engineers and computer scientists. It is meant to explore the full programme of physics possible with LHC collisions and in particular detect the Higgs boson should it be produced inside them.

Unveiling the mechanism of electro-weak symmetry breaking in the Standard Model (SM) has been one primary goal of many experiments. The Standard Model has been a highly successful gauge theory so far and only one constituent of it, a fundamental massive scalar particle – the Higgs boson, has yet to be detected. Without this ingredient, the mechanism with which other particles acquire mass remains unexplained.

Even despite the large success with which the Standard Model has made precision predictions for experimental measurements there are hints that it is not a completely fundamental theory. It contains 19 free parameters which can not be explained further from first principles, and it covers only three of the four fundamental forces, excluding gravity. Furthermore the so-called hierarchy problem poses the question, how the Higgs mass can be small enough to give the observed masses of the W and Z bosons. But also from an experimental point of view certain inconsistencies are starting to

appear. Neutrino oscillations have been observed and contradict massless neutrinos as postulated in the Standard Model. There is also no viable candidate particle explaining the cosmological dark matter observations.

Such considerations have spurred the interest in theories beyond the Standard Model. The most promising of these involve a new symmetry called Supersymmetry (SUSY). It has been suggested as the only possible non-trivial extension of the Poincare group and adds supersymmetric partners for each particle in the SM. Their spin is different by one half but otherwise they carry the same quantum numbers as their SM counterparts. So far no signs of SUSY have been observed, which means the particles have to be significantly heavier than their partners, necessitating a mechanism which breaks SUSY.

It is the foremost objective of experimental particle physics to probe new theories by making measurements which might contradict Standard Model predictions. One of the tricky bits when trying to make such a claim is the smallness of the effects expected by the introduction of new theories. This requires very precise calculations of the prediction not only in the new theory, but also in the dominating Standard Model "background". A big complication in that respect is the nature of Quantum Chromodynamics (QCD), which is part of the SM. Being a non-Abelian gauge theory with a massless gauge boson, QCD brings with it the property of asymptotic freedom: Its coupling constant becomes large at small scales leading to the confinement of its quanta into hadrons. Only at large scales can they be treated as free particles, allowing the application of perturbation theory. Perturbative calculations at large scales and their connection to the hadronisation scale together with a modelling of the confinement process all pose separate challenges which have to be overcome to make predictions for hadron colliders.

One tool to make predictions for collision experiments taking into account all aspects of QCD are Monte-Carlo (MC) event generators. Their most important feature is the ability to generate results at hadron level by the simulation of full events as they would be observed by a detector. The availability of fully exclusive events allows e.g. to study the effect of experimental cuts on signal and background more easily. It also makes it possible for experimentalists to assess the impact of detector effects with the help of a dedicated detector simulation program and correct for them in their measurements. Ideally, and as practised recently in many experimental collaborations, this leads to the presentation of experimental results at the particle level, which has a large advantage over both alternative options: If results are presented at the detector level it becomes difficult, if not impossible to interpret them from a pure particle physics point of view without knowledge of the detector hardware. In the other extreme, if experimental

results are corrected to the parton level using some kind of model e.g. for any non-perturbative QCD effects, they become model-dependent, making them unfit for the further study of any new models.

The most prominent examples of event generators are the highly successful, well-established programs HERWIG [1] and PYTHIA [2]. They have been constructed over the past decades alongside experimental discoveries and most of the features visible in past and present experiments can be described by them. In the last years though, in the run-up to the LHC, the development of Monte-Carlo generators has increased rapidly. There were mainly two reasons for such an effort.

From a technical point of view it became desirable, for maintaining as well as extending the codes, to use an object-oriented language (C++) and a modular design of the programs. This led to improved re-implementations in form of HERWIG++ [3] and PYTHIA 8 [4] – the successors of the Fortran versions mentioned above.

But more importantly, due to the large phase space available at LHC energies, leading to more complex final states and higher scales, it has become necessary to increase the precision of the predictions by incorporating higher-order QCD effects. One example of such an improvement is the inclusion of full next-to-leading order matrix elements in the HERWIG++ generator. Another approach, the correction of the radiation pattern of the shower with higher-order tree-level matrix elements, has lead to the development of the new multi-purpose Monte-Carlo event generator SHERPA [5].

Motivation and outline of this thesis

This thesis is divided into two parts, both of which are related to the improvement of Monte-Carlo simulations at LHC energies. For this reason, Chapter 1 reviews the main principles involved in the construction of a Monte-Carlo event generator, and introduces the basic concepts upon which the improvements of the following chapters are based.

The remainder of the first part of the thesis is concerned with an improvement of the simulation of perturbative QCD in event generators. The large rates for production of multiple hard jets at the LHC in association with e.g. W or Z bosons, $t\bar{t}$ pairs, diboson pairs or photons make it necessary to supplement the leading-order MC generators with higher-order matrix-element corrections.

A formalism based on the efficient replacement of splitting kernels in the parton-shower approximation with exact ratios of higher-order QCD tree-level matrix elements is

rewritten and significantly improved in Chapter 2. Its application to the case of QED emissions is also introduced. Internal consistency checks and a comparison to experimental data exemplifies the performance of the algorithm.

Chapter 3 presents the extension of that formalism to full NLO matrix elements. First the POWHEG method is discussed, which matches an NLO calculation with the parton shower. Results obtained with an automated implementation of that method are displayed. The two methods are then combined into a powerful approach which allows to correct the parton shower with full NLO and higher-order tree-level matrix elements at the same time. Again results are presented including an extensive comparison to existing measurements and predictions at LHC energies.

The second part of the thesis deals with the improvement of non-perturbative Monte-Carlo models. Before the start-up of the LHC it was unclear how models like the ones for multiple parton interactions will change with the large jump in centre of mass energy of the collisions. An energy extrapolation was built into the model, but so far it had only been tested in the relatively low range from 630 GeV to 1960 GeV. A very quick comparison with early measurements at 7 TeV was thus eagerly awaited and the adjustment of the involved parameters became necessary to allow for a good estimate of the non-perturbative effects in future LHC simulations. In the context of the ATLAS Monte-Carlo group the non-perturbative parameters of the PYTHIA event generator have been tuned using early measurements from ATLAS. This constitutes the first comprehensive tuning of a MC event generator to LHC data. Before that work is presented, the ATLAS detector is briefly described in Chapter 5 with an emphasis on the parts used in the early measurements. Analysis strategies and details are explained in Chapter 6. Finally, Chapter 7 documents the procedure for finding the parameter set with the best fit to data and shows the comparison of that tune to ATLAS and Tevatron data.

Part I

Perturbative QCD in Monte-Carlo event generators

1 Monte-Carlo event generation

The main motivation for constructing Monte-Carlo event generators is the need to make theoretical predictions for high-energy reactions in contemporary collider experiments. Almost all of these reactions involve hadrons, either because the colliding particles are hadrons or because hadrons are produced in the final state and are thus used to define observables.

Reactions of hadrons cannot be directly predicted from first principles though. Only their constituents, quarks and gluons, can be described as the quanta of QCD. Due to the asymptotic freedom of QCD, these partons can only then be regarded as free particles if they participate in a scattering process involving large invariant momentum transfer and correspondingly short time scales. In such a case, like at the Tevatron and LHC colliders, QCD allows to describe the interaction of partons using perturbation theory.

At higher orders in the perturbative expansion, such calculations predict infrared divergences of both, real-radiation and virtual contributions. Due to the KLN-theorem [6], these divergences must mutually cancel for an inclusive cross section calculation. However, if measurements or predictions have to be made more exclusively at a certain resolution scale, e.g. the hadronisation scale, the divergences turn into a finite remainder which has a logarithmic dependence on the ratio between the hard scale and the resolution scale. Such potentially large logarithms will appear to each order in perturbation theory and thus spoil the convergence of the perturbative series, which is normally guaranteed by the smallness of the coupling constant. They must therefore be resummed to all orders. Such a resummation can be done analytically or by a numerical method called a parton-shower Monte Carlo.

One big advantage of the parton-shower approach is the ability to connect to a hadronisation model and simulate exclusive hadron level events in a universal manner. Due to the colour-confinement mechanism the application of the free theory and perturbative calculations is not possible anymore at the hadronisation scale. Instead a non-perturbative model has to be employed. As the parton shower allows to “evolve” the partons from their large production scales down to the hadronisation scale, it becomes

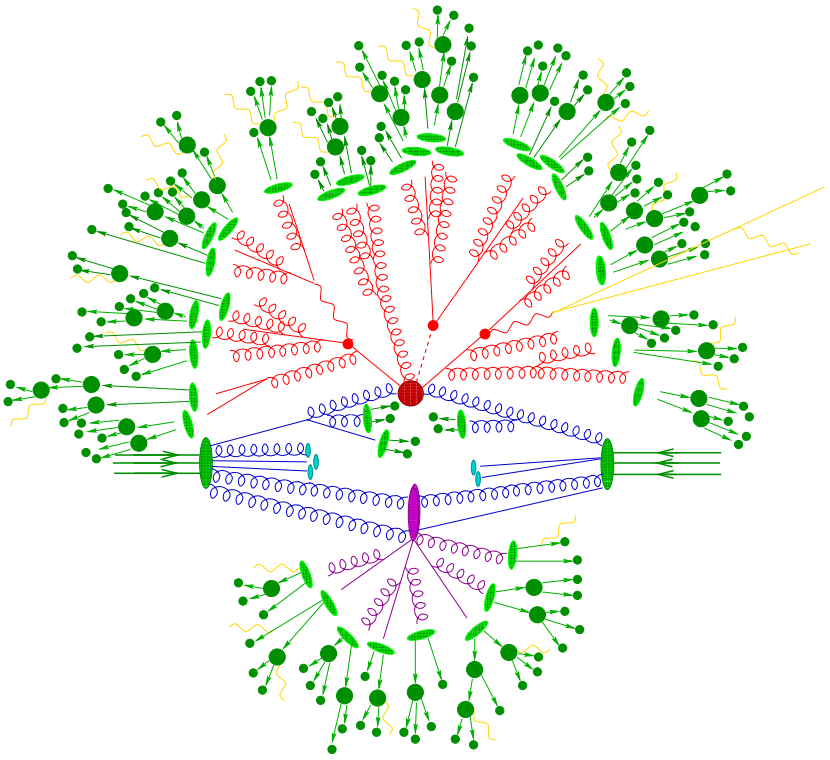

Figure 1.1: Pictorial representation of a $t\bar{t}h$ event as produced by an event generator. The hard interaction (big red blob) is followed by the decay of both top quarks and the Higgs boson (small red blobs). Additional hard QCD radiation is produced (red) and a secondary interaction takes place (purple blob) before the final-state partons hadronise (light green blobs) and hadrons decay (dark green blobs). Photon radiation occurs at any stage (yellow).

possible to apply a universal hadronisation model independent of the hard scattering process in which the partons were produced.

At this stage it should become clear that the simulation of a particle scattering event in a Monte-Carlo event generator is factorised into several event phases. In the description of each of these phases different approximations are employed. To pictorially represent these phases, Figure 1.1 sketches a hadron-collider event, where a $t\bar{t}h$ final state is produced and evolves by including effects of QCD Bremsstrahlung and hadronisation. In general the central piece of the event simulation is provided by the hard process (the dark red blob in the figure), which can be calculated in fixed order perturbation theory in the coupling constants owing to the correspondingly high scales. This part of the simulation is handled by computations based on matrix elements, which are either hard-coded or provided by special programs called parton-level or matrix-element (ME) generators. The QCD evolution (red in the figure) described by parton showers then connects the hard scale of coloured parton creation with the hadronisation scale where the transition to the colourless hadrons occurs. The parton showers model mul-

tiple QCD Bremsstrahlung in an approximation to exact perturbation theory, which is accurate to leading logarithmic order. At the hadronisation scale, which is of the order of a few Λ_{QCD}, QCD partons are transformed into primary hadrons (light green blobs) by applying fragmentation models which are purely phenomenological and have typically around ten parameters to be fitted to data. The primary hadrons finally are decayed into stable particles that can be observed in detectors. In most cases effective theories or simple symmetry arguments are invoked to describe these decays. Another important feature associated with the decays is QED Bremsstrahlung from charged hadrons, which is simulated by techniques that are accurate at leading logarithmic order and, eventually, supplemented with exact first-order results. A particularly difficult scenario arises in hadronic collisions, where remnants of the incoming hadrons may experience secondary hard or semi-hard interactions. This underlying event is pictorially represented by the purple blob in Figure 1.1. Such effects are beyond QCD factorisation theorems and therefore no complete first-principles theory is available. Instead, phenomenological models are employed again, with more parameters to be adjusted by using comparisons with data.

In the remainder of this chapter, the techniques used in each of these event phases is briefly reviewed. The parton shower algorithm is explained in some detail because it lays the foundation upon which the whole first part of this thesis is built.

1.1 Hard scattering process

The hard scattering process is typically the first phase of the event that is simulated. It essentially reduces to the evaluation of the cross section for the production of an N-particle final state e.g. in hadron-hadron collisions,

$$\sigma_N = \sum_{a,b} \int \mathrm{d}x_1 \mathrm{d}x_2 f_a(x_1, \mu^2) f_b(x_2, \mu^2)\ \hat{\sigma}_N^{ab}, \tag{1.1}$$

where the hadronic cross section factorises into universal parton distribution functions (PDF) and the partonic cross section $\hat{\sigma}_N$ for a specific partonic initial state (ab). The PDF $f_a(x_1, \mu^2)$ is the suitably-regularised hadronic matrix element for the inclusive distribution to find a parton a with energy fraction x_1 in the beam hadron renormalised at scale μ^2.

To compute the partonic cross section one has to calculate the following phase-space

n	$\#_{\text{diags}}$
2	4
3	25
4	220
5	2485
6	34300
7	559405
8	10525900

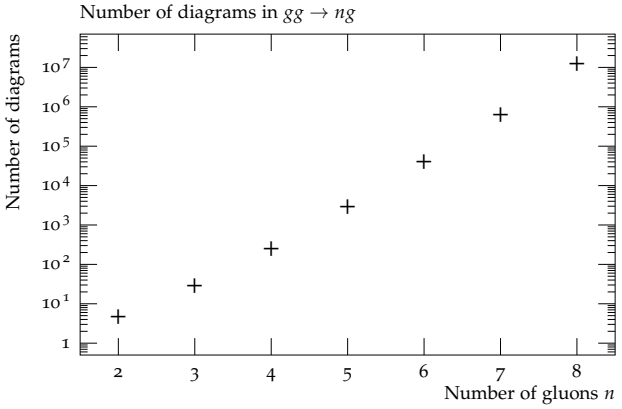

Figure 1.2: Growth of the number of diagrams contributing to the full $gg \to ng$ amplitude.

integral over the differential cross section:

$$\hat{\sigma}_N^{ab} = \int_{\text{cuts}} \mathrm{d}\hat{\sigma}_N^{ab} = \int_{\text{cuts}} \left[\prod_{i=1}^{N} \frac{\mathrm{d}^3 q_i}{(2\pi)^3 2E_i}\right] \delta^4\left(p_1 + p_2 - \sum_i^N q_i\right) \left|\mathcal{M}^{ab}_{p_1 p_2 \to \{\vec{q}\}}\right|^2 . \quad (1.2)$$

The value of the integral $\hat{\sigma}_N^{ab}$ will give the total partonic cross section for the process under consideration and the integrand $\mathrm{d}\hat{\sigma}_N^{ab}$ represents the weight associated with a given kinematical configuration, $p_1 p_2 \to \{\vec{q}\}$, which is used to produce fully differential events. From Equation (1.2) it becomes clear that two tasks are involved in its evaluation: The parton-level matrix element $\left|\mathcal{M}_{p_1 p_2 \to \{\vec{q}\}}\right|^2$ has to be computed fully differentially, and the multi-dimensional phase-space integral has to be performed in an efficient manner.

Various techniques exist to calculate the matrix-element expression at leading order. For $2 \to 2$ and some $2 \to 3$ processes it is straightforward to draw all tree-level Feynman diagrams and apply the Feynman rules to arrive at an expression which can be directly implemented in computer code as e.g. in Table 1.1. For more complicated processes this becomes cumbersome and error prone and it is mandatory to construct computer codes which can build and evaluate Feynman diagrams in an automated fashion.

Typically the final-state multiplicity of such calculations at leading order in QCD is limited, where the example of $t\bar{t}h$ above is already a very complicated case with eight final state particles. For certain applications though, some of which will be the topic of Chapters 2 and 3, it is necessary to calculate higher-order tree-level matrix elements with many additional partons in the final state. Here, even the automated evaluation of Feynman diagrams becomes prohibitively time consuming, because the number of diagrams grows factorially as exemplified for the case of $gg \to ng$ in Figure 1.2. In such cases methods based on off-shell recursion relations have shown their strengths which

Process	Amplitudes	$\overline{\sum} \lvert\mathcal{M}\rvert^2 \,/\, (4\pi\alpha_s)^2$
$q\,q' \to q\,q'$	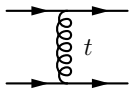	$\frac{4}{9}\frac{s^2+u^2}{t^2}$
$q\,q \to q\,q$	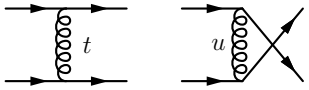	$\frac{4}{9}\frac{s^2+u^2}{t^2} + \frac{4}{9}\frac{s^2+t^2}{u^2} - \frac{8}{27}\frac{s^2}{tu}$
$q\,\bar{q} \to q'\,\bar{q}'$	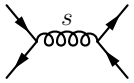	$\frac{4}{9}\frac{t^2+u^2}{s^2}$
$q\,\bar{q} \to q\,\bar{q}$	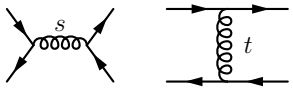	$\frac{4}{9}\frac{s^2+u^2}{t^2} + \frac{4}{9}\frac{t^2+u^2}{s^2} - \frac{8}{27}\frac{u^2}{st}$
$q\,\bar{q} \to g\,g$	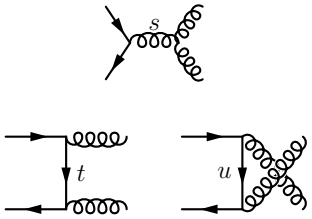	$\frac{32}{27}\frac{t^2+u^2}{tu} - \frac{8}{3}\frac{t^2+u^2}{s^2}$
$g\,g \to q\,\bar{q}$	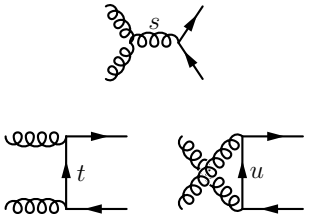	$\frac{1}{6}\frac{t^2+u^2}{tu} - \frac{3}{8}\frac{t^2+u^2}{s^2}$
$q\,g \to q\,g$	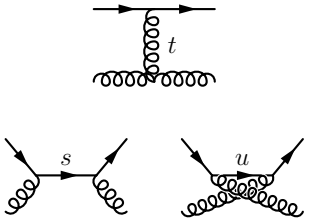	$-\frac{4}{9}\frac{s^2+u^2}{su} + \frac{s^2+u^2}{t^2}$
$g\,g \to g\,g$	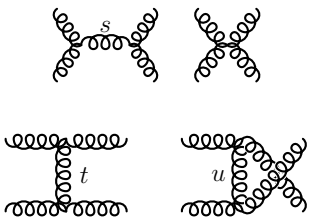	$\frac{9}{2}\left(3 - \frac{tu}{s^2} - \frac{su}{t^2} - \frac{st}{u^2}\right)$

Table 1.1: Diagrams for $2 \to 2$ QCD parton scatterings and the expression for the squared matrix elements when calculated explicitely [7] in terms of the Mandelstam variables $s = (p_1 + p_2)^2$, $t = (p_3 - p_1)^2$ and $u = (p_3 - p_2)^2$.

stem from an optimal elimination of common sub-expressions.

The second of the mentioned tasks, the multi-dimensional phase space integration, then has to be performed using Monte-Carlo methods. This includes the generation of phase-space events in the multi-dimensional phase space, which might be complicated by non-trivial cuts.

1.2 Parton shower

As motivated earlier, the generation of events at parton level like in the previous section is not sufficient for many applications in experimental high energy physics. Instead, they should be connected to a universal hadronisation model operating at scales where α_s becomes large and perturbative methods cannot be applied anymore. The evolution of partons between the scale of the hard scattering and the hadronisation scale is the task of the parton shower.

It is related to the concept of parton distribution functions which are based on the idea that collinear singularities can be factorised off a matrix element calculation. While the PDFs have to be known at a given scale of that process they are typically measured at a different scale and then evolved by a set of equations. The underlying physics of a parton shower can be described by the same kind of evolution equations. Only the question is reformulated: Given a parton that was produced at a scale t', determine a new scale $t < t'$ at which it should branch into two daughter partons and select the flavours and kinematics of those. The term scale is deliberately vague at this stage. Various parton showers exist which use different functional forms of that scale. They are all proportional to the invariant mass of the branching, $t \sim m^2$, but can take the form of e.g. an angle between the partons, or the relative transverse momentum produced. These branchings are then applied recursively to the produced partons and only stopped at a cutoff scale in the order of the hadronisation scale, resulting in a simulation of the parton branching cascade governed by the principles of QCD.

1.2.1 Master evolution equations

The evolution of a parton distribution function g_a between two scales t and t' can be described by the integral form of the DGLAP equation [8],

$$g_a(x,t) = g_a(x,t') + \int_{t'}^{t} \frac{\mathrm{d}\tau}{\tau} \int_x^1 \frac{\mathrm{d}\xi}{\xi} \frac{\alpha_s}{2\pi} \sum_{b=q,g} \hat{\mathcal{K}}_{ab}(\xi,\tau)\; g_b(\frac{x}{\xi},\tau)\;. \tag{1.3}$$

Stated in a simplified manner, the parton ensemble at a lower scale t is given by the ensemble at the higher scale t' and the integrated probability for all parton branchings that can happen between these scales.

The kernels $\hat{\mathcal{K}}_{ab}$ represent the regularised splitting functions. They are obtained from ratios of the corresponding real-emission and Born matrix elements in the soft and collinear limits. As will be detailed in Section 3.1.2, in those limits a real matrix element $\mathcal{R}$ can be approximately factorised into the Born-level matrix element $\mathcal{B}$ and a universal splitting kernel:

$$\mathcal{R}(\xi, \tau; \Phi_N) \;\to\; \sum_{a,b} \mathcal{B}_a(\Phi_N)\, \frac{1}{\tau}\, 8\pi\, \alpha_s\, \mathcal{K}_{ab}(\xi, \tau) \tag{1.4}$$

Here Φ_N denotes the respective N-particle phase space configuration, which does not play a role for the limiting behaviour of $\mathcal{R}(\xi, \tau; \Phi_N)$. For the most common case of standard DGLAP evolution, the kernels are easily identified with the splitting functions $P_{ab}(\xi)$. Another example is given for a dipole-like formulation in Section 1.2.2.

To arrive at a probabilistic interpretation of Equation (1.3), it is rewritten in differential form and divided by $g_a(x,t)$:

$$\frac{t}{g_a(x,t)}\, \frac{\mathrm{d}}{\mathrm{d}t}\, g_a(x,t) = \int_x^1 \frac{\mathrm{d}\xi}{\xi}\, \frac{\alpha_s}{2\pi} \sum_{b=q,g} \hat{\mathcal{K}}_{ab}(\xi, t)\, \frac{g_b(x/\xi, t)}{g_a(x,t)} \;\equiv\; \mathcal{I}_a(x,t)\;, \tag{1.5}$$

defining the differential branching probability $\mathcal{I}_a(x,t)$.

Up to this point the evolution was written in a completely inclusive form, i.e. the energy fraction ξ produced in branchings was allowed to reach $\xi = 1$ and regularised splitting functions had to be used for that reason. If one wants to introduce a resolution criterion like a cutoff at the hadronisation scale in a parton shower, the limit for the ξ integration becomes $\xi_{\max}(t_0) < 1$ and due to unitarity constraints the probability for no branching to happen above the resolution scale becomes non-zero.

The no-branching probability for a parton a produced at scale t' and resolved at t can be derived by multiplying the differential no-branching probabilities $1 - \mathcal{I}_a(x,t)$ for the infinitely many steps of size $\mathrm{d}t$ between t' and t. This leads to an exponentiation to give the no-branching probability [9]:

$$\mathcal{P}^{(B)}_{\mathrm{no},\,a}(x, t, t') = \;\exp\left\{ -\int_t^{t'} \frac{\mathrm{d}\tau}{\tau} \int_x^{\xi_{\max}} \frac{\mathrm{d}\xi}{\xi} \sum_{b=q,g} \frac{\alpha_s(\xi,\tau)}{2\pi}\, \mathcal{K}_{ba}(\xi,\tau)\, \frac{g_b(x/\xi,\tau)}{g_a(x,\tau)} \right\}\;. \tag{1.6}$$

Note that the derivation so far is valid for constrained evolution like in the case of initial-state backward evolution "towards" an incoming hadron. For constrained final state

evolution the ratio of PDFs in Equation (1.6) would turn into a ratio of fragmentation functions (FF) for a specific hadron species. But in Monte-Carlo generators the final state evolution is done in an unconstrained manner and the ratio of FFs drops out of the equation. At the same time the double counting of identical final states must be avoided, which is reflected by the additional factor $\frac{1}{2}$:

$$\mathcal{P}^{(F)}_{\mathrm{no},\,a}(t,t') = \exp\left\{-\int_t^{t'}\frac{\mathrm{d}\tau}{\tau}\int_{\xi_{\min}}^{\xi_{\max}}\frac{\mathrm{d}\xi}{\xi}\sum_{b=q,g}\frac{1}{2}\,\frac{\alpha_s(\xi,\tau)}{2\pi}\,\mathcal{K}_{ab}(\xi,\tau)\right\}. \tag{1.7}$$

The standard procedure for constructing a parton-shower algorithm is to write the branching probability $\mathcal{P}_{\mathrm{branch,\,a}}$ as

$$\mathcal{P}_{\mathrm{branch,\,a}}(x,t,t') = \frac{\partial\mathcal{P}_{\mathrm{no,\,a}}(x,t,t')}{\partial\log(t/\mu^2)} \;\rightarrow\; f(t)\,\exp\left\{-\int_t^{t'}\mathrm{d}\tau\,f(\tau)\right\}, \tag{1.8}$$

where the x argument has been dropped for brevity and $\mathcal{I}(x,t)\to f(t)$. A new scale t is therefore found as

$$t = F^{-1}\left[\,F(t') + \log R\,\right] \qquad \text{where} \qquad F(t) = \int^{t}\mathrm{d}\tau\,f(\tau)\,, \tag{1.9}$$

and where R is a random number between zero and one.

If the integral $F(t)$ is not known analytically, one can resort to the "veto" algorithm [2] for the random generation of the new scale t by using an overestimate $g(t)\geq f(t)$ with a known integral $G(t)$. Firstly, a value t is generated as $t = G^{-1}\left[\,G(t') + \log R\,\right]$. Secondly, the value is accepted with probability $f(t)/g(t)$ using a hit-or-miss method. A splitting at t with n intermediate rejections is then produced with differential probability

$$\begin{aligned}\mathcal{P}_n(t,t') = {}& \frac{f(t)}{g(t)}\,g(t)\,\exp\left\{-\int_t^{t_1}\mathrm{d}\tau\,g(\tau)\right\}\\ &\times\prod_{i=1}^{n}\left[\int_{t_{i-1}}^{t_{n+1}}\mathrm{d}t_i\left(1-\frac{f(t_i)}{g(t_i)}\right)g(t_i)\,\exp\left\{-\int_{t_i}^{t_{i+1}}\mathrm{d}\tau\,g(\tau)\right\}\right],\end{aligned} \tag{1.10}$$

where $t_{n+1} = t'$ and $t_0 = t$. The nested integrals in Equation (1.10) can be disentangled, and summing over n leads to the exponentiation of the factor $g(t) - f(t)$, such that Equation (1.8) is reproduced.

Equations (1.6) and (1.7) can also be written in terms of a Sudakov form factor [10]

defined as:

$$\Delta_a(\mu^2,t) \;=\; \exp\left\{ -\int_{\mu^2}^{t} \frac{\mathrm{d}\tau}{\tau} \int_{\xi_{\min}}^{\xi_{\max}} \mathrm{d}\xi \sum_{b=q,g} \frac{1}{2}\, \frac{\alpha_s(\xi,\tau)}{2\pi}\, \mathcal{K}_{ab}(\xi,\tau) \right\} . \tag{1.11}$$

They then take on the simple forms [7, 11]

$$\begin{aligned} \mathcal{P}^{(B)}_{\mathrm{no},a}(x,t,t') &= \frac{\Delta_a(\mu^2,t')}{\Delta_a(\mu^2,t)}\, \frac{g_a(x,t)}{g_a(x,t')} \\ \mathcal{P}^{(F)}_{\mathrm{no},a}(t,t') &= \frac{\Delta_a(\mu^2,t')}{\Delta_a(\mu^2,t)} \,. \end{aligned} \tag{1.12}$$

1.2.2 Parton shower based on Catani-Seymour dipoles

Note that any parton shower algorithm is uniquely defined by three ingredients: The first is the Sudakov form factor, $\Delta_a(t,t')$, i.e. the probability for a given parton, a, not to radiate another parton between the two evolution scales t' and t. The second is the ordering or evolution variable. While the Sudakov form factor defines the functional form of logarithms which are resummed, the evolution variable selects their argument, i.e. it defines a "direction" in the phase space, into which the evolution is performed. The third ingredient of a parton-shower model is the method, which is applied in order to reshuffle momenta of already existing partons when one of them goes off-shell to allow for a branching process.

It is possible to construct a parton-shower algorithm which uses Catani-Seymour dipole terms [12] as a basis for its splitting functions [13]. This means that the Sudakov form factor for final-state evolution reads

$$\Delta^{\mathrm{QCD}}_{(ij)}(t,t') \;=\; \exp\left\{ -\int_{t}^{t'} \frac{\mathrm{d}\mathrm{k}_\perp^2}{\mathrm{k}_\perp^2} \int_{\tilde{z}_-}^{\tilde{z}_+} \mathrm{d}\tilde{z} \sum_{i,k} \frac{1}{2}\, \frac{\alpha_s(\mathrm{k}_\perp^2)}{2\pi}\, \mathcal{K}^{\mathrm{QCD}}_{(ij)i,k}(\tilde{z},\mathrm{k}_\perp^2) \right\} , \tag{1.13}$$

where

$$\mathcal{K}^{\mathrm{QCD}}_{(ij)i,k}(\tilde{z},\mathrm{k}_\perp^2) \;= J(\mathrm{k}_\perp^2,\tilde{z})\, \langle \mathrm{V}^{\mathrm{QCD}}_{(ij)i,k}(\mathrm{k}_\perp^2,\tilde{z}) \rangle \qquad \text{and} \qquad \tilde{z} \;= \frac{p_i p_k}{(p_i+p_j)p_k} \,. \tag{1.14}$$

The Jacobian factor J and the spin-averaged dipole functions $\langle \mathrm{V} \rangle$ are defined in [13]. The sums run over all possible splitting products i and all possible spectator partons k of the splitting parton (ij). The ordering parameter is the invariant transverse momentum squared

$$\mathrm{k}_\perp^2 \;=\; \left(Q^2 - m_i^2 - m_j^2 - m_k^2\right)\, y_{ij,k}\, \tilde{z}_i(1-\tilde{z}_i) - (1-\tilde{z}_i)^2\, m_i^2 - \tilde{z}_i^2\, m_j^2 \,, \tag{1.15}$$

where $Q = p_i + p_j + p_k$, $y_{ij,k} = p_i p_j/(p_i p_j + p_j p_k + p_k p_i)$ and m are the parton masses.

The functional form of the spin-averaged splitting kernels is largely constrained by the infrared singularity structure of one-loop QCD amplitudes. It is, however, not fixed and one has the freedom to incorporate non-singular pieces, which can help to improve the predictions of dipole-shower simulations, cf. [14]. Likewise, the construction of the splitting kinematics is largely constrained by the phase-space variables selected in the splitting. It is, however, not fixed and one has one additional degree of freedom, which corresponds to the choice of the angular orientation of the splitter-spectator system with respect to the remaining particles.

1.2.3 Interleaved QCD+QED parton evolution

An analogous factorisation as discussed for QCD can be applied to QED real emission matrix elements leading to the development of a QED shower approach. Such emissions can be interleaved with a QCD parton shower, and a formalism to generate the combined QCD+QED parton evolution is recalled in this section. Similar approaches are implemented in most contemporary shower programs [2–4, 15, 16]. For simplicity of the argument the focus lies on pure final-state evolution.

Since QCD and QED emissions do not interfere, their corresponding emission probabilities factorise trivially. A combined QCD+QED evolution scheme is thus obtained by employing the combined Sudakov form factor

$$\Delta(\mu_0^2, Q^2) \;=\; \Delta^{\mathrm{QCD}}(\mu_0^2, Q^2)\, \Delta^{\mathrm{QED}}(\mu_0^2, Q^2)\;, \tag{1.16}$$

where

$$\mathcal{K}^{\mathrm{QED}}_{(ij)i,k}(\tilde{z}, \mathrm{k}_\perp^2) \;=\; J(\mathrm{k}_\perp^2, \tilde{z})\, \langle \mathrm{V}^{\mathrm{QED}}_{(ij)i,k}(\mathrm{k}_\perp^2, \tilde{z}) \rangle \tag{1.17}$$

and $\alpha_s \;\to\; \alpha$ with respect to the corresponding QCD expressions in Section 1.2.2. Note that spin-averaged dipole functions are used not only in the QCD but also in the QED case. One possible improvement of the present algorithm would therefore be to include the spin-dependent splitting kernels.

A crucial benchmark for such a combined QCD+QED shower algorithm is posed by the requirement to reproduce the scale-dependent photon fragmentation function $D_\gamma(z_\gamma, y_{\mathrm{cut}})$ [17], where z_γ is the photon's energy fraction with respect to its containing jet and y_{cut} a resolution scale, given e.g. in the Durham scheme. This observable was measured to very high precision in hadronic Z^0 decays by the ALEPH collaboration [18]. In this analysis events are selected where all final-state particles are

democratically taken into account for jet finding. The events are subdivided into 2-jet, 3-jet and $\geq$ 4-jet topologies with at least one reconstructed jet containing a photon where the photon carries at least 70% of the jet energy ($z_\gamma > 0.7$) and $E_\gamma > 5$ GeV. This is required to suppress contributions from non-prompt photons. The Monte-Carlo simulation agrees very well with the data which is exemplified in Figure 1.3. This can be seen as a strong indication that the combined QCD+QED shower scheme is indeed appropriate to describe hard photon radiation.

It is straightforward to extend the above algorithm to initial-state showering. The only subtlety in this context arises from the fact that the fully democratic approach pursued here also allows initial-state photon splitting into a quark-antiquark pair, with the quark (antiquark) initiating the hard scattering. In this case parton distributions which incorporate QED effects are in principle necessitated. Even though such PDF fits exist (e.g. [19]), the corresponding effects on physical observables should be very small, such that the usage of PDFs without QED contribution does not even pose a conceptual problem.

Efficiency improvements for photon fragmentation

An apparent disadvantage of the above algorithm when comparing to experimental data is the low efficiency with which isolated photons will be produced. To improve the statistical significance of event samples with identified photons described by the parton shower, it is useful to enhance the corresponding QED branching probabilities. When doing so, one must of course correct for this enhancement by means of an event weight, which depends on both, acceptance and rejection probabilities in the parton-shower evolution.

Recalling the veto algorithm in Section 1.2.1, the purpose here is to introduce an additional overestimate $h(t) = C\,g(t)$, where C is a constant. The additional weight $g(t)/h(t) = 1/C$ is then applied analytically rather than using a hit-or-miss method. This leads to the following expression for the differential probability to generate an emission at t with n rejections between t and t'

$$\begin{aligned}\mathcal{P}_n(t,t') \;=\; & \frac{f(t)}{g(t)}\,h(t)\,\exp\left\{-\int_t^{t_1}\mathrm{d}\tau\,h(\tau)\right\}\times\;\frac{1}{C}\prod_{i=1}^{n}\frac{g(t_i)-f(t_i)/C}{g(t_i)-f(t_i)} \\ & \times\prod_{i=1}^{n}\left[\int_{t_{i-1}}^{t_{n+1}}\mathrm{d}t_i\left(1-\frac{f(t_i)}{g(t_i)}\right)h(t_i)\,\exp\left\{-\int_{t_i}^{t_{i+1}}\mathrm{d}\tau\,h(\tau)\right\}\right]\,.\end{aligned} \tag{1.18}$$

The second factor in the first line of Equation (1.18) gives the analytic weight associated with this event, where the term $1/C$ is due to the acceptance of the emission with

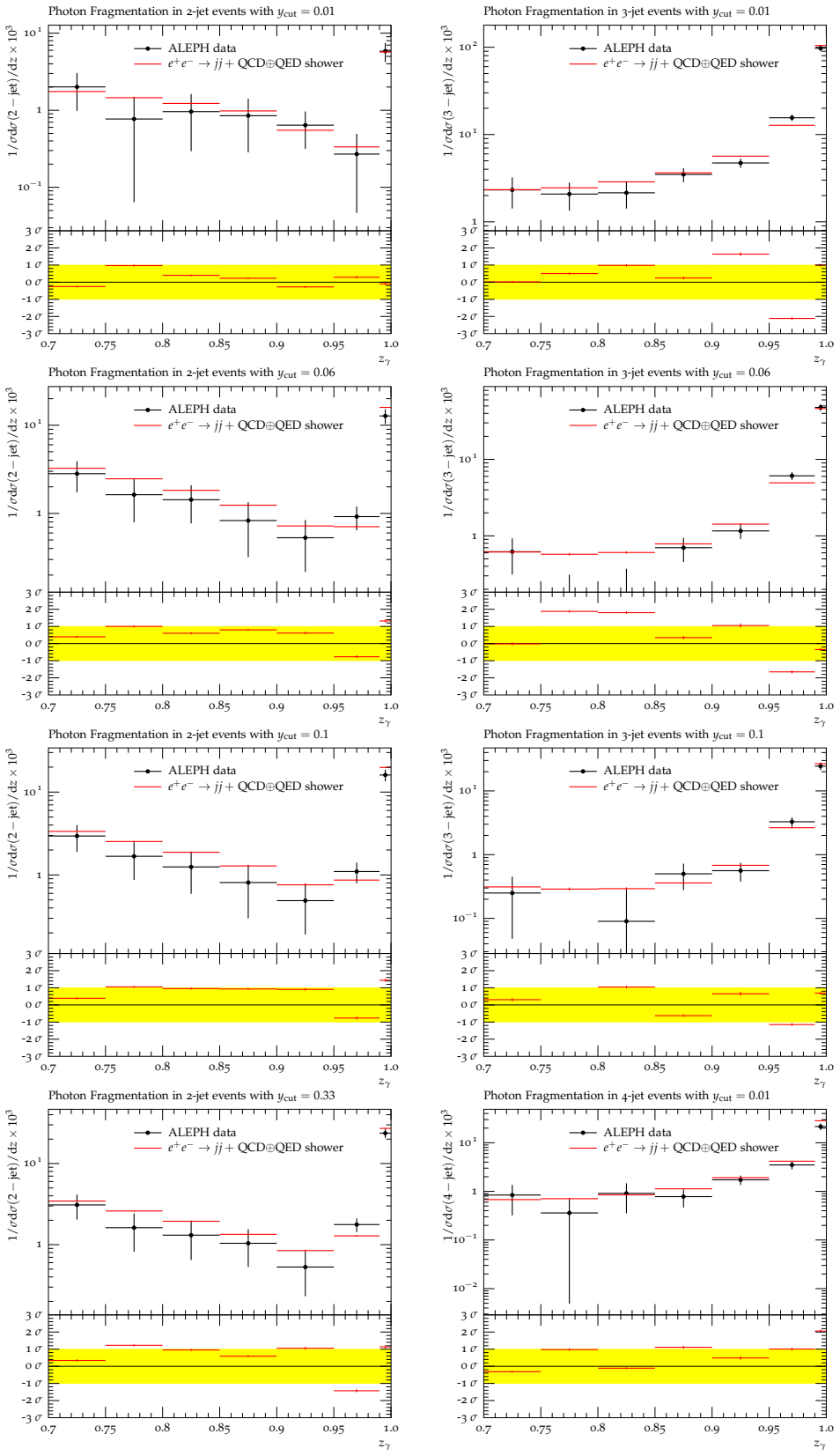

Figure 1.3: The z_γ distribution measured in hadronic Z^0 decays by ALEPH [18] for 2-jet, 3-jet and $\geq$ 4-jet events at different Durham resolution y_{cut}. The theory result corresponds to QCD+QED shower evolution of the leading-order $q\bar{q}$ process, taking into account hadronisation corrections.

probability $f(t)/h(t)$. The product, which is needed for an exponentiation of $h(t)-f(t)$ instead of $g(t)-f(t)$, runs over all correction weights for rejected steps.

Only with such an efficient algorithm is it feasible to make predictions for hard photon production with a pure parton-shower approach.

1.3 Hadronisation and hadron decays

After the parton shower has terminated, a configuration of coloured partons at some low scale of the order of a few GeV emerges. These partons, in order to match experiments, have to be transformed into hadrons. Since there is no first-principles approach yielding quantitative results, hadronisation is achieved by phenomenological models only. Usually, they are based on some qualitative ideas on how the parton-to-hadron transition proceeds, like, e.g. local parton-hadron duality or infrared safety, defining the model's coarse properties. However, many of the important finer details, often related to how flavour is created and distributed in the procedure, are entirely undefined and subject to phenomenological parameters only. These are essentially free and must be fixed by extensive comparisons with data, as done for instance in [20, 21].

The most used hadronisation models can be roughly divided into two categories. In the Lund string model [22], quarks are connected into strings along colour lines, within which an intense chromomagnetic field leads to the creation of more quark pairs through tunnelling. The basic assumption in the cluster-hadronisation model [23] is local parton-hadron duality, i.e. the idea that quantum numbers on the hadron level follow very closely the flow of quantum numbers on the parton level. In this framework, the mass spectrum of the emerging colour-neutral clusters is dominated by typical hadron masses or masses slightly above. It is therefore natural to think of them as some kind of "hadron matter", carrying the flavour and momentum quantum numbers of hadrons. This motivates to translate the light clusters directly into hadrons or, if they are too heavy, to treat them like hitherto unknown heavy hadron resonances, which decay further into lighter ones.

In all cases, the final state of the hadronisation phase will contain hadrons which are unstable and decay further. Experiments usually define particles above a certain mean lifetime as stable and correct their measurements to such a definition. Accordingly, a Monte-Carlo simulation has to account for the decay of all particles with a mean lifetime below that. The complexity of the emerging hadronic final-states and the multitude of hadron decays make it impossible to implement and calculate matrix elements and the phase space for a full final state consisting of stable particles only. It is necessary to

resort to the construction of "chains" of subsequent decays.

A natural starting point for the description of such cascades is the branching ratios collected in the PDG tables [24], and to choose according to them the decay channel for individual hadrons. Having selected a specific decay mode, its decay kinematics needs to be modelled. In order to go beyond an isotropic distribution of decay products in the phase space, explicit matrix elements are often employed. They are usually inferred from the spin structure and similar symmetries of the initial and final state, giving rise to only a few amplitudes. This simple picture can be further refined by invoking form factors for certain transitions – notable examples are the weak transitions of heavy quarks of the type $b \to c$ or $b \to u$, typically used in semileptonic decays of heavy hadrons, or FFs emerging for hadronic currents in τ-decays.

Naively, it looks like a reasonable as well as feasible approximation to deal with each decay of the cascade completely independently. Nevertheless, looking a bit more carefully reveals that complete independence is not always a valid assumption. Clearly, the spin structure of decaying and intermediate particles potentially leads to non-trivial correlations among them and other intermediate particles possibly emerging in the primary decay. An algorithm has been presented in [25] to take such non-trivial correlations into account and is implemented in many event generators.

1.4 Multiple parton interactions

The hardest (primary) partonic interaction in hadronic collisions may be accompanied by softer (secondary) ones between the beam remnants. This is a valid assumption and clear evidence has come from experimental studies carried out by the CDF collaboration at the Fermilab Tevatron during Run I and Run II [26–28]. It was shown that a correct description at the hadron level of particle multiplicities and jet activities can only be achieved by Monte Carlo event generators that incorporate a model for multiple parton interactions (MPI).

Such a model is beyond factorisation and no approach from first principles exists. However, two types of models [29,30] have been developed and implemented in various event generators and successfully compared to data from the Tevatron and LHC. The basic idea of such a model is to postulate the probability distribution for the occurrence of multiple scatterings. The starting point for this postulation is the observation that the dijet cross section as calculated perturbatively exceeds the total non-diffractive cross section determined e.g. from Regge fits [31] and additional assumptions about the ratio of diffractive and non-diffractive cross sections [32]. The solution for this

discrepancy lies in a reinterpretation: The ratio of $\sigma_{\text{hard}}/\sigma_{\text{total}}$ is interpreted as the mean number of scatters per event assuming Poisson statistics. The hard dijet matrix elements have to be regularised e.g. with a minimum jet resolution cut Q_{cut}, to obtain a well-defined differential cross section in perturbation theory. This cut is a crucial parameter of those models, into which a dependence on the centre of mass energy of the respective collider is usually absorbed.

According to the PYTHIA model of [29] the equation for the mean number of scatters per event is further supplemented with a form factor $f(b)$ which models the overlap of the hadrons and depends on the impact parameter of the collision:

$$\langle n \rangle = f_c f(b) \frac{\sigma_{\text{hard}}}{\sigma_{\text{total}}}. \tag{1.19}$$

Different models can be used for the hadron shapes, e.g. exponential, Gaussian or double Gaussian distributions. The impact parameter is calculated on an event-by-event basis from the hardness of the primary collision.

The JIMMY model [30] works with the same master formula, but here the overlap function is motivated by the electromagnetic form factor instead of making an ad-hoc Ansatz. It contains significantly fewer parameters than the PYTHIA model.

Nonetheless, all MPI models come with parameters that cannot be predicted from first principles and have to be tuned using experimental data at various collision energies. This is going to be the topic of the second part of this thesis.

2 Higher-order tree-level matrix elements and parton showers

With the LHC operational, searches for new physics beyond the Standard Model will enter a new stage. Despite all optimism, a majority of the signals currently discussed suffers from severe backgrounds, among them many related to the production of heavy SM particles, such as the weak gauge bosons or top quarks, accompanied with jets. Therefore, it is a central issue for many experimental analyses to correctly describe the production of these particles in conjunction with additional jets. In many cases, the method of choice is to employ simulation programs. In the past, such event generators have proved to be extremely useful and versatile tools, being well capable to describe comparably simple event topologies at sufficiently high precision. However, especially, when additional hard jets complicate the overall event structure, a proper simulation is far from being trivial. Typically such extra radiation is approximated with leading-logarithmic accuracy through the probabilistic description provided by the parton-shower approach. With rising precision needs, however, improved methods become mandatory, which describe the radiation of additional particles beyond the leading-logarithmic approximation employed by the parton showers.

The most traditional of these methods consists in reweighting QCD emissions as described by the parton shower with respective exact matrix elements expressed through parton-shower variables [33]. Unfortunately, the applicability of this method, however elegant, is constrained to cases, where the parton-shower expression either exceeds the matrix element or can be modified accordingly, without hampering the event generation efficiency too badly. This limits the method to a few cases such as the production of a gluon in $e^+e^- \to q\bar{q}$, top-quark decay plus emission of an additional gluon, or the production of vector bosons in hadron collisions.

An alternative approach, aiming at an improved description of multi-jet topologies, has been pioneered in [34] and a complete algorithm was proposed in [35]. The idea here is to separate the phase space for parton emission into two domains, a hard region of jet production and a softer regime of intra-jet evolution. This separation is achieved through a $k_\perp$-type jet measure [36, 37]. Then matrix elements for different parton

multiplicities are used to describe the production of a corresponding number of jets, whereas the parton shower is constrained such that it does not produce any additional jets. Independence of the overall result at logarithmic accuracy on the cut in the jet measure is achieved by the interplay of Sudakov form factors and the vetoed parton shower with suitable starting conditions. A similar approach, formally equivalent in e^+e^- annihilations into hadrons and often called CKKW-L, has been formulated in [38]. In this case a dipole shower rather than a more traditional parton cascade is used to describe QCD radiation beyond fixed order. Another, more simplified method, often called the MLM-prescription, has been introduced in [39]. The differences between the three merging prescriptions have been investigated using the example of W-production at the Tevatron and the LHC [40]. Although the three methods are different and the formal relationship of the latter method with the two former ones could not be completely worked out there, the results presented in these studies are in astonishing agreement. First steps towards such a more formal comparison between the three algorithms has been attempted in [41].

This chapter describes an improved merging algorithm that preserves the logarithmic accuracy of the shower. This is proven in the most general case, including initial state QCD particles. Although the prescriptions above deal with this case as well, up to now no statements of the formal accuracy beyond the leading logarithms has been made in the literature.

Building on top of the concepts introduced in Section 1.2 the procedures necessary to consistently evolve parton showers from matrix elements of arbitrary final-state multiplicity are introduced in Section 2.1. This is one of the key ingredients of the envisaged merging approach. Section 2.2 presents the general merging procedure. It also sets the theoretical background of the new approach and introduces the event generation algorithm. It is viable for, in principle, arbitrary parton-shower algorithms. It is shown that the new procedure exactly reproduces the logarithmic accuracy of the shower.

The same concepts introduced above for QCD emissions are then also applied to the merging of QED emissions from matrix elements and QCD/QED-interleaved parton showers.

Finally, results of the algorithm are presented. QCD corrections are tested in e^+e^- annihilations into hadrons at LEP I and Drell-Yan-like production of gauge bosons at the Tevatron. Results from interleaved QCD/QED merging are compared to data from the Tevatron for hard photon production.

2.1 Prerequisites

Merging matrix elements with parton showers combines two essentially different approaches to perturbative QCD. Hard matrix elements are exact at some fixed perturbative order in the strong coupling α_s and are therefore efficient in describing exclusive events with fixed jet multiplicity, taking into account non-trivial interferences between different amplitudes. Parton showers are employed to generate the QCD radiation pattern, especially at lower scales, close to the hadronisation scale Λ_{QCD}. Their application resums potentially large logarithmic corrections due to Bremsstrahlung effects. In their description they naturally cannot take into account all interferences, although steps towards including more quantum mechanical effects are currently being discussed, cf. [42]. In a simulation, best results can be expected, if the two approaches are combined consistently, such that each of them operates in those regions of phase space that it describes best.

This necessitates that parton showers can evolve from parton configurations which are given by high multiplicity matrix elements at certain points in phase space and colour space. In such cases the starting conditions for parton showers are often ambiguous. One will see in Section 2.2 that for running the shower in merged samples, it is necessary to interpret the matrix element as a core process and a series of predefined shower branchings. The reason is that the parton-shower evolution can take place at any point in this branching history, giving rise to the truncated shower prescription described in Section 2.1.2. There may be various such histories arising from the same matrix-element configuration. Hence the most appropriate one needs to be identified. Typically, in the spirit of the probabilistic picture underlying the parton shower, it is simply assumed that this is chosen according to their respective probabilities.

In this section the formalism and the algorithms necessary to identify that shower history are derived. Also, the concept of truncated showers is explained and various strategies to define colour assignments for the shower input are discussed.

2.1.1 Shower histories from matrix elements

An obvious point in the parton-shower algorithm sketched in Section 1.2 is to define the first or hardest scale, at which the parton shower starts off. In order to obtain such suitable starting conditions for parton showers from arbitrary matrix elements, a clustering algorithm needs to be defined, which corresponds to "running the shower evolution backwards" on the respective matrix element. It identifies how, in a parton-shower picture, the matrix element would have originated from a lower multiplicity

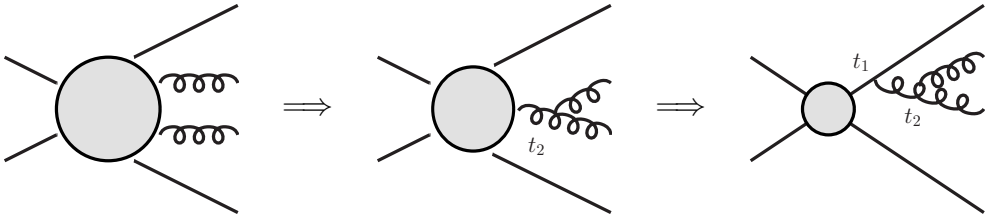

Figure 2.1: Determining a clustering history with two cluster steps.

matrix element and a shower branching. Applied iteratively, it leads to the definition of a core process, which cannot be further decomposed and a sequence of shower branchings yielding the actual final state, as exemplified by Figure 2.1. The tasks for the algorithm are thus twofold: Firstly, within an arbitrary n-parton final state a splitting in terms of shower evolution starting with $n-1$ partons needs to be found according to the splitting probabilities defined by the shower. Secondly, corresponding partons must be recombined to obtain the respective final state. In order to construct this algorithm, the shower evolution simply has to be "inverted", which gives the following recipe:

The criterion of the cluster algorithm is defined by the shower evolution kernels.

The recombination scheme is given by the inverted shower kinematics.

A side effect of this prescription is that during backward clustering the hard matrix elements, potentially no strict hierarchy is found in the shower evolution parameter. However, such situations can only arise for kinematic configurations of the matrix element, which are beyond the accuracy of the shower. Therefore they do not pose a problem here.

2.1.2 Truncated showering

Assume a parton-shower history constructed from a matrix element along the lines of Section 2.1.1 and consisting of a core process plus two additional branchings at scales $t_{1,2}$, which are called matrix-element branching and generate partons separated with $Q_{1,2} > Q_{\text{cut}}$. As a consequence of Equations (1.7) and (1.6), parton shower emissions may take place at scales t' with $t_1 > t' > t_2$ because the requirement $Q' < Q_{\text{cut}} < Q_{1,2}$ does not imply $t' < t_{1,2}$.

This leads to a situation, where, due to additional partons originating from these branchings, the kinematics of the matrix-element branching at t_2 needs to be redefined. This corresponds to a truncated shower, identical to the situation discussed in [43], where a mismatch between hardest emission, in terms of transverse momentum, and

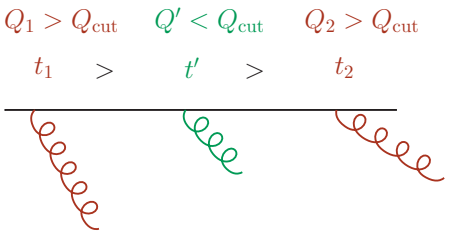

Figure 2.2: Example configuration for truncated showering.

the parton-shower evolution defined in opening angles has been noted and resolved. There the solution to this situation has been coined "truncated showering", because the evolution stops at the lower, dynamical scale t_2, unlike ordinary shower evolution, which stops at the universal cutoff scale. A prescription to unambiguously reconstruct the kinematics of matrix-element branchings is needed. The most natural choice is to compute the evolution, splitting and angular variables of matrix element branchings in the shower scheme and reconstruct the branching using the shower kinematics, after the final state of the branching at $t' > t_2$ is fully determined. In other words:

> Splitting kernels introduced by Equation (1.4) define evolution, splitting and angular variables in the shower scheme, rather than the kinematics of the corresponding branching.

This coincides with the fact that such branchings are interpreted as predetermined nodes during shower evolution. It must simply be guaranteed that the evolution stops at the corresponding scale, inserts the node and restarts afterwards. If for any reason (e.g. energy-momentum conservation) the matrix element branching cannot be reconstructed after a truncated shower branching, this shower branching must be vetoed.

2.1.3 Colour treatment

The treatment of colour is a central issue when dealing with matrix element and shower generation in QCD processes. Shower formulations inherently are correct only at leading order in $1/N_C$, although in [42] first attempts to overcome this limitation have been presented. Therefore, once matrix elements are to be combined with showers, the treatment of colour must be adjusted. A simple and obvious way to do so is to interpret the hard matrix element in the large-N_C limit to define colour partners of splitting partons in the shower language. This problem is more easily solved, when colours are not summed over but if an algorithm is employed, which unambiguously assigns a certain set of colours to the external particles in the hard matrix element. The basic idea is then to sample over colours in a Monte Carlo fashion rather than

summing over them.

It was pointed out in [44, 45] that the colour-flow decomposition of QCD amplitudes is advantageous over both the fundamental and (if existent) the adjoint representation decomposition. The key point is that in the colour-flow decomposition each colour octet is treated as a 3×3 index field whose additional degree of freedom is removed by a projector onto the colour-octet subspace. Since this issue is central to all simulations incorporating fixed colour assignments in the hard matrix element, the basics of the algorithm are briefly recalled. As an example the n-gluon amplitude $\mathcal{A}(1, \ldots, n)$ is considered. This amplitude can be decomposed in the colour-flow basis as [44]

$$\mathcal{A}(1, \ldots, n) = \sum_{\sigma \in S_{n-1}} \delta^{i_1 \bar{\jmath}_{\sigma_2}} \delta^{i_{\sigma_2} \bar{\jmath}_{\sigma_3}} \ldots \delta^{i_{\sigma_n} \bar{\jmath}_1} \, A(1, \sigma_2, \ldots, \sigma_n) \ . \tag{2.1}$$

Here i_{σ_k} and $\bar{\jmath}_{\sigma_k}$ denote the 3- and $\bar{3}$-index of parton σ_k, respectively and the sum runs over all possible permutations of the set $\{2, \ldots, n\}$. The quantities $A(1, \sigma_2, \ldots, \sigma_n)$ are called colour-ordered or partial amplitudes. They depend on the kinematics of the process only. All information about colour is incorporated in respective prefactors. Therefore any colour-ordered amplitude only contains planar diagrams, which greatly alleviates the computation. A convenient way to interpret Equation (2.1) is to consider it as the decomposition of the full QCD amplitude into subamplitudes in the large-N_C limit. Feeding the results from the matrix-element calculation into a shower program, the corresponding colour connections are thus readily determined if one of the terms in the sum is chosen according to its probability and identifies the colour flow according to its colour factor. In this context the fact is used that interference terms between two different colour structures are always subleading in $1/N_C$.[1]

An algorithm to choose a colour structure according to its probability could thus look as follows (cf. [47])

1. Compute the full matrix element with randomly assigned colours for external QCD partons.

2. Identify all possible permutations $\{1, \vec{\sigma}\}$, which yield a non-zero value of

$$\delta^{i_1 \bar{\jmath}_{\sigma_2}} \delta^{i_{\sigma_2} \bar{\jmath}_{\sigma_3}} \cdots \delta^{i_{\sigma_n} \bar{\jmath}_1} \ . \tag{2.2}$$

   Label them by $\vec{\sigma}_i$ and compute the corresponding partial amplitudes $A(1, \vec{\sigma}_i)$.

3. If $N_{\vec{\sigma}}$ is the number of identified permutations, choose a partial amplitude with

[1] This argument holds in the colour-flow decomposition and the fundamental representation decomposition. For the latter, see for example [46].

probability

$$P_{\vec{\sigma}_i} = \frac{|A(1,\vec{\sigma}_i)|^2}{\sum_{j=1}^{N_{\vec{\sigma}}} |A(1,\vec{\sigma}_j)|^2} \tag{2.3}$$

Because of the way potential partial amplitudes are identified in the colour-flow decomposition, this prescription is similar to the following simplified strategy

1. Compute the full matrix element with randomly assigned colours for external QCD partons.

2. Assign colours in the large-N_C limit at random, respecting the actual point in colour space. This translates into two partons only being colour adjacent at large N_C, if they were colour adjacent at finite N_C.

3. Identify the corresponding permutation $\vec{\sigma}$ and compute the partial amplitude $A(1,\vec{\sigma})$. Accept the configuration with probability

$$P_{\vec{\sigma}} = \frac{|A(1,\vec{\sigma})|^2}{|\mathcal{A}(1,\ldots,n)|^2} \tag{2.4}$$

Naively, the drawback of the latter algorithm is, that potentially many points have to be drawn for the colour assignment at large N_C. In practice, however, this is sufficiently fast compared to evaluating all possible partial amplitudes for a single nontrivial point in colour space. Also, in principle the full amplitude squared, $|\mathcal{A}(1,\ldots,n)|$, might be much smaller than the sum of partial amplitudes squared, such that acceptance probabilities are modified. This algorithm is still sufficiently accurate, since respective differences are always subleading in $1/N_C$.

The above algorithm works for arbitrary QCD and QCD-associated matrix elements, since quark pairs can always be reinterpreted as colour octet objects. Matrix-element configurations might exist, which do not allow an immediate projection onto large N_C because of the U(1) pseudo-gluon. In this case, a new point in colour space can safely be assigned, because the respective contribution to the total cross section is subleading.

2.2 An improved merging algorithm

The central idea for algorithms merging matrix elements with parton showers is to replace products of splitting kernels related to hard emissions in the shower evolution with the appropriate matrix elements, thus reinstalling information about the full hard process under consideration. Directly implementing a ratio of hard matrix elements

in form of a splitting kernel has the apparent disadvantage that the respective phase-space integration proceeds in terms of shower kinematics and is thus hard to optimise in a generic way. A better technique is to first compute the matrix element and then reweight it such that, to the accuracy of the parton shower, the corresponding shower expression is obtained. To pursue this strategy, the corresponding no-emission probabilities of the parton shower, i.e. its Sudakov form factors, must be known. This can, however easily be achieved because they emerge directly from the evolution equations on which the shower is based.

Only one additional ingredient is eventually needed, namely a criterion, which defines how to separate matrix-element and parton-shower domain. It will be shown in Section 2.3 that a general form of this criterion can be found, which is based on the soft and collinear behaviour of QCD at the next-to-leading order. This will be referred to as the "jet criterion". At the present stage, the precise form of the jet criterion is unimportant and it is sufficient and helpful to think of it in an abstract way.

2.2.1 Construction of the algorithm

The basic idea of the merging – to separate the matrix-element and parton-shower domains through a cut in the emission phase space, defined by a jet criterion – corresponds to a simple phase-space slicing. Therefore, the evolution kernels for the matrix-element and parton-shower domains are defined

$$\begin{aligned}\mathcal{K}_{ab}^{\mathrm{ME}}(\xi,\bar{t}) &= \mathcal{K}_{ab}(\xi,\bar{t})\,\Theta\left[Q_{ab}(\xi,\bar{t})-Q_{\mathrm{cut}}\right]\\ \mathcal{K}_{ab}^{\mathrm{PS}}(\xi,\bar{t}) &= \mathcal{K}_{ab}(\xi,\bar{t})\,\Theta\left[Q_{\mathrm{cut}}-Q_{ab}(\xi,\bar{t})\right]\ ,\end{aligned}$$

where Q_{ab} denotes the jet criterion and Q_{cut} is its cut value. Correspondingly, the two partial Sudakov form factors are given by

$$\Delta_a^{\mathrm{ME/PS}}(\mu^2,t)=\exp\left\{-\int_{\mu^2}^{t}\frac{\mathrm{d}\bar{t}}{\bar{t}}\int_{\xi_{\min}}^{\xi_{\max}}\mathrm{d}\xi\sum_{b=q,g}\frac{1}{2}\,\frac{\alpha_s(\xi,\bar{t})}{2\pi}\mathcal{K}_{ab}^{\mathrm{ME/PS}}(\xi,\bar{t})\right\}\ . \tag{2.5}$$

They are related to the full Sudakov form factor, Equation (1.11), through

$$\Delta_a(\mu^2,t)=\Delta_a^{\mathrm{PS}}(\mu^2,t)\,\Delta_a^{\mathrm{ME}}(\mu^2,t)\ . \tag{2.6}$$

In fact, Equation (2.6) effectively encodes the complete merging approach. There, ultimately $\mathcal{K}^{\mathrm{ME}}$ will be replaced with a ratio of matrix elements, according to Equation (1.4). During the following rewrite of the evolution equations one simply identifies, how the factorisation property of Sudakov form factors must then be interpreted and

employed for event generation. No further proof for the correctness of the algorithm at any logarithmic order is necessary, because this follows directly from the accuracy implemented in the parton-shower evolution. In other words, the proposed merging scheme does not impair the logarithmic accuracy of the parton shower.

This can be summarised as:

> When correcting parton-shower evolution kernels through higher-order matrix elements, the master evolution equations, cf. Section 1.2.1, must be respected. This ensures that the accuracy generated by the factorisation scheme and the parton shower is fully restored.

To start deriving the implications for event generation, the conditional backward no-branching probability in the parton-shower domain is defined[2],

$$\begin{aligned}\tilde{\mathcal{P}}^{(B)\,\mathrm{PS}}_{\mathrm{no},\,a}(z,t,t') &= \frac{\Delta_a^{\mathrm{PS}}(\mu^2,t')\,\tilde{g}_a(z,t)}{\Delta_a^{\mathrm{PS}}(\mu^2,t)\,\tilde{g}_a(z,t')} \\ &= \exp\left\{-\int_t^{t'}\frac{\mathrm{d}\bar{t}}{\bar{t}}\int_z^{\zeta_{\max}}\frac{\mathrm{d}\zeta}{\zeta}\sum_{b=q,g}\frac{\alpha_s(\zeta,\bar{t})}{2\pi}\,\mathcal{K}^{\mathrm{PS}}_{ba}(\zeta,\bar{t})\,\frac{\tilde{g}_b(z/\zeta,\bar{t})}{\tilde{g}_a(z,\bar{t})}\right\}\,.\end{aligned} \tag{2.7}$$

It would correspond to a modified evolution equation for $\tilde{g}_a(z,\bar{t})$ with respect to the standard parton-shower evolution because of the Θ-function, restricting emissions to $Q < Q_{\mathrm{cut}}$, i.e. the soft and collinear domain. Its interpretation is therefore straightforward and gives a rule for the modified shower algorithm in the merging:

> Standard parton-shower evolution is implemented, but radiation with $Q > Q_{\mathrm{cut}}$ is vetoed.

Note that for the case of an initial-state parton shower, typically described with a backward evolution, the initial scale of the PDFs is set by the core process of the event.

If Equation (2.7) is employed as is, including the phase-space restriction, the newly defined functions $\tilde{g}$ do not obey the same evolution as the original functions g. Factorisation is thus violated. If one wants the two evolutions to agree, one has to guarantee that the full no-branching probability in the merging approach is given by Equation (1.12). This leads to the definition of the no-emission probability in the matrix-element domain according to

$$\mathcal{P}^{(B)\,\mathrm{ME}}_{\mathrm{no},\,a}(t,t') = \frac{\mathcal{P}^{(B)}_{\mathrm{no},\,a}(z,t,t')}{\mathcal{P}^{(B)\,\mathrm{PS}}_{\mathrm{no},\,a}(z,t,t')} = \frac{\Delta^{\mathrm{ME}}(\mu^2,t')}{\Delta^{\mathrm{ME}}(\mu^2,t)}\,, \qquad \text{where} \tag{2.8}$$

[2]From here on the description focuses on backward evolution. The corresponding reasoning for forward evolution follows trivially.

$$\mathcal{P}_{\mathrm{no},a}^{(B)\,\mathrm{PS}}(z,t,t') = \frac{\Delta_a^{\mathrm{PS}}(\mu^2,t')\,g_a(z,t)}{\Delta_a^{\mathrm{PS}}(\mu^2,t)\,g_a(z,t')}\ . \tag{2.9}$$

It is interesting to note that $\mathcal{P}_{\mathrm{no},a}^{(B)\,\mathrm{ME}}$ is independent of z, which effectively is an outcome of the factorisation properties of PDF's and FF's.

If one assumes that a "most probable" shower history of the hard matrix element is identified through a backward-clustering algorithm, which employs the clustering criterion and the recombination scheme of the shower, cf. Section 2.1.1, then one obtains the rule:

> The weight, Equation (2.8), is assigned to any leg with production scale t' and decay scale t found during backward clustering. Strong couplings are evaluated at the nodal scales of parton recombination.

The reasoning is easily explained. Hard matrix elements in the factorisation scheme of the shower have the same limiting behaviour as the splitting kernels $\mathcal{K}$, once colour-adjacent partons become close in phase space. Backward clustering will identify a hierarchical structure for the factorisation of hard matrix elements into lower-multiplicity matrix elements and splitting kernels. Eventually, a core process is found, which cannot be further decomposed and which corresponds to the starting conditions for a respective shower evolution. Matrix elements, however, do not implement the no-branching probabilities generated by parton showers. Also the strong coupling is evaluated at a common scale, rather than the nodal scales of splittings. Corresponding corrections must therefore be implemented.

An immediate consequence of the above defined algorithm is that the total cross section of merged samples can only be influenced by the difference between full hard matrix elements and the corresponding product of splitting kernels times the core process. In this respect, one obtains the rule:

> To compute hadronic cross sections, PDF's must be evaluated at the scale of the core process defined through backward clustering.

This prescription is independent of the multiplicity of the matrix element, because showering always starts at the scale of the core process. A mismatch in the two scales would lead to ill-defined backward no-branching probabilities.

2.2.2 Event generation techniques

Event generation according to the above defined merging procedure proceeds along the following lines:

- Relevant multi-jet cross sections for the process under consideration are calculated with the phase-space restriction $Q > Q_{\text{cut}}$. Strong couplings are computed such that they give an overestimate, which can later on be reweighted. PDF's are evaluated at the scale set by the core process, which is defined by the backward clustering process.

1. Events are generated according to the above defined cross sections with kinematics determined by the respective matrix elements.

2. Matrix elements are interpreted in the large N_C limit according to methods discussed in Section 2.1.3. The most probable shower history of the final state is determined through backward clustering, cf. Section 2.1.1. The clustering is guided by information from the matrix element, which restricts the available shower histories to those, which correspond to a Feynman diagram.

3. The event is accepted or rejected according to a kinematics-dependent weight, which corresponds to evaluating strong couplings in the shower scheme and computing the no-branching probability, Equation (2.8), for each parton, internal or external, in the clustered matrix element.

4. The parton-shower evolution is started with suitably defined scales for intermediate and final-state particles. During showering, any emission harder than Q_{cut} is vetoed. Intermediate partons undergo a truncated shower evolution, cf. Section 2.1.2

This algorithm has the apparent drawback, that the no-emission probability Equation (2.8) must be computed before the parton-shower evolution starts. Ideally, however, it should result as a direct consequence of parton-shower branchings producing hard partons. Such splittings would obviously fall in the realm of matrix elements and are thus forbidden inside the parton shower. To obtain a corresponding prescription, the above algorithm is slightly reformulated.

Firstly, the differential branching probabilities $\mathcal{P}_{\text{no},\,a}^{(B)\,\text{ME/PS}}$ are defined according to Equation (1.5) as

$$\mathcal{I}_a^{(B)\,\text{ME/PS}}(z,\bar{t}) = \int_z^{\zeta_{\max}} \frac{\mathrm{d}\zeta}{\zeta} \sum_{b=q,g} \frac{\alpha_s(\zeta,\bar{t})}{2\pi}\, \mathcal{K}_{ba}^{\text{ME/PS}}(\zeta,\bar{t})\, \frac{g_b(z/\zeta,\bar{t})}{g_a(z,\bar{t})}\,. \tag{2.10}$$

From Equation (1.8) one then obtains the full branching probability in terms of $\mathcal{I}^{(B)\,\text{ME/PS}}$,

$$\mathcal{P}_{\text{branch},\,a}^{(B)\,\text{ME}\oplus\text{PS}}(z,t,t') = \left[\, \mathcal{I}_a^{(B)\,\text{ME}}(z,t) + \mathcal{I}_a^{(B)\,\text{PS}}(z,t) \,\right] \exp\left\{ -\int_t^{t'} \frac{\mathrm{d}\bar{t}}{\bar{t}}\, \mathcal{I}_a^{(B)}(z,\bar{t}) \right\}, \tag{2.11}$$

where $\mathcal{I}_a^{(B)} = \mathcal{I}_a^{(B)\,\mathrm{ME}} + \mathcal{I}_a^{(B)\,\mathrm{PS}}$. Equation (2.11) corresponds to generating an ordering parameter t in unconstrained shower evolution, i.e. without the restriction to $Q < Q_{\mathrm{cut}}$. The first term in the square bracket is however given by hard matrix elements through Equation (1.4). In order not to double count this contribution, corresponding branchings must lead to rejection of the entire event. This modifies the respective cross section by

$$\sigma \to \sigma \cdot \mathcal{P}_{\mathrm{no},\,a}^{(B)\,\mathrm{ME}}(t, t') \,. \tag{2.12}$$

Due to this event rejection, the remaining branching probability for accepted parton-shower steps is given by (cf. the description of the veto algorithm in Section 1.2.1)

$$\begin{aligned} \mathcal{P}_{\mathrm{branch},\,a}^{(B)\,\mathrm{PS}}(z, t, t') = \mathcal{I}_a^{(B)\,\mathrm{PS}}(z, t)\, \exp\left\{ -\int_t^{t'} \frac{\mathrm{d}\bar{t}}{\bar{t}}\, \mathcal{I}_a^{(B)}(z, \bar{t}) \right\} \\ \times \exp\left\{ \int_t^{t'} \frac{\mathrm{d}\bar{t}}{\bar{t}}\, \left[\mathcal{I}_a^{(B)}(z, \bar{t}) - \mathcal{I}_a^{(B)\mathrm{PS}}(z, \bar{t}) \right] \right\} , \end{aligned} \tag{2.13}$$

which yields the vetoed shower algorithm described by Equation (2.7), but with $\tilde{g} = g$, as required.
One therefore obtains the modified rules

3. The event is accepted or rejected according to a kinematics dependent weight, which corresponds to evaluating strong couplings in the parton-shower scheme.

4. The parton-shower evolution is started with suitably defined scales for intermediate and final-state particles. Intermediate partons undergo truncated evolution. During showering, any emission harder than Q_{cut} leads to the rejection of the event.

Note that in principle these two steps could be combined through evaluating the strong couplings during the shower evolution.

2.2.3 Highest multiplicity treatment

An apparent problem of the merging algorithm outlined so far is that only a limited final-state multiplicity $N \leq N_{\max}$ can be generated through full matrix elements. Hence the matrix elements will not produce jet multiplicities $N > N_{\max}$ that are in principle possible. Hence, the parton shower must account for missing emissions above Q_{cut} at large N. This is explained in detail in the following.

Assume a case where $N = N_{\max}$ emissions in the matrix-element domain have been accounted for by the matrix element and have been generated through the above defined

algorithm. This means that up to this point, i.e. up to the scale where the last matrix-element emission can be resolved in terms of the parton-shower evolution parameter, the branching probability, Equation (2.11) has been employed, as it should be. Beyond this point, no further emission can be generated through matrix elements, and the branching probability becomes

$$\mathcal{P}^{(B)\,\mathrm{ME}\oplus\mathrm{PS}}_{\mathrm{branch},\,a}(z,t,t') \to \mathcal{P}^{(B)\,\mathrm{ME}}_{\mathrm{no},\,a}(t,t')\,\frac{\partial\mathcal{P}^{(B)\,\mathrm{PS}}_{\mathrm{no},\,a}(z,t,t')}{\partial\log(t/\mu^2)}\,. \tag{2.14}$$

Relation (2.14) would obviously violate factorisation, because of missing terms, corresponding to the integrated kernel from the matrix-element domain.

This problem can be circumvented by implementing the standard parton-shower evolution beyond the last matrix-element emission.[3] It guarantees that the parton shower respects the description of hard radiation throughout the regime where matrix elements are applicable, while still filling the remaining phase space.

This prescription is referred to as the highest multiplicity treatment and has been suggested in a similar form in [48]. In virtuality ordered DGLAP evolution, it approximately corresponds to setting a local veto scale $Q_{\mathrm{cut}} \to Q_{\mathrm{min}}$ if $N = N_{\mathrm{max}}$, where Q_{min} is the minimum jet criterion found during backward clustering.

2.2.4 Sources of uncertainties

The proposed merging algorithm combines two essentially different approaches to perturbative QCD. Any simulation based on it therefore contains a number of sources of theoretical uncertainties. They can be separated into two categories, merging-related and non-merging-related uncertainties. The latter would occur in standard perturbative approaches as well, when using only hard matrix elements or applying only parton showers. The merging-related uncertainties are instead specific for the combined application of matrix elements and showers and arise from the following:

- The functional form of the jet criterion.
  Since the jet criterion separates matrix-element and parton-shower domain, a variation of its precise definition can enhance or reduce the contribution of the hard matrix elements in certain regions of phase space.

- The value of the phase-space separation cut, Q_{cut}.
  As for the jet criterion itself, the precise value of the separation cut enhances or

[3] The term "beyond" refers to the ordering parameter t. Note that the respective scale is set globally for the event, because the matrix element connects all parton-shower evolutions.

reduces the amount of phase space which is described by hard matrix elements and can therefore lead to variation of the results.

- The maximum number of jets simulated by hard matrix elements, $N_{\max}$.
  This parameter limits the number of hard partons up to which correlations can be expected to be correctly described at tree-level.

Other uncertainties are related to the perturbative calculations carried out in the matrix-element and parton-shower simulation itself. They include:

- Scale uncertainties from matrix elements.
  They arise due to the particular choice of factorisation and renormalisation scale of the leading-order process.

- Scale uncertainties from parton showers.
  They arise due to the particular choice of coupling scales within the evolution.

- Uncertainties from the parton density functions employed.
  Parton density functions not only enter the cross section calculation when considering hadronic initial states but also appear in the calculation of the branching probabilities for the initial-state parton shower, for a detailed discussion of the latter see e.g. [49].

- Uncertainties due to the choice of the leading-order process.
  These uncertainties arise in processes which potentially contain many additional jets with shower evolution parameters above the factorisation scale of the leading-order process.

In the following the merging-related uncertainties will be studied. The functional form of the jet criterion is not varied though, but rather an optimal choice for the merging is employed, see Section 2.3.

2.3 The jet criterion

An important aspect in the QCD evolution equations, cf. Section 1.2.1, is that QCD branchings are logarithmically enhanced at small values of the evolution parameter t and/or at logarithmically large values of the evolution kernels $\mathcal{K}$. This is the manifestation of the singular infrared behaviour of QCD amplitudes in the respective regions of phase space. In perturbative calculations employing hard matrix elements these regions therefore must be regularised. This is typically achieved by identifying parton

samples or individual partons with jets and demanding the jets to be sufficiently isolated. Algorithms defining jets are, for example, the Durham k_T-algorithm [36] and the longitudinally invariant k_T algorithms for deep inelastic scattering and hadron-hadron collisions [37]. Extensions of those algorithms to include jet flavour have been presented in [50]. Their respective measures are often used as a variable in which phase-space separation is defined for matrix element - parton shower merging, cf. [35].

Here a similar criterion is proposed. However, in contrast to jet measures like the ones above, which can be applied to experimentally observable final states and which yield experimentally well defined jets, this criterion is designed and applied on purely theoretical grounds. It is based on the behaviour of QCD amplitudes at the next-to-leading order and employs flavour and colour information of the respective partons. For the purposes here this criterion proved to be advantageous over standard k_T algorithms as it correctly identifies individual infrared enhanced QCD branchings.

2.3.1 Definition

Consider two partons i and j, which can, in terms of flavour and colour, originate from a common mother parton (the splitter) $\widetilde{ij}$. The following jet criterion is then proposed

$$Q_{ij}^2 \;=\; 2\,p_i p_j \,\min_{k\neq i,j}\, \frac{2}{C_{i,j}^k + C_{j,i}^k}\;, \tag{2.15}$$

where for final state partons i and j

$$C_{i,j}^k \;=\; \begin{cases} \dfrac{p_i p_k}{(p_i+p_k)p_j} - \dfrac{m_i^2}{2\,p_i p_j} & \text{if } j = g \\[2ex] 1 & \text{else} \end{cases}\;. \tag{2.16}$$

For initial state partons a, the splitting process $a \to (aj)\; j$ is considered. With the momentum of the combined particle (aj) given by $p_{aj} = p_a - p_j$, one defines

$$C_{a,j}^k \;=\; C_{(aj),\,j}^k\;. \tag{2.17}$$

The minimum in Equation (2.15) is over all possible colour partners k of the combined parton $\widetilde{ij}$, which can be thought of to act as spectators in the splitting process.

In the following, it is shown that this jet criterion indeed correctly identifies soft and collinear parton splittings in QCD matrix elements and is thus suited to separate the matrix-element from the parton-shower domain in the merging.

2.3.2 Soft limit

If the energy of a single gluon j tends to zero in any fixed direction q, described through $p_j = \lambda q$, $\lambda \to 0$, the above jet criterion behaves as

$$\frac{1}{Q_{ij}^2} \to \frac{1}{2\,\lambda^2}\,\frac{1}{2\,p_i\,q}\,\max_{k\neq i,j}\left[\frac{p_i p_k}{(p_i+p_k)\,q} - \frac{m_i^2}{2\,p_i q}\right] . \tag{2.18}$$

The corresponding singularity of the matrix element is thus correctly identified, cf. [12].

2.3.3 Quasi-collinear limit for final-state splittings

Consider two final-state partons i and j and an arbitrary spectator-parton k. Let $p_{ij} = p_i + p_j$ and let the light-like helper vectors l and n be defined by

$$\begin{aligned} p_{ij} &= l + \alpha_{ij}\,n\ , \\ p_k &= n + \alpha_k\,l\ . \end{aligned} \tag{2.19}$$

This system has the solution

$$l = \frac{1}{1-\alpha_{ij}\alpha_k}\,(p_{ij} - \alpha_{ij}\,p_k)\ , \qquad n = \frac{1}{1-\alpha_{ij}\alpha_k}\,(p_k - \alpha_k\,p_{ij})\ , \tag{2.20}$$

where $\alpha_{ij} = p_{ij}^2/\gamma$, $\alpha_k = p_k^2/\gamma$ and $\gamma = 2\,ln = p_{ij}p_k + \sqrt{(p_{ij}p_k)^2 - p_{ij}^2 p_k^2}$, cf. [51]. The momenta p_i and p_j can now be expressed in terms of l, n and a transverse component, $k_\perp$.

$$\begin{aligned} p_i^\mu &= z\,l^\mu + \frac{m_i^2 + \mathrm{k}_\perp^2}{z}\,\frac{n^\mu}{2\,ln} + k_\perp^\mu\ , \\ p_j^\mu &= (1-z)\,l^\mu + \frac{m_j^2 + \mathrm{k}_\perp^2}{1-z}\,\frac{n^\mu}{2\,ln} - k_\perp^\mu\ . \end{aligned} \tag{2.21}$$

A relation for p_{ij}^2 is immediately obtained,

$$p_{ij}^2 - m_i^2 - m_j^2 = \frac{\mathrm{k}_\perp^2}{z(1-z)} - \frac{1-z}{z}\,m_i^2 - \frac{z}{1-z}\,m_j^2\ . \tag{2.22}$$

Taking the quasi-collinear limit amounts to the simultaneous rescaling [52]

$$\mathrm{k}_\perp \to \lambda \mathrm{k}_\perp\ , \qquad m_i \to \lambda m_i\ , \qquad m_j \to \lambda m_j\ , \qquad m_{ij} \to \lambda m_{ij}\ . \tag{2.23}$$

Then, $2\,p_i p_j \to \lambda^2(p_{ij}^2 - m_i^2 - m_j^2)$ and, independent of k,

$$\frac{1}{Q_{ij}^2} \to \frac{1}{2\,\lambda^2}\,\frac{1}{p_{ij}^2 - m_i^2 - m_j^2}\,\left(\tilde{C}_{i,j} + \tilde{C}_{j,i}\right)\,. \tag{2.24}$$

Here,

$$\tilde{C}_{i,j} = \begin{cases} \dfrac{z}{1-z} - \dfrac{m_i^2}{2\,p_i p_j} & \text{if } j = g \\ \\ 1 & \text{else} \end{cases}\,. \tag{2.25}$$

Equation (2.25) corresponds to the leading term of the massive Altarelli-Parisi splitting function for $z \to 1$ [52]. The corresponding term for $z \to 0$ (if present) is generated by $\tilde{C}_{j,i}$.

2.3.4 Quasi-collinear limit for initial-state splittings

Now consider the initial-state parton a, the final-state parton j and an arbitrary spectator parton k. Let $p_{aj} = p_a - p_j$, and let the light-like helper vectors l and n be defined by

$$\begin{aligned} p_a &= l + \alpha_a\, n\,, \\ p_k &= n + \alpha_k\, l\,. \end{aligned} \tag{2.26}$$

Then l and n are found as before, Equation (2.20). The momenta p_{aj} and p_j are decomposed as follows

$$\begin{aligned} p_{aj}^\mu &= z\,l^\mu + \frac{p_{aj}^2 + \mathrm{k}_\perp^2}{z}\,\frac{n^\mu}{2\,ln} + k_\perp^\mu\,, \\ p_j^\mu &= (1-z)\;l^\mu + \frac{m_j^2 + \mathrm{k}_\perp^2}{1-z}\,\frac{n^\mu}{2\,ln} - k_\perp^\mu\,. \end{aligned} \tag{2.27}$$

Taking the quasi-collinear limit yields $2\,p_a p_j \to \lambda^2\left|p_{aj}^2 - m_a^2 - m_j^2\right|$ such that, independent of k

$$\frac{1}{Q_{aj}^2} \to \frac{1}{2\,\lambda^2}\,\frac{1}{\left|p_{aj}^2 - m_a^2 - m_j^2\right|}\,\left(\tilde{C}_{(aj),j} + \tilde{C}_{j,(aj)}\right)\,, \tag{2.28}$$

where $\tilde{C}_{(aj),j}$ is given by Equation (2.25).

2.4 Extension to QED emissions

The measurement of final states containing photons at large transverse momenta plays a key role in collider experiments. Most prominently at hadron colliders inclusive diphoton or diphoton + jet signatures are promising channels to search for a light Higgs boson [53]. Signatures with photons might furthermore provide access to physics beyond the Standard Model like supersymmetry or extra spatial dimensions [54]. Less spectacular but extremely important though, the photon + jet final state can be used to determine the absolute energy scale of low-p_T jets [55] and to constrain the gluon distribution inside the beam hadron [56]. The success of the outlined physics menu however strongly depends on the ability to thoroughly understand and accurately simulate such prompt-photon production processes in the context of the Standard Model.

In the framework of perturbation theory the mechanism of hard-photon production is twofold. A photon can be well-separated from any other particle in the collision, which makes it possible to describe the reaction with fixed-order matrix elements. The fact that these matrix elements include initial- and/or final-state QCD partons necessitates an all-orders resummation of large logarithmic QCD corrections, which are then absorbed into Parton Distribution Functions (PDFs) and Fragmentation Functions (FFs). Due to its vanishing mass, a photon can also be infinitely close to an initial- or final-state QCD parton. The related singularities in hard matrix elements are absorbed into process-independent photon fragmentation functions [57], describing the transition of a QCD parton into a bunch of hadrons and a not well-separated photon during the process of hadronisation. Due to the nonperturbative nature of the hadronisation process, parton-to-photon fragmentation functions contain a nonperturbative component and must therefore be determined from experimental data. Their evolution with the factorisation scale $\mu_{F,\gamma}$ can however be calculated perturbatively. While the description of hard photons through matrix elements is said to yield the direct component of photon observables, the description by fragmentation functions gives the so-called fragmentation component. Both components are related by factorisation and must be combined to obtain a meaningful prediction of QCD-associated photon production.

The standard method to theoretically devise a meaningful prompt-photon cross section is to reflect certain experimental photon-isolation criteria in perturbative calculations. However, one must allow for a minimal hadronic activity in the vicinity of the photon. Only then it can then be ensured that all QCD infrared divergences are properly cancelled. Several such criteria are on disposal, e.g. the cone approach [58, 59], the democratic approach [17, 60] and the smooth isolation procedure [61]. For both, single- and diphoton production at hadron colliders, the complete next-to-leading order QCD corrections to respective direct and fragmentation components are known [58, 62–65]. The

parton-level Monte Carlo programs JetPhox [66] and DiPhox [67] implement these NLO results numerically and allow the user to choose from different photon-isolation criteria. The NLO corrections to the direct channel $\gamma\gamma$ + 1jet have been calculated in [68]. The results for the loop-induced processes $gg \to \gamma\gamma$ [69] and $gg \to \gamma\gamma g$ [70, 71] are also available. Beyond calculations at fixed order in the strong coupling large efforts were spent on the evaluation of soft-gluon emission effects and on the resummation of corresponding large logarithms. Soft-gluon resummation up to next-to-next-to leading logarithmic accuracy is taken into account in the program ResBos [71, 72]. The analytic result for resumming threshold logarithms was presented in [73] while small-x logarithms have been studied in [74]. Only recently a first study of the prompt-photon process in the framework of Soft-Collinear Effective Theory has been presented [75].

There is a further source of final-state photons, namely decays of hadrons, such as π^0 or η. However, such non-prompt production processes can to some approximation be separated from the other two experimentally and measurements are usually corrected for these effects.

A different strategy of simulating final states including photons is pursued here. The hard scattering process, the QCD evolution of initial- and final-state partons, as well as the transition of QCD partons into hadrons is accounted for by means of a multi-purpose Monte-Carlo event generator. In this context the lowest-order matrix elements for single- and diphoton production supplemented with QCD parton showers correspond to the above mentioned direct component. The fragmentation contribution is modelled by the incorporation of QED effects into the parton shower, cf. Section 1.2.3. In fact, a generic algorithm to treat photon radiation is also given by the approach of Yennie, Frautschi and Suura [76]. This scheme is particularly suited to compute logarithmic corrections arising from soft photon radiation, where the coherent emission off all QED charges involved in the process plays an important role. Here, however, the interest lies primarily in the production of hard, well-separated photons. Such emissions need to be treated by an improved algorithm, see for example [77]. Photon radiation is therefore simulated using a dipole-like QED shower model. This approach only presents a primitive approximation to soft photon effects, but is easily realised and no additional free parameters are introduced in the parton-shower algorithm, cf. [78]. An apparent advantage is, that this method also allows for a direct comparison with experimental data since it yields predictions at the level of the experimentally observed particles. In particular the parton-to-photon fragmentation functions are explicitly modelled this way. As a consequence no further corrections accounting for the non-perturbative parton-to-hadron transition need to be applied and again no additional free parameters need to be introduced. This is crucial also for the validation of a separation of non-prompt photons from prompt photons as mentioned above. The

democratic treatment of partons and photons in this approach combines the direct and the fragmentation component in a very natural way. It is well suited for comparison to experiments, where it is often necessary to study the impact of photon-isolation criteria.

An apparent disadvantage of the approach is that it relies on lowest-order matrix elements only and correspondingly higher-order QCD corrections are taken into account in the approximation of the parton shower only. Here this deficiency is improved on by including higher-order real-emission matrix elements as described above.

2.4.1 Formalism

The formalism built up in Section 2.2 is extended to the case of prompt-photon production. This process, as stated before, introduces the additional complication of a second source of photon production – the fragmentation component – which is not present for massive gauge bosons. While in most cases of W- or Z-boson production the massive boson is the hardest object in the interaction, the photon is unlikely to play this role in most prompt-photon events. The presented formalism copes with this situation and allows to consistently combine tree-level matrix elements of variable photon and QCD parton multiplicity with a combined QCD+QED parton-shower model. Photons and QCD partons are treated democratically, i.e. higher-order tree-level matrix elements can be of order $\alpha^n \alpha_s^m$ compared to the leading order. If $n > 0$, they may directly contribute to an observed hard-photon final state. In this respect, the inclusion of higher-order real corrections corresponds to shifting the simulation of hard-photon production from the parton-shower to the matrix-element domain.

It is obvious that the same procedure as described for QCD in Section 2.2 can be applied to QED emissions, once they are resummed by the parton shower using Equation (1.16). It is then in principle possible to define two separate slicing cuts, $Q_{\text{cut}}^{\text{QCD}}$ and $Q_{\text{cut}}^{\text{QED}}$, which account for the merging of QCD and QED tree-level matrix elements with the parton shower, respectively. Within the context of this work, these slicing cuts are left identical, since the typical "hardness" of a hard well-separated final-state photon is similar to the one of a final-state QCD jet. But the functional form of the separation criterion can be adapted to the isolation definitions in experimental analyses.

2.4.2 Parton separation criterion

In prompt photon production processes one might be confronted with a situation which cannot arise in pure QCD events, namely that a single, perturbatively produced particle

– the photon – is identified out of potentially many particles forming a broad jet. Several methods exist to achieve this identification. In the democratic approach [17,60] final state particles are clustered into jets, treating photons and hadrons equally. The obtained object is called a photon or a photon jet, if the energy fraction $z = E_\gamma/(E_\gamma + E_{had})$ of an observed photon inside the jet is larger than an experimentally defined value z_{cut}. In the cone approach [58, 59] photons are required to have a minimum transverse momentum and to be isolated from any significant hadronic activity within a cone in η-ϕ-space. Minimal hadronic activity in the vicinity of the photon (adding of the order of a few GeV to the total transverse momentum in the cone) must thereby be admitted to ensure the infrared finiteness of observables.

While the jet criterion Equation (2.15) works very well also for photons defined by the democratic approach, in the case of the cone approach it might not be appropriate to separate matrix-element and parton-shower domain. Note that the main idea of the merging procedure is to improve the parton-shower prediction with fixed-order matrix elements in those regions of phase space which are relevant for the analysis of multi-jet (multi-photon) topologies. In this respect, it is certainly desirable that experimental requirements are reflected by Q^2_{ij}. This is possible because the jet criterion, Equation (2.15), is not fixed, but rather chosen conveniently to reflect the singularity structure of next-to-leading order real-emission amplitudes in QCD [11]. Moreover it is a flavour-dependent measure, which allows to redefine it just for branching processes involving photons. The most common experimental requirements of a minimum transverse momentum and an isolation cone in η-ϕ-space could for example be reflected by

$$Q^2_{ij} \;=\; \min\left\{p^2_{\perp,i}, p^2_{\perp,j}\right\} \frac{\Delta\eta^2_{ij} + \Delta\phi^2_{ij}}{D^2} \qquad \text{and} \qquad Q^2_{ib} \;=\; p^2_{\perp,i}\,, \tag{2.29}$$

where the first equation applies to final-state photons and charged final state particles, while the second applies to photons and charged beams. Note that Equation (2.29) is essentially equivalent to a longitudinally invariant jet measure [37]. One can now increase the ratio of photons produced through matrix elements over photons produced in the shower by simply lowering the value of $Q^{\mathrm{QED}}_{\mathrm{cut}}$. A convenient way to obtain the largest fraction of events from hard matrix elements is to require a jet separation below the experimental cut on the photon transverse momentum and by setting D lower than the radius of the experimentally imposed isolation cone.

2.5 Results

The methods described in this chapter have been implemented in full generality in the SHERPA event generator. The aim of this section is to exemplify the performance of these algorithms in various processes. Only a short selection of plots is shown for QCD jet production at LEP and Drell-Yan production at the Tevatron as these are going to be much improved and extensively discussed in Chapter 3.

The results shown here have been obtained using the SHERPA framework and the RIVET package [79] for the comparison to experimental analyses.

2.5.1 QCD jet production in e^+e^- collisions

To compare with LEP data from the Run I period, a setup with cms energy $\sqrt{s} = 91.25\,\text{GeV}$ is chosen and a merged sample of $e^+e^- \to (N+2)$ jets is produced at parton level, with N denoting the number of additional jets in the matrix element and $N \leq N_{\text{max}}$. N_{max} is varied between zero, i.e. no merging at all, and four.

Due to the close correspondence between the jet criterion, Equation (2.15), and the Durham measure for jets in e^+e^- collisions, differential jet rates are particularly suited to assess merging systematics. The rate $y_{n\,n+1}$ shows the jet measure at which $n+1$ jets are clustered into n jets according to the Durham k_T-algorithm. The phase-space separation cut Q_{cut} manifests itself as a narrow transition region between matrix-element and parton-shower domain around $y_{n\,n+1} \approx Q^2_{\text{cut}}/s$. Merging systematics can thus be inferred from deviations between samples with different phase-space separation cuts in this region.

Figure 2.3 shows the differential jet rates for a merged sample of up to four additional jets from the matrix element. The merging cuts, which have been used, are $\log_{10}(Q^2_{\text{cut}}/s) = -2.25$, $\log_{10}(Q^2_{\text{cut}}/s) = -1.75$ and $\log_{10}(Q^2_{\text{cut}}/s) = -1.25$. Only very small deviations between the predictions of the various samples are found.

Event-shape observables like thrust, sphericity and the energy-energy correlation are presented in Figure 2.4. Details about their definition and the corresponding data from experiment can be found in [21]. These observables are well described by an appropriately tuned pure parton-shower setup already, and no matrix element improvement is therefore necessary. On the other hand, the comparison between the pure parton-shower sample and merged samples constitutes an important consistency check. Very good agreement of the respective predictions is found.

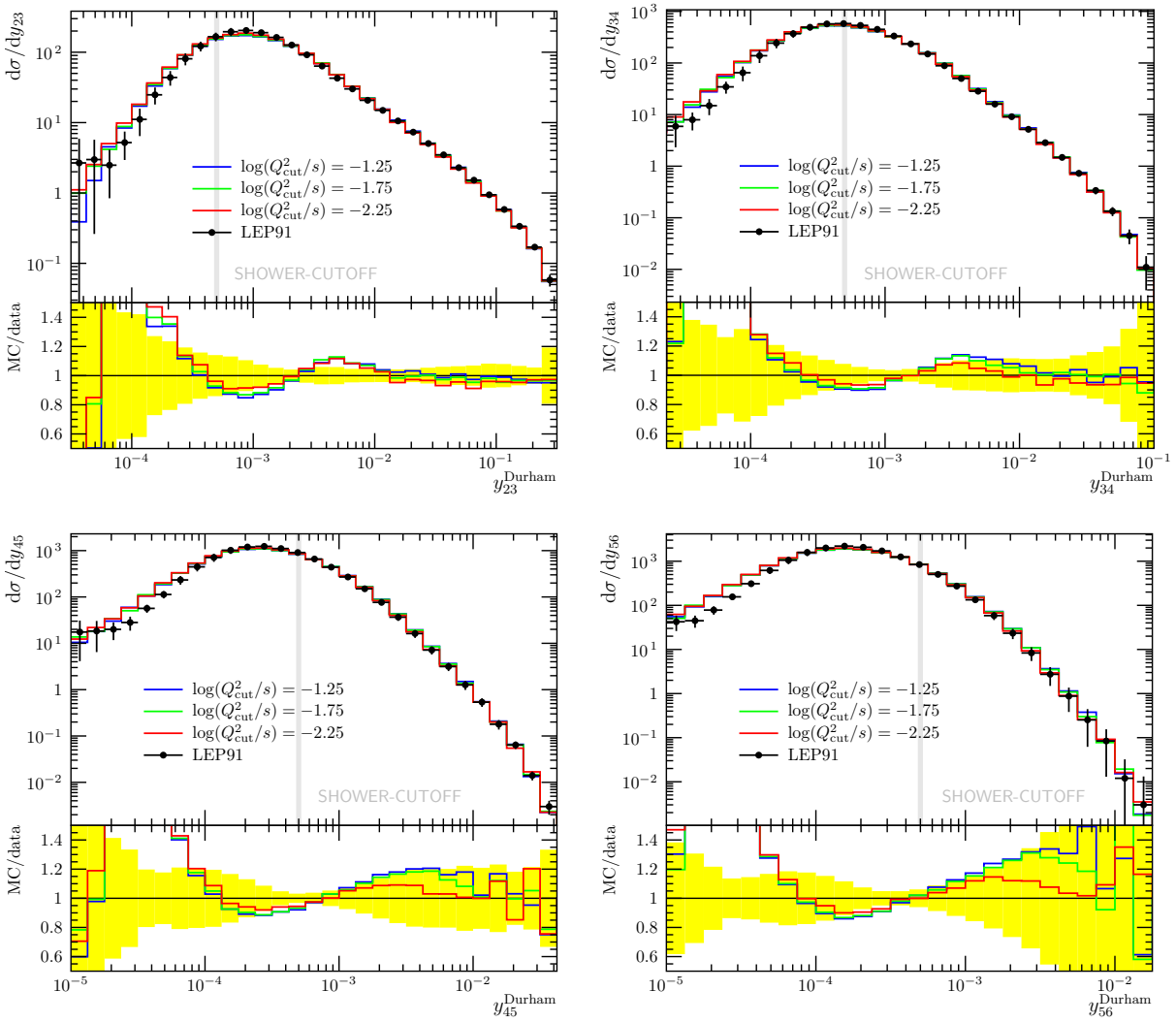

Figure 2.3: Differential jet rates for three different merging cuts compared to data from LEP [80].

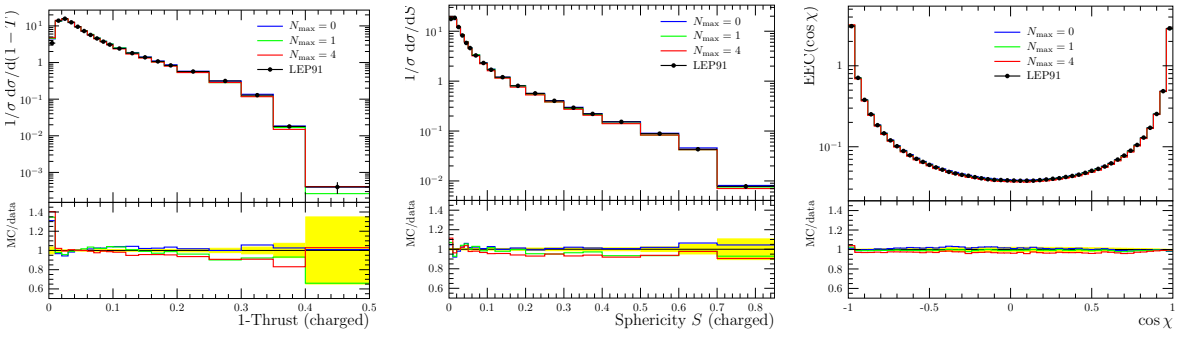

Figure 2.4: Event-shape observables simulated using different numbers of additional jets in the ME compared to data from LEP [21].

To investigate the influence of different strategies to handle colour in matrix-element generation and merging, the generators COMIX and AMEGIC++ are compared. COMIX is run in two different modes, corresponding to the two strategies of assigning colours in the large-N_C limit explained in Section 2.1.3. The following nomenclature is introduced:

'partial σ'
: selection of a colour assignment according to the proportionate squared partial amplitude corresponding to this large-N_C configuration (i.e. the *first* method presented in Section 2.1.3)

'random'
: selection of a colour assignment according to the ratio of the squared partial amplitude corresponding to this large-N_C configuration and the total amplitude squared (i.e. the *second* method presented in Section 2.1.3)

'heuristic'
: heuristic colour assignment to colour-summed amplitudes in AMEGIC++: The kinematics of the core process after backward clustering defines which diagram contributes most at the given phase space point and colour is assigned according to the colour structure of that diagram as a starting point.

Figure 2.5 shows predictions for the three different choices. Since the first configuration where different colour assignments could take effect arises in four-jet events, the selected observables are the $3 \to 4$ jet rate and the angle α_{34} between the two softest jets, selected on an event-by-event basis. Furthermore, the energy-energy correlation typically shows sensitivity to the connection of the hadronisation phase to the parton-shower output, and could thus depend on the colour setting as well. No significant differences between the various options is observed. This encourages to proceed with even the heuristic method, which allows to employ the merging technique with various kinds of matrix element generators, including those which do not allow a projection onto the large-N_C limit.

2.5.2 Drell-Yan lepton production in $p\bar{p}$ collisions

The scope of this section is to validate the proposed merging algorithm in collisions with hadronic initial states. One of the simplest processes in this setup is Drell-Yan lepton pair production. It constitutes an important testing ground to validate the applicability of the proposed jet criterion and the interplay of the merging algorithm with the PDF's.

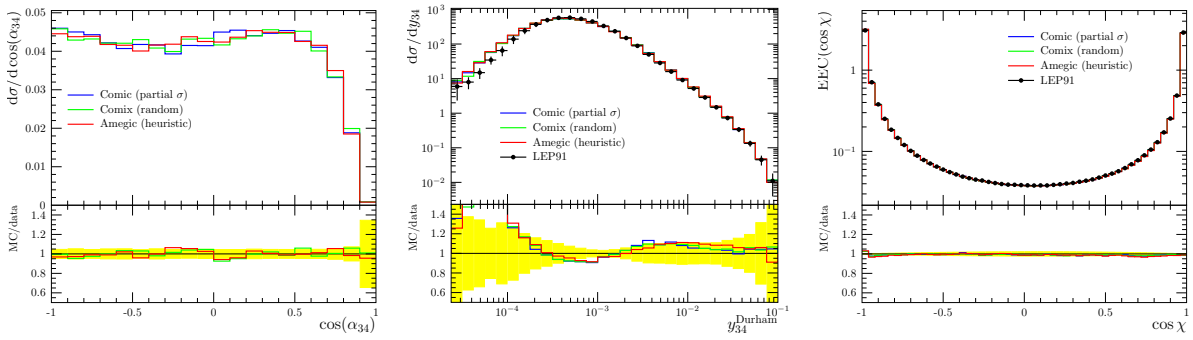

Figure 2.5: Different approaches to colour treatment and their effects on y_{34}, α_{34} and EEC. Data are taken from [21, 80].

		$N_{\max}$						
		0	1	2	3	4	5	6
Q_{cut}	20 GeV	192.6(1)	191.0(3)	190.5(4)	189.0(5)	189.4(7)	188.2(8)	189.9(10)
	30 GeV		192.3(2)	192.7(2)	192.6(3)	192.9(3)	192.7(3)	193.2(3)
	45 GeV		193.6(1)	194.4(1)	194.3(1)	194.4(1)	194.6(2)	194.4(1)

Table 2.1: Total cross sections [pb] in $p\bar{p} \to e^+e^- + \text{jets}$ at $\sqrt{s} = 1960\,\text{GeV}$ and their dependence on the merging cut.

Event generation has been set up for $p\bar{p}$-collisions at a centre-of-mass energy of $\sqrt{s} = 1960\,\text{GeV}$. For the hard process a merged sample of $p\bar{p} \to e^+e^- + N\,\text{jets}$ has been produced, where $N \leq N_{\max}$ with $0 \leq N_{\max} \leq 6$. In addition, a cut of $66\,\text{GeV} < m_{e^+e^-} < 116\,\text{GeV}$ has been applied at the matrix-element level. The factorisation scale has been chosen as $m^2_{e^+e^-}$. Note that the transverse mass squared of the lepton pair, $m^2_{T,e^+e^-} = m^2_{e^+e^-} + \text{k}^2_{\perp,e^+e^-}$, which is often selected as the factorisation scale in other merging approaches, is not a proper choice for the proposed algorithm. It is non-continuous with respect to the transverse momentum, $\text{k}^2_{\perp,e^+e^-}$, because the leading-order configuration is generated with $\text{k}^2_{\perp,e^+e^-} = 0$ and the minimum transverse momentum of events with one additional jet is limited by the phase-space separation cut.

At first a comparison of total cross sections predicted by the merging algorithm for various values of the separation criterion Q_{cut} and the maximum jet multiplicity $N_{\max}$ is presented. Table 2.1 shows the respective results. Differences range up to 2.3%, between the leading-order cross section and predictions for the merged samples, which is a reasonably low variation.

To study the merging systematics in more detail, again the differential jet rates $d_{n\,n+1}$ are investigated, describing the scales at which $n+1$ jets are clustered into n jets according to the CDF Run II k_T-algorithm. This algorithm has a free parameter, D, which accounts for the missing information on beam partons. Hence, in this setup, no firm relation can be established between the jet measure of the k_T-algorithm and the jet criterion, Equation (2.15). Nevertheless, a certain correspondence between the

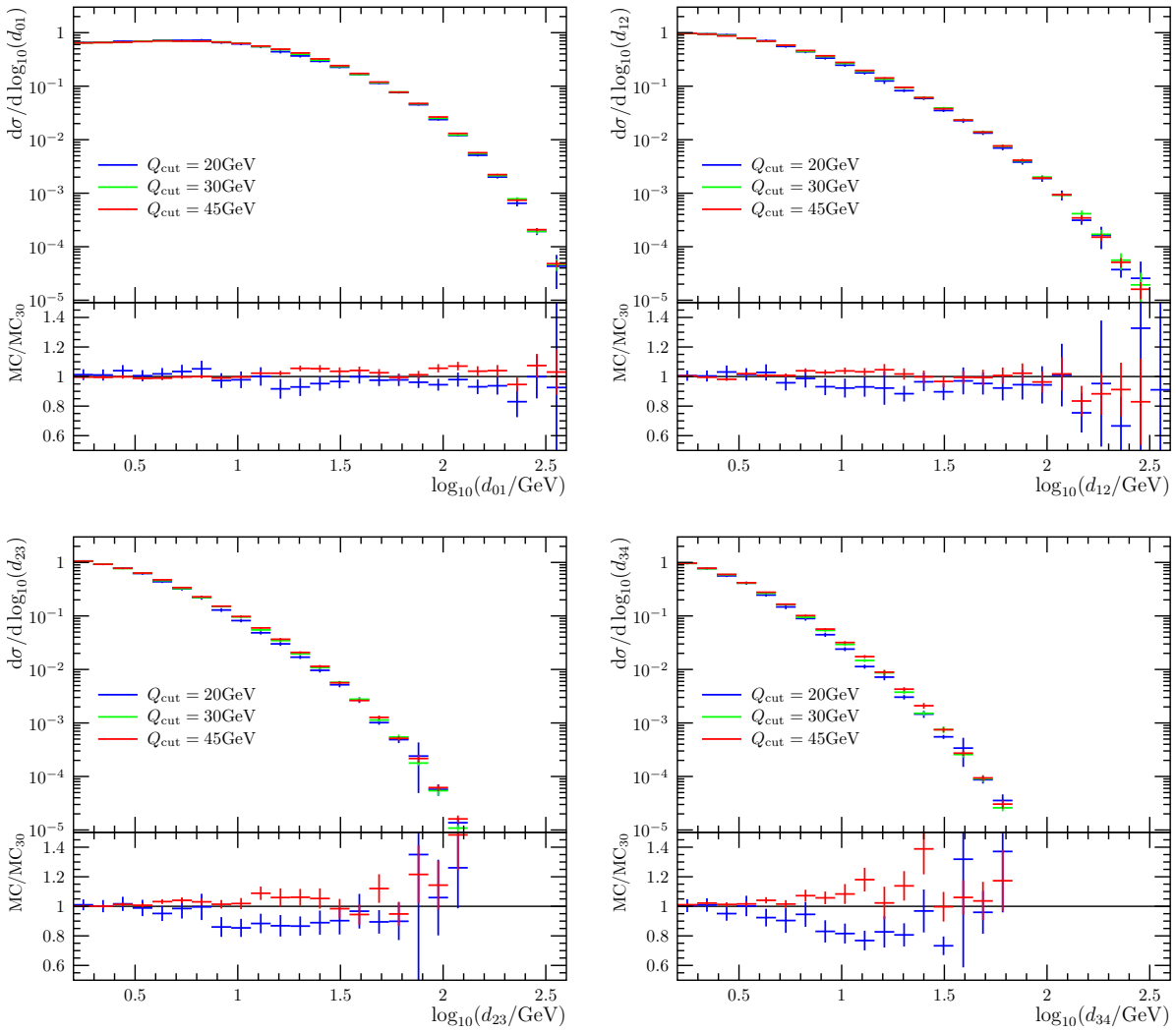

Figure 2.6: Differential jet rates $d_{n\,n+1}$ for three different merging cuts with fixed $N_{\text{max}} = 5$.

two quantities exists, making these distributions a good testing ground for variations around the merging cuts.

To produce Figure 2.6 a merged sample of up to five jets from the matrix element has been generated with COMIX and showered with the CSS. The merging cuts, which have been used, are $Q_{\text{cut}} = 20\,\text{GeV}$, $Q_{\text{cut}} = 30\,\text{GeV}$, and $Q_{\text{cut}} = 45\,\text{GeV}$. As in the case of e^+e^- collisions, the deviations between the predictions of the various samples are small.

2.5.3 Prompt-photon hadroproduction

The inclusive production of isolated photons has been measured over a wide range of photon transverse energies by the CDF and DØ experiments at the Fermilab Tevatron

at $\sqrt{s} = 1.96$ GeV. In [81] CDF has presented a measurement covering $|\eta_\gamma| < 1.0$ and transverse energies between $30 < E_{T,\gamma} < 400$ GeV. The photon isolation criterion used corresponds to the requirement that the additional transverse energy found in a cone of $R = \sqrt{(\Delta\phi)^2 + (\Delta\eta)^2} = 0.4$ around the photon is less than 2 GeV. A similar DØ measurement was described in [82]. It covers photons of transverse momentum $p_{T,\gamma} > 23$ GeV up to $p_{T,\gamma} = 300$ GeV and $|\eta_\gamma| < 0.9$. Photon isolation is implemented by demanding $(E_{R=0.4} - E_{R=0.2})/E_{R=0.2} < 0.1$, where E_R is the total energy found in a cone of size R around the photon. Both measurements have been corrected to particle level and the dominant background of photon production from hadron decays, such as $\pi^0 \to \gamma\gamma$ and $\eta \to \gamma\gamma$, has been subtracted. A comparison with Monte-Carlo predictions at the parton level after jet evolution but without hadronisation is therefore warranted.

Figure 2.7a compares the data for $d^2\sigma/(dE_{T,\gamma}d\eta_\gamma)$ from [81] and $d^2\sigma/(dp_{T,\gamma}d\eta_\gamma)$ from [82], to parton-level Monte-Carlo results, obtained using leading-order matrix elements in the democratic approach combined with QCD+QED shower evolution. In addition to the total result (red histograms), the contributions from the different classes of partonic core processes are displayed, i.e. from dijet production ($jj \to jj$), single-photon production ($jj \to \gamma j$) and diphoton production ($jj \to \gamma\gamma$). Taking into account the uncertainties of the measurements and the finite Monte-Carlo statistics in the high-$E_{T,\gamma}$ bins, the calculation agrees well with the data. For the CDF measurement the data has a somewhat steeper slope at low $E_{T,\gamma}$ and the Monte-Carlo calculation makes the high $E_{T,\gamma}$ end of the spectrum more pronounced. Regarding the different sources of final-state photons in the theoretical model, the main contribution to this observable stems from single photon production. But even though strict isolation criteria are applied, there is a considerable fraction of dijet events, where a hard, isolated photon is produced during the parton-shower evolution in both data samples. This substantiates the argument that the combined shower scheme is crucial for a proper description of such photon final states. The diphoton core process on the other hand is negligible here.

Let us now turn to study the impact of higher-order real-emission matrix elements on the results. Therefore the pure parton-shower evolution is supplemented by tree-level matrix elements with up to two additional light QCD partons or photons using the matrix-element parton-shower merging formalism described in this chapter. The comparison with measurements from CDF and DØ is shown in Figure 2.7b. Besides the total results (red histograms) this again presents the sub-contributions assigned to matrix-element core processes with exclusively $0, 1$ and 2 photons plus a variable number of additional QCD partons. When comparing to Figure 2.7a, where the pure shower result is shown, it is apparent that the majority of events with a dijet core

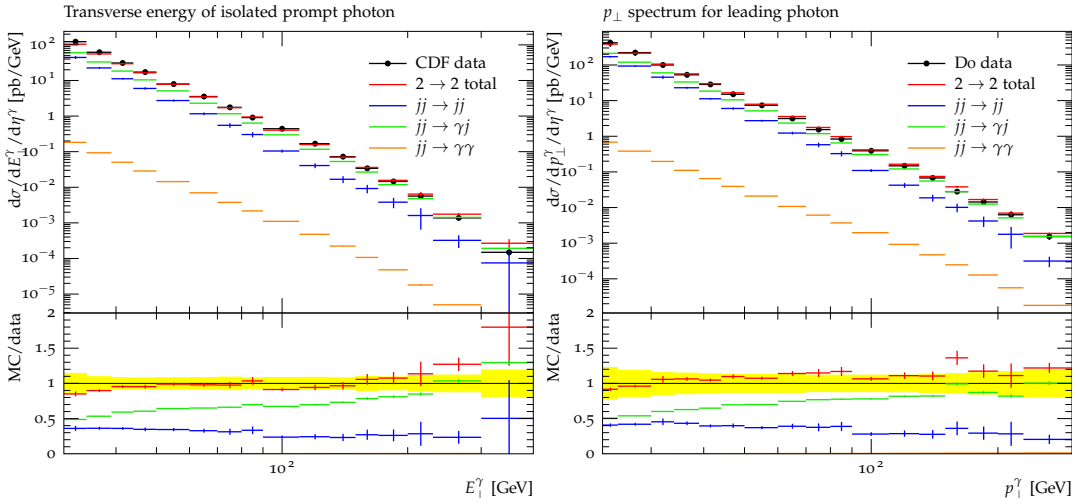

(a) QCD+QED parton shower

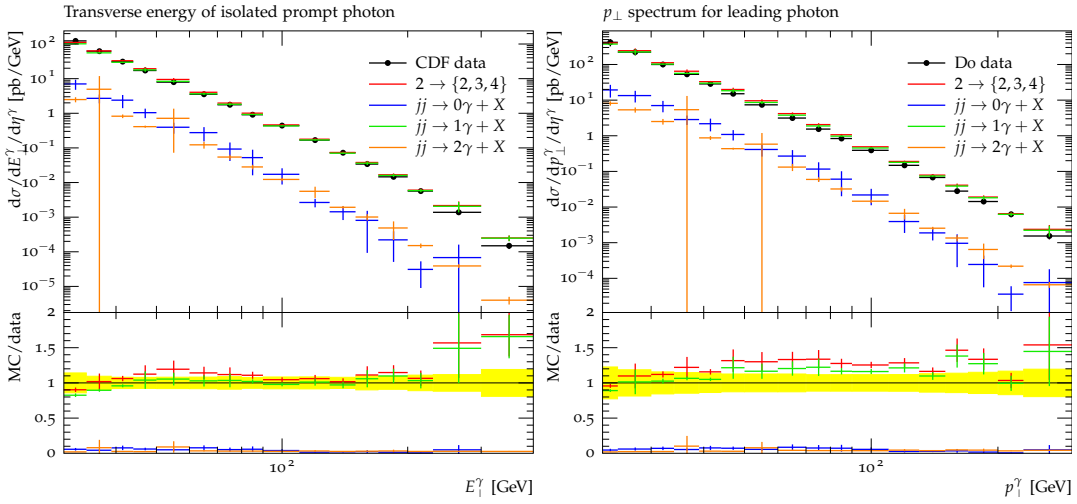

(b) ME+PS approach

Figure 2.7: Transverse momentum distribution of the photon in prompt photon production as measured by the CDF [81] and DØ [82] experiments. Contributions from different classes of partonic core processes to the total result are displayed.

process in the shower simulation is now ascribed to matrix-element cores with one photon plus additional QCD partons. Thereby, what might traditionally be called *fragmentation* component is now split into two parts, one generated by higher-order matrix elements and the other by the QED shower. Since the "shower fragmentation component" is negligible here it would be justifiable to use only $jj \to \gamma j$+jets matrix elements in the simulation of these observables. Of course, this statement holds only as long as the isolation criterion in the analysis and the separation criterion of the merging are similar enough.

In this process no strong variation of the total result due to the inclusion of real-emission matrix elements is observed. The biggest effect is a somewhat larger inclusive

rate for the merged samples $\lesssim 20\%$. The shape of the distributions is preserved. This in fact has to be understood as a highly non-trivial consistency check of the merging formalism.

DØ has also published [83] a slightly less inclusive measurement of the transverse momentum of the leading photon. Here the differential cross section $\mathrm{d}\sigma/\mathrm{d}pT^{\gamma}\mathrm{d}\eta_{\gamma}\mathrm{d}\eta_{\mathrm{jet}}$ is measured in four regions determined by the rapidity of the jet (central or forward) and the orientation of the photon with respect to the leading jet (same-sign or opposite-sign rapidity). A comparison of this data to the ME+PS merging approach with up to 4 particles in the matrix-element final state is shown in Figures 2.8 and 2.9 with very good agreement.

2.5.4 Prompt-diphoton production

An interesting further testbed for the democratic merging approach is diphoton production at hadron colliders.

The CDF collaboration has measured properties of the corresponding final states in some detail. The analysis presented in [84] selects leading/subleading photons with transverse momenta larger than 14/13 GeV. Those must be isolated from any significant hadronic activity within a distance of $R = 0.4$, by requiring the hadronic activity within this cone to yield $E_T < 1$ GeV. For the selected events the invariant mass and transverse momentum of the photon pair are analysed as well as the azimuthal separation between the photons.

Recently, the DØ experiment has also published a measurement in this process [85] including significantly more data than the CDF analysis. Like the CDF measurement, this analysis corrects for effects from the underlying event as well as from photons out of hadron decays. It is thus meaningful to compare it to parton-shower level events. Photons are analysed in $|\eta| < 0.9$ and the leading/subleading photons are required to have transverse momenta larger than 21/20 GeV. To isolate the photons, this analysis requires a low level of activity, $\sum_{R=0.4} E_T < 2.5$ GeV in a cone of $R = 0.4$ around the photons.

To again exemplify the importance of the fragmentation contribution even for the required isolated photons in these analyses, Figure 2.10 compares the Monte-Carlo prediction for leading-order matrix elements plus shower evolution to the CDF analysis. It displays the contributions from the previously introduced classes of matrix elements (i.e. $jj \to jj$, $jj \to \gamma j$ and $jj \to \gamma\gamma$). It is evident, that the democratic treatment of photons and QCD partons is absolutely mandatory to describe these observables.

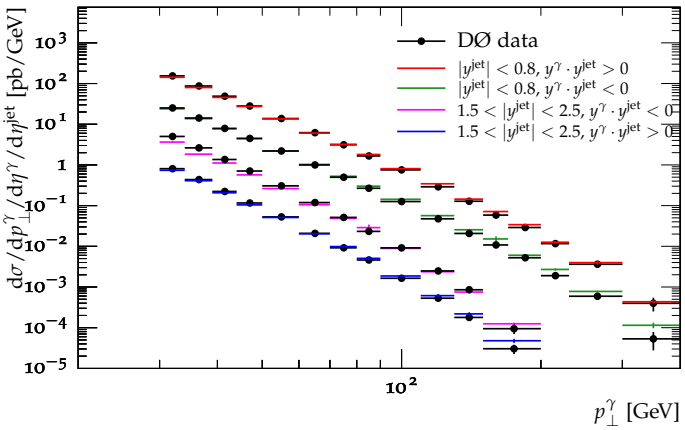

Figure 2.8: Transverse momentum of the photon in γ + jet events as measured by the DØ experiment [83]. The differential cross section is displayed in four different regions of phase space as explained in the main text, and have been scaled by factors of 5, 1, 0.3 and 0.1 respectively from top to bottom.

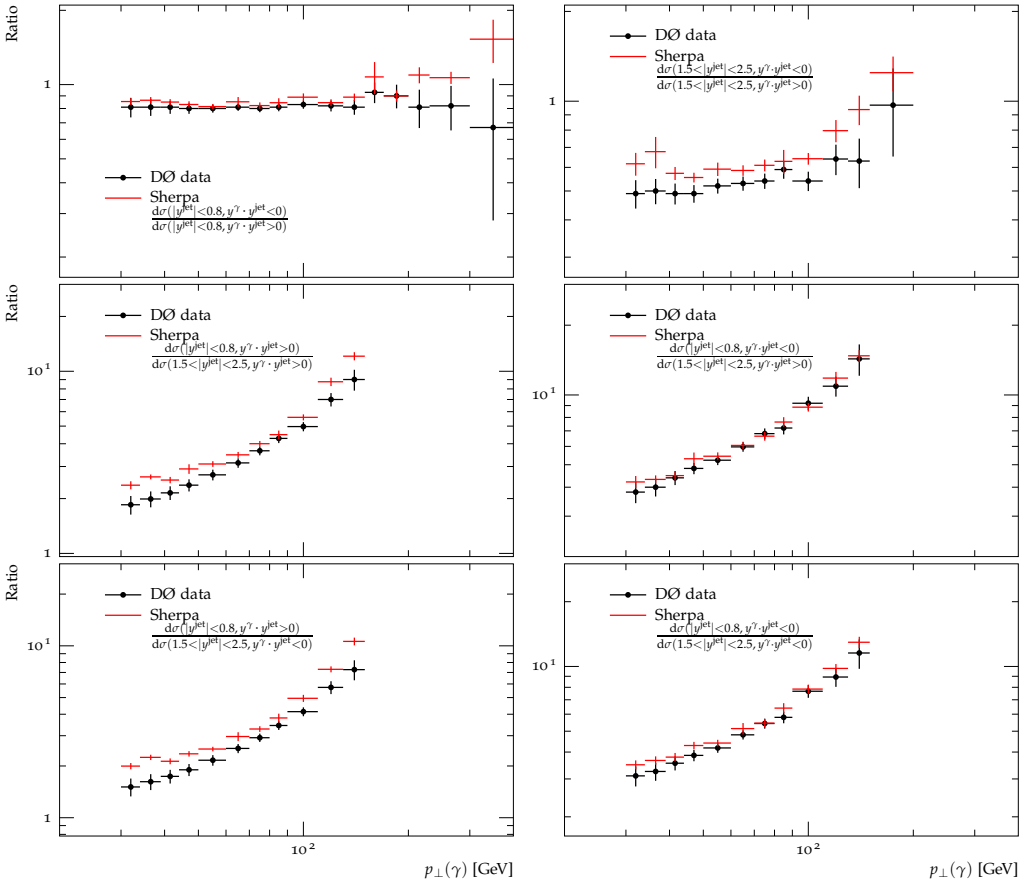

Figure 2.9: Transverse momentum of the photon in γ + jet events as measured by the DØ experiment [83]. Displayed are the ratios of the differential cross section in four different regions of phase space as explained in the main text.

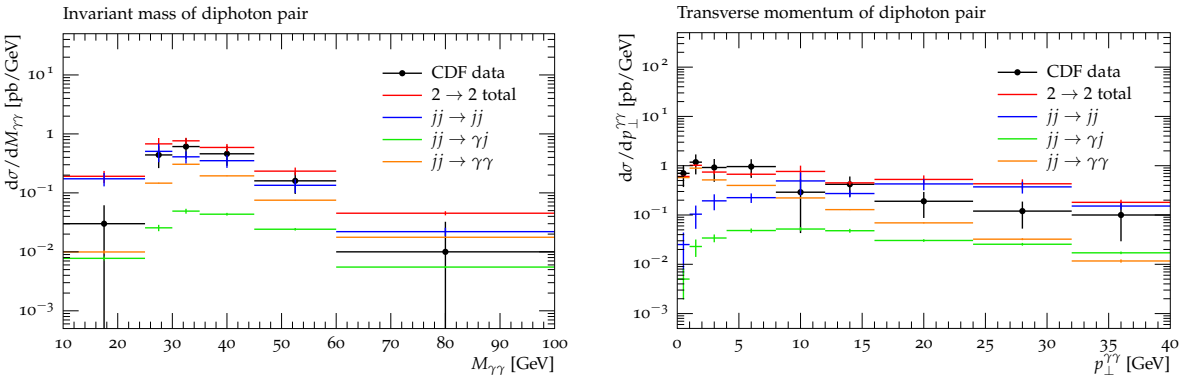

Figure 2.10: Properties of diphoton events measured by CDF [84]. Displayed are the sub-contributions from different leading-order matrix elements and their sum.

From a theoretical perspective this reaction is interesting because the diphoton system does not have a transverse momentum when described by leading-order matrix elements. Hence its transverse-momentum spectrum depends strongly on the proper inclusion of higher-order effects. In addition, the azimuthal angle gives a measure for the correlation of the two photons which is also sensitive to higher-order corrections. Especially in the region of large transverse momenta or large decorrelation one expects these corrections to be better described by matrix elements than by the parton shower.

In this context the parton-shower kinematics might become important, because the recoil scheme discussed in Section 1.2.2 plays an important role for the generation of transverse momentum for the diphoton system. Thus, as a first step, Figure 2.11a compares parton-level Monte-Carlo predictions using two different splitting kinematics. Both, the algorithm outlined in the appendix of [86], denoted "Scheme 1", and the method proposed in [13], denoted "Scheme 2", have difficulties describing the critical regions mentioned above.

As shown in Figure 2.11b, with the inclusion of higher-order real-emission matrix elements, the simulation is able to describe the measurement significantly better. Especially the transverse-momentum distribution exemplifies two unique features: The resummation of large logarithms correctly reproduces the Sudakov-shape of the low-$p_\perp$ region which is not possible with fixed-order calculations. At the same time exact matrix elements allow for a consistent simulation of the high-$p_\perp$ tail where a traditional parton-shower approach would fail. Also the decorrelation between the photons is now matched very well.

Apart from a finer binning in the observables and much reduced statistical fluctuations, the DØ analysis also brings one new observable with it, the polar scattering angle of the photons. All four observables are displayed in Figure 2.12 and the agreement with

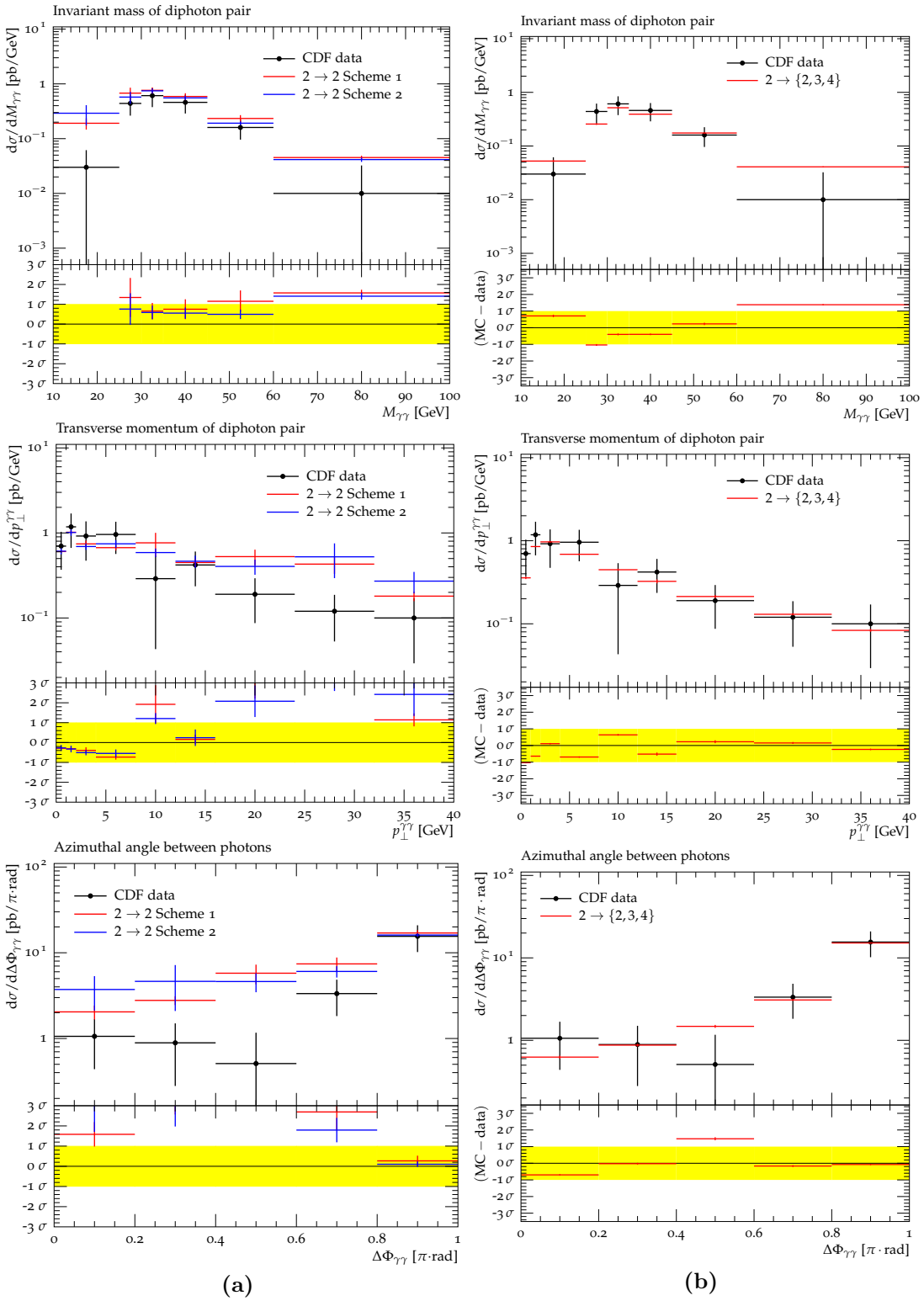

Figure 2.11: Properties of diphoton events measured by the CDF collaboration [84]. Figure (a) compares the influence of different parton-shower kinematics when using leading-order matrix elements. Scheme 1 refers to the algorithm outlined in [86], scheme 2 stands for the original implementation [13]. Figure (b) shows the same observables for merged event samples with up to two additional particles in the matrix-element final state.

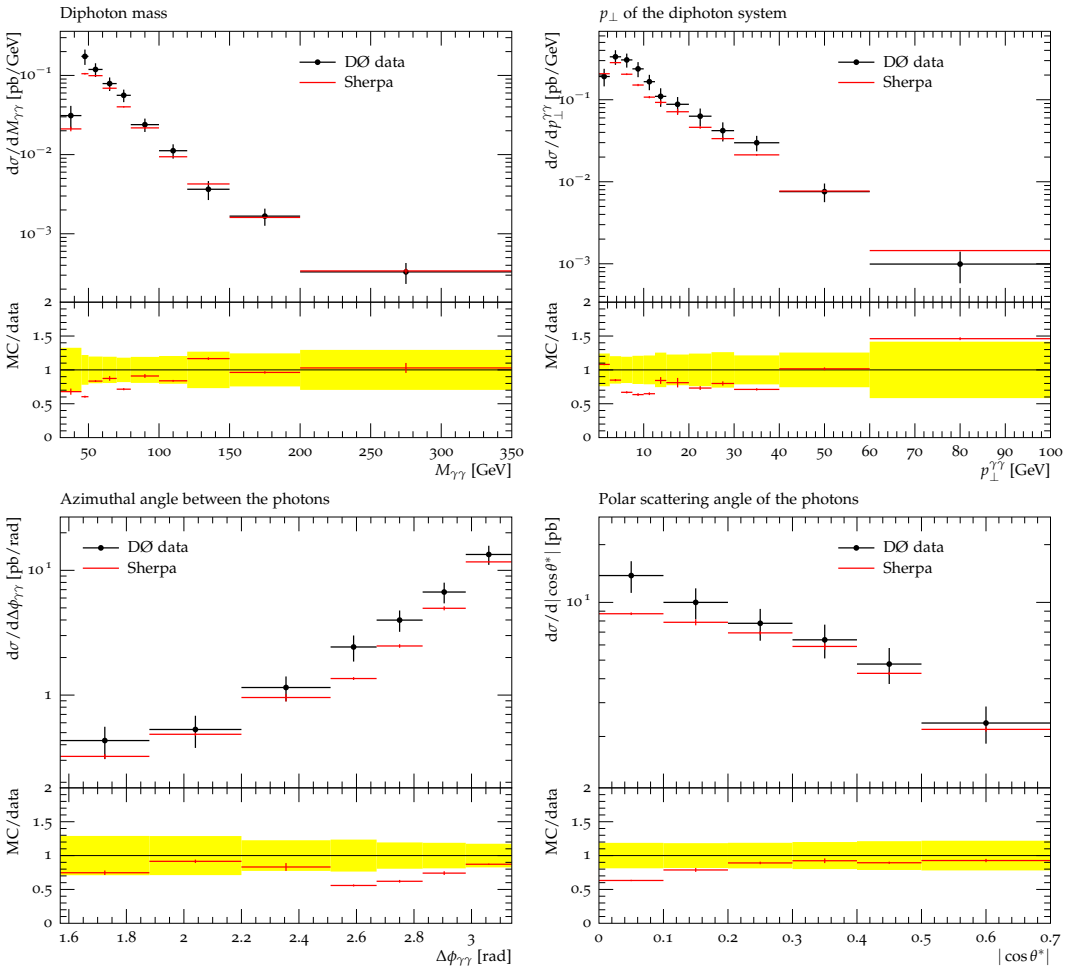

Figure 2.12: Properties of diphoton events measured by the DØ collaboration [85] compared to predictions from a merged sample with up to two additional partons in the matrix-element final state.

Monte-Carlo predictions is impressive, especially when compared to the other theory predictions in [85].

It is worth noting that the MC simulations include the loop-induced contribution $gg \to \gamma\gamma$. It has been shown [84] that its main influence is seen in the invariant mass spectrum around 30 GeV where it accounts for a significant enhancement of the cross section.

Even with the inclusion of this leading-order contribution one still finds that the total inclusive cross section predicted by this leading-order approach is roughly 30% lower than the measurement. This can be explained by the missing NLO components in the matrix element, in particular the virtual contribution. Eliminating this deficiency will be the topic of the next chapter.

3 NLO accuracy for Monte-Carlo simulations

Higher-order QCD corrections form an important ingredient to many phenomenological studies and experimental analyses at both the Tevatron and the LHC. The impact of these corrections has been similarly important for various studies of HERA and LEP data.

In the previous chapter a matrix-element parton-shower merging (ME+PS) method was presented which allows for the correction of the shapes of observables to higher orders. At the same time it was made explicit that the inclusive cross section of samples produced in such a way is still at leading-order accuracy only.

Many matrix-element calculations on the other hand have already provided results at next-to-leading (NLO) or even next-to-next-to-leading order (NNLO) accuracy. There has been a number of proposals of how to include at least the full NLO results in a parton-shower simulation. However only two of them have been fully worked out and implemented in publicly available programs.

The first method, MC@NLO, pioneered in [87], and implemented for a large number of processes [88] relies on using the parton-shower kernels and their universal soft and collinear properties to subtract the infrared divergences of the real contribution to the NLO cross section. The subsequent parton shower then starts from either a Born-like configuration or from a configuration determined by the residual real correction contribution of the NLO calculation. By construction, there is some dependence on the details of the actual shower algorithm, which, to a certain extent, up to now seemed to limit the versatility of the method.

This dependence was overcome by the second method, POWHEG, which was initially presented in [43]. This technique essentially is an improvement of the reweighting method mentioned earlier, which has been known for nearly two decades and was applied individually to a plethora of processes [33]. To promote it to full NLO accuracy, it was supplemented with a local, phase-space dependent K-factor. Also the POWHEG method has been worked out for a number of processes [89, 90], in the framework of

different parton-shower algorithms. A framework incorporating the core technology, independent of the specific parton-shower implementation and the matrix elements for the processes in question has been published in [91].

These methods for matching of the parton-shower with NLO matrix elements have one deficiency with respect to the ME+PS method: They only include matrix-element corrections for the first emission on top of an inclusive process. Having at hand two, somewhat orthogonal, methods (ME+PS and POWHEG) to improve both the hard QCD radiation activity *and* the total event rate in a given process, the question naturally arises whether it is possible to combine both into an even more powerful approach. This is the topic addressed by this chapter, resulting in a practical algorithm for merging both techniques. It has been directly implemented into the multi-purpose event generator SHERPA [5], and will be made publicly available in a future version of this program. In a parallel development, Hamilton and Nason [92] suggested an identical method; however, their actual implementation only approximates the formal result. Due to the formal equivalence of both proposals, they shall generally be referred to as the MENLOPS approach here.

This chapter is outlined as follows: In Section 3.1 a brief review of NLO accuracy in the matrix element will be given. Section 3.2 describes the POWHEG method, interpreting it as an advanced reweighting technique for standard parton showers. Results obtained with an automated implementation of it are discussed for a large variety of processes. Finally, Section 3.3 introduces an algorithm that combines the ME+PS approach with the POWHEG method. A common language is introduced which allows to read off the bits missing in the ME+PS approach to correct it to full NLO accuracy as implemented through POWHEG, while still retaining the tree-level matrix-element corrections for higher-order multiplicities.

3.1 NLO matrix element calculations

3.1.1 Cross sections at $\mathcal{O}(\alpha_s)$

The value of a given infrared and collinear safe observable, O, computed at NLO, is given in terms of the Born term B, the real emission term R, and the virtual contribution (including the collinear mass factorisation counter-terms), denoted by $\tilde{\mathrm{V}}$, as

$$\langle O \rangle^{(\mathrm{NLO})} = \int \mathrm{d}\Phi_B \, O(\Phi_B) \left[\mathrm{B} + \tilde{\mathrm{V}} \right] + \int \mathrm{d}\Phi_R \, O(\Phi_R) \, \mathrm{R} \, . \tag{3.1}$$

It is obvious that the real-emission contribution cannot be simply combined with the Born and virtual terms, as it depends on different kinematics. They can also not be integrated separately in a Monte-Carlo fashion as both the real and virtual contributions contain divergences which cancel each other only when combined. This cancellation is a consequence of the Kinoshita-Lee-Nauenberg theorem [6].

Before reviewing a framework that allows to calculate such NLO cross sections, some notation has to be introduced which will also be beneficial in the rest of this chapter.

In the following, sets of n particles in a $2 \to (n-2)$ process will summarily be denoted by $\{\vec{a}\} = \{a_1, \ldots, a_n\}$, and the particles will be specified through their flavours $\{\vec{f}\,\} = \{f_1, \ldots, f_n\}$ and momenta $\{\vec{p}\} = \{p_1, \ldots, p_n\}$. The generic expression for a fully differential Born-level cross section in a scattering process with $(n-2)$ final-state particles can be written as a sum over all contributing flavour combinations as

$$\mathrm{d}\sigma_B(\{\vec{p}\}) \;=\; \sum_{\{\vec{f}\,\}} \mathrm{d}\sigma_B(\{\vec{a}\})\,, \qquad \text{where} \qquad \mathrm{d}\sigma_B(\{\vec{a}\}) \;=\; \mathrm{d}\Phi_B(\{\vec{p}\})\,\mathrm{B}(\{\vec{a}\})\,, \tag{3.2}$$

The individual terms in the sum are given by

$$\begin{aligned}
\mathrm{B}(\{\vec{a}\}) \;&=\; \mathcal{L}(\{\vec{a}\})\,\mathcal{B}(\{\vec{a}\})\,,\\
\mathcal{B}(\{\vec{a}\}) \;&=\; \frac{1}{F(\{\vec{p}\})}\,\frac{1}{S(\{\vec{f}\,\})}\,\left|\mathcal{M}_B\right|^2(\{\vec{a}\})\,,\\
\mathrm{d}\Phi_B(\{\vec{p}\}) \;&=\; \frac{\mathrm{d}x_1}{x_1}\frac{\mathrm{d}x_2}{x_2}\,\mathrm{d}\,\Phi_B(\{\vec{p}\})\,,\\
\mathcal{L}(\{\vec{a}\};\mu^2) \;&=\; x_1 f_{f_1}(x_1,\mu^2)\; x_2 f_{f_2}(x_2,\mu^2)\,.
\end{aligned} \tag{3.3}$$

Here, $\left|\mathcal{M}_B\right|^2(\{\vec{a}\})$ denotes the partonic matrix element squared, with all factors due to averaging over initial state quantum numbers such as spin or colours absorbed into it, and $\mathrm{d}\,\Phi_B(\{\vec{p}\})$ is the corresponding differential n-particle partonic phase-space element; $S(\{\vec{f}\,\})$ is the symmetry factor due to identical flavours associated to the partonic subprocess, while $F(\{\vec{p}\})$ denotes the flux factor and $\mathcal{L}$ is the parton luminosity given by the corresponding parton distribution functions (PDFs). In the case of leptonic initial states, ignoring QED initial state radiation, the parton distribution functions $f(x,\mu^2)$ are replaced by $\delta(1-x)$.

In a similar fashion, the real-emission part of the QCD next-to-leading order cross section can be written as a sum, this time over parton configurations $\{a_1, \ldots, a_{n+1}\}$, i.e. including one additional parton. A corresponding subprocess cross section reads

$$\mathrm{d}\sigma_R(\{\vec{a}\}) \;=\; \mathrm{d}\Phi_R(\{\vec{p}\})\,\mathrm{R}(\{\vec{a}\})\,. \tag{3.4}$$

At this point, it is helpful to introduce a notation for mappings from real-emission parton configurations to Born parton configurations. Such mappings combine the partons a_i and a_j into a common "mother" parton $a_{\widetilde{ij}}$, in the presence of the spectator a_k by defining a new flavour $f_{\widetilde{ij}}$ and by redefining the particle momenta. To be specific,

$$b_{ij,k}(\{\vec{a}\}) \;=\; \begin{cases} \{\vec{f}\,\} \setminus \{f_i, f_j\} \cup \{f_{\widetilde{ij}}\} \\ \{\vec{p}\,\} \to \{\vec{\tilde{p}}\,\} \end{cases} \tag{3.5}$$

The flavour of the "mother" parton, $f_{\widetilde{ij}}$, is thereby fixed unambiguously by the QCD interactions, while the flavour of the spectator, f_k, remains unaltered. The momentum map guarantees that all partons are kept on their mass shell.

Conversely, any Born parton configuration and a related branching process $\widetilde{ij}, \tilde{k} \to ij, k$ determine the parton configuration of a real-emission subprocess as

$$r_{\widetilde{ij},\tilde{k}}(f_i, \Phi_{R|B}\,; \{\vec{a}\}) \;=\; \begin{cases} \{\vec{f}\,\} \setminus \{f_{\widetilde{ij}}\} \cup \{f_i, f_j\} \\ \{\vec{\tilde{p}}\,\} \to \{\vec{p}\,\} \end{cases} \quad . \tag{3.6}$$

The radiative variables $\Phi_{R|B}$ are thereby employed to turn the n-parton momentum configuration into an n+1-parton momentum configuration using the inverse of the phase-space map defined by Equation (3.5). The flavour f_j is again determined unambiguously by the QCD interactions. Here, also two obvious generalisations of Equation (3.5) shall be defined, $b_{ij,k}(\{\vec{f}\,\})$ and $b_{ij,k}(\{\vec{p}\,\})$, which act on the parton flavours and on the parton momenta only. Correspondingly, such generalisations exist for Equation (3.6).

Equation (3.1) can now be rewritten using the introduced notation:

$$\begin{aligned} \langle O \rangle^{(\mathrm{NLO})} \;=\; & \sum_{\{\vec{f}\,\}} \int \mathrm{d}\Phi_B(\{\vec{p}\,\}) \Big[\mathrm{B}(\{\vec{a}\}) + \tilde{\mathrm{V}}(\{\vec{a}\}) \Big] O(\{\vec{p}\,\}) \\ & + \sum_{\{\vec{f}\,\}} \int \mathrm{d}\Phi_R(\{\vec{p}\,\})\, \mathrm{R}(\{\vec{a}\})\, O(\{\vec{p}\,\}) \;. \end{aligned} \tag{3.7}$$

3.1.2 Subtraction methods

In order to compute Equation (3.7) in a Monte-Carlo approach, subtraction terms are introduced, that render the real emission finite in $D = 4$ space-time dimensions. The parts that are subtracted from the real contribution are then integrated analytically over the one-particle phase space and added to the virtual contribution, where they cancel the corresponding divergences.

Such subtraction terms are constructed from the fact that in the soft and collinear limits, the partonic real matrix element squared, $\mathcal{R}(\{\vec{a}\})$, can be decomposed as a sum of terms $\mathcal{D}_{ij,k}(\{\vec{a}\})$,

$$\mathcal{R}(\{\vec{a}\}) \to \sum_{\{i,j\}} \sum_{k\neq i,j} \mathcal{D}_{ij,k}(\{\vec{a}\}) \,. \tag{3.8}$$

The $\mathcal{D}_{ij,k}(\{\vec{a}\})$ factorise into a Born-level term and a universal splitting kernel, encoding the transition of $a_{\tilde{ij}}$ to a_i and a_j [12]. The splitting is associated with a universal procedure for factorising the phase-space integral into a Born level part and a one-particle radiative phase space:

$$\mathrm{d}\Phi_R(\{\vec{p}\}) \;=\; \mathrm{d}\Phi_B(b_{ij,k}(\{\vec{p}\}))\,\mathrm{d}\Phi^{ij,k}_{R|B}(\{\vec{p}\}) \,. \tag{3.9}$$

The existence of universal decompositions like in Equation (3.8) forms the basis of subtraction methods like the Catani-Seymour dipole subtraction [12], antenna subtraction [93], or the subtraction method of Frixione, Kunszt, and Signer [94].

In the dipole subtraction method [12], the equation above can then be written as

$$\begin{aligned}\langle O\rangle^{(\mathrm{NLO})} \;=\; &\sum_{\{\vec{f}\}} \int \mathrm{d}\Phi_B(\{\vec{p}\}) \left[\mathrm{B}(\{\vec{a}\}) + \tilde{\mathrm{V}}(\{\vec{a}\}) + \mathrm{I}(\{\vec{a}\})\right] O(\{\vec{p}\}) + \\ &\sum_{\{\vec{f}\}} \int \mathrm{d}\Phi_R(\{\vec{p}\}) \left[\mathrm{R}(\{\vec{a}\})\, O(\{\vec{p}\}) - \sum_{\{i,j\}} \sum_{k\neq i,j} \mathrm{S}_{ij,k}(\{\vec{a}\})\, O(b_{ij,k}(\{\vec{p}\}))\right] .\end{aligned} \tag{3.10}$$

The real and integrated subtraction terms $\mathrm{S}_{ij,k}(\{\vec{a}\})$ and $\mathrm{I}(\{\vec{a}\})$ fulfil the relation

$$\sum_{\{\vec{f}\}} \int \mathrm{d}\Phi_B(\{\vec{p}\})\,\mathrm{I}(\{\vec{a}\}) \;=\; \sum_{\{\vec{f}\}} \sum_{\{i,j\}} \sum_{k\neq i,j} \int \mathrm{d}\Phi_R(\{\vec{p}\})\,\mathrm{S}_{ij,k}(\{\vec{a}\}). \tag{3.11}$$

Note that each $\mathrm{S}_{ij,k}$ defines a separate phase-space map and that the observable O in the last term depends on $b_{ij,k}(\{\vec{p}\})$, rather than $\{\vec{p}\}$, which is a crucial feature of the subtraction procedure.

When the subtraction term in its integrated form is added to the virtual contribution, their respective poles are cancelled:

$$\left\{\epsilon \left[\tilde{\mathrm{V}}(\{\vec{a}\}) + \mathrm{I}(\{\vec{a}\})\right]\right\}_{\epsilon=0} \;=\; 0 \,. \tag{3.12}$$

The implementation in Sherpa's matrix element generator Amegic++, expanding upon its tree-level capabilities to generate B and R, is able to generate both the subtraction

terms S and their integrated counterparts I as well as the collinear mass factorisation counter-term in an automated fashion [95]. The virtual contributions V, however, are obtained from dedicated external codes interfaced using the Binoth-Les Houches Accord [96].

3.1.3 Decomposition of real-emission cross sections

It is important to stress that, also away from the infrared limits, $\mathcal{R}(\{\vec{a}\})$ can be decomposed into a number of terms $\mathcal{R}_{ij,k}$ analogous to $\mathcal{D}_{ij,k}$ in Equation (3.8):

$$\mathcal{R}_{ij,k}(\{\vec{a}\}) \;:=\; \rho_{ij,k}(\{\vec{a}\})\,\mathcal{R}(\{\vec{a}\}),\quad \text{where}\quad \rho_{ij,k}(\{\vec{a}\}) \;=\; \frac{\mathcal{D}_{ij,k}(\{\vec{a}\})}{\sum_{\{m,n\}}\sum_{l\neq m,n}\mathcal{D}_{mn,l}(\{\vec{a}\})}\,. \tag{3.13}$$

Equation (3.4) can now be rewritten as a sum of trivially factorised contributions

$$\mathrm{d}\sigma_R(\{\vec{a}\}) \;=\; \sum_{\{i,j\}}\sum_{k\neq i,j}\mathrm{d}\sigma_B(b_{ij,k}(\{\vec{a}\}))\,\mathrm{d}\sigma_{R|B}^{ij,k}(\{\vec{a}\})\,, \tag{3.14}$$

where

$$\mathrm{d}\sigma_{R|B}^{ij,k}(\{\vec{a}\}) \;=\; \mathrm{d}\Phi_{R|B}^{ij,k}(\{\vec{p}\})\,\frac{\mathrm{R}_{ij,k}(\{\vec{a}\})}{\mathrm{B}(b_{ij,k}(\{\vec{a}\}))}\,. \tag{3.15}$$

and $\mathrm{R}_{ij,k}(\{\vec{a}\}) = \mathcal{L}(\{\vec{a}\})\mathcal{R}_{ij,k}(\{\vec{a}\})$. These equations will be key ingredients to understanding and implementing the POWHEG method.

3.2 The POWHEG method

In this section, the POWHEG method is reinterpreted as an advanced reweighting technique for standard parton showers. The starting point of the discussion is the factorisation theorem underlying the specific parton-shower model, like collinear factorisation [8], Catani-Seymour factorisation [12], antenna factorisation [93] or FKS factorisation [94]. Except in collinear factorisation, the splitting functions of the parton shower depend on (at least) one additional parton, which is often referred to as the "spectator". In order to make this connection explicit, the notation of a dipole-like factorisation is adopted, which is sufficiently general to discuss all relevant features of the POWHEG method and its implementation into the SHERPA event generator.

3.2.1 Construction of the parton shower

Due to the non-Abelian nature of QCD, the terms $\mathcal{D}_{ij,k}$ in Equation (3.8) in general do not factorise on the level of squared matrix elements, including all colour contributions. To arrive at a practical model for a parton shower, sub-leading colour configurations are therefore neglected, which leads to an *assumed* factorisation on the level of squared matrix elements. In the infrared limits one can then write

$$\mathcal{D}_{ij,k}(\{\vec{a}\}) \;\to\; \mathcal{B}(b_{ij,k}(\{\vec{a}\}))\,\frac{S(b_{ij,k}(\{\vec{f}\}))}{S(\{\vec{f}\})}\,\frac{1}{2\,p_i p_j}\,8\pi\,\alpha_s\,\mathcal{K}_{ij,k}(p_i,p_j,p_k)\;, \tag{3.16}$$

where the set of momenta $b_{ij,k}(\{\vec{p}\})$ is determined by the phase-space map of the parton-shower model.[1] The quantities $\mathcal{K}_{ij,k}$ are the parton-shower evolution kernels, which depend on the parton flavours f_i, f_j and f_k and on the radiative phase space. The denominator factor $2\,p_i p_j$ or any linearly dependent quantity is usually used to define the parton shower evolution variable, in the following denoted by t.

Using the above model, the parton-shower approximation of Equation (3.15) can be derived as

$$\mathrm{d}\sigma^{(\mathrm{PS})\,ij,k}_{R|B}(\{\vec{a}\}) \;=\; \mathrm{d}\Phi^{ij,k}_{R|B}(\{\vec{p}\})\,\frac{S(b_{ij,k}(\{\vec{f}\}))}{S(\{\vec{f}\})}\,\frac{8\pi\,\alpha_s}{2\,p_i p_j}\mathcal{K}_{ij,k}(p_i,p_j,p_k)\,\frac{\mathcal{L}(\{\vec{a}\})}{\mathcal{L}(b_{ij,k}(\{\vec{a}\}))}\;. \tag{3.17}$$

Particles produced in the parton shower are resolved at a certain evolution scale and can therefore be distinguished from particles at higher and lower scales. At most the two particles a_i and a_j, emerging from the same splitting process, can be seen as identical. Hence, the ratio of symmetry factors in Equation (3.15) changes to

$$\frac{S(b_{ij,k}(\{\vec{f}\}))}{S(\{\vec{f}\})} \;\to\; \frac{1}{S_{ij}} \;=\; \begin{cases} 1/2 & \text{if } \; i,j>2 \text{ and } b_i = b_j \\ 1 & \text{else} \end{cases}\;. \tag{3.18}$$

The integral over the radiative phase space can be written as

$$\mathrm{d}\Phi^{ij,k}_{R|B}(\{\vec{p}\}) \;=\; \frac{1}{16\pi^2}\,\mathrm{d}t\,\mathrm{d}z\,\frac{\mathrm{d}\phi}{2\pi}\;J_{ij,k}(t,z,\phi)\;, \tag{3.19}$$

with t the evolution variable, z the splitting variable, and ϕ an azimuthal angle. Here, J denotes the Jacobian factor, that potentially arises due to the transformation of

[1] Note that here only parton showers with local energy-momentum conservation are considered. Therefore, the phase-space maps $\{\vec{p}\}_{\mathrm{R}} \to \{\vec{p}\}_{\mathrm{B}}$ exist.

variables. Equation (3.17) thus becomes

$$\mathrm{d}\sigma_{R|B}^{(\mathrm{PS})\,ij,k}(\{\vec{a}\}) \;=\; \frac{\mathrm{d}t}{t}\,\mathrm{d}z\,\frac{\mathrm{d}\phi}{2\pi}\,\frac{\alpha_s}{2\pi}\,\frac{1}{S_{ij}}\,J_{ij,k}(t,z,\phi)\,\mathcal{K}_{ij,k}(t,z,\phi)\,\frac{\mathcal{L}(\{\vec{a}\};t)}{\mathcal{L}(b_{ij,k}(\{\vec{a}\});t)}\;. \tag{3.20}$$

The assignment of the mother parton, the spectator and the underlying Born process can now be assumed to be fixed. Then, the sum runs over all possible real-emission configurations originating from this particular Born-level state instead. Furthermore, assuming independence of the individual emissions, i.e. Poissonian statistics, this leads to the constrained no-branching probability of the parton-shower model [7,97] between the two scales t'' and t'

$$\begin{aligned}\Delta_{\widetilde{ij},\tilde{k}}^{(\mathrm{PS})}(t',t'';\{\vec{a}\}_{\mathrm{B}}) \;=\; \exp\Bigg\{ &-\sum_{f_i=q,g}\int_{t'}^{t''}\frac{\mathrm{d}t}{t}\int_{z_{\min}}^{z_{\max}}\mathrm{d}z\int_0^{2\pi}\frac{\mathrm{d}\phi}{2\pi}\,J_{ij,k}(t,z,\phi)\\ &\times\frac{1}{S_{ij}}\,\frac{\alpha_s}{2\pi}\,\mathcal{K}_{ij,k}(t,z,\phi)\,\frac{\mathcal{L}(r_{\widetilde{ij},\tilde{k}}(f_i,t,z,\phi;\{\vec{a}\});t)}{\mathcal{L}(\{\vec{a}\};t)}\Bigg\}\;.\end{aligned} \tag{3.21}$$

It is worth noting that Equation (3.21) depends on the underlying Born process, since the flavour and momentum of the spectator enter as arguments of $J_{ij,k}$ and $\mathcal{K}_{ij,k}$. The ratio of $\mathcal{L}$ in Equation (3.21) accounts for a potential change of the parton luminosity when integrating over the initial-state phase space[2]. Note that the partons $\{\vec{a}\}_{\mathrm{B}}$ denote a Born-level set, while in Equation (3.17) and Equation (3.20) $\{\vec{a}\}$ denote a set of partons at real-emission level. This is also indicated by the subscript B in Equation (3.21).

Using the definition

$$\Delta(t_0,\mu^2;\{\vec{a}\}) = \prod_{\{\widetilde{ij},\tilde{k}\}}\Delta_{\widetilde{ij},\tilde{k}}(t_0,\mu^2;\{\vec{a}\}) \tag{3.22}$$

the total cross section in the parton-shower approximation reads

$$\begin{aligned}\sigma_B \;=\; \sum_{\{\vec{f}\}}\int \mathrm{d}\Phi_B(\{\vec{p}\})\,\mathrm{B}(\{\vec{a}\})\Bigg[\;&\Delta^{(\mathrm{PS})}(t_0,\mu^2;\{\vec{a}\})\\ &+\sum_{\{\widetilde{ij},\tilde{k}\}}\sum_{f_i=q,g}\int_{t_0}^{\mu^2}\frac{\mathrm{d}t}{t}\int_{z_{\min}}^{z_{\max}}\mathrm{d}z\int_0^{2\pi}\frac{\mathrm{d}\phi}{2\pi}\,J_{ij,k}(t,z,\phi)\\ &\quad\times\frac{1}{S_{ij}}\,\frac{\alpha_s}{2\pi}\,\mathcal{K}_{ij,k}(t,z,\phi)\,\frac{\mathcal{L}(r_{\widetilde{ij},\tilde{k}}(f_i,t,z,\phi;\{\vec{a}\});t)}{\mathcal{L}(\{\vec{a}\};t)}\,\Delta^{(\mathrm{PS})}(t,\mu^2;\{\vec{a}\})\Bigg]\;.\end{aligned} \tag{3.23}$$

The scale t_0 acts as the infrared cutoff of the parton shower. Simple inspection shows

[2]Note that, depending on the parton shower model, the x_i do not necessarily fulfil the relation $x_i = \tilde{x}_i/z$ [86,98].

that the sum in the square bracket equals unity, since the second term can be written as

$$\int_{t_0}^{\mu^2} \mathrm{d}t \, \frac{\mathrm{d}\Delta^{(\mathrm{PS})}(t, \mu^2; \{\vec{a}\})}{\mathrm{d}t} \, . \tag{3.24}$$

This makes the probabilistic properties of the parton shower explicit. At the same time it also shows that this unitarity leads to the cross section in standard parton-shower Monte Carlos to be exactly the respective leading-order cross section.

3.2.2 Correcting parton showers with matrix elements

The aim of this section is to devise a simple method for reinstating $\mathcal{O}(\alpha_s)$ accuracy in the emission pattern of the parton shower, i.e. the hardest emission in the parton shower should follow the distribution given by the corresponding real-emission matrix element. Loosely speaking, the key idea is to replace the splitting kernels $\mathcal{K}$ with the ratio of real-emission and Born-level matrix elements. Thus, instead of the splitting kernels, this ratio is exponentiated in the Sudakov form factor and employed in simulating the splitting.

Comparing Equations (3.15) and (3.17), a corresponding factor correcting $\mathcal{K}$ to resemble R/B can be easily identified. Using Equation (3.18) it reads

$$w_{ij,k}(\{\vec{a}\}) = \frac{\mathrm{d}\sigma^{ij,k}_{R|B}(\{\vec{a}\})}{\mathrm{d}\sigma^{(\mathrm{PS})\,ij,k}_{R|B}(\{\vec{a}\})} = \frac{2\,p_i p_j}{8\pi\,\alpha_s} \frac{S(\{\vec{f}\,\})}{S(b_{ij,k}(\{\vec{f}\,\}))} \frac{\rho_{ij,k}(\{\vec{a}\})\,\mathcal{R}(\{\vec{a}\})}{\mathcal{B}(b_{ij,k}(\{\vec{a}\}))\,\mathcal{K}_{ij,k}(\{\vec{a}\})} \, . \tag{3.25}$$

Employing the parton-shower approximation, Equation (3.16), to replace $\rho_{ij,k}$ yields

$$w(\{\vec{a}\}) = \left[\sum_{\{m,n\}} \sum_{l \neq m,n} \frac{S(b_{mn,l}(\{\vec{f}\,\}))}{S(\{\vec{f}\,\})} \frac{\mathcal{B}(b_{mn,l}(\{\vec{a}\}))}{\mathcal{R}(\{\vec{a}\})} \frac{8\pi\,\alpha_s}{2\,p_m p_n} \mathcal{K}_{mn,l}(\{\vec{a}\}) \right]^{-1} \, . \tag{3.26}$$

Note that this implies a corrective weight, which is actually *splitter-spectator independent*.

Correcting the parton shower to the full matrix element can thus be achieved through the following algorithm:

1. Determine an overestimate for Equation (3.26), i.e. find a set of $W_{\widetilde{ij},f_i}(\{\vec{f}\,\})$, such that $w(r_{\widetilde{ij},\tilde{k}}(f_i, \Phi_{R|B}; \{\vec{a}\})) \leq W_{\widetilde{ij},f_i}(\{\vec{f}\,\})$ for all $\tilde{k}$ and throughout the real-emission phase space.

2. Replace the parton shower splitting kernels $\mathcal{K}_{ij,k}$ by $W_{\widetilde{ij},f_i}(\{\vec{f}\,\})\,\mathcal{K}_{ij,k}$.

3. Accept parton-shower branchings with probability
   $w(r_{\widetilde{ij},\tilde{k}}(f_i, \Phi_{R|B}; \{\vec{a}\}))/W_{\widetilde{ij},f_i}(\{\vec{f}\})$.

It is straightforward to show that the constrained no-branching probability of such a matrix-element corrected parton shower reads

$$\Delta^{(\mathrm{ME})}_{\widetilde{ij},\tilde{k}}(t', t''; \{\vec{a}\}) = \exp\left\{ - \sum_{f_i=q,g} \frac{1}{16\pi^2} \int_{t'}^{t''} \mathrm{d}t \int_{z_{\min}}^{z_{\max}} \mathrm{d}z \int_0^{2\pi} \frac{\mathrm{d}\phi}{2\pi} J_{ij,k}(t,z,\phi) \right. \\ \left. \times \frac{1}{S_{ij}} \frac{S(r_{\widetilde{ij},\tilde{k}}(f_i; \{\vec{f}\}))}{S(\{\vec{f}\})} \frac{\mathrm{R}_{ij,k}(r_{\widetilde{ij},\tilde{k}}(f_i,t,z,\phi;\{\vec{a}\}))}{\mathrm{B}(\{\vec{a}\})} \right\} . \tag{3.27}$$

The ratio R/B in Equation (3.27) coincides with the ratio in the original publications presenting the POWHEG method. In the relatively simple cases treated so far, the various symmetry factors in the equation above cancel and can be neglected. For more complicated flavour structures this factor may differ from one and therefore must be retained.

Employing again the definition of Equation (3.22), but this time for the Sudakov form factor constructed from the ratio R/B yields the cross section in the matrix-element improved parton-shower approximation. It reads

$$\sigma_B = \sum_{\{\vec{f}\}} \int \mathrm{d}\Phi_B(\{\vec{p}\})\, \mathrm{B}(\{\vec{a}\}) \left[\Delta^{(\mathrm{ME})}(t_0, \mu^2; \{\vec{a}\}) \right. \\ + \sum_{\{\widetilde{ij},\tilde{k}\}} \sum_{f_i=q,g} \frac{1}{16\pi^2} \int_{t_0}^{\mu^2} \mathrm{d}t \int_{z_{\min}}^{z_{\max}} \mathrm{d}z \int_0^{2\pi} \frac{\mathrm{d}\phi}{2\pi} J_{ij,k}(t,z,\phi) \\ \left. \times \frac{1}{S_{ij}} \frac{S(r_{\widetilde{ij},\tilde{k}}(f_i; \{\vec{f}\}))}{S(\{\vec{f}\})} \frac{\mathrm{R}_{ij,k}(r_{\widetilde{ij},\tilde{k}}(f_i,t,z,\phi;\{\vec{a}\}))}{\mathrm{B}(\{\vec{a}\})} \Delta^{(\mathrm{ME})}(t, \mu^2; \{\vec{a}\}) \right] . \tag{3.28}$$

Again, the term in the square bracket equals one and thus reflects the probabilistic nature of this approach. Consequently, in the matrix-element improved parton-shower approximation the total cross section is given by the Born cross section, although the radiation pattern has improved. For a detailed discussion of the real-emission term see Section 3.2.4.

3.2.3 Approximate NLO cross sections

In the previous two sections it has become clear that the total cross section of events simulated in a parton-shower Monte-Carlo is determined by the "seed" cross section,

typically computed at Born level. While matrix-element improvement of the naive parton-shower picture will lead to radiation patterns which are accurate to $\mathcal{O}(\alpha_s)$, the total cross section of the event sample and any observable that can be defined at Born level will still be given by the respective leading-order expression. To allow for a simulation with next-to-leading order accuracy, including the cross section of the event sample, a prescription to assign a corresponding weight and multiplicity of the seed event must be found.

The solution is to replace the original Born-level matrix element with a modified one [43], denoted by $\bar{\mathrm{B}}$,

$$\mathrm{d}\sigma_B(\{\vec{a}\}) \;\to\; \mathrm{d}\sigma_{\bar{B}}(\{\vec{a}\}) \;:=\; \mathrm{d}\Phi_B(\{\vec{p}\})\,\bar{\mathrm{B}}(\{\vec{a}\}) \tag{3.29}$$

such that the "seed" cross section, $\mathrm{d}\sigma_{\bar{B}}$, integrates to the full NLO result. When constructing such an *NLO-weighted differential cross section for the Born configuration*, certain approximations must be made.

The expression for a given infrared and collinear safe observable, O, computed at NLO using a subtraction method has been given in Equation (3.10). Identifying $\mathrm{D}_{ij,k}$ with $\mathrm{S}_{ij,k}$, the term with real-emission kinematics in Equation (3.10) can then be decomposed according to Equation (3.13), resulting in

$$\sum_{\{\vec{f}\}} \mathrm{d}\Phi_R(\{\vec{p}\}) \sum_{\{i,j\}} \sum_{k\neq i,j} \Big[\mathrm{R}_{ij,k}(\{\vec{a}\})\, O(\{\vec{p}\}) - \mathrm{S}_{ij,k}(\{\vec{a}\})\, O(b_{ij,k}(\{\vec{p}\})) \Big] \;. \tag{3.30}$$

In the POWHEG method, this term is *approximated* as

$$\begin{aligned}
&\sum_{\{\vec{f}\}} \mathrm{d}\Phi_R(\{\vec{p}\}) \sum_{\{i,j\}} \sum_{k\neq i,j} \Big[\mathrm{R}_{ij,k}(\{\vec{a}\}) - \mathrm{S}_{ij,k}(\{\vec{a}\}) \Big]\, O(b_{ij,k}(\{\vec{p}\})) \\
&\quad = \sum_{\{\vec{f}\}} \mathrm{d}\Phi_B(\{\vec{p}\}) \sum_{\{\widetilde{ij},\tilde{k}\}} \sum_{f_i=q,g} \mathrm{d}\Phi^{ij,k}_{R|B} \Big[\mathrm{R}_{ij,k}(r_{\widetilde{ij},\tilde{k}}(\{\vec{a}\})) - \mathrm{S}_{ij,k}(r_{\widetilde{ij},\tilde{k}}(\{\vec{a}\})) \Big]\, O(\{\vec{p}\}) \;.
\end{aligned} \tag{3.31}$$

This allows the recombination of all contributions to the NLO cross section. Employing Equation (3.29), therefore

$$\begin{aligned}
\bar{\mathrm{B}}(\{\vec{a}\}) \;&= \mathrm{B}(\{\vec{a}\}) + \tilde{\mathrm{V}}(\{\vec{a}\}) + \mathrm{I}(\{\vec{a}\}) \\
&\quad + \sum_{\{\widetilde{ij},\tilde{k}\}} \sum_{f_i=q,g} \int \mathrm{d}\Phi^{ij,k}_{R|B} \Big[\mathrm{R}_{ij,k}(r_{\widetilde{ij},\tilde{k}}(\{\vec{a}\})) - \mathrm{S}_{ij,k}(r_{\widetilde{ij},\tilde{k}}(\{\vec{a}\})) \Big] \;.
\end{aligned} \tag{3.32}$$

Having all contributions at hand in SHERPA, cf. Section 3.1.2, the assembly of the

$\bar{\mathrm{B}}$-function, integrable in $D = 4$ dimensions, is feasible in an automated way. This involves integrating over the real-emission subspace of the phase space of the NLO real correction to the Born process and adding the result to the terms with Born-level kinematics. In SHERPA, this integration is performed in a Monte-Carlo fashion, by selecting a single point in the real-emission phase space. This technique potentially generates negative weights. In the standard POWHEG method, the emergence of such negative weights is suppressed by either performing the integration analytically or by sampling over sufficiently many real-emission phase-space points. Tests to decide which method is better for practical applications are beyond the scope of this work and will be addressed in a future work; here it should suffice to state that, of course, sampling over more than one phase-space point is neither a conceptual problem nor a practical obstacle. Also, for all processes under study in this work, no problems have been encountered by the possibility of having negative weighted events. Loosely speaking, the problem can in no case be more severe than the possibility of having negative weights in a standard NLO calculation.

Therefore, the only remaining issue is to construct an integration method, which, starting from a given Born configuration, is able to fill the real-emission phase space in an efficient manner. Having an implementation of the Catani-Seymour subtraction method at hand, the construction of an integrator for the real-emission subspace based on CS-subtraction terms is rendered a straightforward exercise. The actual integration can be decomposed into three one-dimensional integrals similar to Equation (3.19), where the integration variables t and z have a slightly different form for each dipole configuration.

Several different integration channels, each based on a separate CS dipole, can be combined to yield a multi-channel integrator [99] for the real-emission phase space. The a-priori weights in the multi-channel can be employed to better adapt to the emission pattern of the process under consideration. Additionally, every one-dimensional integrator can be individually improved using the VEGAS algorithm [100].

In the next section it will be shown that the combination of the term $\bar{\mathrm{B}}$ with a matrix-element reweighted parton shower yields the attempted $\mathcal{O}(\alpha_s)$ accuracy, not only of the total cross section, but also of the real-emission contribution.

3.2.4 The POWHEG method and its accuracy

The key point of the POWHEG method is, to supplement Monte Carlo event samples from matrix-element corrected parton showers with a next-to-leading order weight to arrive at full NLO accuracy. This is achieved by combining the two methods discussed in Sections 3.2.2 and 3.2.3. To obtain the $\mathcal{O}(\alpha_s)$ approximation to the cross section in

the POWHEG method, the parton-shower expression of the real-emission probability is combined with the approximated initial cross section, $\mathrm{d}\sigma_{\bar{B}}$. This yields the following master formula for the value of an infrared and collinear safe observable, O,

$$\begin{aligned}\langle O\rangle^{(\mathrm{POWHEG})} = \sum_{\{\vec{f}\}}\int \mathrm{d}\Phi_B(\{\vec{p}\})\,\bar{\mathrm{B}}(\{\vec{a}\})\Bigg[&\underbrace{\Delta^{(\mathrm{ME})}(t_0,\mu^2;\{\vec{a}\})}_{\text{unresolved}}\,O(\{\vec{a}\}) \\ &+\sum_{\{\widetilde{ij},\tilde{k}\}}\sum_{f_i=q,g}\frac{1}{16\pi^2}\int_{t_0}^{\mu^2}\mathrm{d}t\int_{z_{\min}}^{z_{\max}}\mathrm{d}z\int_0^{2\pi}\frac{\mathrm{d}\phi}{2\pi}\,J_{ij,k}(t,z,\phi)\,O(r_{\widetilde{ij},\tilde{k}}(\{\vec{a}\})) \\ &\times\underbrace{\frac{1}{S_{ij}}\,\frac{S(r_{\widetilde{ij},\tilde{k}}(\{\vec{f}\}))}{S(\{\vec{f}\})}\,\frac{\mathrm{R}_{ij,k}(r_{\widetilde{ij},\tilde{k}}(\{\vec{a}\}))}{\mathrm{B}(\{\vec{a}\})}\,\Delta^{(\mathrm{ME})}(t,\mu^2;\{\vec{a}\})}_{\text{resolved}}\Bigg]\,.\end{aligned} \tag{3.33}$$

where obvious arguments of the parton maps $r_{\widetilde{ij},\tilde{k}}$ have been suppressed. Clearly, if the observable $\mathcal{O}$ on the right hand side of Equation (3.33) becomes one, the quantity computed is the total cross section, as for the cases discussed in Sections 3.2.1 and 3.2.2. This particular case, however, is insensitive to the details of the radiation pattern. To continue the discussion, note that the second term in the square bracket of Equation (3.33) can be rewritten as

$$\sum_{\{\widetilde{ij},\tilde{k}\}}\int_{t_0}^{\mu^2}\mathrm{d}t\,\frac{\mathrm{d}\log\Delta^{(\mathrm{ME})}_{\widetilde{ij},\tilde{k}}(t,\mu^2;\{\vec{a}\})}{\mathrm{d}t}\,\Delta^{(\mathrm{ME})}(t,\mu^2;\{\vec{a}\})\,O(r_{\widetilde{ij},\tilde{k}}(\{\vec{p}\}))\,, \tag{3.34}$$

which allows to rearrange the expressions in Equation (3.33) as

$$\begin{aligned}\langle O\rangle^{(\mathrm{POWHEG})} = \sum_{\{\vec{f}\}}\int \mathrm{d}\Phi_B(\{\vec{p}\})\,\bar{\mathrm{B}}(\{\vec{a}\})\Bigg\{ &O(\{\vec{p}\}) \\ &+\sum_{\{\widetilde{ij},\tilde{k}\}}\int_{t_0}^{\mu^2}\mathrm{d}t\,\frac{\mathrm{d}\log\Delta^{(\mathrm{ME})}_{\widetilde{ij},\tilde{k}}(t,\mu^2;\{\vec{a}\})}{\mathrm{d}t}\,\Delta^{(\mathrm{ME})}(t,\mu^2;\{\vec{a}\})\,\left[\,O(r_{\widetilde{ij},\tilde{k}}(\{\vec{p}\}))-O(\{\vec{p}\})\,\right]\Bigg\}\,.\end{aligned} \tag{3.35}$$

Two special cases should now be considered

- The infrared limit ($t\to 0$)
  In this case, only the first term in Equation (3.35) contributes, as any infrared safe observable maps the real-emission kinematics for collinear (soft) emissions to the kinematics of the (any) underlying Born configuration

$$O(r_{\widetilde{ij},\tilde{k}}(\{\vec{p}\}))\overset{t\to 0}{\to}O(\{\vec{p}\})$$

The contribution to $\langle O \rangle^{(\text{POWHEG})}$ from this phase-space region is therefore correct to $\mathcal{O}(\alpha_s)$.

- Hard emissions ($t \to \mu^2$)
  In this case, a cancellation between the first and the last term in Equation (3.35) is achieved and only the second term remains. Also, $\Delta(t, \mu^2) \to 1$ as $t \to \mu^2$. To $\mathcal{O}(\alpha_s)$ one can then replace $\bar{\mathrm{B}} \to \mathrm{B}$, leading to

$$\sum_{\{\vec{f}\}} \int \mathrm{d}\Phi_B(\{\vec{p}\}) \sum_{\{\tilde{ij},\tilde{k}\}} \sum_{f_i=q,g} \frac{1}{16\pi^2} \int^{\mu^2} \mathrm{d}t \int \mathrm{d}z \int \frac{\mathrm{d}\phi}{2\pi} J_{ij,k}(t,z,\phi) \times \frac{S(r_{\tilde{ij},\tilde{k}}(\{\vec{f}\}))}{S(\{\vec{f}\})\, S_{ij}} \mathrm{R}_{ij,k}(r_{\tilde{ij},\tilde{k}}(\{\vec{a}\})) \; .$$

  Comparing this result with the real-emission term in Equation (3.32) reveals that both expressions differ by the factor $S(\{\vec{f}\})\, S_{ij}/S(r_{\tilde{ij},\tilde{k}}(\{\vec{f}\}))$, which arises solely due to the way the real-emission phase space is populated by the parton shower (cf. Section 3.2.1).
  Therefore, the contribution to $\langle O \rangle^{(\text{POWHEG})}$ from this phase-space region is correct to $\mathcal{O}(\alpha_s)$.

In the phase-space regions "between" these limits, the POWHEG method interpolates smoothly between the two above results.

3.2.5 Automatic identification of Born zeros

It was noted in [90] that Equation (3.26) can develop spurious singularities as the matrix element of the underlying Born process may be zero, while the real-emission matrix element is not. Such configurations do not exponentiate, as $\mathcal{R}$ is not singular when $\mathcal{B} \to 0$. This fact can be employed to formulate a general solution to the problem [90]. One can split $\mathcal{R}$ into two parts, a singular one, $\mathcal{R}^{(\mathrm{s})}$, and a regular one, $\mathcal{R}^{(\mathrm{r})}$.

$$\mathcal{R}^{(\mathrm{s})} = \mathcal{R}\,\frac{Z}{Z+H} \; , \qquad \text{and} \qquad \mathcal{R}^{(\mathrm{r})} = \mathcal{R}\,\frac{H}{Z+H} \; , \tag{3.36}$$

where

$$Z = \frac{\mathcal{B}}{\mathcal{B}_{\max}} \; , \qquad \text{and} \qquad H = \kappa_{\mathrm{res}}^2\,\frac{t}{t_{\max}} \; . \tag{3.37}$$

Note that $\mathcal{B}_{\max}$ can be determined during the integration of the seed cross section, while $t_{\max}$ is given as a universal function of the hadronic centre-of-mass energy, depending only on the definition of t in the parton shower model. The resolution factor κ_{res} then

determines the relative splitting between $\mathcal{R}^{(\mathrm{s})}$ and $\mathcal{R}^{(\mathrm{r})}$: the larger κ_{res}, the larger the fraction $\mathcal{R}^{(\mathrm{r})}$ of $\mathcal{R}$.

The necessity of such a splitting of the real emission matrix element can be determined on an event-by-event basis by comparing the correction factor of Equation (3.25), $w_{ij,k}$, to a predefined threshold $w_{ij,k}^{\mathrm{th}}$. Thus, regular non-exponentiated $\mathcal{R}^{(\mathrm{r})}$ events are only produced if $w_{ij,k} > w_{ij,k}^{\mathrm{th}}$. Such a treatment ensures that both the exponentiation of the real-emission matrix element is as inclusive as possible and the parton-shower correction factor does not get too large, rendering event generation too inefficient.

3.2.6 Results

This section collects results obtained with the implementation of the POWHEG algorithm in the SHERPA event generator. Its performance is exemplified in a variety of processes which are listed in Section 3.2.6.1 with their respective cuts and relevant settings. In Section 3.2.6.2 the internal consistency of the implementation is checked by performing scale variations, cross section comparisons with ordinary NLO calculations, and variations of internal parameters of POWHEG. Comparisons of results from the new implementation with predictions from tree-level matrix-element parton-shower merging (ME+PS) are presented in Section 3.2.6.3. Finally, comparisons with experimental data are made in Section 3.2.6.4.

3.2.6.1 Process listing

Jet production in e^+e^- collisions The annihilation of e^+e^- into hadrons is studied at LEP Run 1 energies, $E_{\mathrm{CMS}} = 91.25$ GeV. This setup allows to validate the algorithms of Section 3.2 in pure final-state QCD evolution, which is the simplest testing ground. The parton shower cut-off scale has been set to $k_{T,\,\mathrm{min}}^2 = 1.6\ \mathrm{GeV}^2$. Even though the improvements in this work are purely related to perturbative physics, the results are presented after hadronisation with the Lund model [2, 22] to make comparison to experimental results more meaningful. The ME+PS samples have been generated with up to one additional jet in the matrix elements and the phase space slicing parameter was set to $\log(y_{\mathrm{cut}}) = -2.25$. For the virtual matrix elements, the code provided by the BlackHat collaboration [101] was used.

Deep-inelastic lepton-nucleon scattering Hadronic final states in deep-inelastic lepton-nucleon scattering (DIS) are studied at HERA Run 1 energies, $E_{\mathrm{CMS}} = 300$ GeV. Just

like e^+e^--annihilation into hadrons, this process boasts a wealth of precise experimental data. From the theoretical perspective, it is invaluable, as it allows to test QCD factorisation in an extremely clean environment. The associated scale, given by the virtuality of the exchanged γ^*/Z-boson is not fixed, but potentially varies by orders of magnitude, which allows to test perturbative QCD predictions in various kinematic limits. Results are presented at the parton level only, as hadronisation corrections have little effect on the observables and the focus lies on the potential improvements in the perturbative part of the simulation. The CTEQ6.6 [102] parton distribution functions have been employed and the strong coupling has been defined accordingly as $\alpha_s(m_Z) = 0.118$ with NLO running for both the matrix elements and the parton shower. The remaining settings correspond to those in [14]. ME+PS samples have been generated with up to one additional jet in the matrix element and the phase space slicing parameters were set to $\bar{Q}_{\text{cut}} = 5$ and $S_{\text{DIS}} = 0.6$ (cf. [14]). Virtual matrix elements were provided by BlackHat [101].

Drell-Yan lepton pair production Drell-Yan lepton pair production is investigated at Tevatron Run 2 energies, simulating $p\bar{p}$ collisions at $E_{\text{CMS}} = 1.96$ TeV. The CTEQ6.6 [102] parton distribution functions are employed and the strong coupling is defined accordingly as $\alpha_s(m_Z) = 0.118$ with NLO running for both the matrix elements and the parton shower. A cut on the invariant mass of the lepton pair of $66 < m_{\ell\ell}/\text{GeV} < 116$ is applied at the matrix-element level. For the ME+PS samples matrix elements with up to one additional jet were generated and a phase-space slicing cut of $Q_{\text{cut}} = 20$ GeV was applied. Virtual matrix elements were provided by BlackHat [101]. The factorisation and renormalisation scales for the NLO matrix element were chosen as $\mu_R^2 = \mu_F^2 = m_{\perp,\ell\ell}^2$. In all tree-level matrix elements SHERPA's default scale choice was employed: The matrix element is clustered onto a core $2 \to 2$ configuration using a k_T-type algorithm with recombination into on-shell particles. Scales are defined as the lowest invariant mass or negative virtuality in the core process. Hadronisation and multiple parton interactions have been disabled to allow for a study at the parton-shower level. The $Z \to \ell\ell$ decay is corrected for QED next-to-leading order and soft-resummation effects in the Yennie-Frautschi-Suura (YFS) approach [103].

These first three reactions essentially amount to one and the same process at the parton level, as they only differ by crossing of initial- and final-state legs. Their combination allows to validate the implementation of the matrix-element reweighting in Section 3.2.2 for all possible dipole configurations with quark splitters.

***W* boson production** Production of W bosons is presented in $p\bar{p}$ collisions at $E_{\mathrm{CMS}} = 1.8$ TeV. Although in principle similar to the Drell-Yan case, this process is of special interest to validate the automatic decomposition of the real-emission term into singular and non-singular pieces, as outlined in Section 3.2.5. If not stated otherwise, the parameters for this decomposition are set to $\kappa_{\mathrm{res}} = 4$ and $w_{ij,k}^{\mathrm{th}} = 100$. The CTEQ6.6 [102] parton distribution functions have been employed and the strong coupling has been defined accordingly as $\alpha_s(m_Z) = 0.118$ with NLO running for both the matrix elements and the parton shower. A cut on the invariant mass of the lepton-neutrino pair of $m_{\ell\nu} > 10$ GeV was applied at the matrix-element level. For the ME+PS samples matrix elements with up to one additional jet were used and a phase space slicing cut of $Q_{\mathrm{cut}} = 20$ GeV was applied. Virtual matrix elements were provided by BlackHat [101]. The factorisation and renormalisation scales for the NLO matrix element were chosen as $\mu_R^2 = \mu_F^2 = m_{\perp,\ell\nu}^2$. In all tree-level matrix elements SHERPA's default scale choice was employed. Hadronisation and multiple parton interactions have been disabled. The $W \to \ell\nu$ decay is corrected for QED next-to-leading order and soft-resummation effects in the YFS approach [103].

Higgs boson production through gluon-gluon fusion The production of Higgs bosons through gluon-gluon fusion is simulated for proton-proton collisions at $E_{\mathrm{CMS}} = 14$ TeV. The coupling to gluons is mediated by a top-quark loop and modelled through an effective Lagrangian [104]. Again, this process is technically very similar to the Drell-Yan case, but it also allows to validate matrix-element corrections to the remaining initial-state splitting functions. Next-to-leading order corrections are rather large at nominal LHC energies, with a ratio of $K \approx 2$ between the NLO and the LO result for the total cross section. This fact has spurred tremendous efforts to perform fully differential calculations at NNLO [105] and several predictions have been presented which merged such fixed-order results with resummation at next-to-next-to-leading logarithmic accuracy [106], as the process is expected to have high phenomenological relevance at LHC energies. However, this work centres on the behaviour of the theory at NLO only, as a prediction beyond this level of accuracy is clearly not within the capabilities of the POWHEG method.

The CTEQ6.6 [102] parton distribution functions have been employed and the strong coupling has been defined accordingly as $\alpha_s(m_Z) = 0.118$ with NLO running for both the matrix elements and the parton shower. A cut for the invariant mass of the τ pair of $115 < m_{\tau\tau}/\mathrm{GeV} < 125$ was applied at the matrix-element level. For the ME+PS merged samples matrix elements with up to one additional jet were used and a phase-space slicing cut of $Q_{\mathrm{cut}} = 20$ GeV was applied. The virtual matrix elements have been implemented according to [104]. The factorisation and renormalisation scales for

the NLO matrix element were chosen as $\mu_R^2 = \mu_F^2 = m_{\perp,\tau\tau}^2$. In all tree-level matrix elements SHERPA's default scale choice was employed. Hadronisation and multiple parton interactions have been disabled. The $h \to \tau\tau$ decay is corrected for QED soft-resummation and approximate next-to-leading order effects in the YFS approach [103].

Z–pair production The production of pairs of Z bosons is studied for proton-proton collisions at $E_{\mathrm{CMS}} = 14$ TeV. This is an important background for the golden-plated Higgs-boson discovery mode at the LHC. Detailed studies of the decay properties of the Z bosons and their correlations are known to allow for a determination of some properties of the Higgs boson, when found. Among these correlations are, e.g. the relative orientation of the decay planes of the bosons.

The CTEQ6.6 [102] parton distribution functions have been employed and the strong coupling has been defined accordingly as $\alpha_s(m_Z) = 0.118$ with NLO running for both the matrix elements and the parton shower. A cut on the invariant mass of each lepton pair of $66 < m_{\ell\ell}/\mathrm{GeV} < 116$ was applied at the matrix-element level. For the ME+PS samples matrix elements with up to one additional jet were used and a phase-space slicing cut of $Q_{\mathrm{cut}} = 20$ GeV was applied. Virtual matrix elements were provided by MCFM [107,108]. The factorisation and renormalisation scales were chosen as $\mu_R^2 = \mu_F^2 = m_{ZZ}^2$. Hadronisation and multiple parton interactions have been disabled to allow for a study at the parton shower level. Each $Z \to \ell\ell$ decay is corrected for QED next-to-leading order and soft-resummation effects in the YFS approach [103].

W^+W^-–production W^+W^-–production is also studied for proton-proton collisions at $E_{\mathrm{CMS}} = 14$ TeV. It is worth noting that this process hitherto has not been treated in the POWHEG approach. Similar to the Z–pair production, it is an important background to the search channel for the Standard-Model Higgs boson, at masses around and above 130 GeV. Again, in order to suppress this background, distributions which depend on correlations of decay products of the W's in phase space are heavily used.

In the simulation here, again the CTEQ6.6 [102] parton distribution functions have been employed and the strong coupling has been defined accordingly as $\alpha_s(m_Z) = 0.118$ with NLO running for both the matrix elements and the parton shower. A cut on the invariant mass of each lepton-neutrino pair of $m_{\ell\nu} > 10$ GeV was applied at the matrix-element level. For the ME+PS samples matrix elements with up to one additional jet were used and a phase-space slicing cut of $Q_{\mathrm{cut}} = 20$ GeV was applied. Virtual matrix elements were provided by MCFM [107, 108]. The factorisation and renormalisation scales were chosen as $\mu_R^2 = \mu_F^2 = m_{WW}^2$. Hadronisation and multiple parton interactions have been disabled to allow for a study at the parton-shower level. Each $W \to \ell\nu$ decay

		$e^+e^- \to$ hadrons		$e^+p \to e^+ + j + X$	
		$E_{\text{cms}} = 91.2$ GeV		$E_{\text{cms}} = 300$ GeV $Q^2 > 150$ GeV^2	
$\mu = \mu_R = \mu_F$	Factor	POWHEG	NLO	POWHEG	NLO
$\sqrt{Q^2}$	1/2	30179(18)	30195(20)	3906(9)	3908(10)
	1	29411(17)	29416(18)	4047(10)	4050(11)
	2	28680(16)	28697(18)	4180(10)	4188(11)

Table 3.1: Cross sections in pb for e^+-e^- annihilation into hadrons at LEP and deep-inelastic positron-proton scattering at HERA as calculated in the POWHEG framework and in a conventional fixed order NLO calculation [95].

		$p\bar{p} \to W^+ + X$		$p\bar{p} \to Z + X$		$pp \to h + X$	
		$E_{\text{cms}} = 1.8$ TeV $m_{\ell\nu} > 10$ GeV		$E_{\text{cms}} = 1.96$ TeV $66 < m_{\ell\ell} < 116$ GeV		$E_{\text{cms}} = 14$ TeV $115 < m_{\tau\tau} < 125$ GeV	
$\mu_R = \mu_F$	Factor	POWHEG	NLO	POWHEG	NLO	POWHEG	NLO
$m_{\ell\nu}/m_{\ell\ell}$	1/2	1235.4(5)	1235.1(1.0)	243.96(14)	243.84(16)	2.3153(13)	2.3130(13)
	1	1215.0(5)	1214.9(9)	239.70(13)	239.59(16)	2.4487(12)	2.4474(13)
	2	1201.4(5)	1202.0(9)	236.72(13)	236.77(15)	2.5811(13)	2.5786(13)
$m_\perp$	1/2	1231.0(5)	1230.3(1.0)	243.00(14)	243.06(16)	2.2873(13)	2.2869(14)
	1	1211.8(5)	1211.7(9)	239.01(13)	238.96(15)	2.4255(12)	2.4231(19)
	2	1198.8(5)	1199.3(9)	236.23(13)	236.13(14)	2.5623(13)	2.5620(14)

Table 3.2: Cross sections in pb for inclusive $W^+[\to e^+\nu_e]$ and $Z[\to e^+e^-]$ production at the Tevatron and $h[\to \tau^+\tau^-]$ production via a top-quark loop at the LHC as calculated in the POWHEG framework and in a conventional fixed order NLO calculation [95].

is corrected for QED next-to-leading order and soft-resummation effects in the YFS approach [103].

3.2.6.2 Tests of internal consistency

The aim of this section is to provide consistency checks on the different aspects of the POWHEG implementation in SHERPA. At first, total cross sections as obtained from POWHEG are compared with the corresponding results from a standard NLO calculation. In this case, the public release SHERPA-1.2.2 [3] serves as the reference, which includes an implementation of [95]. Results for e^+e^- annihilation into hadrons and deep-inelastic positron-proton scattering are presented in Table 3.1. Numbers for inclusive Z-boson production with decay to an electron-positron pair, for inclusive W-boson production with decay to an electron-neutrino pair, and for Higgs-boson production via a top-quark loop with decay into τ are listed in Table 3.2. The agreement

[3] See http://www.sherpa-mc.de.

between the POWHEG results and those of the standard integration method typically is within a 1σ range as given by the respective Monte-Carlo errors.

To examine differences between POWHEG and a parton-shower Monte Carlo regarding the exponentiation of the real-emission matrix elements in POWHEG, $\mathcal{R}$ can be approximated by $\mathcal{R}^{(\mathrm{PS})}$ in Equation (3.26). Performing this replacement does not only constitute a mandatory cross-check, whether the parton-shower approximation is retained, but it also estimates the size of corrections that can be expected at all when switching to NLO accuracy in the event simulation. Apart from the overall normalisation, in processes with no additional phase space dependence introduced by the loop matrix element, the emission pattern in POWHEG should be identical to the parton-shower result. This is verified in inclusive Z-boson production at Tevatron energies as displayed in Figure 3.1. For low transverse momentum (low jet resolution) $p_\perp \ll \mu_F$ both distributions coincide within statistical errors. For large values the emission phase space is severely restricted in the parton-shower approach, as $t < \mu_F^2 \approx m_Z^2$ and $p_\perp \lesssim t$. Any contribution to this phase-space region must therefore originate from configurations where more than one hard parton recoils against the lepton pair. Such configurations are suppressed by higher orders of α_s, and therefore the emission rate is gravely underestimated by the parton shower. As a direct consequence, all deviations are then manifestations of the exponentiation of non-logarithmic terms, which can be sizable in the hard wide-angle emission region.

The automatic splitting of the real-emission matrix element into singular and regular contributions as presented in Section 3.2.5 contains two unphysical parameters: κ_{res}, which governs the relative sizes of the exponentiated, singular part $\mathcal{R}^{(\mathrm{s})}$ and the non-exponentiated, regular part $\mathcal{R}^{(\mathrm{r})}$, and $w_{ij,k}^{\mathrm{th}}$, which determines when the above separation is actually employed. The effect of κ_{res} on the central parton shower reweighting factor $w_{ij,k}$ is detailed Figure 3.2. There, it can be seen that for values of κ_{res} chosen neither too low, such that the maximum of the reweighting factor rises beyond reasonable bounds rendering the reweighting of the parton shower inoperable, nor too high, such that parts of leading logarithmic structure of $\mathcal{R}$ are not exponentiated, event generation with the accuracy aimed at by the POWHEG algorithm is feasible. Hence, the results of the Monte-Carlo simulation should be fairly independent of κ_{res} and $w_{ij,k}^{\mathrm{th}}$, if varied within a reasonable range. Figure 3.3 displays predictions for transverse momentum spectra in W-boson production for several values of κ_{res}. As expected, no significant variations of the emission pattern can be observed. The small differences that can be seen when changing the resolution scale κ_{res} are entirely within the logarithmic accuracy of the parton-shower approach and therefore also within the logarithmic accuracy of the real-emission contribution in POWHEG. Variations in $w_{ij,k}^{\mathrm{th}}$ only have very little influence on physical distributions.

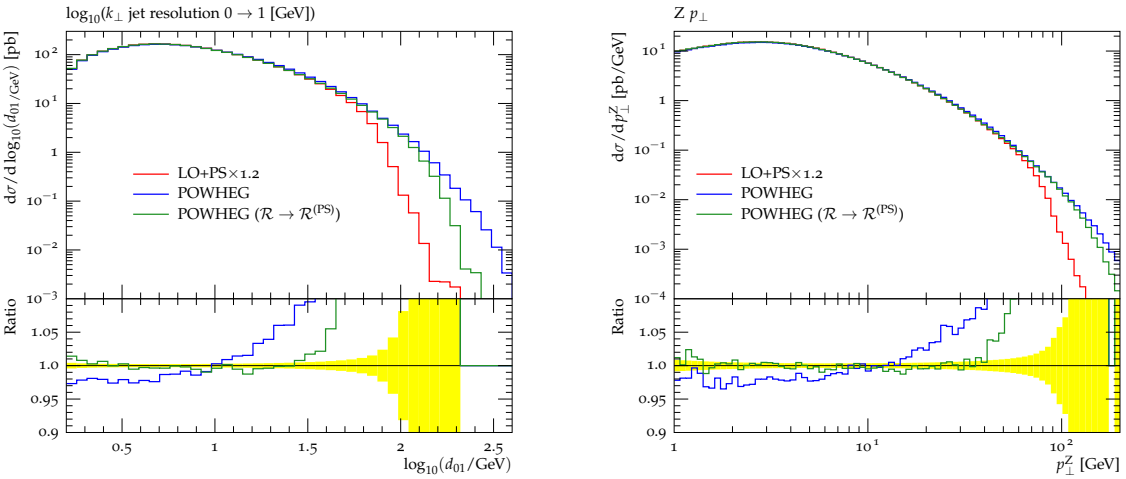

Figure 3.1: $0 \to 1$ k_T jet resolution and $p_\perp$ of the reconstructed Z-boson in Drell-Yan production at the Tevatron. The standard parton shower effected on the LO matrix elements (red) is compared to the POWHEG formulation (blue) and to POWHEG with the real emission matrix element $\mathcal{R}$ replaced by its parton-shower approximation $\mathcal{R}^{(\mathrm{PS})}$ (green).

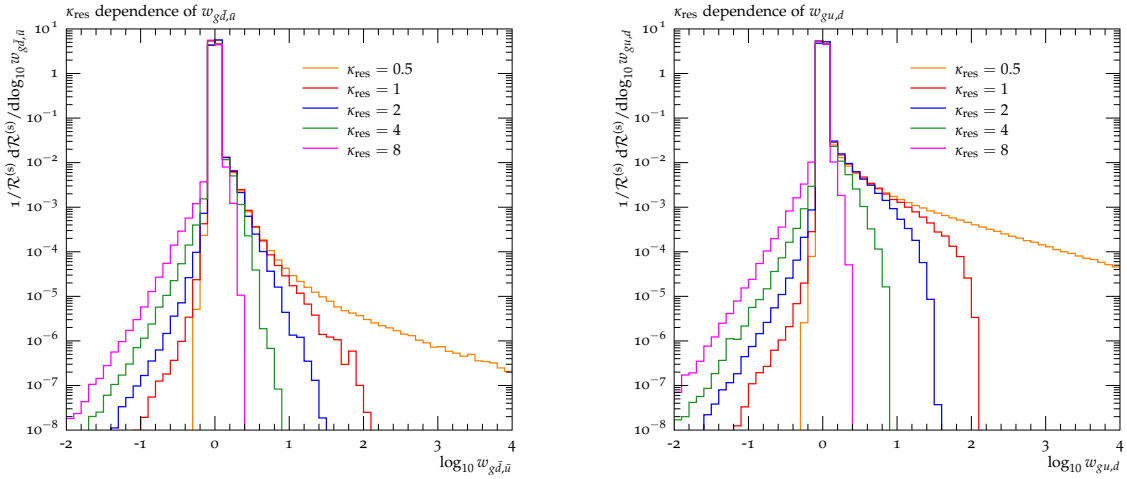

Figure 3.2: Dependence of the parton shower correction factor $w_{ij,k}$ on the Z-H-splitting parameter κ_{res} for W^- production at the Tevatron.

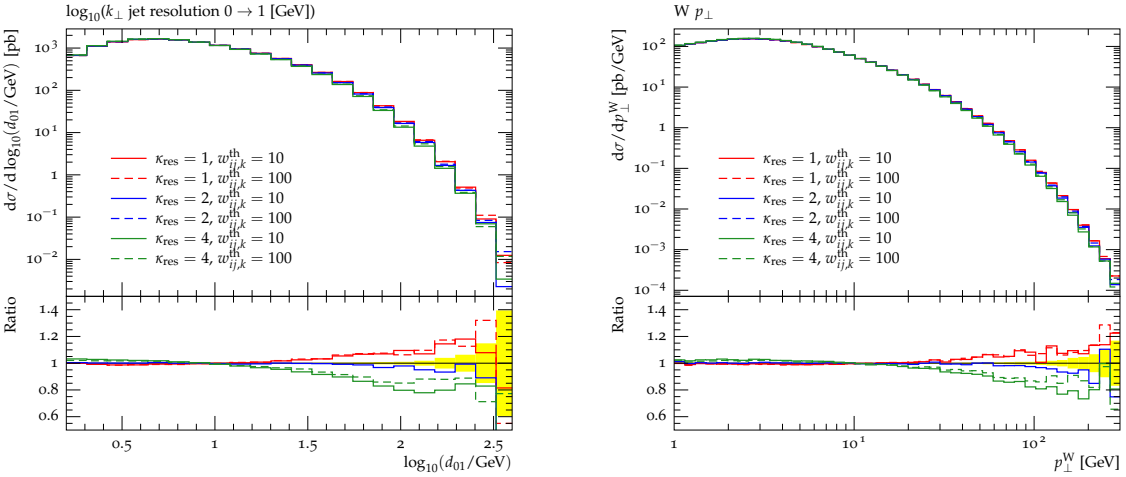

Figure 3.3: The $0 \to 1$ k_T jet resolution and $p_\perp$ of the reconstructed W boson in W-boson production at the Tevatron for different settings of the Z-H-splitting parameters κ_{res} and $w^{\mathrm{th}}_{ij,k}$.

3.2.6.3 Comparison with tree-level matrix-element parton-shower merging

By comparing POWHEG results to a standard parton shower combined with LO matrix elements (LO+PS), it can be established whether observables are produced correctly in regions where the soft/collinear approximations in the parton shower are equivalent to the R/B ratios in POWHEG. An example is the distribution of the jet resolution scale d_{01}, using the longitudinally invariant k_T-algorithm in W/Z + jets production. This observable amounts to the k_T-scale where a 1-jet event is clustered into a 0-jet event. Figure 3.4 shows that there is good agreement between the LO+PS and POWHEG results for $d_{01} < 50$ GeV. For harder emissions the LO+PS approach fails due to the restricted phase space, as explained in the previous section.

In this work, the POWHEG method is regarded as an advanced matrix-element reweighting technique for the parton-shower algorithm; the reweighting is supplemented with *local* K-factors to implement full NLO corrections. It is therefore useful to compare the respective results with matrix-element parton-shower merged samples (ME+PS), which are rescaled by a suitably chosen *global* K-factor. Such samples are known to yield approximate NLO radiation patterns by effectively implementing higher-order matrix-element corrections into the parton shower. An implementation of one of the most advanced ME+PS algorithms to date is available within the SHERPA framework [11] such that a direct comparison with POWHEG is a straightforward exercise. However, because of the lack of virtual contributions in the LO+PS and ME+PS samples, an agreement of the total rate cannot be expected. Thus, in the comparisons below the following *global* K-factors were employed:

- $K = 1.038$ for $e^+e^- \to$ hadrons at LEP energies,
- $K = 1.2$ for Z/γ^* and W production at Tevatron energies,
- $K = 1.2$ for ZZ production at the LHC (14 TeV),
- $K = 1.34$ for W^+W^- production at the LHC (14 TeV), and
- $K = 2.1$ for Higgs production through gluon fusion at the same LHC energies.

When comparing POWHEG results to ME+PS results including matrix elements up to the 1-jet final state one should obtain a very similar radiation pattern. The observed agreement indeed is very good, as expected. Figure 3.4 shows that, for example, the differential one-jet rates in W/Z-boson production agrees on the 20% level, even for relatively large scales ($d_{01} > 50$ GeV). The remaining differences can be attributed to the differences in the Sudakov form factors: While POWHEG exponentiates R/B, the

ME+PS method uses standard Sudakov form factors at the logarithmic accuracy of the parton shower.

Such differences become visible also in the multiplicity distribution of k_T jets with $p_\perp > 20$ GeV in Drell-Yan and W production, cf. Figure 3.5. The 0-jet and 1-jet rates agree within 10% between POWHEG and ME+PS, but for higher multiplicity final states the POWHEG method predicts significantly more jets. Here a ME+PS simulation with more jets in the matrix element would lead to better agreement.

Now focusing on the properties of the leading jet produced in association with a W or Z boson, the transverse momentum of the leading jet is shown in Figure 3.7. Here the LO+PS approach fails to describe the hard tail of the distribution, again due to lacking phase space, while the POWHEG and ME+PS approaches agree within 20%. The separation in η-ϕ space between this jet and the W/Z boson is displayed in Figure 3.6. Clear differences in the shape of the distribution comparing the LO+PS approach with both POWHEG and ME+PS are found, as expected, since the other hand, parton showers cover only a restricted area of the phase space, and, in addition, they do not encode the full final-state correlations described by the matrix elements. Results from the POWHEG and ME+PS methods agree very well, with differences below 10% only. A similar finding applies to the transverse momentum of the leading jet, which is shown in Figure 3.7. Here the LO+PS approach fails to describe the hard tail of the distribution, while the POWHEG and ME+PS approaches agree within 20%.

The transverse momentum of the Higgs boson and the transverse momentum of the leading jet displayed in Figure 3.8 give a similar picture as in vector boson production: All three methods agree very well for low transverse momenta. In the high $p_\perp$ region the POWHEG and ME+PS approaches show differences up to 40%.

Figure 3.9 shows that minor differences arise between the LO+PS and the POWHEG and ME+PS approaches in the pseudorapidity spectrum of the leading jet. This can be understood as a direct consequence of the different transverse momentum distributions in the LO+PS method, as harder jets tend to be more central than softer ones. The POWHEG and ME+PS approaches agree well in the central rapidity region and show up to 10% difference only in the forward region. The distribution of η-ϕ separation between the two leading jets proves again that the POWHEG and ME+PS predictions are very similar, with deviations below the 5% level. Again, the LO+PS prediction shows a slightly different behaviour, because of the reasons stated above.

Now the focus lies on diboson production at nominal LHC energies of 14 TeV. Figure 3.10 (left) shows a comparison of the scalar sum H_T of the transverse momenta of jets and leptons in Z-pair production. Deviations of up to 50% become visible between

the three compared approaches. This is especially true in the high-H_T region. It is well understood that the predictions of the LO+PS approach are softer than either of the two other approaches, due to the restricted emission phase space. The relatively large differences between the ME+PS approach and POWHEG are naively not expected, but might stem from using consistent but somewhat oversimplified scale schemes. This surely should be analysed in more detail, in a forthcoming publication, where pair production processes, including WH and ZH would be studied. The transverse momentum distributions of the individual Z bosons (Figure 3.10 right) on the other hand agree very well in both approaches, while it is again obvious that the LO+PS sample cannot describe the hard region of this spectrum.

In the azimuthal separation of the two Z bosons, see Figure 3.11, a similar feature as in H_T can be found: The events are harder in ME+PS than in POWHEG, leading to increased decorrelation of the boson pair. In Figure 3.11 (right) it can be seen that the angle between the boson decay planes is predicted very consistently in all three approaches.

Properties of the leading jet in W^+W^- pair production at LHC energies are displayed in Figure 3.12. On the left hand side one can see the transverse momentum of the leading jet and on the right hand side the separation between lepton and leading jet. For both the ME+PS and POWHEG approaches agree well within 20% and the LO+PS sample severely underestimates the hardness of the first jet due to its phase-space restrictions.

Figure 3.13 displays observables related to the two oppositely charged leptons from the two decays. The pseudorapidity difference (left) agrees within 20% for all three approaches, while their azimuthal decorrelation is significantly lower in the LO+PS sample than in the ME+PS and POWHEG approaches, which agree very well.

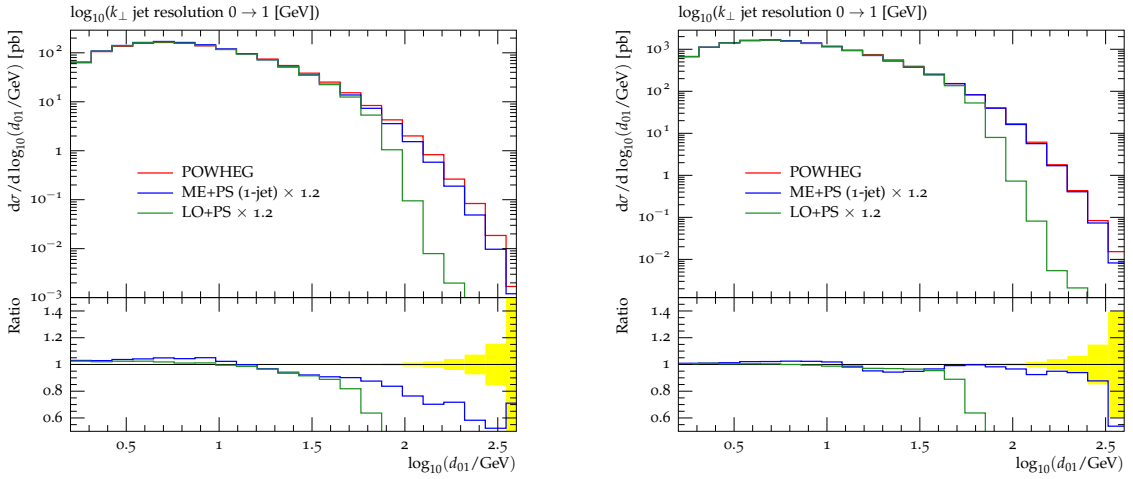

Figure 3.4: Predictions for the $0 \to 1$ jet resolution in k_T clustered jets in Z/γ^* (left) and W (right) boson production at the Tevatron.

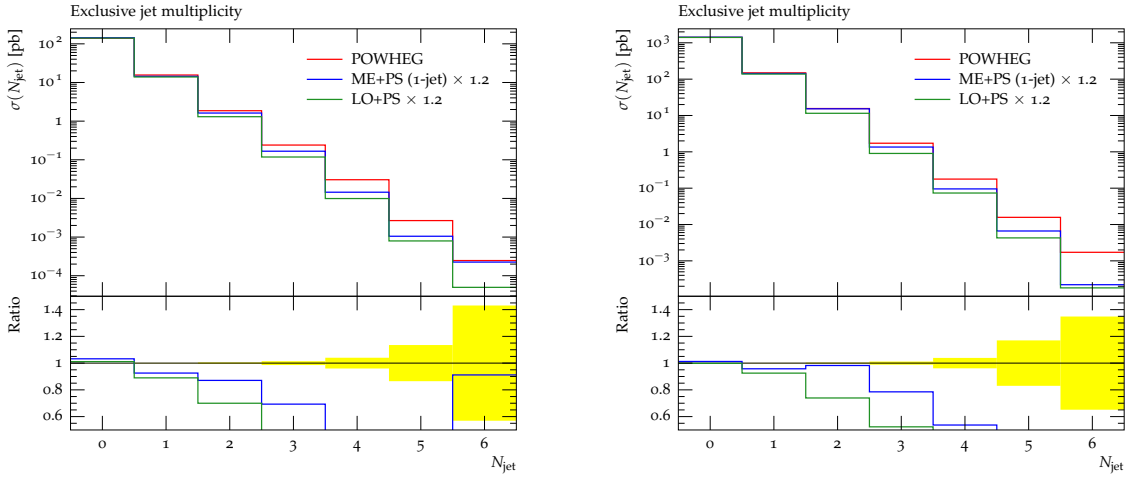

Figure 3.5: Exclusive jet multiplicity for jets with $p_\perp > 20$ GeV in the k_T algorithm in Z/γ^* (left) and W (right) boson production at the Tevatron.

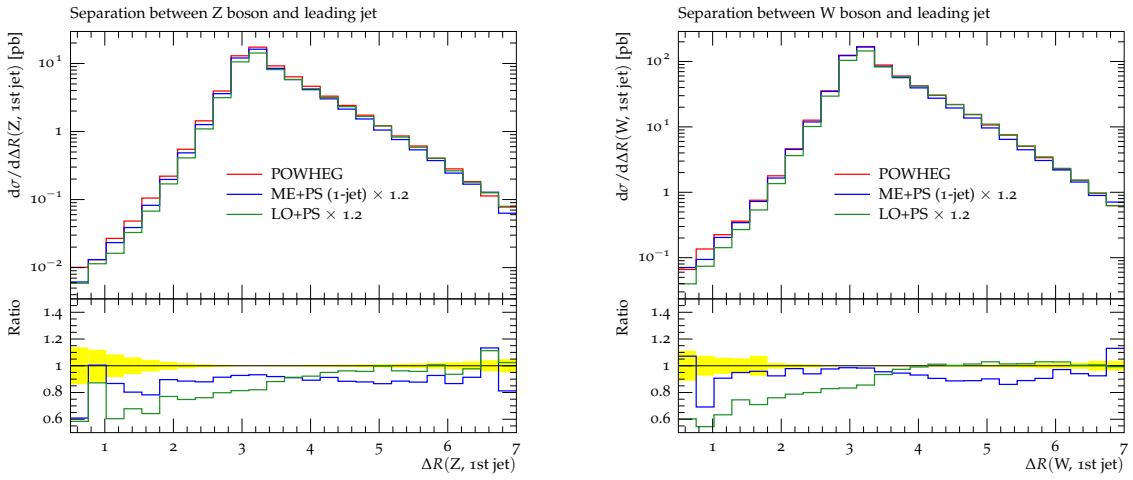

Figure 3.6: Separation between vector boson and leading jet in Z/γ^* (left) and W (right) boson production at the Tevatron.

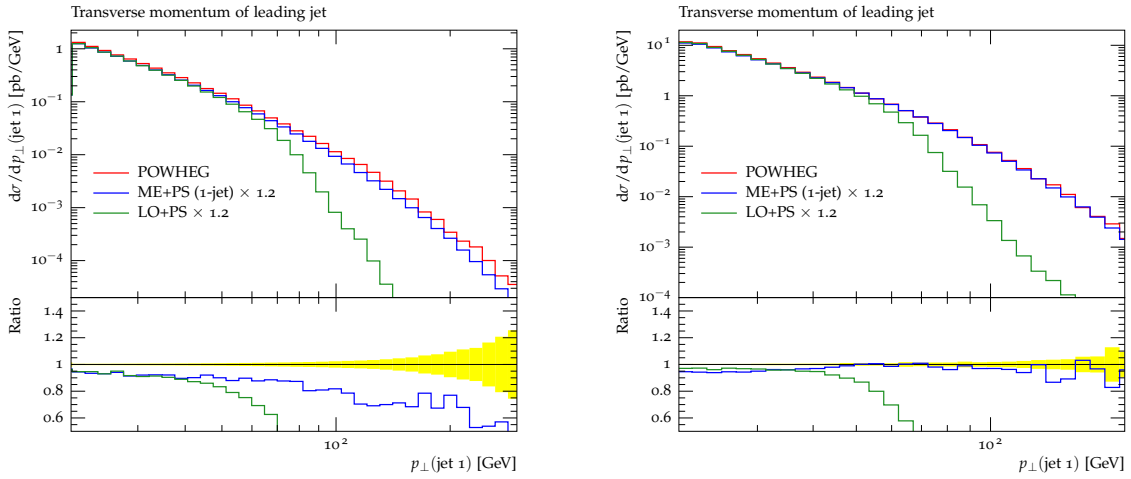

Figure 3.7: Transverse momentum of the leading jet in Z/γ^* (left) and W (right) boson production at the Tevatron.

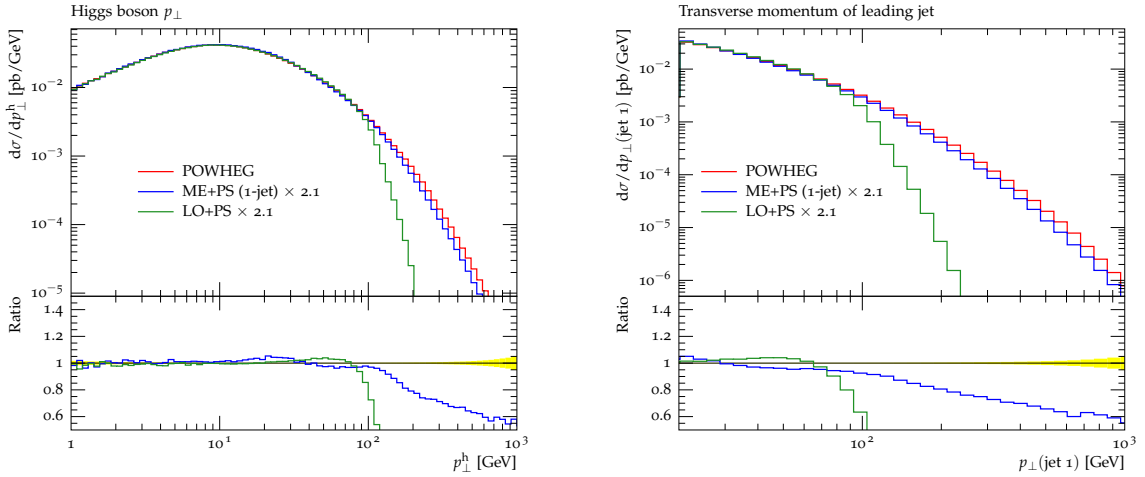

Figure 3.8: Transverse momentum of the Higgs boson (left) and leading jet (right) in $gg \to h$ fusion at nominal LHC energies.

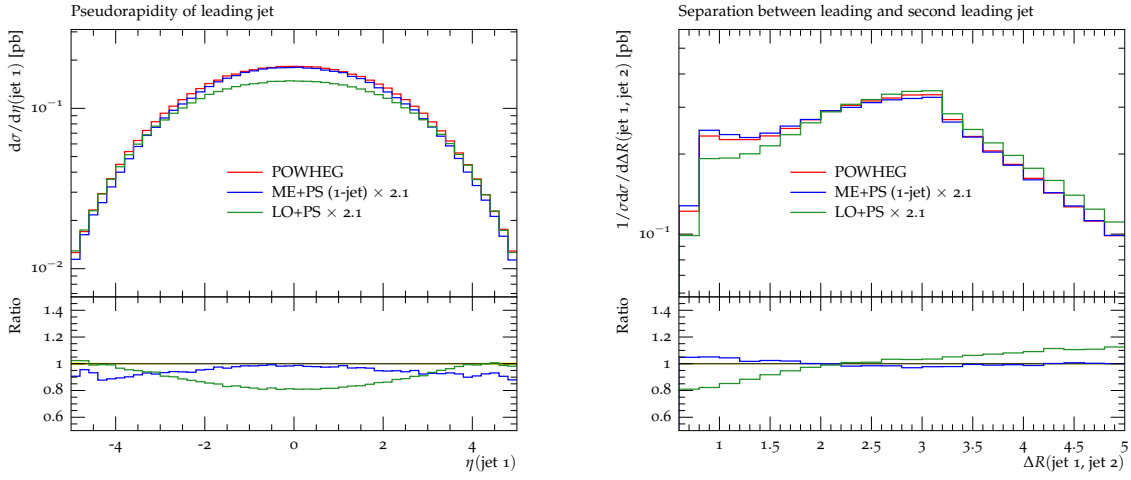

Figure 3.9: Rapidity of the leading jet (left) and separation of the leading and second-leading jet (right) in $gg \to h$ fusion at nominal LHC energies.

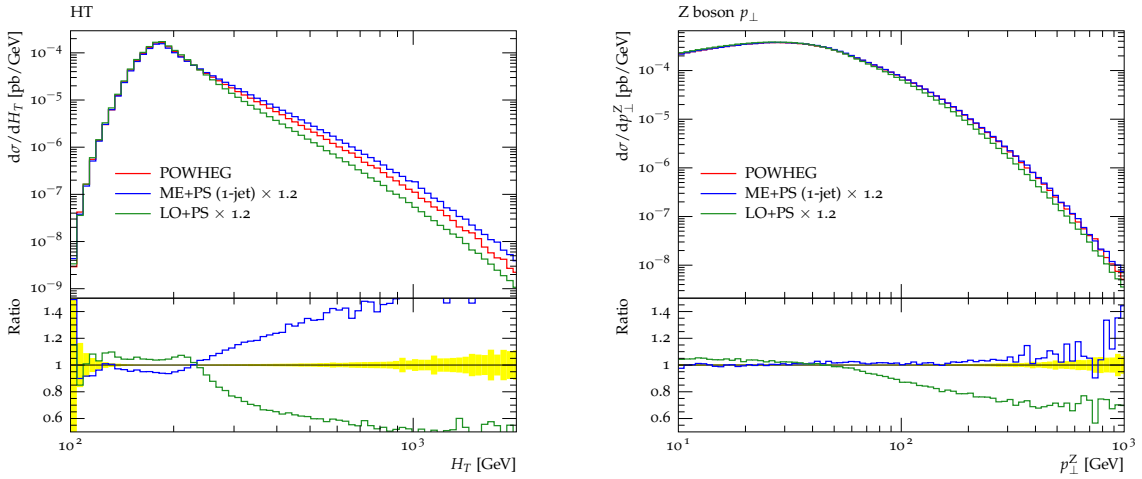

Figure 3.10: H_T (left) and transverse momentum of the individual Z bosons (right) in ZZ production at nominal LHC energies.

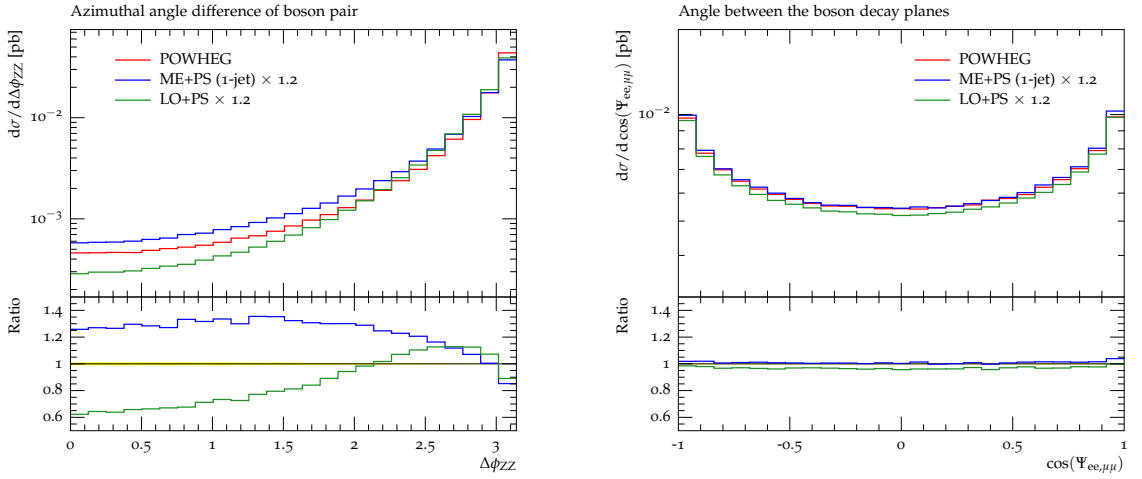

Figure 3.11: Azimuthal angle between the two Z bosons (left) and angle between the two Z decay planes (right) in ZZ production at nominal LHC energies.

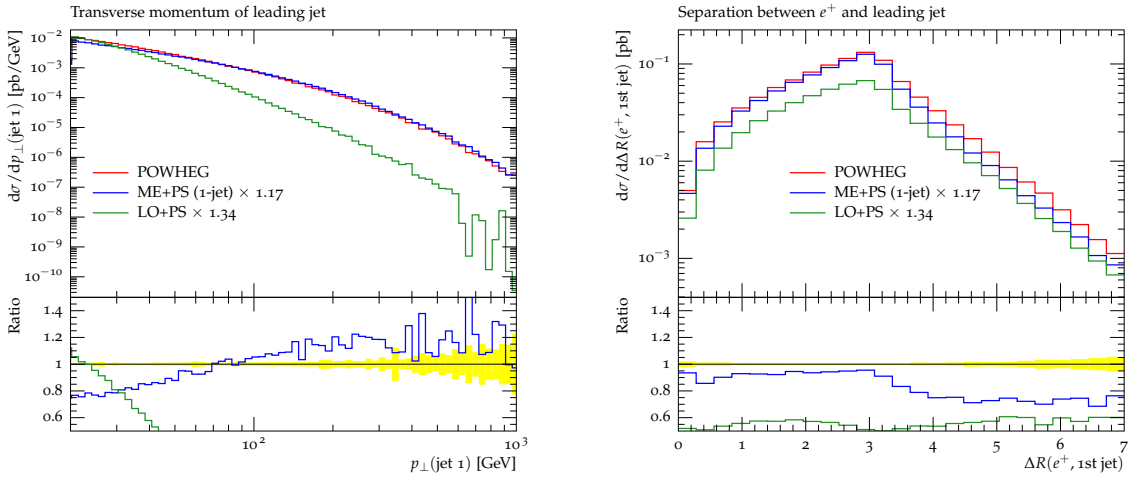

Figure 3.12: Transverse momentum of the leading jet (left) and separation of the lepton and leading jet (right) in W^+W^- production at LHC energies.

3.2.6.4 Comparison with experimental data

The remainder of this section is dedicated to a comparison of results from the POWHEG approach with experimental data to assert the improved description of data, provided by this method.

For the reaction $e^+e^- \to$ hadrons at LEP1 energies the LO+PS and ME+PS predictions do not show significant differences except in extreme regions of phase space. The POWHEG prediction confirms that picture. This is largely due to the fact that the parton-shower algorithm, which is employed in SHERPA is based on Catani-Seymour subtraction terms and those terms constitute a rather good approximation to the real-emission matrix element in the process $e^+e^- \to q\bar{q}g$.

In the distribution of the Durham jet resolution at which 3-jet events are clustered into 2-jet events (Figure 3.14 left) all three approaches agree very well with the measurement over large parts of the phase space. Only in the hard emission region $y_{23} > 0.05$ deviations from the LO+PS result can be seen. It is encouraging, although not surprising to note that both POWHEG and ME+PS describe the data better. Good agreement of all three approaches with each other and with the measurement is also observed e.g. for the thrust distribution (Figure 3.14 right), the total jet broadening (Figure 3.15 left) and the C-Parameter (Figure 3.15 right).

As was discussed in [14], deep-inelastic scattering processes offer the opportunity to test perturbative QCD in a region where the factorisation scale of the inclusive process, Q^2, is smaller than the scale of the actual event, which might be set e.g. by the transverse momentum of a hard jet. As measurements can be performed down to very low values of Q^2, many hard jets must usually be included in the simulation to achieve a good description of data throughout the phase space. This method cannot be used in the context of this work, as the POWHEG implementation in SHERPA can so far only be employed for the core process $e^\pm q \to e^\pm q$. Therefore, results are presented for the high-Q^2 region only and the discussion of the low-Q^2 domain is postponed to Section 3.3.3, where the merging of POWHEG samples with higher-multiplicity matrix elements will be discussed. Figure 3.16 shows reasonable agreement between the POWHEG results and experimental data in a measurement of the di-jet cross section performed at the H1 experiment [109, 110]. Deviations from the LO+PS result are apparent, especially at lower values of Q^2, as the phase space of the parton shower is severely restricted by the low factorisation scale. Similar findings apply to the rapidity spectra shown in Figure 3.17.

The probably most discussed observable probing the influence of QCD radiation in hadron-hadron collisions is the transverse momentum of the lepton pair in Drell-Yan

production, which is displayed in Figure 3.18. Very good agreement, compared to a recent measurement, is found for both the POWHEG and ME+PS approaches, while the LO+PS method is not able to describe large parts of the spectrum because of the restricted real-emission phase space. The rapidity of the Z boson in Figure 3.18 is described very well by all three approaches.

The situation is very similar in W-boson production. A comparison of POWHEG predictions with Tevatron data from the DØ experiment [111] is shown in Figure 3.19, where very good agreement between the Monte-Carlo result and the data can be observed. In addition to the direct comparison the uncertainties related to a variation of the renormalisation and factorisation scales are also shown. Thereby, two different strategies are pursued: While the inner (dark) band shows the uncertainty related to a variation of the scale in the hard matrix elements only, the outer (light) band shows the influence of varying the scales also in the parton-shower evolution. It is rather obvious that the latter approach yields the larger variations, as it is associated with an uncertainty in the choice of the strong coupling for the real-emission subprocess. While this process essentially determines the shape of the transverse momentum distribution in Figure 3.19, it enters at tree-level accuracy only, thus leading to a rather large scale dependence.

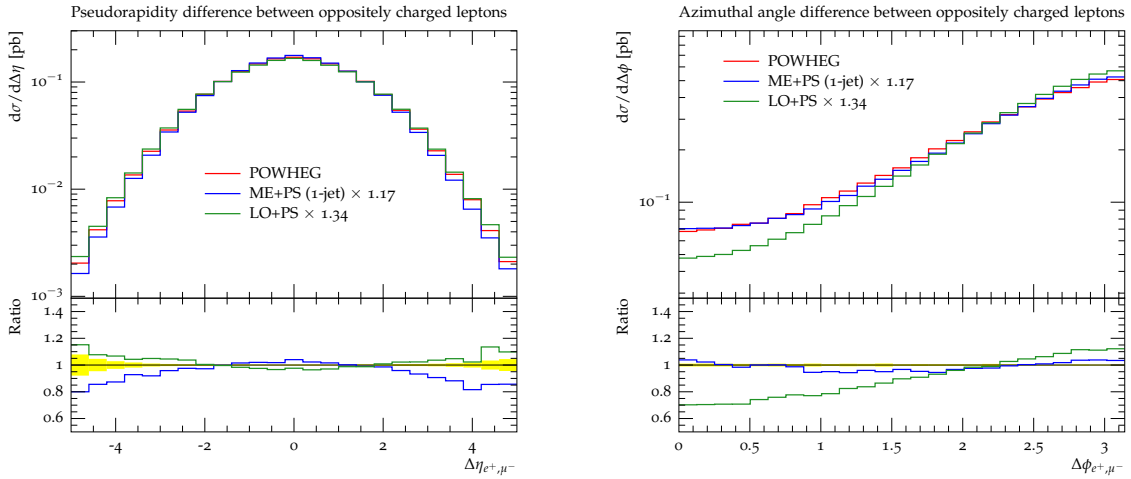

Figure 3.13: Pseudorapidity difference (left) and azimuthal angle (right) between the two oppositely charged leptons in W^+W^- production at nominal LHC energies.

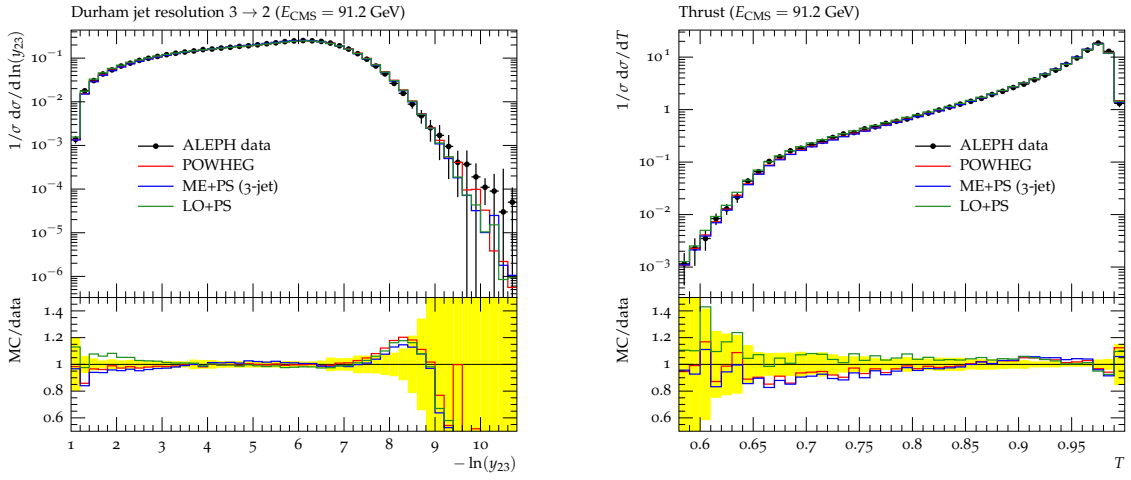

Figure 3.14: Durham $2 \to 3$ jet resolution (left) and thrust distribution (right) compared to data from the ALEPH experiment [112].

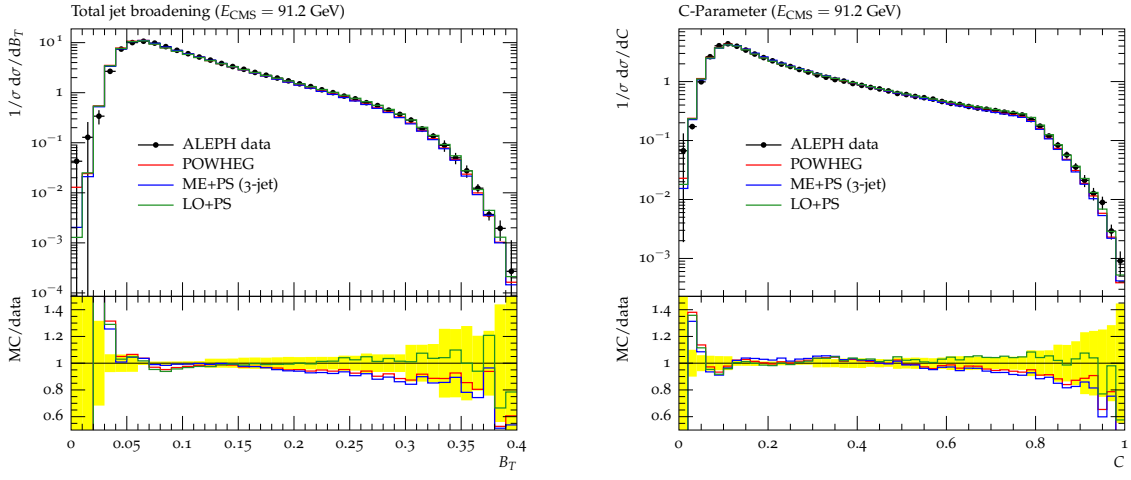

Figure 3.15: Total jet broadening (left) and C-Parameter (right) compared to data from the ALEPH experiment [112].

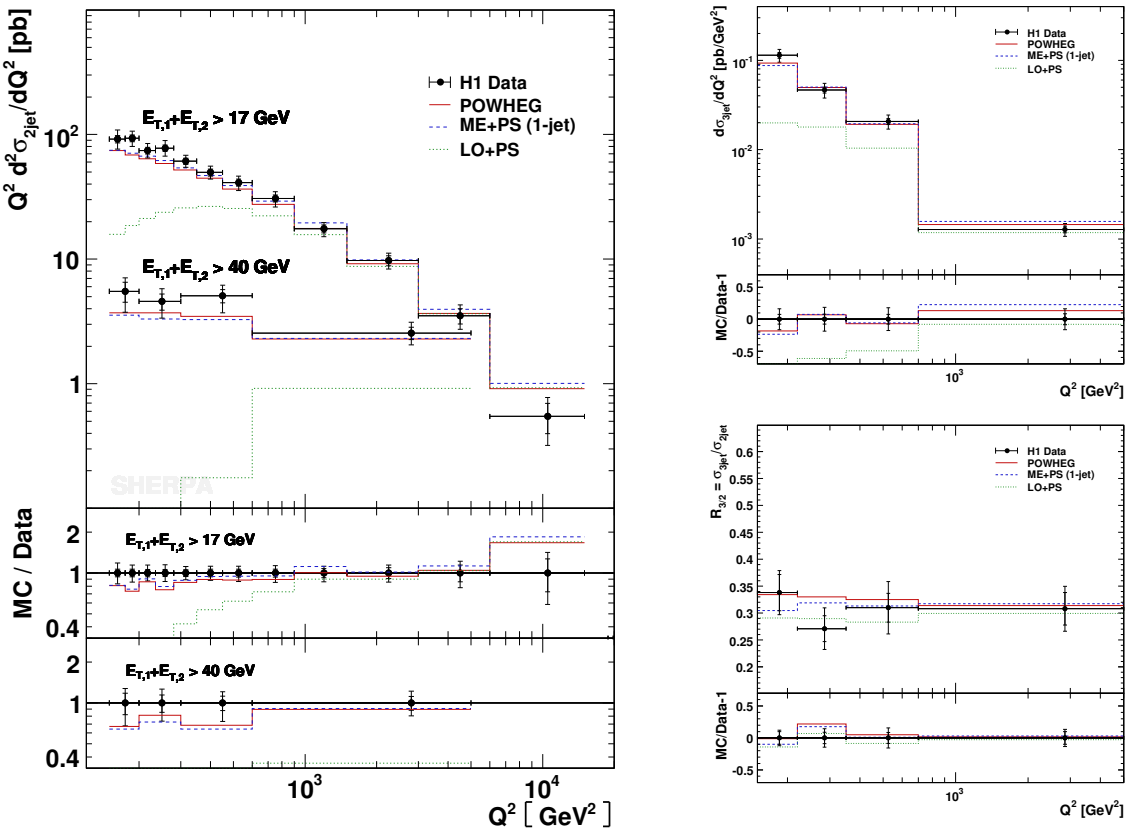

Figure 3.16: The di-jet cross section as a function of Q^2 in bins of $E_{T,1} + E_{T,2}$ (left), the three-jet cross section as a function of Q^2 (right top) and the ratio of the three- over the two-jet rate as a function of Q^2 (right bottom) compared to data from the H1 experiment [109, 110].

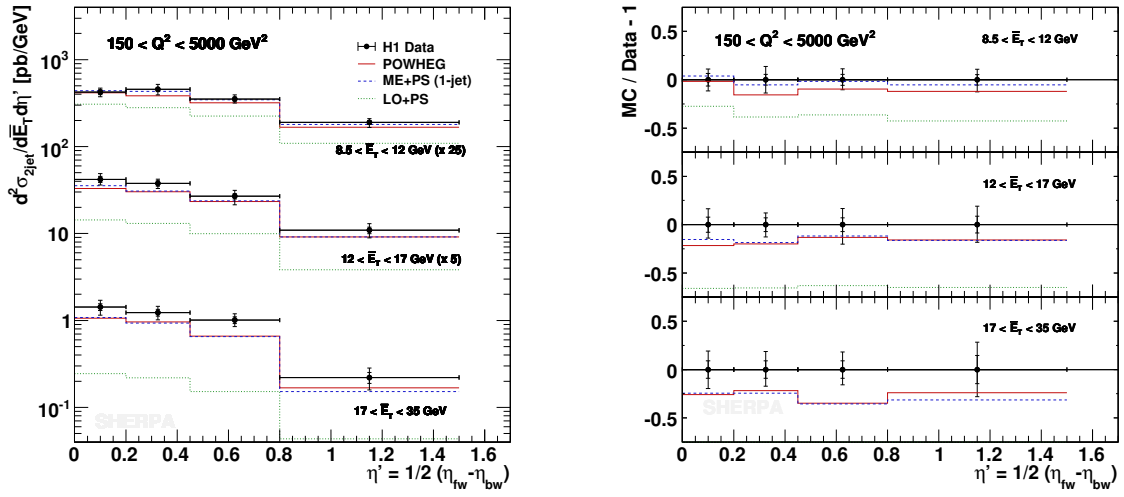

Figure 3.17: The di-jet cross section as a function of η', compared to data from the H1 experiment [109]. η' denotes half the rapidity difference of the two leading jets in the Breit frame.

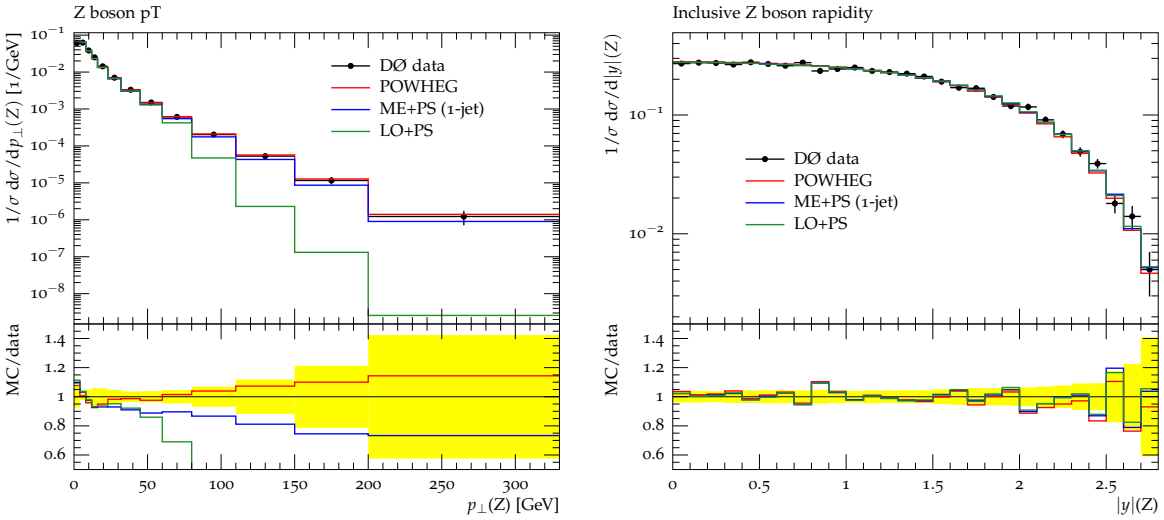

Figure 3.18: Transverse momentum and rapidity of the Z boson in Drell-Yan lepton-pair production at the Tevatron compared to data from the DØ experiment [113, 114].

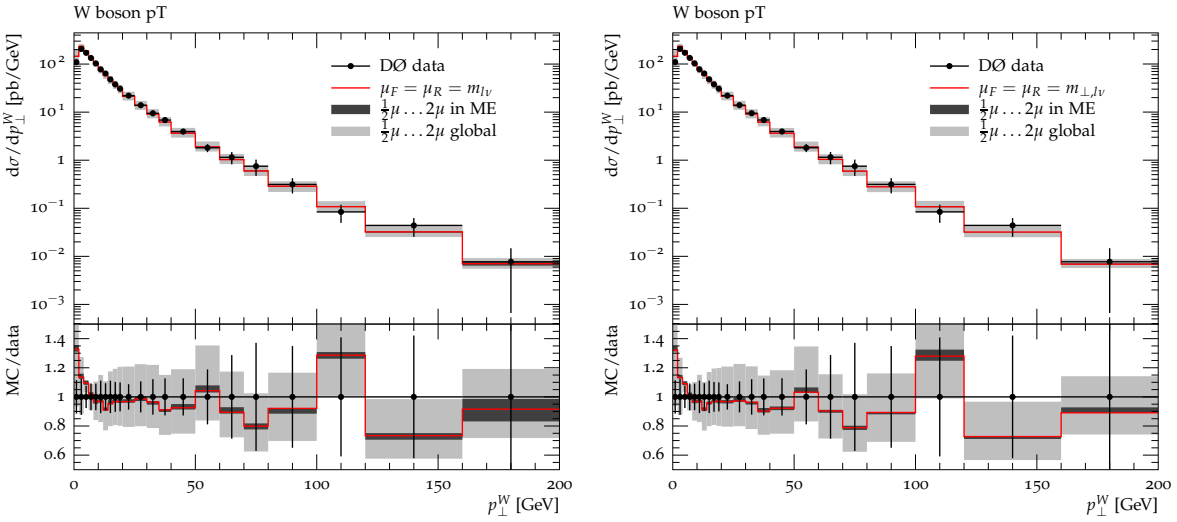

Figure 3.19: Transverse momentum of the W boson in W+jets production at the Tevatron compared to data from the DØ experiment [111]. Scale variations of the POWHEG prediction by factors of 1/2 and 2 are displayed for two different scale schemes, $\mu_F = \mu_R = m_{l\nu}$ (left) and $\mu_F = \mu_R = m_{\perp,l\nu}$ (right). The inner (dark) band displays the variations associated with redefining the scales for matrix elements alone, while the outer (light) band also takes variations in the running coupling of the parton shower evolution into account.

3.3 NLO matrix elements in ME+PS merging

Sections 2.2 and 3.2 have introduced two formalisms with which parton showers can be corrected for higher-order corrections. Both approaches are to some extent complementary: POWHEG has full NLO accuracy in the inclusive cross section while ME+PS is a LO method, but on the other hand ME+PS allows to correct higher-order emissions beyond the first one while POWHEG uses the ordinary parton shower for those. The only overlap of the two methods regards the first emission, which is generated by both approaches and thus cannot be naively summed. To make a discussion of this overlap explicit, Section 3.3.1 casts the ME+PS formalism into a form slightly different from Section 2.2. The actual combination is then performed in Section 3.3.2. Results from internal consistency checks and a comparison to experimental data are presented in Section 3.3.3.

3.3.1 Prerequisites

Similar to the POWHEG case in Equation (3.33), a master formula for the first emission, describing the expectation value of an arbitrary infrared safe observable O in the ME+PS scheme can be written as:

$$
\begin{aligned}
\langle O \rangle^{(\mathrm{MEPS})} = \sum_{\{\vec{f}\}} \int \mathrm{d}\Phi_B(\{\vec{p}\})\, \mathrm{B}(\{\vec{a}\}) \Bigg[& \underbrace{\Delta^{(\mathrm{PS})}(t_0, \mu^2; \{\vec{a}\})}_{\text{unresolved}}\, O(\{\vec{a}\}) \\
+ \sum_{\{\widetilde{ij},\tilde{k}\}} \sum_{f_i = q,g} & \frac{1}{16\pi^2} \int_{t_0}^{\mu^2} \mathrm{d}t \int_{z_{\min}}^{z_{\max}} \mathrm{d}z \int_0^{2\pi} \frac{\mathrm{d}\phi}{2\pi}\, J_{ij,k}(t,z,\phi)\, O(r_{\widetilde{ij},\tilde{k}}(\{\vec{a}\})) \\
& \times \frac{1}{S_{ij}} \Bigg(\underbrace{\frac{8\pi\,\alpha_s}{t}\, \mathcal{K}_{ij,k}(t,z,\phi)\, \frac{\mathcal{L}(r_{\widetilde{ij},\tilde{k}}(f_i,t,z,\phi;\{\vec{a}\});t)}{\mathcal{L}(\{\vec{a}\};t)}\, \Theta\left(Q_{\mathrm{cut}} - Q_{ij,k}(t,z,\phi)\right)}_{\text{resolved, PS domain}} \\
& \quad + \underbrace{\frac{S(r_{\widetilde{ij},\tilde{k}}(\{\vec{f}\}))}{S(\{\vec{f}\})}\, \frac{\mathrm{R}_{ij,k}(r_{\widetilde{ij},\tilde{k}}(\{\vec{a}\}))}{\mathrm{B}(\{\vec{a}\})}\, \Theta\left(Q_{ij,k}(t,z,\phi) - Q_{\mathrm{cut}}\right)}_{\text{resolved, ME domain}} \Bigg)\, \Delta^{(\mathrm{PS})}(t,\mu^2;\{\vec{a}\}) \Bigg] .
\end{aligned}
\tag{3.38}
$$

There are three components to the differential cross section: The term describing unresolved emissions, which is generated in the standard parton-shower approach, and the resolved part, which is now split between the PS and the ME domain. Within the ME domain, the matrix-element generator is directly invoked to define the real-emission configuration. This is possible due to the restricted phase space, removing all infrared divergent regions by applying the cut in $Q_{ij,k}$ and rendering the matrix element finite. In this case, the Sudakov form factor $\Delta^{(\mathrm{PS})}$, which makes the matrix

element exclusive, must be added explicitly. It can either be calculated analytically, like in the original formulation of [35], or by utilising the shower itself to generate the correct probabilities, as in Section 2.2.2. This latter option is commonly referred to as the pseudoshower approach [38].

In contrast to a reweighting technique, only emission terms are modified and no correction is applied to the no-emission probabilities. This ultimately leads to unitarity violations in the ME+PS method, which will be discussed later.

A complication arises if the phase-space separation criterion $Q_{ij,k}$ is different from the parton-shower evolution variable t. This can lead to the possibility of a shower emission $Q < Q_{\text{cut}}$ being allowed "between" two branchings at $Q > Q_{\text{cut}}$ in the parton-shower history of the matrix element. In such cases, in order not to spoil the logarithmic accuracy of the parton shower, the existing branchings need to be embedded into the subsequent parton-shower evolution. This leads to a truncated shower algorithm [43], cf. Section 2.1.2.

3.3.2 Merging POWHEG and ME+PS – The MENLOPS approach

In this section, the two master equations for the POWHEG (Equation (3.33)) and ME+PS (Equation (3.38)) approaches are combined into one single expression, defining the MENLOPS approach. The aim of this combined algorithm is to simultaneously have NLO accuracy in the cross section, leading logarithmic accuracy as implemented in the parton shower and hard higher-order emissions corrected using tree-level matrix elements.

The method of choice is to simply replace the unresolved and the PS resolved part in Equation (3.38) with the respective POWHEG expression. This essentially amounts to the replacement of the parton-shower no-emission probability with the corresponding POWHEG result, $\Delta^{(\text{PS})} \to \Delta^{(\text{ME})}$ and a substitution of the leading-order weight B by $\bar{\text{B}}$, like in the POWHEG method itself.

The ME part of the cross section is then generated separately, starting from real-emission matrix elements, as described in Section 2.2. This immediately implies that it will not automatically benefit from a POWHEG implementation regarding the local K-factor $\bar{\text{B}}/\text{B}$, and it is therefore necessary to supply this K-factor explicitly. There is no a-priori definition of the Born-level parton configuration, $\{\vec{a}\}_{\text{B}}$ in this context, because the ME event is defined in terms of a real-emission configuration $\{\vec{a}\}_{\text{R}}$. One rather has to identify a POWHEG branching history $\{\vec{a}\}_{\text{B}} \to \{\vec{a}\}_{\text{R}}$, defining a mapping onto $\{\vec{a}\}_{\text{B}}$ such that $\bar{\text{B}}/\text{B}$ can be computed.

Implementing these ideas, the master formula for the first emission in MENLOPS is obtained as

$$\begin{aligned}\langle O\rangle^{(\text{MENLOPS})} \;=\; &\sum_{\{\vec{f}\}}\int \mathrm{d}\Phi_B(\{\vec{p}\})\,\bar{\mathrm{B}}(\{\vec{a}\})\left[\underbrace{\Delta^{(\text{ME})}(t_0,\mu^2;\{\vec{a}\})}_{\text{unresolved}}\,O(\{\vec{a}\})\right.\\
&+\sum_{\{\widetilde{ij},\tilde{k}\}}\sum_{f_i=q,g}\frac{1}{16\pi^2}\int_{t_0}^{\mu^2}\mathrm{d}t\int_{z_{\min}}^{z_{\max}}\mathrm{d}z\int_0^{2\pi}\frac{\mathrm{d}\phi}{2\pi}\,J_{ij,k}(t,z,\phi)\;O(r_{\widetilde{ij},\tilde{k}}(\{\vec{a}\}))\\
&\quad\times\frac{1}{S_{ij}}\,\frac{S(r_{\widetilde{ij},\tilde{k}}(\{\vec{f}\}))}{S(\{\vec{f}\})}\,\frac{\mathrm{R}_{ij,k}(r_{\widetilde{ij},\tilde{k}}(\{\vec{a}\}))}{\mathrm{B}(\{\vec{a}\})}\left(\underbrace{\Delta^{(\text{ME})}(t,\mu^2;\{\vec{a}\})\,\Theta\left(Q_{\text{cut}}-Q_{ij,k}\right)}_{\text{resolved, PS domain}}\right.\\
&\qquad\left.\left.+\underbrace{\Delta^{(\text{PS})}(t,\mu^2;\{\vec{a}\})\,\Theta\left(Q_{ij,k}-Q_{\text{cut}}\right)}_{\text{resolved, ME domain}}\right)\right].\end{aligned}\tag{3.39}$$

Note that the arguments of $Q_{ij,k}$ have been suppressed for ease of notation. The resolved-ME part of the expression in square brackets can be rewritten as

$$\sum_{\{\widetilde{ij},\tilde{k}\}}\int_{t_0}^{\mu^2}\mathrm{d}t\;\frac{\mathrm{d}\log\Delta^{(\text{ME})}_{\widetilde{ij},\tilde{k}}(t,\mu^2;\{\vec{a}\})}{\mathrm{d}t}\;\Delta^{(\text{PS})}(t,\mu^2;\{\vec{a}\})\;O(r_{\widetilde{ij},\tilde{k}}(\{\vec{a}\}))\;,\tag{3.40}$$

Comparing this with Equation (3.34) reveals an additional factor

$$\frac{\Delta^{(\text{ME})}(t,\mu^2;\{\vec{a}\})}{\Delta^{(\text{PS})}(t,\mu^2;\{\vec{a}\})}\tag{3.41}$$

in the ME domain compared to the POWHEG master formula. This makes the unitarity violation of the MENLOPS method explicit. However, the expectation value of O is still determined correctly to $\mathcal{O}(\alpha_s)$, as can be seen by expanding Equation (3.41) and inserting the result as a correction into Equation (3.39), rather than using $\Delta^{(\text{PS})}$ directly. Any unitarity violation is caused by the mismatch between exact higher-order tree-level matrix elements and their respective parton-shower approximation. This feature of MENLOPS is simply inherited from the ME+PS approach.

In a publication parallel to the work presented here, Hamilton and Nason arrived at the same ideas [92].

3.3.3 Results

This section collects results obtained with an implementation of the algorithm described in the previous sections in the SHERPA framework. It aims at detailing the improved description of data collected in various collider experiments and at quantifying some of the systematic uncertainties inherent to the MENLOPS method, in particular those related to the merging of the multijet tree-level contributions. Note again, that the MENLOPS approach is designed to merge the next-to-leading order accurate description of a given core interaction (like for example $e^+e^- \to q\bar{q}$) through the POWHEG method with higher-order tree-level contributions (like $e^+e^- \to q\bar{q}gg$) described in the ME+PS approach. Since the total cross section is defined by the POWHEG expression of the core process in question, uncertainties like those related to the choice of scales are encoded there. They have been discussed in Section 3.2, while uncertainties related to the ME+PS method were discussed in Section 2.2.4.

However, a comparison with results of the ME+PS and POWHEG techniques alone is extremely useful to assess the quality of the approach and the improvements related to it. The precise setup of SHERPA for this comparison was described in detail in Section 3.2. Throughout the section, the CTEQ6.6 parton distribution functions [102] (and, correspondingly, the $\overline{\text{MS}}$ subtraction scheme) are used, with $\alpha_S(m_Z) = 0.118$ and running at two-loop. If not stated otherwise, hadronisation is not accounted for. Multiple parton interactions are not included in the simulation.

Merging Systematics

As pointed out in the previous section, the ME+PS approach violates the unitarity of the parton-shower simulation. This discrepancy is directly inherited by the MENLOPS method. The extent of the problem depends entirely on the quality of the parton-shower algorithm, as can be seen in Equation (3.41): If the parton-shower approximation to the real-emission matrix element is good, the correction factor, Equation (3.41), is close to one.

The quality of the algorithms is tested in the reactions $e^+e^- \to$ hadrons and Drell-Yan lepton-pair production by varying the phase-space separation cut, Q_{cut}, and the maximum number of partons, N_{max}, which is simulated with matrix elements in the MENLOPS approach. This is in close correspondence to the sanity checks of the ME+PS method which have been done in Section 2.5. The respective results are summarised in Table 3.3. Unitarity violations of the method are observed to be below 5.3% for the e^+e^- annihilation process and 3.9% for the Drell-Yan process. Only in processes

$\log_{10} y_{\text{cut}}$	N_{max}				
	0	1	2	3	4
-1.25	29.45(3)	29.64(6)	29.56(7)	29.54(6)	29.58(7)
-1.75		29.70(7)	29.92(9)	29.81(9)	29.85(9)
-2.25		30.28(10)	30.91(14)	30.90(15)	31.01(17)

Q_{cut}	N_{max}			
	0	1	2	3
15 GeV	478.3(4)	484(3)	490(4)	497(4)
20 GeV		482(3)	486(3)	489(3)
40 GeV		481(2)	483(2)	482(2)

Table 3.3: Top: Total cross sections for $e^+e^- \to jets$ at $\sqrt{s} = 91.25$ GeV in nb and their dependence on $y_{\text{cut}} = Q^2_{\text{cut}}/s$ and the maximum number, N_{max} of additional partons produced by matrix elements. Bottom: Total cross sections for $p\bar{p} \to \gamma^*/Z\,[\to \ell\ell\,]$+jets at $\sqrt{s} = 1.96$ TeV in pb and their dependence on Q_{cut} and N_{max}. The definition of leptons, ℓ, includes $e^{\pm}$ and $\mu^{\pm}$, but not $\tau^{\pm}$.

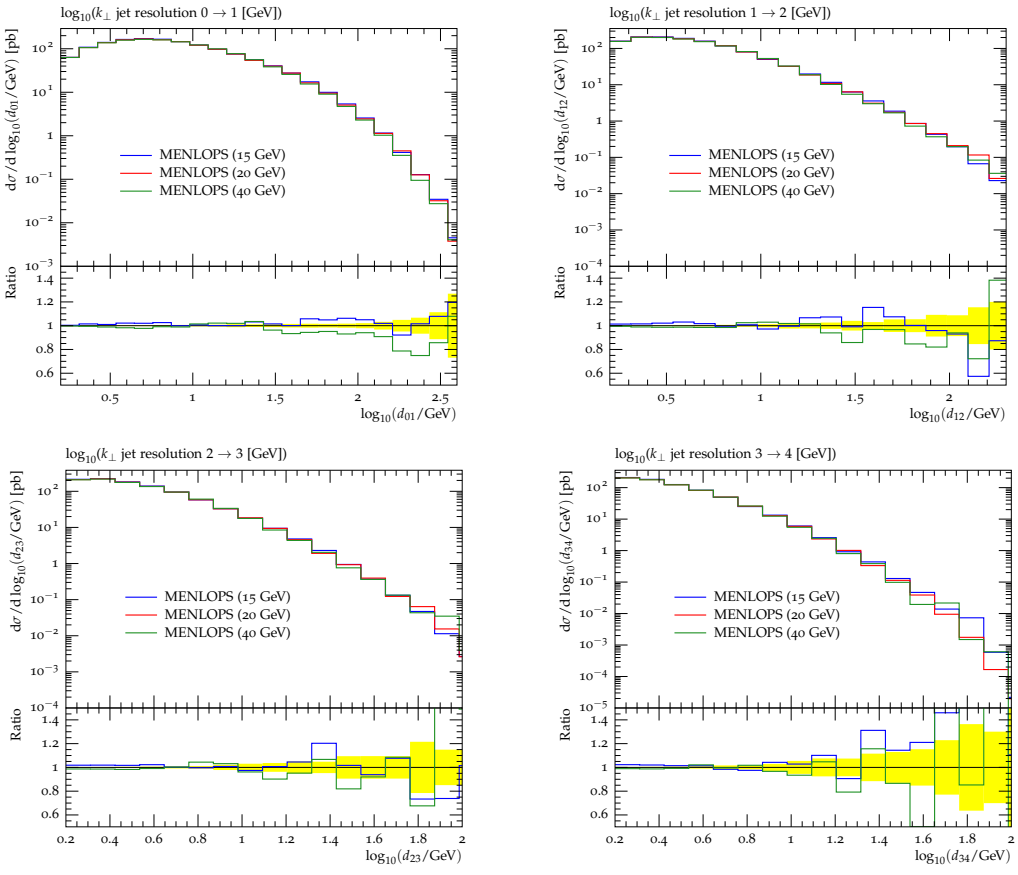

Figure 3.20: Differential jet rates $d_{n\,n+1}$ for three different merging cuts, Q_{cut}, in Drell-Yan lepton-pair production at the Tevatron at $\sqrt{s} = 1.96$ TeV.

where the next-to-leading order corrections are small they are of a similar magnitude. For all other processes the inherent unitarity violation of the MENLOPS approach does not exceed the NLO corrections. Note again that a comparison between the two is a judgement of the relative influence of higher-logarithmic corrections compared to fixed-order NLO corrections. The MENLOPS predictions are in any case correct to $\mathcal{O}(\alpha_s)$ and to the logarithmic accuracy of the parton shower.

Usually, the biggest intrinsic uncertainty of the ME+PS approach stems from the freedom to choose the phase-space separation cut, Q_{cut}, as explained and exemplified in a number of processes in Section 2.5. Since the MENLOPS method relies on identical ideas to separate the real-emission phase space, it naturally inherits this source of uncertainty. Deviations of MENLOPS results from results with different values of Q_{cut} are to be expected. However, their small size in a reasonable range of Q_{cut} is a sign of the algorithm working well. The following rule of thumb can be applied: If the value of Q_{cut} is chosen too large, too much extra emission phase space is left to the POWHEG simulation, typically leading to an underestimation of jet rates, since POWHEG only simulates the first emission through matrix elements. If, on the other hand, this value is too small, too much phase space is filled by matrix elements with large final-state multiplicity, which may lead to noticeable unitarity violations. The value of Q_{cut} should therefore lie well between the parton-shower cutoff and the factorisation scale of the core process, with some margin on either side of this interval.

The stability of the MENLOPS implementation with respect to variations of Q_{cut} is exemplified in Figure 3.20. Due to their similarity to $Q_{ij,k}$, the differential jet rates shown there are extremely sensitive to the details of the radiation pattern and thus to the accuracy of the ME+PS implementation. They tend to expose even the slightest mismatch between PS and ME subsamples, which then shows up as a kink in the distribution. However, when varying Q_{cut} in a rather wide range, no sizable discrepancies between the respective MENLOPS predictions are found, which is a very encouraging result regarding the quality of the algorithm and its implementation in SHERPA.

3.3.3.1 $e^+e^- \to$ jets

This section focuses on electron-positron annihilation into hadrons at LEP energies ($\sqrt{s}$ =91.25 GeV). The core process of the simulation is therefore the reaction $e^+e^- \to q\bar{q}$. A full wealth of experimental data has been provided by the LEP experiments, which allows to assess the quality of the MENLOPS approach in this simplest realistic scenario. Although the improvements discussed here concern only the perturbative QCD part of the Monte-Carlo simulation, the results account for hadronisation effects

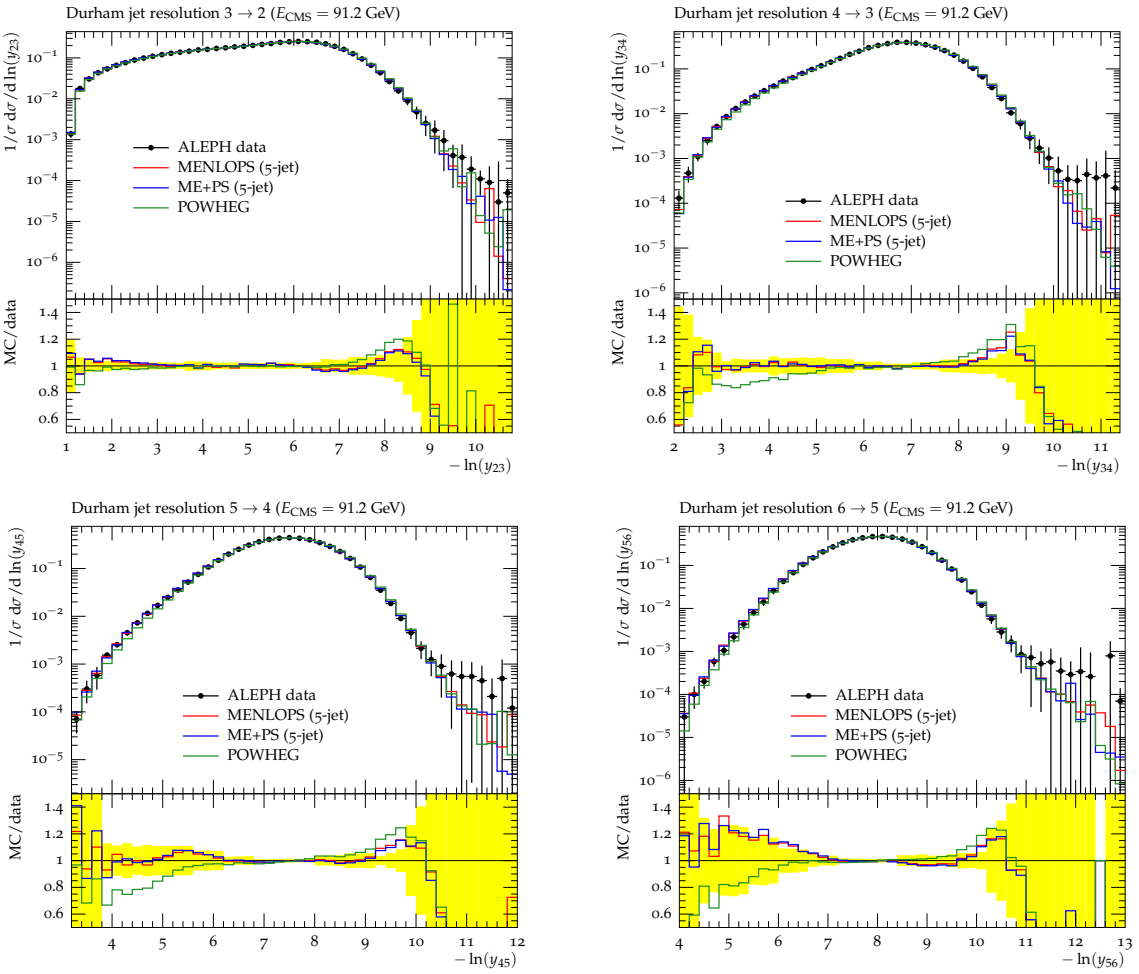

Figure 3.21: Durham $d_{n\,n+1}$ jet resolutions at LEP compared to data taken by the ALEPH experiment [112].

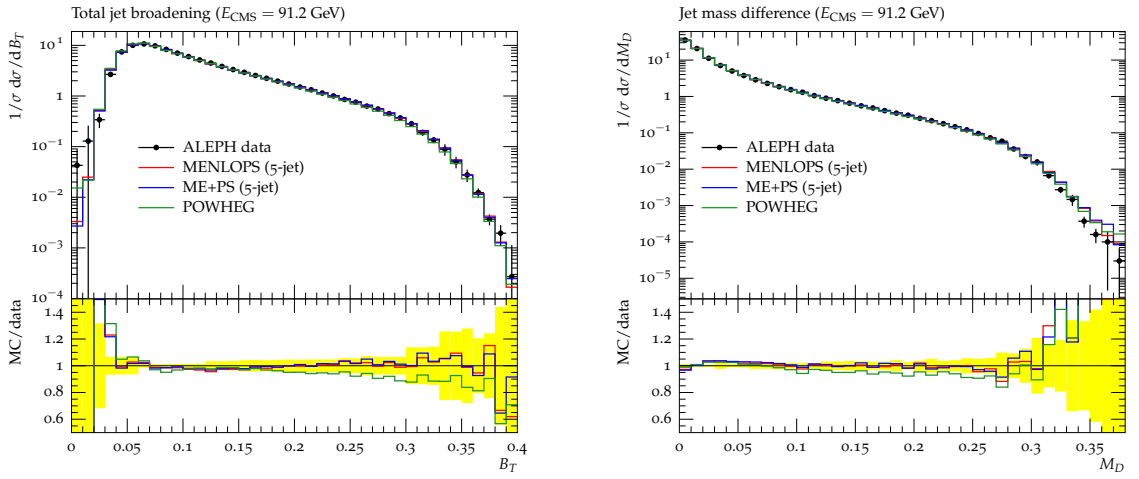

Figure 3.22: Total jet broadening and jet mass difference at LEP compared to data taken by the ALEPH experiment [112].

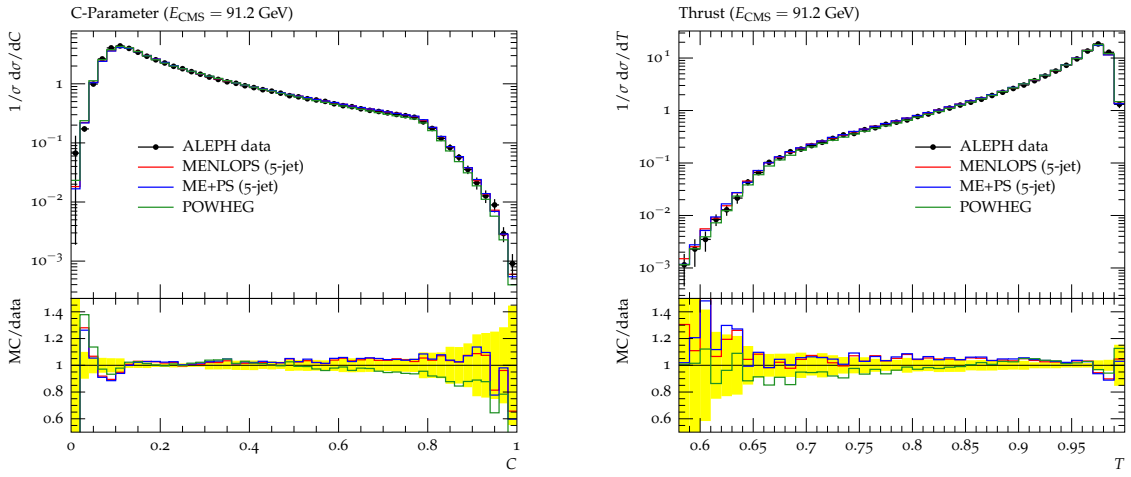

Figure 3.23: C parameter and thrust distribution at LEP compared to data taken by the ALEPH experiment [112].

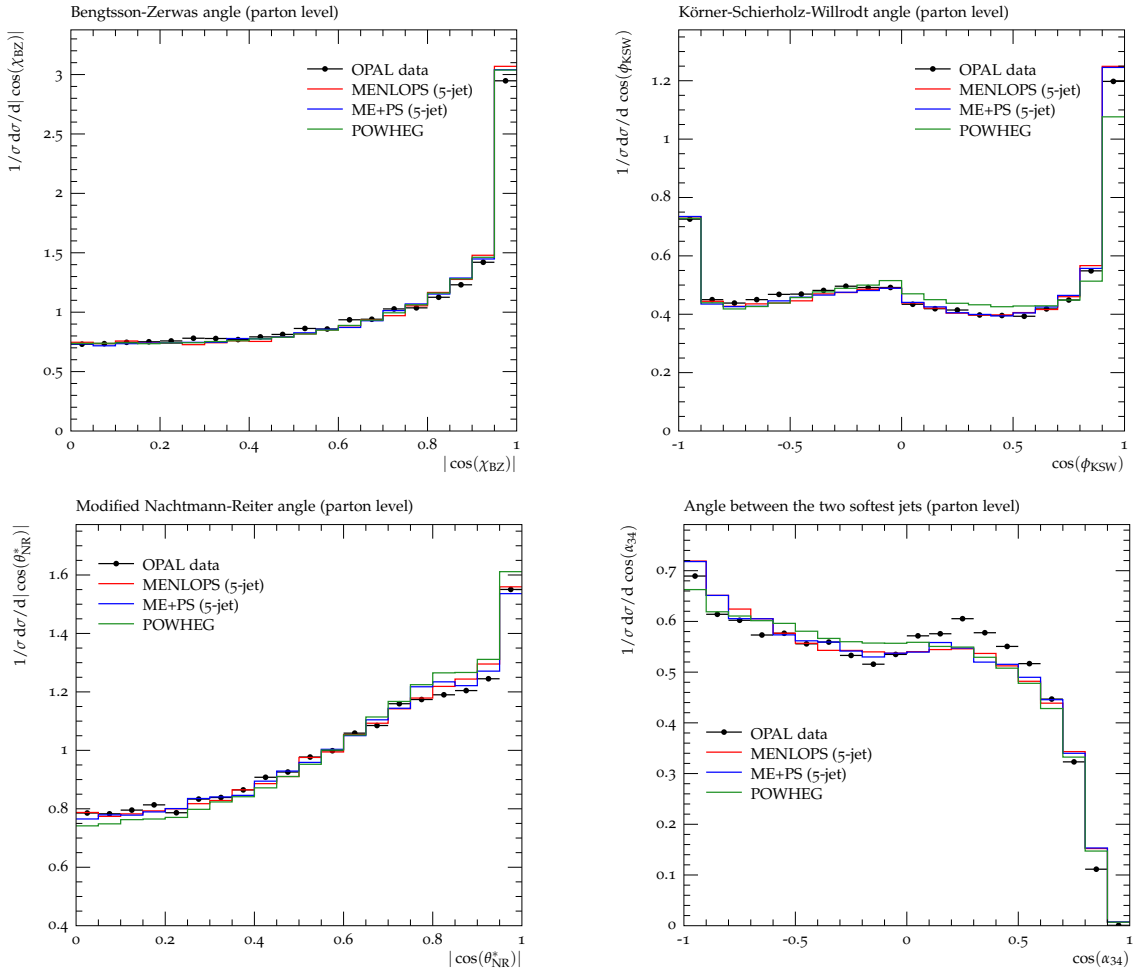

Figure 3.24: Angles between the leading (in energy) four jets defined using the Durham algorithm with $y_{\text{cut}} = 0.008$. Results at the parton level are compared to data from the OPAL experiment [115].

using the Lund model [2, 22] to make them comparable to experimental data. Virtual matrix elements needed for the simulation were supplied by code provided by the BlackHat collaboration [101].

Figure 3.21 highlights the improvement in the description of jet data. In the hard-emission region the MENLOPS results for the $2 \to 3$-, the $3 \to 4$- and the $4 \to 5$-jet rate are generally closer to the data than the POWHEG ones, which hints at the success of the simulation. Deviations in the $5 \to 6$-jet rate are most likely due to the fact that matrix elements for six-jet production are not included. Note that these distributions are normalised to the total cross section, such that no rate difference between the ME+PS and the MENLOPS samples can be observed.

Figures 3.22 and 3.23 show examples of event-shape variables, which are all very well described in the hard-emission region by the MENLOPS simulation. Several distributions for jet angular correlations in 4-jet production, that have been important for the analysis of QCD and searches for physics beyond the Standard Model are investigated in Figure 3.24. The good fit to those data proves that correlations amongst the final-state partons are correctly implemented by the higher-order matrix elements.

3.3.3.2 Deep-inelastic lepton-nucleon scattering

Deep-inelastic scattering (DIS) is one of the best understood processes in perturbative QCD. However, it has been an obstacle for a very long time to properly simulate hadronic final states in DIS using general-purpose Monte Carlo based on collinear factorisation. Only recently, a consistent approach was presented [14], that allows to describe jet data throughout the experimentally accessible range of Q^2, the negative virtuality of the exchanged virtual γ^*/Z-boson. It is absolutely mandatory for this method that a large number of final-state partons can be described by hard matrix elements in order to lift the severe restrictions on the real-emission phase space of the parton shower, which are imposed by the factorisation theorem.

Results for two analyses are presented. The first is the measurement of inclusive jet production in [116], which covers different ranges of jet-pseudorapidity in the laboratory frame, η_{lab}, in the low-Q^2 domain $5 < Q^2 < 100\,\mathrm{GeV}^2$. Jets are defined using the inclusive k_T-algorithm [37,117] and are constrained to $E_{T,B} > 5\,\mathrm{GeV}$ and the pseudorapidity range $-1 < \eta_{lab} < 2.8$, where $E_{T,B}$ is the jet transverse energy in the Breit frame. The second analysis corresponds to the measurement of dijet production in [109], which covered a wider range of Q^2 and produced many doubly differential jet spectra. The acceptance region is $5 < Q^2 < 15000\,\mathrm{GeV}^2$ and $-1 < \eta_{lab} < 2.5$. Jet transverse energies are subject to the cuts $E_{T,B\,1,2} > 5\,\mathrm{GeV}$ and $E_{T,B\,1} + E_{T,B\,2} > 17\,\mathrm{GeV}$. The latter

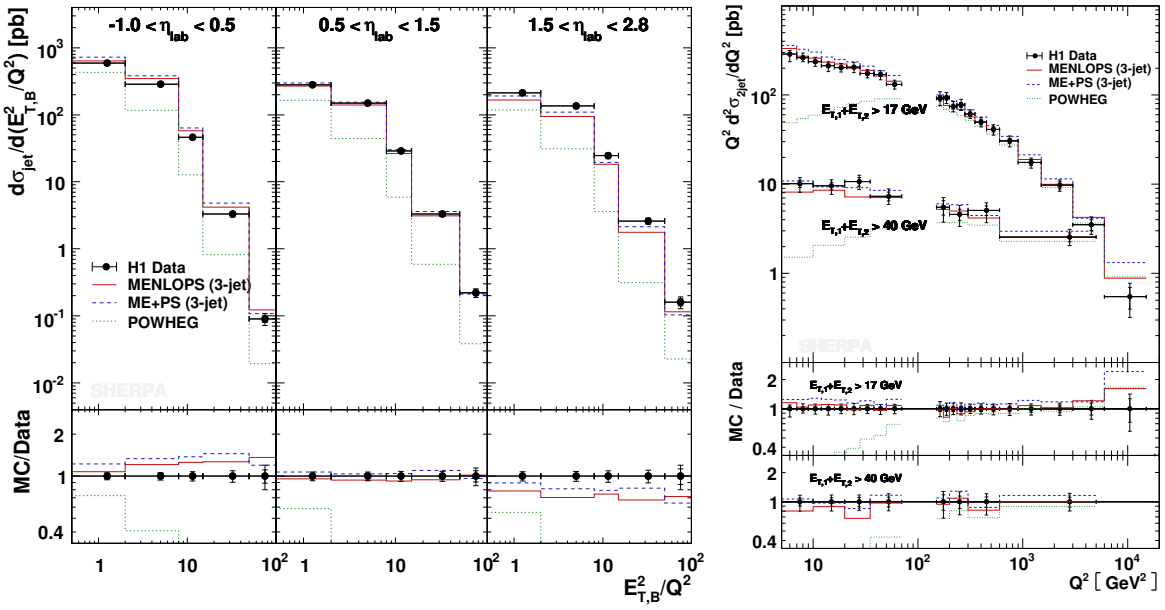

Figure 3.25: Left: The inclusive jet cross section as a function of $E^2_{T,B}/Q^2$ in bins of η_{lab}, compared to data from the H1 collaboration [116]. $E^2_{T,B}$ is the jet transverse energy in the Breit frame, while η_{lab} denotes the jet rapidity in the laboratory frame. Right: The dijet cross section as a function of Q^2 in bins of $E_{T,1} + E_{T,2}$, compared to data from the H1 collaboration [109].

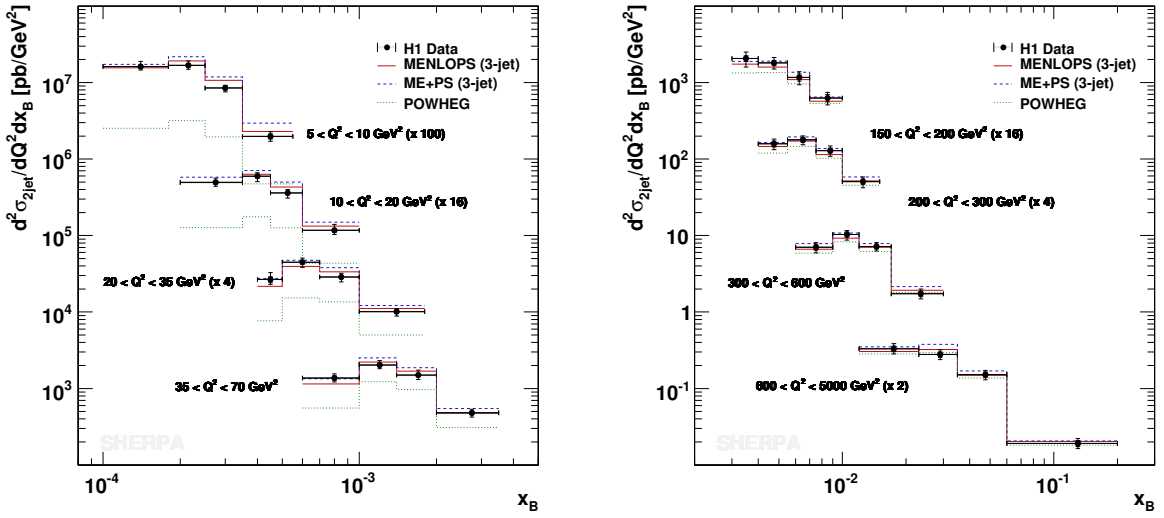

Figure 3.26: The dijet cross section as a function of the Bjørken variable x_B, compared to data from the H1 collaboration [109].

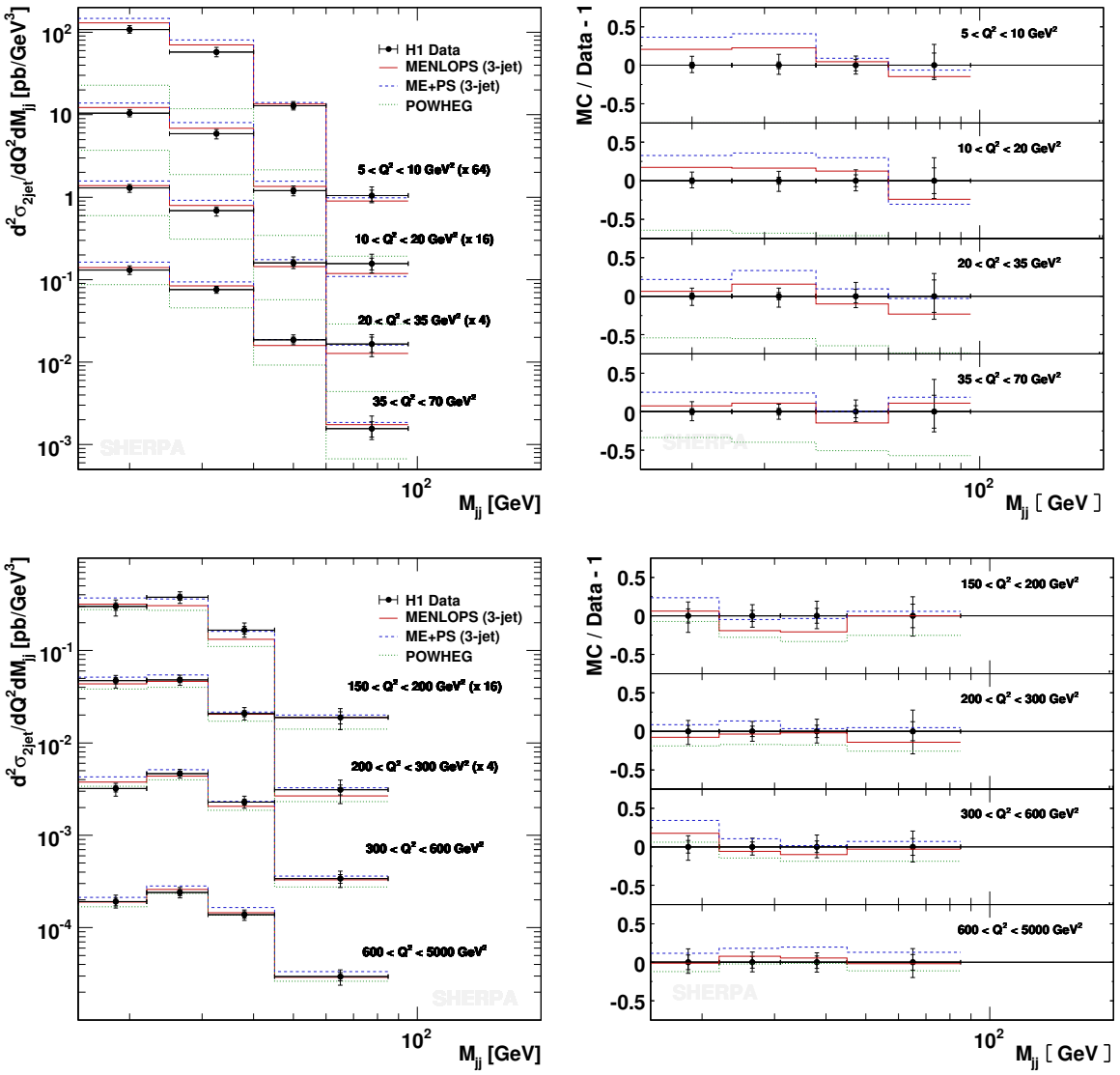

Figure 3.27: The dijet cross section as a function of the dijet mass m_{jj}, compared to data from the H1 collaboration [109].

requirement is introduced to avoid $E_{T,B\,1} \approx E_{T,B\,2}$, which is the region of the phase space where next-to-leading order corrections are unstable due to implicit restrictions on soft emissions [118].

As outlined in [14], a crucial observable is given by the inclusive jet cross section, differential with respect to $E_{T,B}^2/Q^2$. For $E_{T,B}^2/Q^2 > 1$ it probes a part of the phase space where leading order Monte-Carlo models without the inclusion of low-x effects are bound to fail in their description of jet spectra. Another very good observable to validate the proper Monte-Carlo simulation is the dijet cross section as a function of Q^2. While still a relatively inclusive quantity, it is an important indicator for the correct simultaneous implementation of inclusive DIS and the additional production of hard QCD radiation. The high quality of the MENLOPS prediction for the two above observables is confirmed in Figure 3.25. Discrepancies in the description of the $E_{T,B}^2/Q^2$-spectrum in the forward region can be attributed to the fact that the simulation is limited to three additional partons in the hard matrix elements. This restriction is imposed by the usage of the matrix-element generator AMEGIC++ [119]. Figures 3.26 and 3.27 exemplify again that the MENLOPS simulation correctly predicts multijet differential distributions in all regions of the phase space, while the POWHEG approach fails in the low-Q^2 domain.

3.3.3.3 Drell-Yan lepton-pair production

Results for lepton-pair production through the Drell-Yan process are compared to data from the Tevatron at $\sqrt{s} = 1.96$ TeV in Figures 3.28-3.31, using the core process $q\bar{q} \to \ell\ell$, where $\ell = e, \mu$. The invariant lepton-pair mass was restricted to be within $66 < m_{\ell\ell}/\text{GeV} < 116$ in the simulation. The MENLOPS and ME+PS samples use tree-level matrix elements up to $Z + 3$ jets with a merging cut of $Q_{\text{cut}} = 20$ GeV. Virtual matrix elements are provided by BlackHat [101]. The $Z \to \ell^+\ell^-$ decay is corrected for QED next-to-leading order and soft-resummation effects using the Yennie-Frautschi-Suura (YFS) approach [103].

The Tevatron experiments provide a wealth of measurements sensitive to QCD corrections in Drell-Yan production. Figure 3.28 shows the transverse momentum distribution of the lepton pair in two different analyses from the DØ experiment. The left hand plot displays a very recent analysis using the $Z \to \mu\mu$ channel [113] to measure the Z-$p_\perp$ distribution normalised to the inclusive cross section. It requires muons with $p_\perp > 15$ GeV in a mass window of $65 < m_{\mu\mu}/\text{GeV} < 115$ and with $|\eta| < 1.7$. The muon signal is corrected to the particle level including photons clustered in a cone of radius $R = 0.2$ around each lepton. The plot on the right hand side stems from an analysis in the electron channel [120] which uses Monte-Carlo models to correct the leptons for all acceptances including the pseudorapidity range and minimal transverse momentum. Here the peak region of the transverse momentum of forward Z bosons with $|y_Z| > 2$ is displayed. The agreement between all three approaches and the measurement is outstanding. In the bins at $p_\perp < 10$ GeV non-perturbative effects like the intrinsic transverse momentum of partons in a proton might play a role. Related Monte-Carlo models in SHERPA could be tuned to reach an even better agreement. Still, the Monte-Carlo prediction lies within the experimental error band over the full range.

Two more measurements from the DØ experiment are displayed in Figure 3.29. The pseudorapidity of the Z boson [114] was measured in the electron channel requiring electrons with $p_\perp > 15$ GeV in the mass window $71 < m_{\text{ee}}/\text{GeV} < 111$. Again, all three Monte-Carlo approaches agree very well with the experimental data. The right hand plot shows the azimuthal correlation between the Z boson and the leading jet [121]. This is a measurement in the muon channel with the same selection cuts as described above. The distribution has been normalised using the inclusive Z cross section and the comparison shows that the three approaches underestimate the total rate for Z+jet production with respect to inclusive Z production by approximately 10%. This might hint at the need for NLO accuracy also in the Z+jet process. It is remarkable though that the inclusion of higher-order tree-level matrix elements significantly improves the

shape of the distribution with respect to the POWHEG simulation.

The observables presented so far are mainly sensitive to the correct description of the leading jet. For that reason even the POWHEG approach is well capable of providing sufficient accuracy in their prediction. The discussion now proceeds to observables sensitive to higher-order corrections.

Figure 3.30 (left) shows the inclusive jet multiplicity [122] for jets constructed using the DØ improved legacy cone algorithm [123] with a cone radius of $R = 0.5$ and $p_\perp > 20$ GeV. Jets were required to lie in $|\eta| < 2.5$ and to be separated from the leptons by $\Delta R(\ell, \text{jet}) > 0.4$. While POWHEG agrees with the data for the $N_{\text{jet}} = 1$ bin it fails to predict the rate of events with more than one jet. The MENLOPS and ME+PS predictions impressively demonstrate the effect of higher-order corrections provided by tree-level matrix elements up to the third jet. They agree with the measurement within the error bands for $N_{\text{jet}} = 2, 3$ and as expected fail to predict the correct four-jet rate because no matrix-element corrections have been applied at that multiplicity.

Transverse momentum spectra of the three leading jets accompanying the Z boson were measured by DØ in [124]. The distributions in Figure 3.30 (right) and 3.31 are normalised to the inclusive cross section for Z production and the jets have been constructed using the same settings as in the multiplicity measurement. Both MENLOPS and ME+PS deliver a very good description of these spectra while POWHEG fails to describe the rate and shape for the second and third jet.

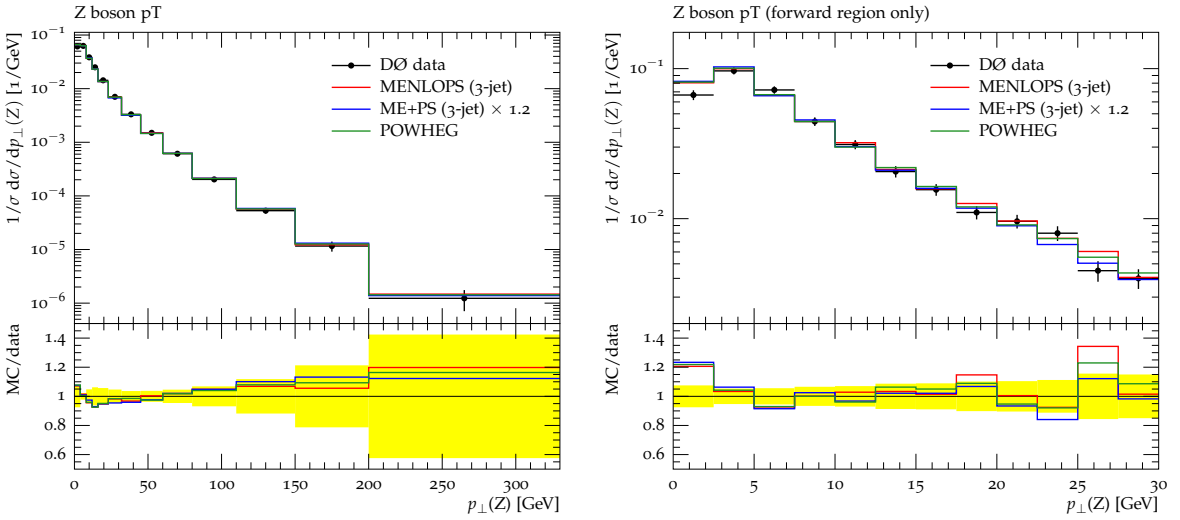

Figure 3.28: The transverse momentum of the reconstructed Z boson in Drell-Yan lepton-pair production at the Tevatron at $\sqrt{s} = 1.96$ TeV. Experimental data stem from the DØ experiment [113, 120] and are described in the text.

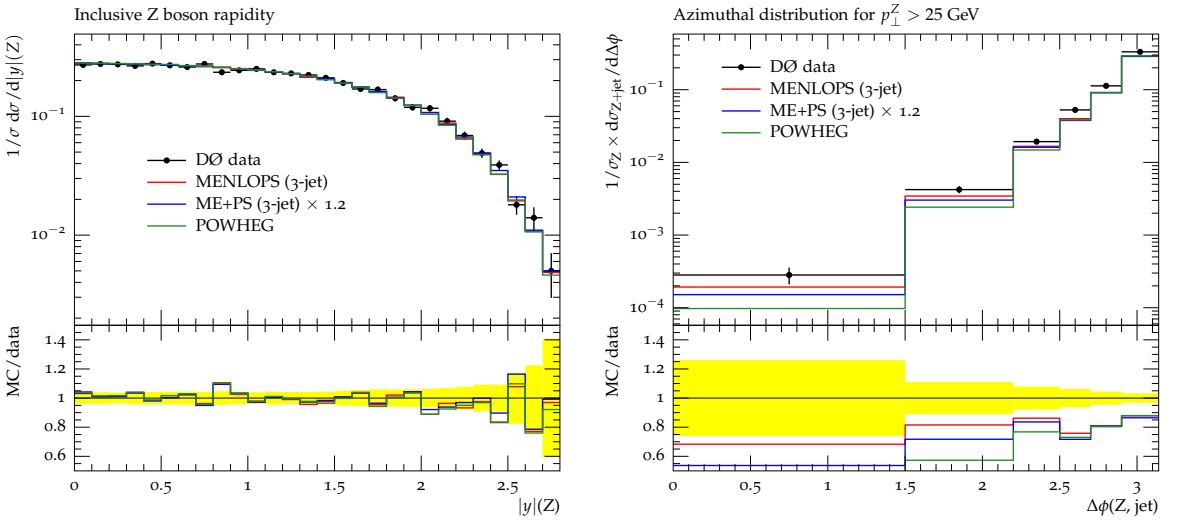

Figure 3.29: Rapidity of the reconstructed Z boson [114] (left) and azimuthal separation of the boson and the leading jet [121] (right) in Drell-Yan lepton-pair production at the Tevatron at $\sqrt{s} = 1.96$ TeV.

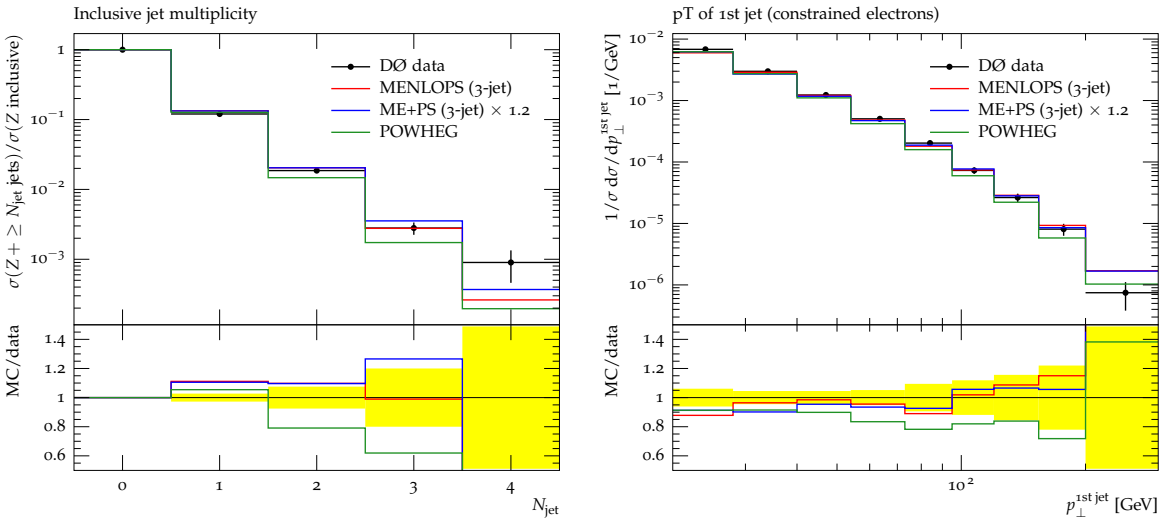

Figure 3.30: Inclusive jet multiplicity [122] (left) and transverse momentum of the leading jet [124] (right) in Z+jets events at the Tevatron at $\sqrt{s} = 1.96$ TeV.

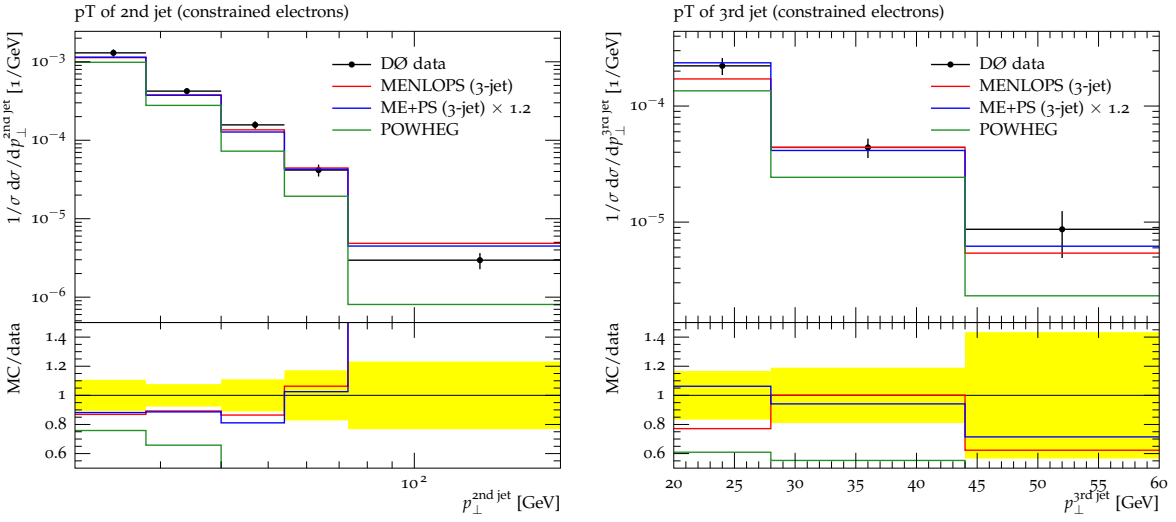

Figure 3.31: Transverse momentum of the second and third jet [124] in Z+jets events at the Tevatron at $\sqrt{s} = 1.96$ TeV.

3.3.3.4 W+jets Production

This section deals with the production of W-bosons and their subsequent decay into an electron-neutrino pair at the Tevatron at $\sqrt{s} = 1.8$ TeV. The core process of the Monte-Carlo simulation is therefore $q\bar{q}' \to \ell\bar{\nu}$. The separation criterion is set to $Q_{\text{cut}} = 20$ GeV and up to three extra jets are taken into account. The electron-neutrino pair is required to have an invariant mass of $m_{e\nu} > 10$ GeV. The $W \to e\nu$ decay is corrected for QED next-to-leading order and soft-resummation effects using the YFS approach [103]. Virtual matrix elements are supplied by BlackHat [101].

The left panel of Figure 3.32 displays the transverse momentum of the W-boson as compared to data taken by the DØ collaboration [111], while the right panel shows the exclusive jet multiplicity of $k_\perp$-clustered jets ($D=0.7$) with at least 20 GeV. Although the event sample generated using the POWHEG technique only provides the best match to the central value of the data, all three event samples are well within the experimental uncertainties. On the other hand, already in the rate of single-jet events deviations between the POWHEG sample and both the MENLOPS and ME+PS samples are visible, with the latter two agreeing very well. Similarly, the POWHEG sample underestimates the amount of radiation into the central detector region, as exemplified in Figure 3.33. The right panel of this figure shows that, since the POWHEG approach is capable of modelling the second hardest emission using the soft-collinear approximation of the parton shower only, its description of the angular separation of the the first two hardest jets is missing prominent features originating in the wide angle region. These features are of course present in the approaches having fixed-order matrix elements at their disposal.

Figure 3.34 shows the differential jet rates d_{01}, d_{12}, d_{23} and d_{34} using the above $k_\perp$-algorithm. While the first three of them, for the matrix-element merged samples, are described by matrix element to matrix element transitions, only the softer part of d_{01} is described by such a transition for the POWHEG sample. The harder part of the d_{01} receives corrections by matrix elements of higher jet multiplicity which are clustered into a single hard jet first. Of course, these corrections are missing in the POWHEG sample. Furthermore, d_{12} is described by a matrix element to parton shower transition only in the POWHEG sample. Hence, it strongly underestimates the amount of hard wide-angle radiation. Similarly, both d_{23} and d_{34} are described by the parton shower only in the POWHEG sample, showing the same behaviour. It is worth noting that both the MENLOPS sample, implementing local K-factors, and the ME+PS, scaled by a global K-factor, agree within their respective statistical uncertainties over the whole range, indicating the well known fact of the approximate momentum independence of the virtual corrections to the leading order process.

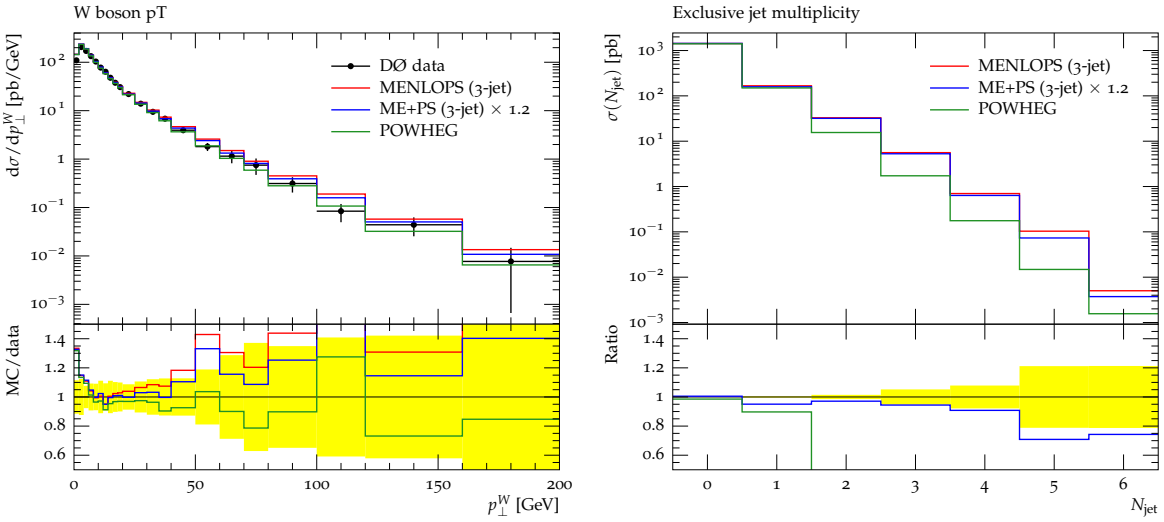

Figure 3.32: Transverse momentum of the W, compared to data taken by the DØ collaboration [111], and the exclusive jet multiplicity in inclusive W production at the Tevatron at $\sqrt{S} = 1.8$ TeV.

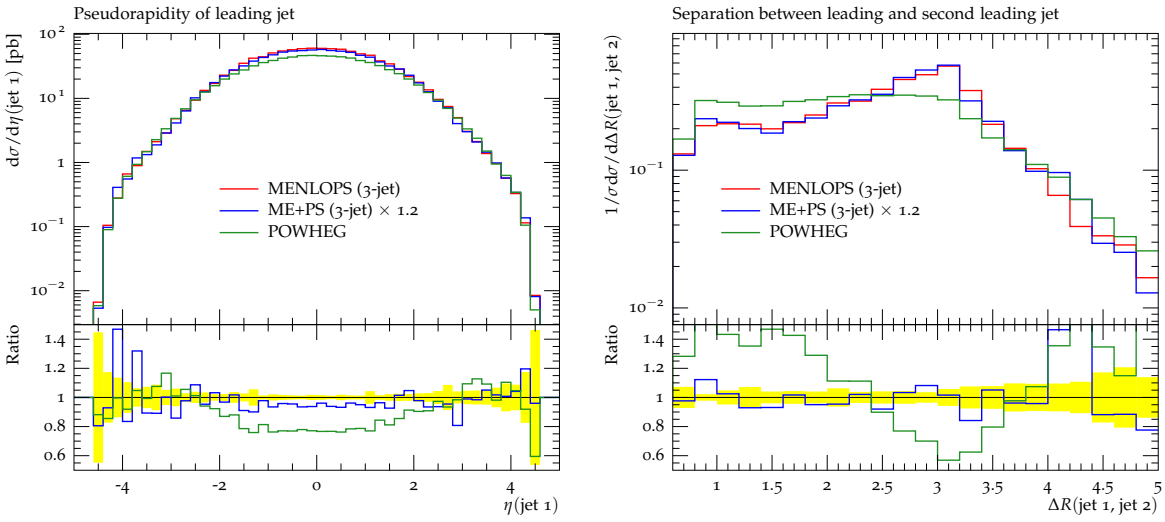

Figure 3.33: Pseudorapidity of the hardest jet and angular separation of the first two hardest jets in inclusive W production at the Tevatron at $\sqrt{S} = 1.8$ TeV.

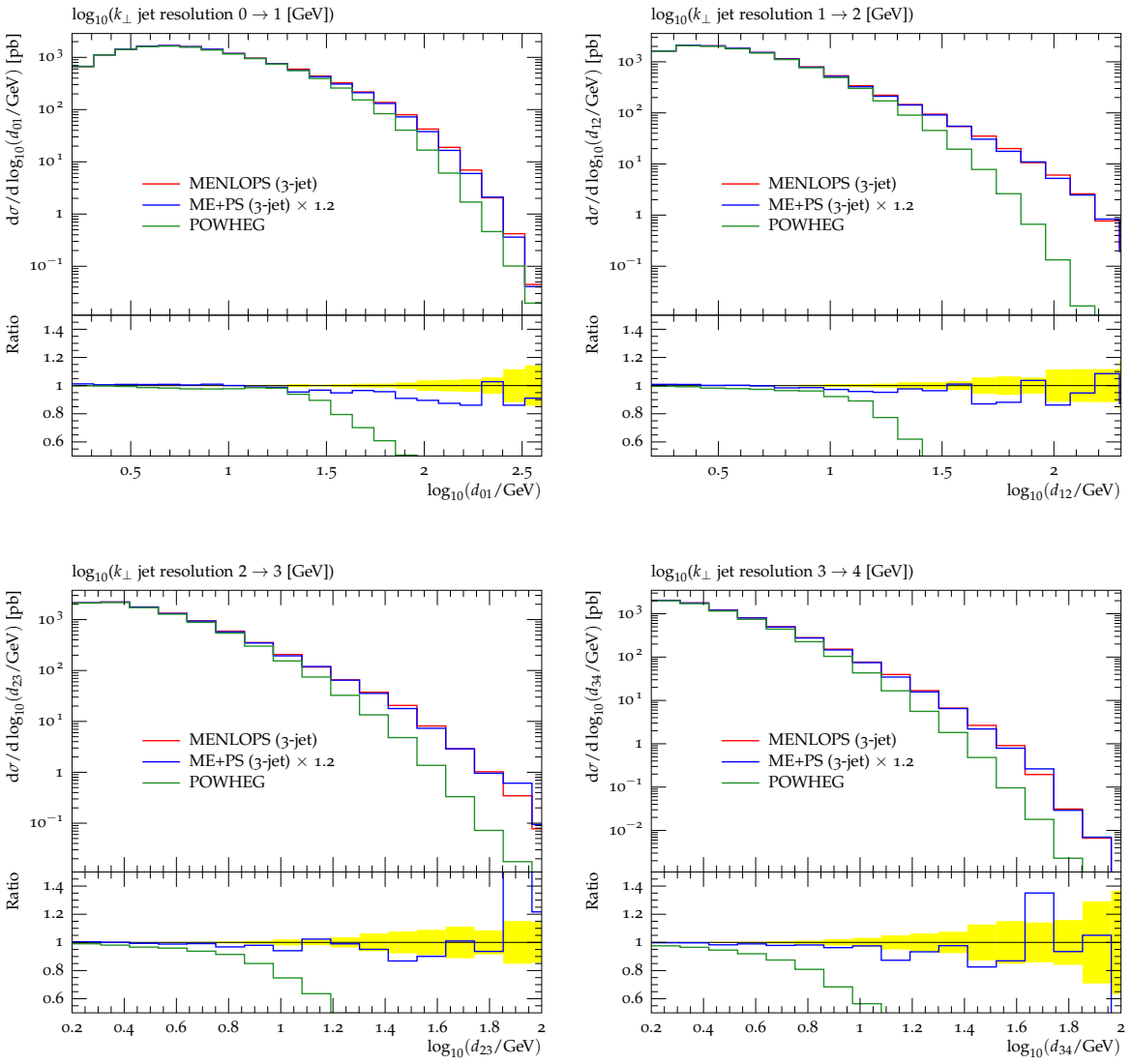

Figure 3.34: Differential jet rates $d_{n\,n+1}$ for three different merging cuts in W production at the Tevatron at $\sqrt{s} = 1.96$ TeV.

3.3.3.5 Higgs boson production

This section presents predictions for Higgs boson production via gluon fusion at nominal LHC energies of $\sqrt{s} = 14$ TeV. As NLO corrections to the core process $gg \to h \to \tau^+\tau^-$ are rather large, tremendous efforts have been made to perform fully differential calculations at NNLO [105] and several predictions have been presented which merged such fixed-order results with resummation at next-to-next-to-leading logarithmic accuracy [106]. In this work, there are no means for an improvement of the resummed calculation, instead it is restricted by the limitations of the parton-shower model. However, the systematic inclusion of higher-order tree-level matrix elements through the MENLOPS method can yield a significant improvement of existing NLO predictions, thus partially closing the gap between full NNLO predictions and Monte-Carlo results. It was shown, for example, in [125] that the predictions from ME+PS algorithms are often competitive to NNLO results if only the shape, not the normalisation, of observable distributions is concerned.

In these simulations the Higgs mass is set to $m_H = 120$ GeV and the decay $h \to \tau^+\tau^-$ is included, however, the analysis focuses on the properties of QCD radiation associated with production of the Higgs boson. The invariant τ-pair mass is restricted to $115 < m_{\tau\tau}/\text{GeV} < 125$ at the matrix-element level. Virtual matrix elements are implemented according to [104]. The decay $h \to \tau^+\tau^-$ is corrected for QED soft-resummation and approximate next-to-leading order effects using the YFS approach [103].

Figure 3.35 shows the transverse momentum spectrum of the reconstructed Higgs boson. One observes that the POWHEG and MENLOPS samples are very consistent in the prediction of this rather inclusive observable. On the other hand, differences are observed in the results for individual jet transverse momentum spectra, cf. Figure 3.36. They increase with jet multiplicity and with increasing transverse momentum, as can be expected, since the higher multiplicity jets are described by the uncorrected parton shower in the POWHEG method. Deviations are also found in the prediction of the dijet separation in $\eta - \phi$ space, which is shown in Figure 3.37. However, it was previously found that the ME+PS result yields a prediction which is very similar to the NNLO result [125]. This feature is naturally retained in the MENLOPS simulation.

3.3.3.6 W^+W^-+jets Production

In this section predictions for the production of the $W^+[\to e^+\nu_e]\, W^-[\to \mu^-\bar{\nu}_\mu]$ final state at nominal LHC energies of $\sqrt{s} = 14$ TeV are presented. The lepton-neutrino pairs are required to have an invariant mass of $m_{\ell\nu} > 10$ GeV each. The $W \to \ell\nu$ decays are

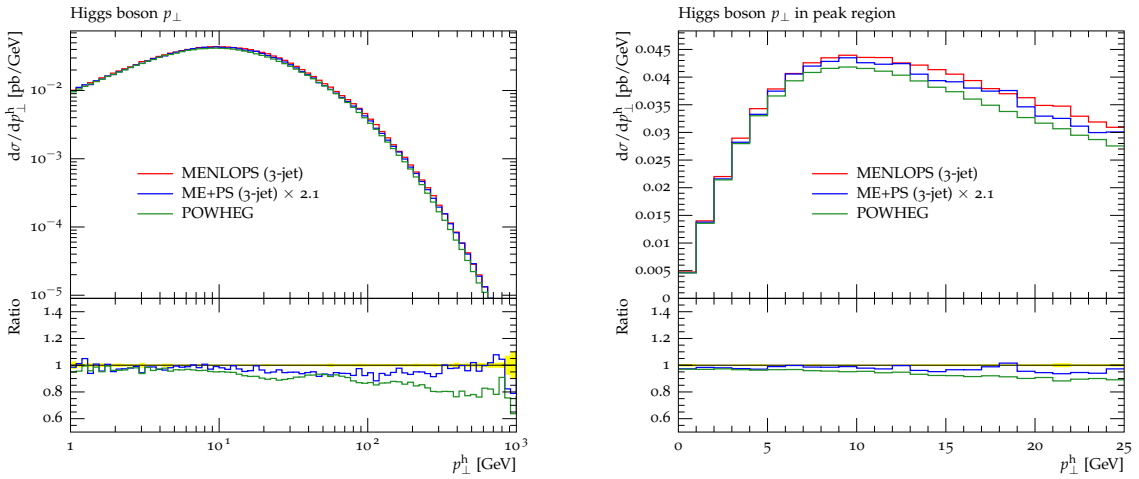

Figure 3.35: Transverse momentum of the reconstructed Higgs boson in the gluon-fusion process at nominal LHC energies (14 TeV).

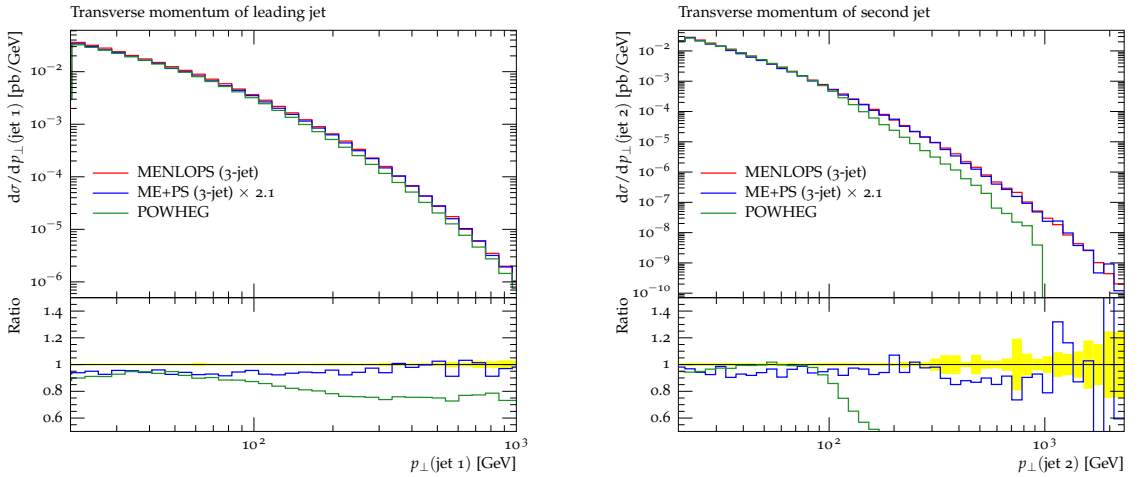

Figure 3.36: Transverse momentum of the first and second hardest jet in Higgs-boson production via gluon fusion at nominal LHC energies (14 TeV).

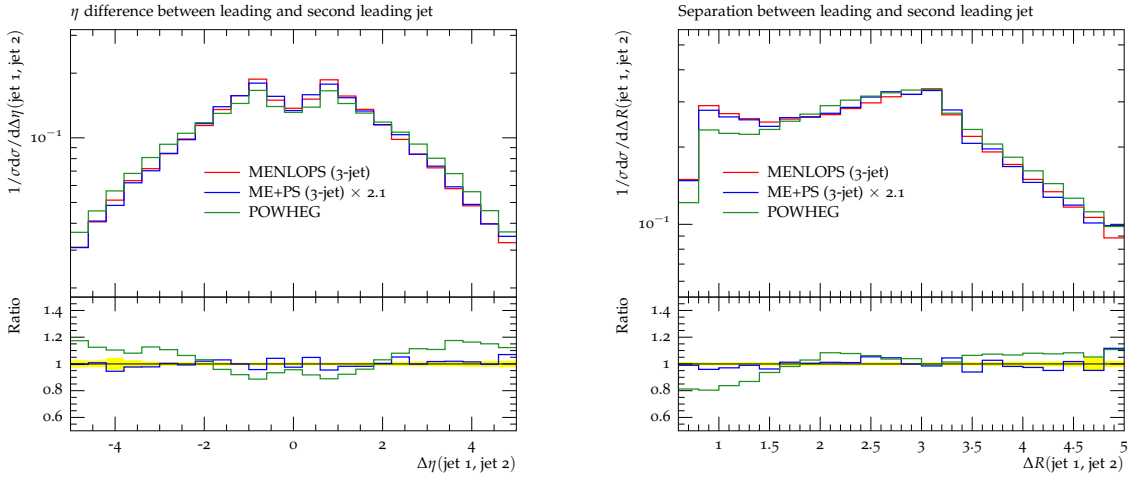

Figure 3.37: Pseudorapidity difference and angular separation of the first and second jet in Higgs-boson production via gluon fusion at LHC energies (14 TeV).

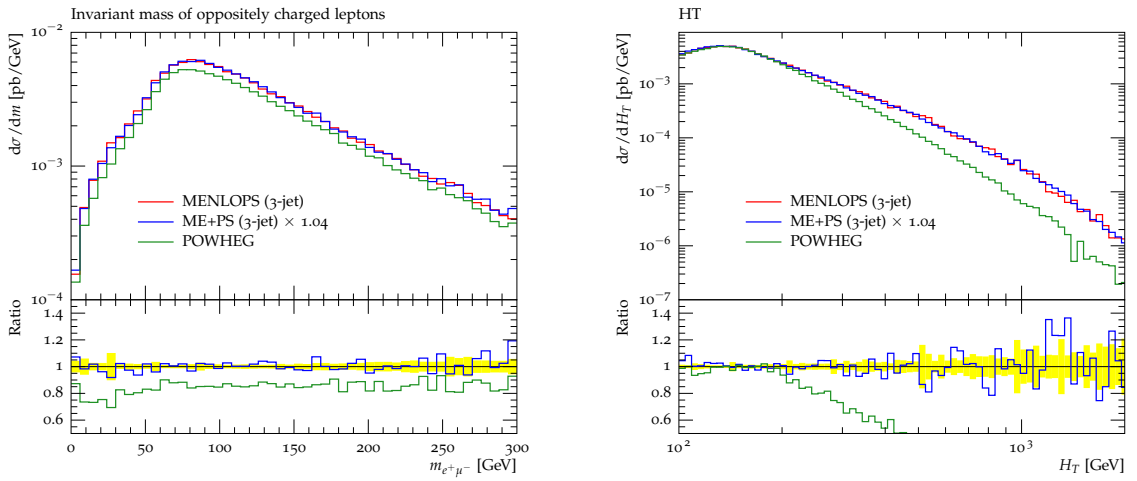

Figure 3.38: Invariant mass of the electron-muon pair (left) and H_T (right) in W^+W^- production at nominal LHC energies (14 TeV).

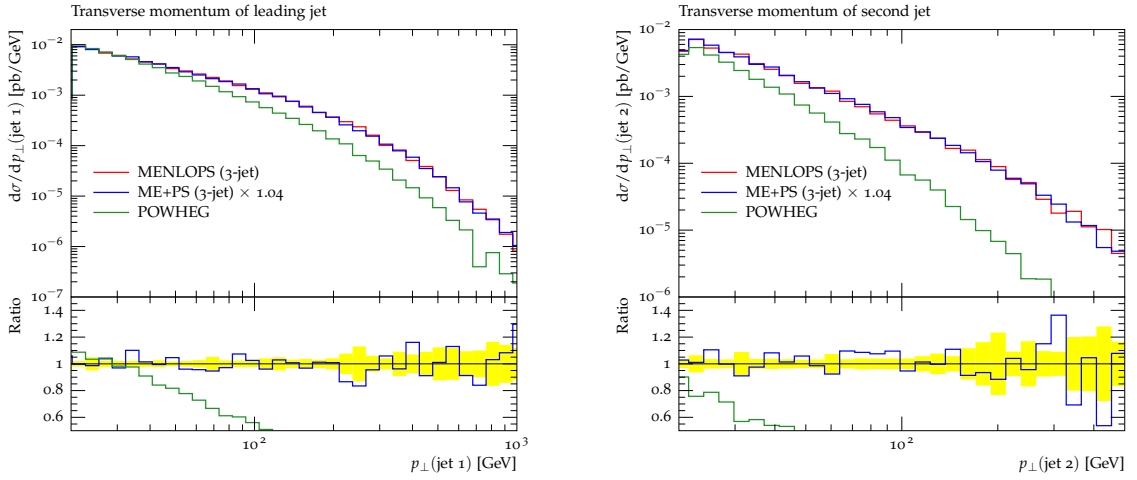

Figure 3.39: Transverse momentum of the first and second hardest jet in W^+W^- production at nominal LHC energies (14 TeV).

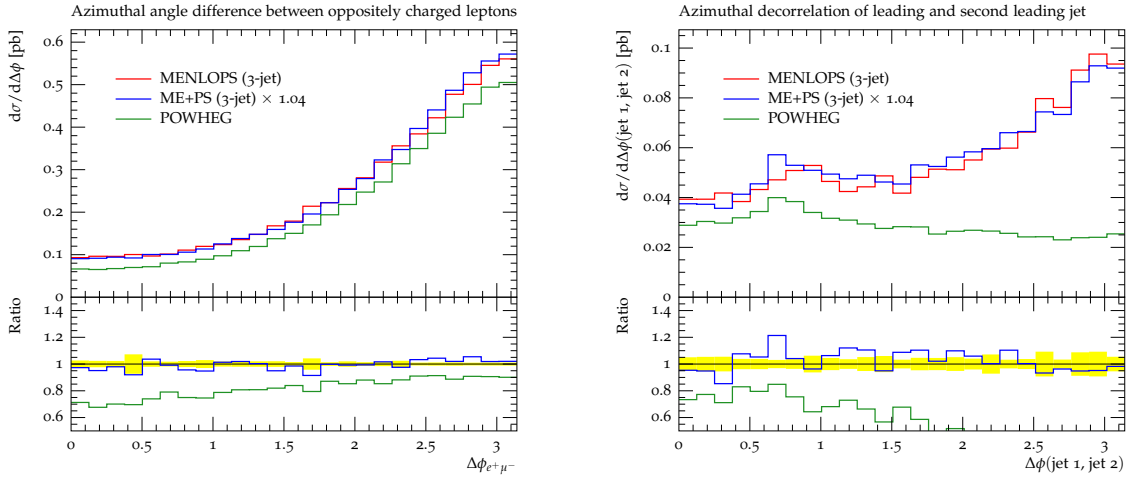

Figure 3.40: Azimuthal separation of the electron and the muon (left) and of the two hardest jets (right) in W^+W^- production at LHC energies (14 TeV).

corrected for QED next-to-leading order and soft-resummation effects using the YFS approach [103]. Virtual matrix elements are supplied by MCFM [107, 108]. Again, this study focuses mainly on the properties of QCD radiation accompanying the diboson production process. Up to three additional jets at $Q_{\text{cut}} = 20$ GeV are simulated in both, the MENLOPS and the ME+PS sample. It is known that high-multiplicity matrix elements in the ME+PS approach yield sizable effects on total event rates and shapes in this reaction [126], a feature which is inherited by the MENLOPS method. Setting the phase space criterion to a rather low value compared to the average partonic centre-of-mass energy will thus always lead to sizable unitarity violations, which might be an indication of potentially large higher-order corrections. A similar effect was observed in a recent analysis of Z-boson pair production in association with a hard jet [127]. While the NLO corrections to this process are comparably small at Tevatron, they can be rather large at nominal LHC energies. Restricting the available final-state phase space by a jet veto, the corrections were again limited to smaller values, which makes the importance of the ZZ+2 jets final state explicit. As up to two additional jets are included in the simulation of W^+W^- production, one observes similar effects.

Figure 3.38 displays the invariant mass of the lepton pair and the scalar sum of transverse momenta of the jets, leptons and the missing transverse energy, H_T. While the former is described very well by the next-to-leading order calculation used in the POWHEG sample and receives only mild corrections from higher-order matrix elements, H_T receives sizable corrections at rather low values already. The reason for this is easily found in the sensitivity of H_T to *any* jet activity and thus to higher-order matrix element corrections of the parton shower. Figure 3.39 exemplifies that the ME+PS part of the MENLOPS simulation predicts significantly harder radiation than the POWHEG subsample. The corresponding corrections naturally amplify the deviations between the respective predictions of H_T.

Figure 3.40 presents predictions for the azimuthal separation of the leptons and the two hardest jets. Again, the former receives only comparably small corrections, while higher-order matrix-element corrections have large impact on the latter. This hints at the importance to include higher-order matrix elements in Monte-Carlo simulations of hadron-collider events if the hadronic centre-of-mass energy is large.

4 Conclusions

Several state-of-the-art methods for the improvement of Monte-Carlo parton showers have been presented in the first part of this thesis. Their common aim is the correction of hard/wide-angle radiation patterns using exact matrix elements while leaving the logarithmic accuracy of the parton shower intact.

The approach of tree-level ME+PS merging based on the CKKW algorithm has been revisited and significantly improved to formally preserve the logarithmic accuracy provided by the parton shower in both initial and final state radiation. In this construction, special emphasis is placed on an invariant formulation of the respective phase-space separation criterion. Because this criterion is not identical with the parton-shower evolution parameter, the logarithmic accuracy can only be maintained by running a truncated shower. These formal improvements greatly reduce the uncertainties induced by the merging procedure compared to previously employed methods. This statement holds for inclusive quantities such as total cross sections and jet rates, as well as for differential distributions.

For the first time, QED emissions have been consistently incorporated into the ME+PS merging algorithm using parton showers with interleaved QCD+QED evolution. This achievement allows a study of hard photon production including the effect of the fragmentation component, which is otherwise very difficult to generate with a parton shower. Comparisons to Tevatron data show very good agreement and major improvements with respect to other theoretical approaches based either on fixed-order calculations or a pure parton shower.

While ME+PS merging has been shown to be well capable of predicting higher-order corrections to the shape of observables it still only provides a leading-order prediction for the inclusive cross section. Another approach, the POWHEG method, aims at correcting a parton-shower Monte Carlo to full NLO accuracy in the inclusive cross section as well as the radiation pattern of the first emission. An implementation of the POWHEG algorithm into the SHERPA event generator was reported. It is worth stressing that this is the first time that the POWHEG method has been fully automated and applied simultaneously to various higher-order calculations using Catani-Seymour

dipole terms for partitioning the real-emission phase space. Additional processes are easily added by merely linking the corresponding code for the virtual correction terms. The implementation was validated by a number of systematic checks, including the stability of cross sections, the radiation patterns through comparison with ME+PS samples and with a fake POWHEG algorithm based on shower kernels, and comparison with a variety of data. The process of W-pair production has been investigated for the first time using the POWHEG technique.

To benefit from the advantages of both the ME+PS and POWHEG methods, a combination of them has been worked out formally and implemented in the SHERPA framework. The new algorithm represents the so far most advanced method to include higher-order corrections in a parton shower. Previously these two approaches were considered orthogonal and were thus used independently from each other, in the regime of their respective strengths and validity. Here the shortcomings of each method, i.e. the description of higher jet multiplicities in POWHEG and lack of the correct NLO cross section in ME+PS, have been expunged. Results have been compared to experimental data in a wide variety of processes and excellent agreement was found. Predictions for various processes at LHC energies have been presented. In the future, the description of many more processes with this combined NLO matching and multijet merging will become feasible. This is possible, because *both* the POWHEG and the ME+PS part of the implementation are fully automated in SHERPA.

The methods developed so far will naturally serve as a starting point to promote the ME+PS idea to full NLO, in the sense that merging sequences of multijet matrix elements at NLO into one inclusive sample becomes feasible.

Part II

Monte-Carlo and early ATLAS data

5 The ATLAS Experiment

5.1 The Large Hadron Collider

The year 2010 was the first year to see the Large Hadron Collider (LHC) near Geneva explore a new high energy frontier by colliding proton beams at a centre-of-mass energy 3.5 times higher than any experiment previously.

The LHC has been designed to accelerate beams of either protons to an energy of 7 TeV or lead nuclei to an energy of 574 TeV each in the former LEP tunnel which has a circumference of 27 km. It is embedded into the CERN accelerator complex with several pre-accelerators feeding protons into each other and finally the LHC as shown in Figure 5.1.

In September 2008, only a few days after the first LHC beams ever had been celebrated, an incident caused a significant delay to the LHC schedule. An electrical fault in the connection between two magnets had caused a leak leading to the loss of six tonnes of liquid helium and damage to the magnets. Repairs and commissioning of the LHC then took one year and to avoid similar incidents in the future it has been decided to run the collider only up to half of its design energy, i.e. 7 TeV centre of mass energy, until the end of 2011. In autumn 2009 first collisions were delivered at 0.9 TeV and 2.36 TeV for several days and the data have been recorded and analysed by the experiments. March 2010 saw the first collisions at 7 TeV.

While the LHC has been designed to operate at instantaneous luminosities up to $10^{34}\text{cm}^{-2}\text{s}^{-1}$, the objective for the year 2010 is to reach $10^{32}\text{cm}^{-2}\text{s}^{-1}$ and to collect an integrated luminosity of 1fb^{-1} by the end of 2011. The instantaneous luminosity of the accelerator is influenced by several variables, of which the following have seen significant improvements over the running of the first months:

Colliding bunches per beam

Instead of forming a continuous beam, protons are separated into bunches, with ultimately 2808 bunches per beam. The first 7 TeV collisions in March 2010 have

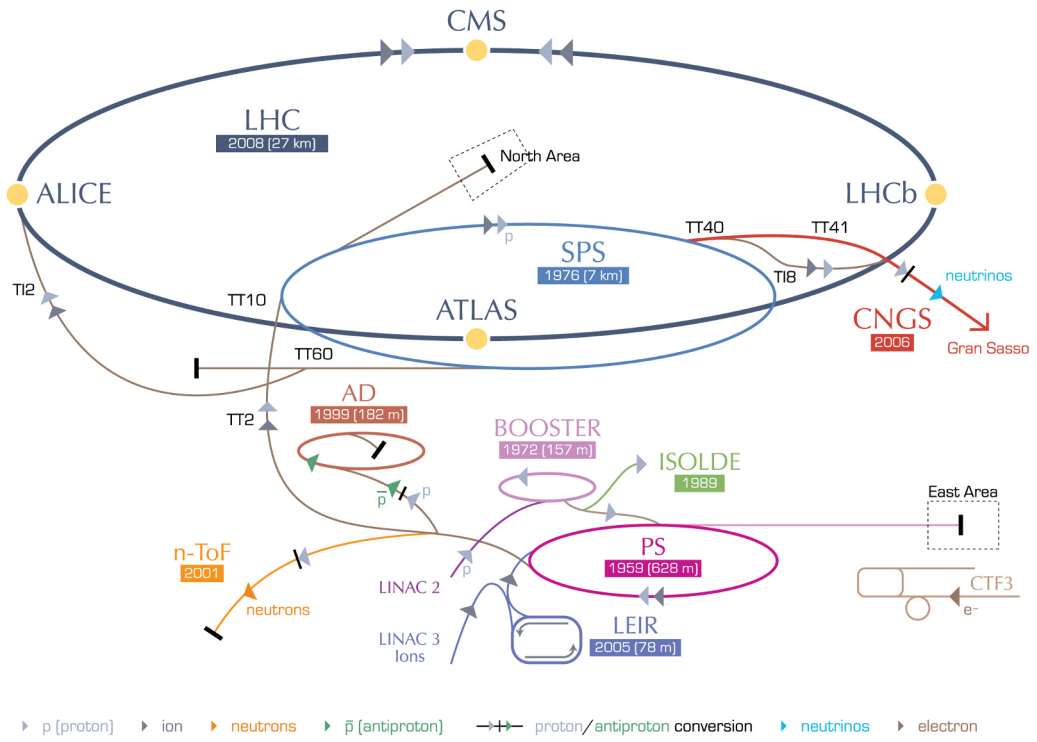

Figure 5.1: Layout of the accelerator complex at CERN including the Large Hadron Collider. Figure taken from [128].

been done with one colliding bunch per beam and since then this number has been increased to 36 in late August.

Protons per bunch

The number of protons per bunch has risen by an order of magnitude to 10^{11} in July 2010.

Beam size at interaction

The beam is squeezed at the interaction point to increase the number of collisions. Before squeezing the distance from the interaction point at which the beam has doubled its size is $\beta^* = 11$ m. Since April 2010 a value of $\beta^* = 2$ m has been achieved, and the design goal is $\beta^* = 0.55$ m.

These improvements have lead to an enormous increase in instantaneous luminosity which has risen from $10^{27}\text{cm}^{-2}\text{s}^{-1}$ in March to $10^{31}\text{cm}^{-2}\text{s}^{-1}$ in August 2010. The effect on the delivered integrated luminosity can be seen in Figure 5.2.

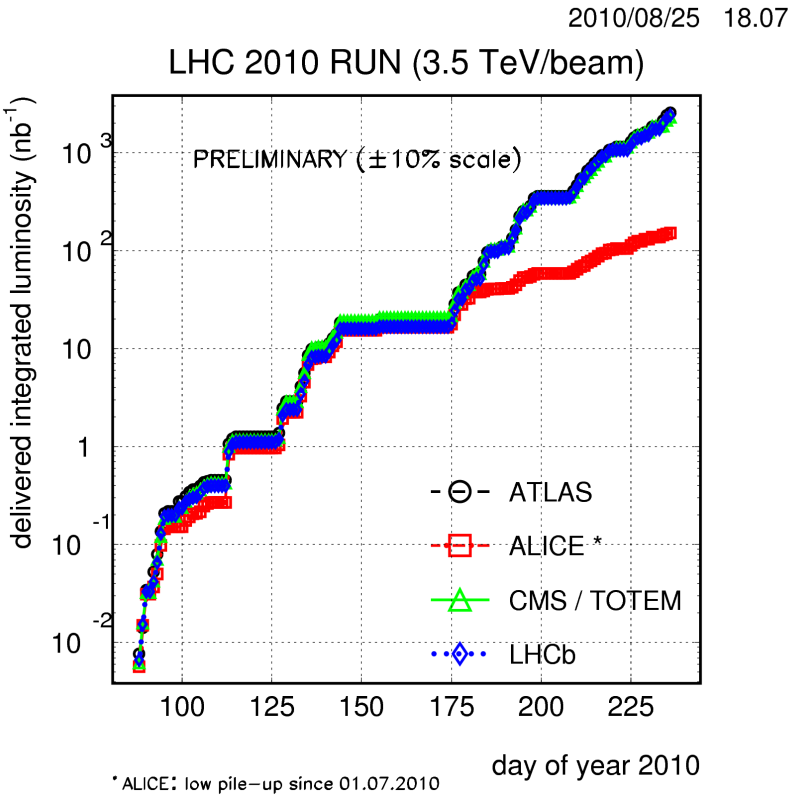

Figure 5.2: Integrated luminosity delivered by the LHC machine to the four LHC experiments up to August 2010. Figure taken from [129].

5.2 The ATLAS Detector

ATLAS [130] is one of the two multi-purpose detectors at the Large Hadron Collider and its main goal is the observation of new particles with high masses which might be produced due to the new energy frontier opened up by the LHC.

The fact that 3000 physicists from more than 174 universities and laboratories participate in the ATLAS collaboration already signals the complexity and size of this effort. A schematic view of the detector can be found in Figure 5.3. It is 44 m long and has a height of 25 m, weighing about 7000 tonnes.

To fulfil the broad mission of detecting the wide spectrum of particles and energies produced in LHC collisions ATLAS consists of many subdetectors with specific tasks. Broadly they can be divided into four categories: The Inner Detector (ID) which is embedded into a solenoidal magnetic field, the calorimeters which measure the energy of electrons, photons and hadron jets, the muon spectrometer on the outside embedded in a toroidal magnetic field, and the forward detectors which are placed in the very far forward regions and serve specialised purposes like luminosity measurement.

The remainder of this chapter will briefly summarise the Inner Detector, because it is

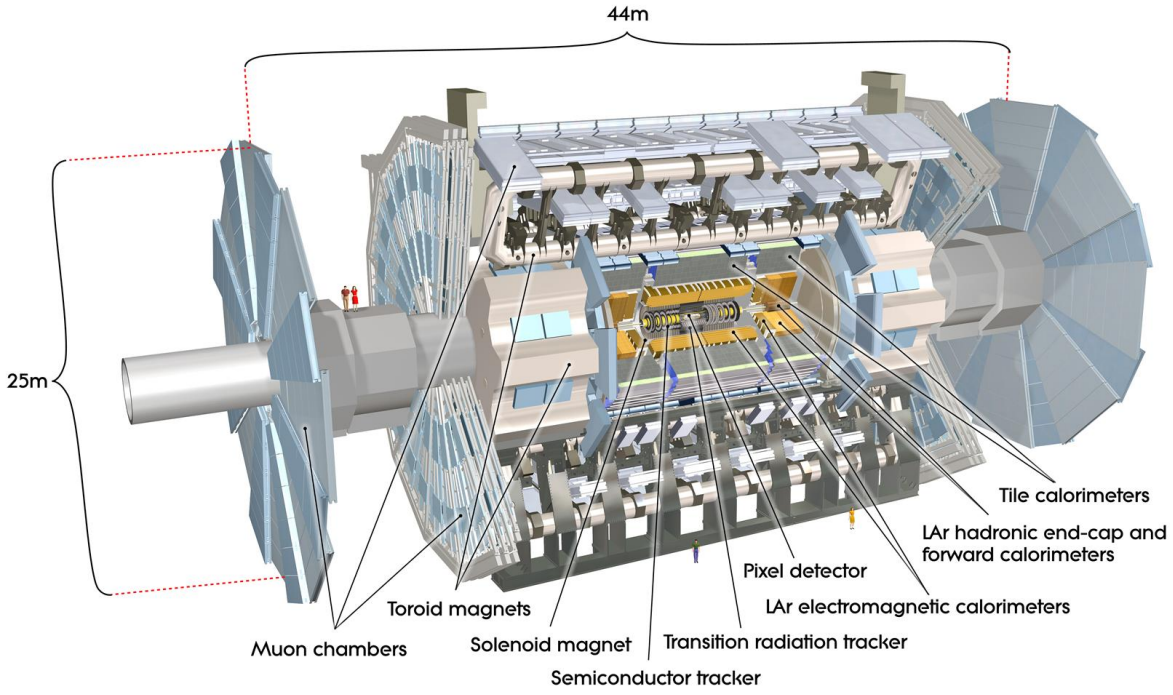

Figure 5.3: The ATLAS detector (from [131]).

going to be relevant for the analyses presented in Chapter 6.

5.3 The Inner Detector

As the name implies, the Inner Detector is the detector group closest to the interaction point, being only a few centimetres away from the beam axis and extending to an outer radius of 1.15 m with a total length of 7 m. Most of its parts cover a pseudorapidity range of $|\eta| < 2.5$. Its purpose is the detection of charged particle tracks and a measurement of their charge and momenta from the curvature caused by the solenoidal magnetic field of 2 T it is embedded into. At the same time, by reconstructing the tracks it is possible to find secondary displaced vertices which signal decays of beauty and charm hadrons and can thus be used for b-tagging.

The Inner Detector itself consists of three parts:

The Pixel Detector is designed to give very high precision in tracking near the interaction point. It hosts a total of 1456 modules in three barrels of mean radii of 5 cm, 9 cm and 12 cm, and another 288 modules in three disks on each side. Each module contains 46080 pixel elements of size $50 \times 400 \mu$m and is 62 mm long and 21 mm

wide. Charged tracks are detected because they create electron-hole pairs by ionisation in the silicon material, which is depleted by an applied voltage. The resulting electrons are then collected at the cathode side and readout by the 80 million channels in total. A typical track will give three hits in the Pixel Detector and is expected to be resolved to ≈ 14 μm in $R\phi$ and ≈ 115 μm in z.

The Semi-Conductor Tracker (SCT) is similar to the Pixel Detector but segmented in strips rather than pixels. It feeds 6.2 million readout channels coming from strips with a pitch of 80 μm and a length of 12.6 cm. They are arranged in four barrel layers which cover a pseudorapidity of $|\eta| < 1.4$ and in nine disks on each side of the barrels covering the remaining region up to $|\eta| = 2.5$.

The Transition Radiation Tracker (TRT) builds on the concept of straw detectors. They contain a gold-plated Tungsten-Rhenium wire of 30 μm diameter in the centre of a 4 mm wide tube filled with a gas mixture of Xenon (70%), carbon dioxide (27%) and oxygen (3%). The wire is held at about -1500 V and when charged particles traverse the tube they ionise the gas and the produced electrons drift towards the wire. The detection resolution is significantly worse than in the two innermost subdetectors at about 200 μm. But due to the large volume covered it gives 36 space point measurements on average per track. Another advantage of the TRT are its capabilities of particle identification: Due to a radiator material surrounding the straw tubes a traversing particle passes many layers with varying refraction indices. This leads to transition radiation which is stronger for ultra-relativistic particles, allowing to distinguish between electrons and pions due to their mass difference. Its pseudorapidity range $|\eta| < 2.1$ is slightly smaller than the other components of the ID.

6 Early ATLAS measurements

This chapter aims to introduce the first measurements made using the ATLAS detector. The focus lies on analyses which were possible even with a very low integrated luminosity as available in the first days of data taking. Such analyses have to use minimal selection cuts as to make maximal use of the delivered luminosity. The trigger setting which implements such a cut is consequently called "Minimum Bias" and its ATLAS specifications will be explained in Section 6.1. Two analyses using that trigger to measure charged particle multiplicities will be described in Section 6.2. Section 6.3 describes the measurement of variables related to the Underlying Event.

6.1 Minimum Bias Trigger

All measurements described in this chapter study what one can call the "average event", i.e. events which have been selected without restrictive selection criteria. So although one does not require features like Z bosons or even just relatively hard jets in them it is still necessary to find some kind of minimum definition of inelastic proton-proton collision events at which the detector is triggered to record its state. Since this is constructed such that it otherwise introduces as little bias as possible it is called a "Minimum Bias" trigger.

In ATLAS the Minimum Bias Trigger Scintillators (MBTS) supply the hardware part for such a trigger system. The MBTS consist of two disks, one on each beam side of the detector inside the end caps. Each disk is segmented in azimuth (8 segments) and pseudorapidity (inner and outer), covering a range of $2.09 < |\eta| < 3.84$. The MBTS are designed only for the initial data-taking period, because they will yellow due to radiation damage in higher-luminosity operation.

When hit by charged particles, these scintillator elements emit light which is then guided to a photomultiplier tube using wavelength-shifting optical fibres. From these hardware signals the MBTS multiplicity is calculated for each side independently and three Level-1 triggers are formed from them: `L1_MBTS_1`, `L1_MBTS_2` and `L1_MBTS_1_1`,

which require respectively at least one hit, at least two hits and at least one hit per side.

The L1_MBTS_1 trigger has been used in all analyses in this chapter. Its efficiency has been determined in [132] and is corrected for in the analyses.

6.2 Charged particle multiplicities

Distributions of charged particles in very inclusive hadron collisions have been measured by many experiments previously in both $p\bar{p}$ as well as pp collisions [133] [134] [135] [136] [137, 138]. Early data from the LHC has also already led to publications from ALICE [139], CMS [140] and ATLAS [141]. The aim of this section is the description of the ATLAS measurements.

Traditionally, the non-ATLAS analyses used a double-arm trigger to largely remove diffractive events. Using theory models, the remaining diffractive component was then subtracted, either only for the single-diffractive component or also for the double-diffractive component. This lead to results presented on the level of "non-single-diffractive" or "inelastic non-diffractive" events respectively. A disadvantage of this procedure is the model dependence which enters these results through the subtraction. The theoretical modelling of diffraction is currently poorly understood and when used in these analyses introduces an unnecessary source of uncertainty and makes them unfit for further studies of diffraction models.

The strategy of the ATLAS analyses both at 0.9 and 7.0 TeV is significantly different from all previous measurements. After the application of a one-arm trigger no attempt is made to correct in terms of the theoretical categories of non/single/double-diffractive events, but instead the event selection is only defined in terms of quantities measurable at the particle level. Specifically, the results are corrected for trigger and detector efficiencies back to the following selection criterion: At least one charged particle has to be found with a transverse momentum $p_\perp > 0.5$ GeV within $|\eta| < 2.5$. Only charged particles with a mean lifetime of $\tau > 0.3 \times 10^{-10}$ s are taken into account.

For the selected events several distributions of the charged particles obtained after the detector corrections are prepared:

$\frac{1}{N_{\mathrm{ev}}} \cdot \frac{\mathrm{d}N_{\mathrm{ch}}}{\mathrm{d}\eta}$
: Pseudorapidity distribution of charged particles normalised by the number of events.

$\frac{1}{N_{\mathrm{ev}}} \cdot \frac{1}{2\pi p_{\perp}} \cdot \frac{\mathrm{d}^2 N_{\mathrm{ch}}}{\mathrm{d}\eta\, \mathrm{d}p_{\perp}}$
: Charged particle distribution in bins of $p_{\perp}$ where each entry is weighted by $1/p_{\perp}$ and the distribution is normalised by the number of events.

$\frac{1}{N_{\mathrm{ev}}} \frac{\mathrm{d}N_{\mathrm{ev}}}{\mathrm{d}n_{\mathrm{ch}}}$
: Distribution of the multiplicity of charged particles per event.

$\langle p_{\perp} \rangle$ **vs.** n_{ch}
: Average $p_{\perp}$ as a function of n_{ch}

6.2.1 Correction to particle level

The most important and complex part of the whole analysis is the correction of track properties measured by the inner detector back to the particle level as it can be simulated by theory models like Monte-Carlo event generators. Here the correction procedure is briefly summarised.

Background events for this fully-inclusive inelastic measurement can come from two different sources: cosmic rays and collisions of protons with collimators or residual particles inside the beam pipe. Cosmic rays have been shown to contribute only with a fraction smaller than 10^{-6}. The beam-induced background was studied with the same trigger and event selection requirements during un-paired proton bunch-crossings and was found to make up a fraction lower than 10^{-4} of the selected events.

Correcting the tracks back to charged particles with $\tau > 0.3 \times 10^{-10}$ s requires an understanding of $f_{\mathrm{secondaries}}$, the fraction of "secondary" particles in the measured tracks, e.g. long-lived particles which decay inside the tracker. The distribution of their decay length is well understood and its modelling has been shown to agree very well with data, such that it can be used to determine the corresponding correction factors.

Another detector level quantity that particle-level results have to be corrected for is the efficiency of the trigger ($\epsilon_{\mathrm{Trigger}}$) and vertex requirement (ϵ_{vtx}). The trigger has already been described in Section 6.1 and has been shown to be nearly 100% efficient in the complete phase space of this measurement. In addition to the trigger, the analysis required one reconstructed vertex close to the beam spot position with at least three tracks of $p_{\perp} > 150$ MeV pointing towards it. The efficiency of this requirement is relatively low for events with only one selected track, $\epsilon_{\mathrm{vtx}} \approx 67\%$, but quickly rises to 100% for events with higher track multiplicities. Its dependence on the number of selected tracks n_{sel} was taken into account for the correction.

Last, but not least, one also has to correct for the efficiency of detecting tracks in the

first place, η_{track}. This correction factor has been determined in bins of $p_\perp$ and η using the detector simulation after showing in other track distributions that its agreement with data is satisfactory.

Unifying all these corrections leads to an event-by-event weight,

$$w_{\text{ev}}(n_{\text{sel}}) = \frac{1}{\epsilon_{\text{Trigger}}(n_{\text{sel}})} \cdot \frac{1}{\epsilon_{\text{vtx}}(n_{\text{sel}})}$$

and a track-by-track weight

$$w_{\text{track}}(p_\perp, \eta) = \frac{1}{\epsilon_{\text{track}}(p_\perp, \eta)} \cdot (1 - f_{\text{secondaries}}(p_\perp)) \cdot (1 - f_{\text{okr}}(p_\perp, \eta)),$$

where f_{okr} is the fraction of tracks in the acceptance which were reconstructed from particles outside the kinematic range due to resolution effects. All other quantities are described in the text above.

6.2.2 Diffraction-limited phase space

Since diffractive events have not been subtracted in the measurement procedure described above, one cannot use the distributions for a direct comparison to theory predictions without a reliable diffractive model [1]. Unfortunately, there is no reliable model of diffractive events available in any Monte-Carlo event generator currently. Consequently, not even the non-diffractive parts of these generators can be validated or tuned using this data without introducing large uncertainties from the treatment of the diffractive components.

To remedy this deficiency without sacrificing the minimal model dependence, this measurement has been repeated with a slightly changed selection criterion [142]: By selecting only events with $n_{\text{ch}} > 6$, the diffractive component is sufficiently suppressed without rejecting too many events. Figure 6.1 shows the fraction of non-diffractive, single-diffractive and double-diffractive events as defined by the PYTHIA event generator in bins of the charged multiplicity and confirms the choice of $n_{\text{ch}} > 6$.

The same distributions as listed above have been analysed using this additional event selection criterion. They will be used in Chapter 7 to obtain an improved parameter tune of the PYTHIA 6 event generator.

[1] Note, that this problem might seem to be solved if results are presented at the "non-diffractive" level, but in fact it is only hidden in the subtraction procedure, and still inherently present.

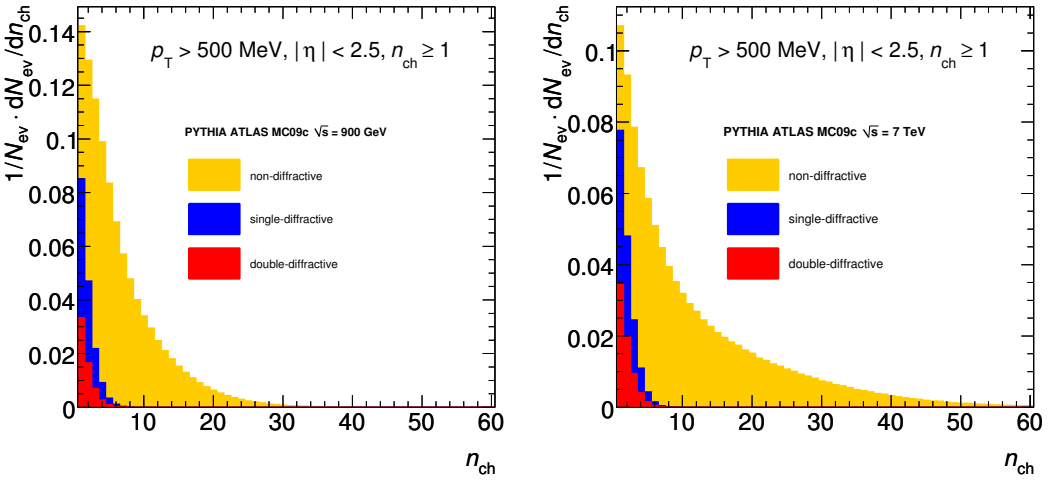

Figure 6.1: Contributions of non-diffractive, single-diffractive and double-diffractive processes as defined by the PYTHIA event generator to the charged multiplicity distribution (from [142]).

6.3 Underlying Event observables

In addition to the charged multiplicity measurements presented above, ATLAS has also measured [143] the charged particle flow in the same minimum bias events selected with $n_{\mathrm{ch}} > 1$ as described in Section 6.2. Special emphasis has been placed on observables sensitive to the Underlying Event which have been measured for different regions relative to the leading track in the event.

The event and particle selections described in Section 6.2 were used with the additional requirement of at least one primary charged particle with $p_{\perp} > 1$ GeV in the acceptance. This reduces diffractive contributions significantly and minimises systematic uncertainties.

Charged particles in each event are analysed in three regions in terms of azimuthal angle with respect to the track with maximum transverse momentum (leading track):

- "Towards" region $|\Delta\Phi| < 60°$
- "Transverse" region $60° < |\Delta\Phi| < 120°$
- "Away" region $|\Delta\Phi| > 120°$

Of most interest for UE studies is the transverse region, as it is perpendicular to the axis of the hardest scattering. The following two observables will be used in Section 7:

$\langle \frac{\mathrm{d}^2 N_{\mathrm{chg}}}{\mathrm{d}\eta \mathrm{d}\phi} \rangle$ Number of stable charged particles per unit of $\eta - \phi$

$\langle \frac{\mathrm{d}^2 \sum p_{\perp}}{\mathrm{d}\eta \mathrm{d}\phi} \rangle$ Scalar $p_{\perp}$ sum of stable charged particles per unit of $\eta - \phi$

7 Monte-Carlo tuning with early ATLAS data

With the very quick availability of results for the analyses presented in the previous chapter one can start making the first comparisons of different Monte-Carlo models to measurements at LHC energies, as has been done in the various early publications from the LHC experiments, ALICE [139], ATLAS [141] and CMS [140].

As the ATLAS analyses are all corrected to the particle level one can even go one step further and use them to adjust the non-perturbative parameters of Monte-Carlo event generators to give a better fit to data. This chapter deals with such a tuning for the PYTHIA 6 generator, taking into account the ATLAS analysis as well as previous measurements from Tevatron experiments.

7.1 Tuning setup

The tune described here is based on the ATLAS MC09c parameter setup of the PYTHIA 6 generator, which is described in detail in reference [144]. MC09c uses the modified LO* parton density functions [145] and was tuned to available Tevatron underlying event and minimum bias data, itself being an evolution of the ATLAS MC09 tune with a reduced amount of colour reconnection. In [141] it was shown that the MC09c tune gives an overall satisfactory description of the ATLAS minimum bias data at 0.9 TeV and 7 TeV. Some MC–data deviations are visible though, summarised briefly as follows:

- The MC09c tune predicts more events with a very small multiplicity than observed in data. This region of phase space is populated mainly by diffractive events. A discrepancy can thus be easily created if either the simulated cross section of these diffractive processes is too low in the MC generator, or if the diffractive model used does not describe nature properly. The problem is not limited to the lowest multiplicity bins, as the normalisation of all other observables presented in [141] is derived from the multiplicity distribution. Thus this diffractive contamination biases also the other distributions.

- The very high multiplicity tail is not completely described by the MC09c tune, which falls short of the data.
- For the transverse momentum distribution of charged particles, a discrepancy of all PYTHIA 6 tunes using the p_T-ordered parton shower is observed: Around a transverse momentum of 10 GeV the MC predicts significantly more charged particles than seen in the data. The Perugia0 tune [146] describes the data in this region better than the MC09c tune.
- For the measurement of the average transverse momentum, the MC09c tune is close to the data at 0.9 TeV, but about 10% too high at 7 TeV

These deviations make it worthwhile to improve upon the old tune by including the ATLAS data.

7.1.1 Tuning parameters

From the large number of parameters in PYTHIA 6 it is clear that a tune of all of them would be impossible. Instead, some of the main parameters for the description of multi-parton-interactions (MPI), colour reconnection (CR) and matter overlap distribution (MO) were considered. In addition, the cut-off parameter for initial state radiation (ISR) was considered in the tuning. These parameters are described in more detail in the following.

MPI parameters

The amount of the MPI component in the PYTHIA 6 model is regulated by a simple cut-off parameter for the $\hat{p}_T$ of $2 \to 2$ scattering processes. This cut-off parameter is fixed at a reference energy, which is generally taken as 1.8 TeV. The cut-off at this reference scale is called PARP(82). It is then rescaled for other center-of-mass energies using a parameter PARP(90). The rescaling is done according to the following formula:

$$p_T^{\min} = \text{PARP(82)} \left(\frac{E}{1.8\,\text{TeV}} \right)^{\text{PARP(90)}} \tag{7.1}$$

Both PARP(82) and PARP(90) were considered as tuning parameters.

Matter overlap parameters

The amount of scatterings is described by a matter overlap distribution between the two protons, which regulates how many central, hard scatterings and how many less central, softer scatterings happen. This distribution is chosen to be a double Gaussian pdf, where the parameter PARP(83) describes the fraction of matter in the inner Gaussian, and PARP(84) the relative size of the inner Gaussian.

Colour-reconnection parameters

The colour annealing scenario of PYTHIA 6 which is used in MC09c minimises the total string length. It is the most sophisticated scenario available in PYTHIA 6 so far. As described in [2], the probability that a given string piece does not participate in the colour annealing is given by $(1 - \text{PARP}(78))^{n_{MI}}$, where n_{MI} is the number of multi-parton interactions. In addition to this parameter, since PYTHIA 6.4.20, an additional parameter, PARP(77) is present in PYTHIA 6, which is used to describe a suppression factor for the colour annealing of fast moving string pieces. The suppression factor is given by $1/(1 + \text{PARP}(77)^2 \cdot p^2_{\text{avg}})$, where p^2_{avg} is a measure of the average squared momentum that hadrons produced by the string piece would have (see [147]). Both of these parameters were considered for the tuning. It should be noted that PARP(77) was set to its default value of zero in the MC09c tune, and thus the suppression factor for fast moving string pieces was set to unity.

Other parameters changed w.r.t. MC09c

In addition to the parameters described above, the cut-off parameter for ISR PARP(62) was considered for the tuning. In addition, the cut-off for momentum smearing in primordial k_T, PARP(93), was increased to 10.0 from its default value of 5.0. The influence of this parameter on distributions used in the tuning is negligible, but a value of 10.0 is preferred for example in the Perugia tunes [146].

7.1.2 Tuning procedure with PROFESSOR

For the actual tuning procedure, the PROFESSOR tool [148] was used. It is based on an interpolation of the generator response in each bin of the distributions considered for tuning. This interpolation is done in dependence of the parameters $\vec{\alpha}$ considered in the tune. The interpolation is performed using randomly sampled parameter points in the

multi-dimensional tuning space and is calculated based on singular value decomposition techniques. Using this interpolation, a simple χ^2 variable can be minimised for tuning, based on the bin-by-bin interpolation and the measured data:

$$\chi^2(\vec{\alpha}) = \sum_{\text{bins } i} \left(\frac{(\text{Interpolation}_i(\vec{\alpha}) - \text{Data}_i)}{\text{Error}_i} \right)^2 . \tag{7.2}$$

The best tuning set is then derived by minimising the χ^2 with respect to the parameters.

In order to achieve stability of the interpolation, it is strongly advisable to generate more random points than the minimum necessary to form the interpolation. In the case of 7 free parameters and using a cubic polynomial for the interpolation, at least 120 randomly distributed runs are necessary to form an interpolation. This drops to 56, if only 5 parameters are tuned. In the following all results are based on using a cubic interpolation.

The analysis of the generator runs has been performed using the RIVET tool [79], which provides an easy interface also to previous datasets. The output of RIVET can be used directly as input for PROFESSOR.

7.1.3 7 parameter pre-tune

In a first tuning step, all 7 parameters described previously were left free to vary. In total 135 randomly selected parameter points were used. Due to the small degree of oversampling (at least 120 points are needed), it was observed that the interpolation is not stable in all regions of phase space. As a consequence it was difficult to assess the stability of the tuned parameters. Nevertheless, a parameter set that gives an adequate description of the ATLAS minbias data sets was found using this pre-tune step. The derived parameters are summarised in Table 7.1. The pre-tune was made to preliminary datasets, which are slightly different from the final ones used for the main tune. However, the pre-tune was made only to possibly reduce the range and number of free parameters. The remaining free parameters are expected to be flexible enough to accommodate any changes of the data.

As the high dimensionality of the parameter space made an efficient oversampling of the parameter sampling difficult, it was decided to reduce the dimensionality of the problem, by fixing two of these seven parameters by fixing their values to the numbers obtained from the pre-tune. These were:

- PARP(62) was fixed to 1.025, which is close to the default value of 1.0. This is

Parameter	Value in MC09c	Value found in pre-tune
PARP(62)	1.0	1.025
PARP(77)	0.0	0.803
PARP(78)	0.224	0.405
PARP(82)	2.315	2.300
PARP(83)	0.8	0.356
PARP(84)	0.7	0.603
PARP(90)	0.2487	0.245

Table 7.1: Parameters found by PROFESSOR in the pre-tune.

motivated because this parameter mainly influenced the shape of the pseudorapidity distribution of charged particles, which is already described adequately by the MC09c tune, as shown in [141]. In addition, this parameter also has potential influence on high-p_T observables, which were not studied for this tuning. The difference to the default value of 1.0 is sufficiently small that no adverse effects can be expected.

- PARP(83) was fixed to 0.356, based on visual inspection of the charged multiplicity distribution in the ATLAS minimum bias data. Other observables were only weakly influenced by this parameter. Instead it was observed that PARP(84) has a significant influence on the tail of the minimum bias multiplicity distribution. To be able to improve on this weak point of the MC09c tune, the parameter PARP(84) was still allowed to be free.

7.1.4 Datasets and weights used for tuning

The datasets used for tuning are listed in Tables 7.2 and 7.3 for ATLAS data and Tevatron data respectively. The non-ATLAS analyses are described briefly in [144] and in more detail in the references of each analysis while the ATLAS analyses have been summarised in Chapter 6. The weights and fitting ranges were chosen in the following way:

- ATLAS analyses got a high weight.
- The CDF Run II measurement of $\langle p_\perp \rangle$ vs. N_{ch} got another down-weighting. Otherwise it would have dominated the tune due to its small uncertainties.
- For the ATLAS minimum bias analyses only the high-$p_\perp$ and high-multiplicity part of the spectra was used. It should be noted that the pseudorapidity distribution essentially fixes the mean value of the multiplicity distribution.

Analysis	Observable	Tuning range	Weight
ATLAS 0.9 TeV, minimum bias, $N_{ch} \geq 6$	$\frac{1}{N_{evt}} \frac{dN_{ch}}{d\eta}$	-2.5 – 2.5	10.0
ATLAS 0.9 TeV, minimum bias, $N_{ch} \geq 6$	$\frac{1}{2\pi\Delta\eta p_T} \frac{1}{N_{evt}} \frac{dN_{ch}}{dp_T}$	≥ 5.0	10.0
ATLAS 0.9 TeV, minimum bias, $N_{ch} \geq 6$	$\frac{1}{N_{evt}} \frac{dN_{ev}}{dN_{ch}}$	≥ 20	100.0
ATLAS 0.9 TeV, minimum bias, $N_{ch} \geq 6$	$\langle p_\perp \rangle$ vs. N_{ch}	≥ 10	10.0
ATLAS 7 TeV, minimum bias, $N_{ch} \geq 6$	$\frac{1}{N_{evt}} \frac{dN_{ch}}{d\eta}$	-2.5 – 2.5	10.0
ATLAS 7 TeV, minimum bias, $N_{ch} \geq 6$	$\frac{1}{2\pi\Delta\eta p_T} \frac{1}{N_{evt}} \frac{dN_{ch}}{dp_T}$	≥ 5.0	10.0
ATLAS 7 TeV, minimum bias, $N_{ch} \geq 6$	$\frac{1}{N_{evt}} \frac{dN_{ev}}{dN_{ch}}$	≥ 40	100.0
ATLAS 7 TeV, minimum bias, $N_{ch} \geq 6$	$\langle p_\perp \rangle$ vs. N_{ch}	≥ 10	10.0
ATLAS 0.9 TeV, UE	$\langle \frac{\mathrm{d}^2 N_{\mathrm{chg}}}{\mathrm{d}\eta \mathrm{d}\phi} \rangle$ (towards)	≥ 5.5 GeV	10.0
ATLAS 0.9 TeV, UE	$\langle \frac{\mathrm{d}^2 N_{\mathrm{chg}}}{\mathrm{d}\eta \mathrm{d}\phi} \rangle$ (transverse)	≥ 5.5 GeV	10.0
ATLAS 0.9 TeV, UE	$\langle \frac{\mathrm{d}^2 N_{\mathrm{chg}}}{\mathrm{d}\eta \mathrm{d}\phi} \rangle$ (away)	≥ 5.5 GeV	10.0
ATLAS 0.9 TeV, UE	$\langle \frac{\mathrm{d}^2 \sum p_\perp}{\mathrm{d}\eta \mathrm{d}\phi} \rangle$ (towards)	≥ 5.5 GeV	10.0
ATLAS 0.9 TeV, UE	$\langle \frac{\mathrm{d}^2 \sum p_\perp}{\mathrm{d}\eta \mathrm{d}\phi} \rangle$ (transverse)	≥ 5.5 GeV	10.0
ATLAS 0.9 TeV, UE	$\langle \frac{\mathrm{d}^2 \sum p_\perp}{\mathrm{d}\eta \mathrm{d}\phi} \rangle$ (away)	≥ 5.5 GeV	10.0
ATLAS 7 TeV, UE	$\langle \frac{\mathrm{d}^2 N_{\mathrm{chg}}}{\mathrm{d}\eta \mathrm{d}\phi} \rangle$ (towards)	≥ 10 GeV	10.0
ATLAS 7 TeV, UE	$\langle \frac{\mathrm{d}^2 N_{\mathrm{chg}}}{\mathrm{d}\eta \mathrm{d}\phi} \rangle$ (transverse)	≥ 10 GeV	10.0
ATLAS 7 TeV, UE	$\langle \frac{\mathrm{d}^2 N_{\mathrm{chg}}}{\mathrm{d}\eta \mathrm{d}\phi} \rangle$ (away)	≥ 10 GeV	10.0
ATLAS 7 TeV, UE	$\langle \frac{\mathrm{d}^2 \sum p_\perp}{\mathrm{d}\eta \mathrm{d}\phi} \rangle$ (towards)	≥ 10 GeV	10.0
ATLAS 7 TeV, UE	$\langle \frac{\mathrm{d}^2 \sum p_\perp}{\mathrm{d}\eta \mathrm{d}\phi} \rangle$ (transverse)	≥ 10 GeV	10.0
ATLAS 7 TeV, UE	$\langle \frac{\mathrm{d}^2 \sum p_\perp}{\mathrm{d}\eta \mathrm{d}\phi} \rangle$ (away)	≥ 10 GeV	10.0

Table 7.2: ATLAS datasets and ranges used in the tuning.

Observable	weight
CDF Run I underlying event in dijet events [28] (leading jet analysis)	
N_{ch} density vs leading jet p_T (transverse), JET20	1.0
N_{ch} density vs leading jet p_T (toward), JET20	1.0
N_{ch} density vs leading jet p_T (away), JET20	1.0
$\sum p_T$ density vs leading jet p_T (transverse), JET20	1.0
$\sum p_T$ density vs leading jet p_T (toward), JET20	1.0
$\sum p_T$ density vs leading jet p_T (away), JET20	1.0
N_{ch} density vs leading jet p_T (transverse), min bias	1.0
N_{ch} density vs leading jet p_T (toward), min bias	1.0
N_{ch} density vs leading jet p_T (away), min bias	1.0
$\sum p_T$ density vs leading jet p_T (transverse), min bias	1.0
$\sum p_T$ density vs leading jet p_T (toward), min bias	1.0
$\sum p_T$ density vs leading jet p_T (away), min bias	1.0
p_T distribution (transverse), leading $p_T > 5$ GeV	1.0
p_T distribution (transverse), leading $p_T > 30$ GeV	1.0
CDF Run I underlying event in MIN/MAX-cones [27] ("MIN-MAX" analysis)	
$\langle p_T^{\text{max}} \rangle$ vs. E_T^{lead}, $\sqrt{s} = 1800\,\text{GeV}$	1.0
$\langle p_T^{\text{min}} \rangle$ vs. E_T^{lead}, $\sqrt{s} = 1800\,\text{GeV}$	1.0
$\langle p_T^{\text{diff}} \rangle$ vs. E_T^{lead}, $\sqrt{s} = 1800\,\text{GeV}$	1.0
$\langle N_{\text{max}} \rangle$ vs. E_T^{lead}, $\sqrt{s} = 1800\,\text{GeV}$	1.0
$\langle N_{\text{min}} \rangle$ vs. E_T^{lead}, $\sqrt{s} = 1800\,\text{GeV}$	1.0
Swiss Cheese p_T^{sum} vs. E_T^{lead} (2 jets), $\sqrt{s} = 1800\,\text{GeV}$	1.0
$\langle p_T^{\text{max}} \rangle$ vs. E_T^{lead}, $\sqrt{s} = 630\,\text{GeV}$	1.0
$\langle p_T^{\text{min}} \rangle$ vs. E_T^{lead}, $\sqrt{s} = 630\,\text{GeV}$	1.0
$\langle p_T^{\text{diff}} \rangle$ vs. E_T^{lead}, $\sqrt{s} = 630\,\text{GeV}$	1.0
Swiss Cheese p_T^{sum} vs. E_T^{lead} (2 jets), $\sqrt{s} = 630\,\text{GeV}$	1.0
D0 Run II dijet angular correlations [149]	
Dijet azimuthal angle, $p_T^{\text{max}} \in [75, 100]$ GeV	1.0
Dijet azimuthal angle, $p_T^{\text{max}} \in [100, 130]$ GeV	1.0
Dijet azimuthal angle, $p_T^{\text{max}} \in [130, 180]$ GeV	1.0
Dijet azimuthal angle, $p_T^{\text{max}} > 180$ GeV	1.0
CDF Run II minimum bias [138]	
$\langle p_\perp \rangle$ of charged particles vs. N_{ch}, $\sqrt{s} = 1960\,\text{GeV}$	0.2
CDF Run I Z $p_\perp$ [150]	
$\frac{d\sigma}{dp_\perp^Z}$, $\sqrt{s} = 1800\,\text{GeV}$	5.0

Table 7.3: Non-ATLAS datasets used in the tuning. No specific cuts on the tuning ranges were made.

Parameter	MC09c value	scanning range	tuned value
PARP(62)	1.0	fixed	1.025
PARP(93)	5.0	fixed	10.0
PARP(77)	0.0	0.25 — 1.15	1.016
PARP(78)	0.224	0.2 — 0.6	0.538
PARP(82)	2.31	2.1 — 2.5	2.292
PARP(83)	0.8	fixed	0.356
PARP(84)	0.7	0.0 — 1.0	0.651
PARP(90)	0.2487	0.18 — 0.28	0.250

Table 7.4: Scanning ranges and tuned parameters for the main tune.

7.2 Tuning results

7.2.1 Central tune values

The chosen scanning ranges for random sampling and the resulting set of parameters minimising the χ^2 for the main tune are listed in Table 7.4. None of the tuning parameters are in a region of extrapolation, i.e. outside the sampling boundaries. Compared to MC09c, the new tune prefers very similar values of PARP(82) and PARP(90). Regarding the colour reconnection parameters, clearly a non-zero value of PARP(77) is preferred. The matter overlap parameters PARP(83) and PARP(84) were not tuned in deriving MC09c, so it is not surprising that different values are preferred in the new tune.

7.2.2 Stability of tuning results

The stability of the tuning results was checked by a sub-sample test: Whereas for the derivation of the central values all 152 completed random parameter space samplings have been used to derive the interpolation, here 100 different combinations of only 117 points have been used to derive the interpolation. For each of these interpolations the minimisation has been made. The resulting parameter values are shown in Figure 7.1. A small scattering of the resulting tuned values corresponds to a very good constraint on the parameter in question. This is the case for example for PARP(82) and PARP(90) – these parameters are very well constrained by the chosen datasets. On the other hand a large spread of the tuned parameter means that only a small sensitivity on the parameter has been achieved. It seems that this is the case for PARP(77) and PARP(78), but this is misleading: As shown in Figure 7.2, these two parameters are strongly correlated with each other. This means that in principle one of them can be traded of with the other. Overall the tuning results are rather stable and also safely within the chosen sampling ranges.

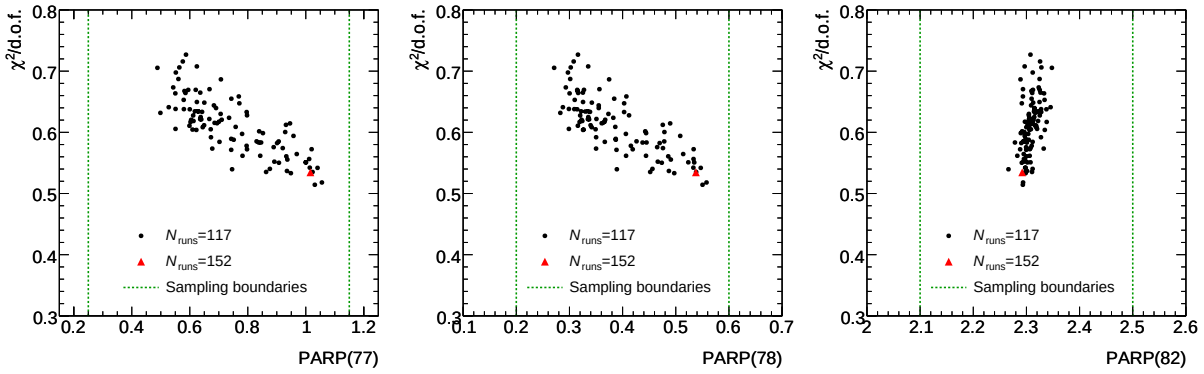

(a) Tune results for PARP(77) **(b)** Tune results for PARP(78) **(c)** Tune results for PARP(82)

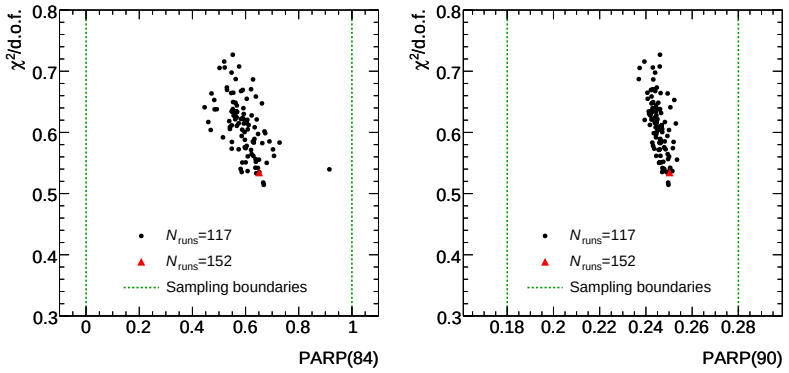

(d) Tune results for PARP(84) **(e)** Tune results for PARP(90)

Figure 7.1: Tuning results for a cubic interpolation of the generator response using all 152 completed generator runs (red circles) and using subsets of 117 generator runs (black crosses).

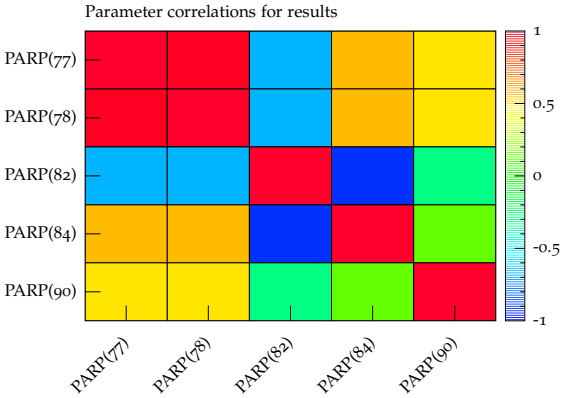

Figure 7.2: Correlation between tune results for individual tune parameters.

7.3 Comparison to experimental data

In this section the new tuned (dubbed Atlas Minimum Bias Tune 1 – AMBT1) is compared to experimental measurements and several other PYTHIA 6 tunes. Most of the data have been used as input for obtaining the tune, cf. Tables 7.2 and 7.3. ATLAS data were used with very high weights, to ensure that the ATLAS data is well described by the AMBT1 tune.

7.3.1 ATLAS results

ATLAS Minimum Bias, $n_{ch} \geq 6$

This dataset is described in Section 6.2 and consists of the same analysis as in [141], but with an additional requirement on the number of selected charged primary particles ($p_\perp > 500\,\text{MeV}, |\eta| < 2.5$) of at least six. This requirement ensures that the diffractive component is reduced sufficiently.

The comparison of the tunes with the data is shown in Figure 7.3 for 900 GeV and in Figure 7.4 for 7 TeV.

As it is designed for, the AMBT1 tune gives a largely improved description of the data, especially at 7 TeV, as it is the only tune where these data were used. Still, especially at 7 TeV the transverse momentum distribution deviates about 40% from the data. The source of this is under investigation, it should be noted that all tunes using the $p_\perp$-ordered parton shower in PYTHIA 6 show a similar behaviour.

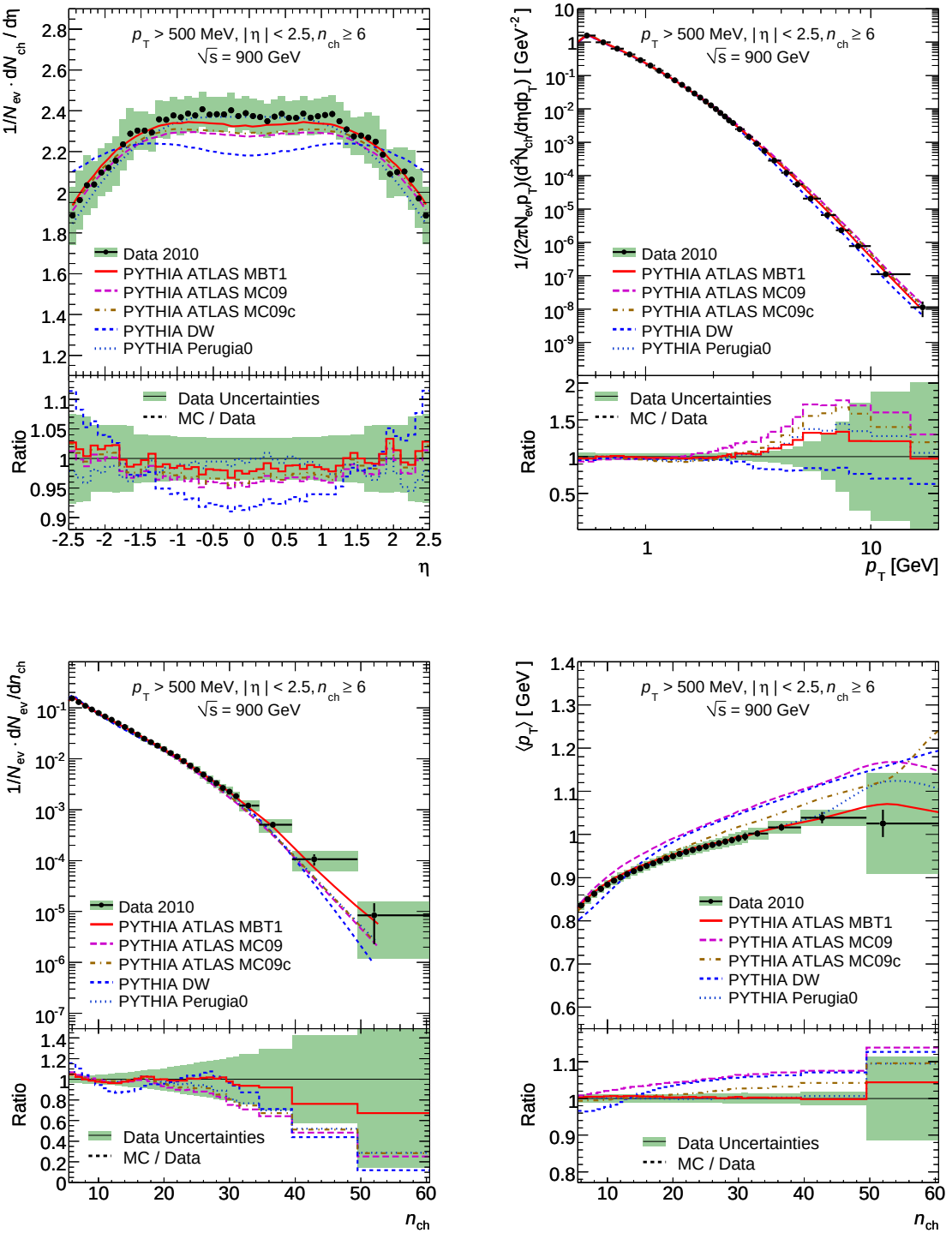

Figure 7.3: ATLAS minimum bias distributions for $\sqrt{s} = 900\,\text{GeV}$, $n_{ch} \geq 6$.

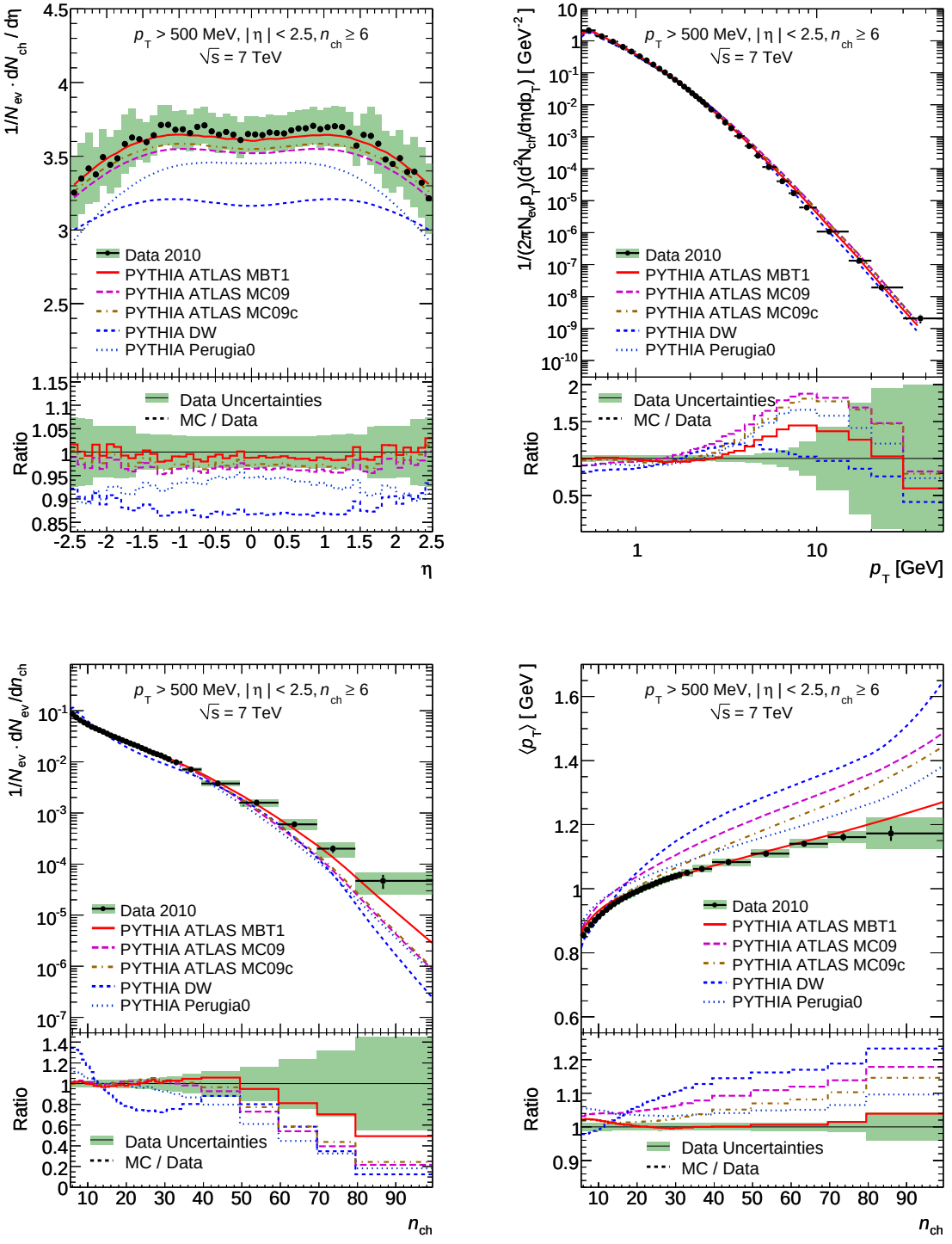

Figure 7.4: ATLAS minimum bias distributions for $\sqrt{s} = 7\,\text{TeV}$, $n_{ch} \geq 6$.

ATLAS Underlying Event with leading tracks, 900 GeV and 7 TeV.

The ATLAS measurement of the underlying event is described in more detail in Section 6.3. Similar to the CDF measurements of the underlying event, the event is divided into three different regions, but in this analysis the leading track is used to define the towards region. Observables reported in the measurement and used in the tuning are the charged particle densities and transverse momentum sum densities in the three regions. Other measurements, e.g. of the average transverse momentum in dependence of the number of charged particles were not considered in this round of tuning, since they were not ready at the time the input set for the tune was fixed.

The comparison of the tunes with the data is shown in Figures 7.5 to 7.6. It should be noted that only the final plateau region was used for the AMBT1 tune, as it seems to be difficult to describe the turn-on region properly. The tunes show an about 10% discrepancy with the data in this region. The source of this discrepancy is under investigation. Contrary to the ATLAS minimum bias measurement, the AMBT1 tune does not give as large improvements in this Underlying Event analysis.

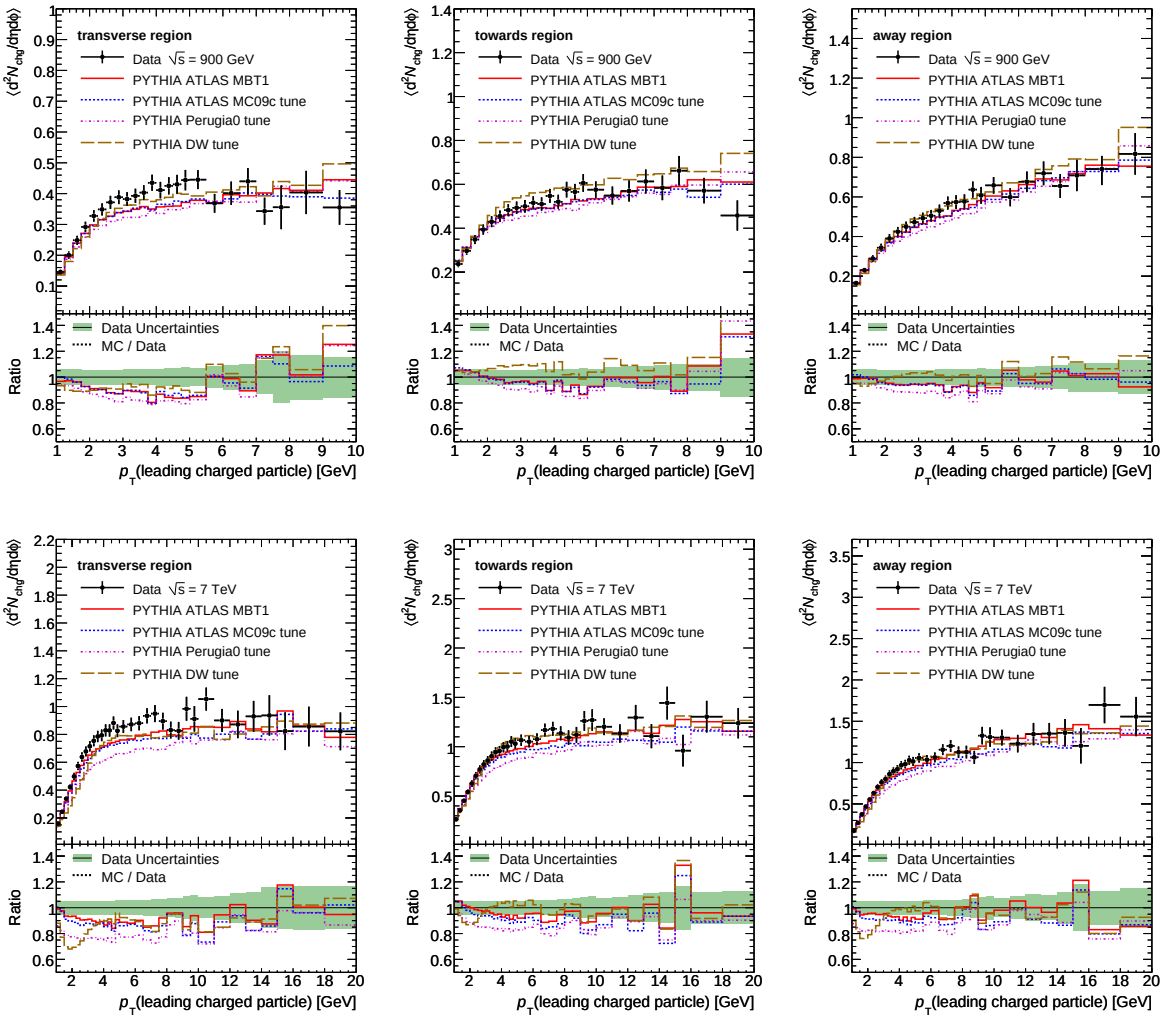

Figure 7.5: ATLAS Underlying event analysis: Charged particle density in the region transverse to, towards to and away from the leading track at $\sqrt{s} = 900$ GeV and $\sqrt{s} = 7$ TeV.

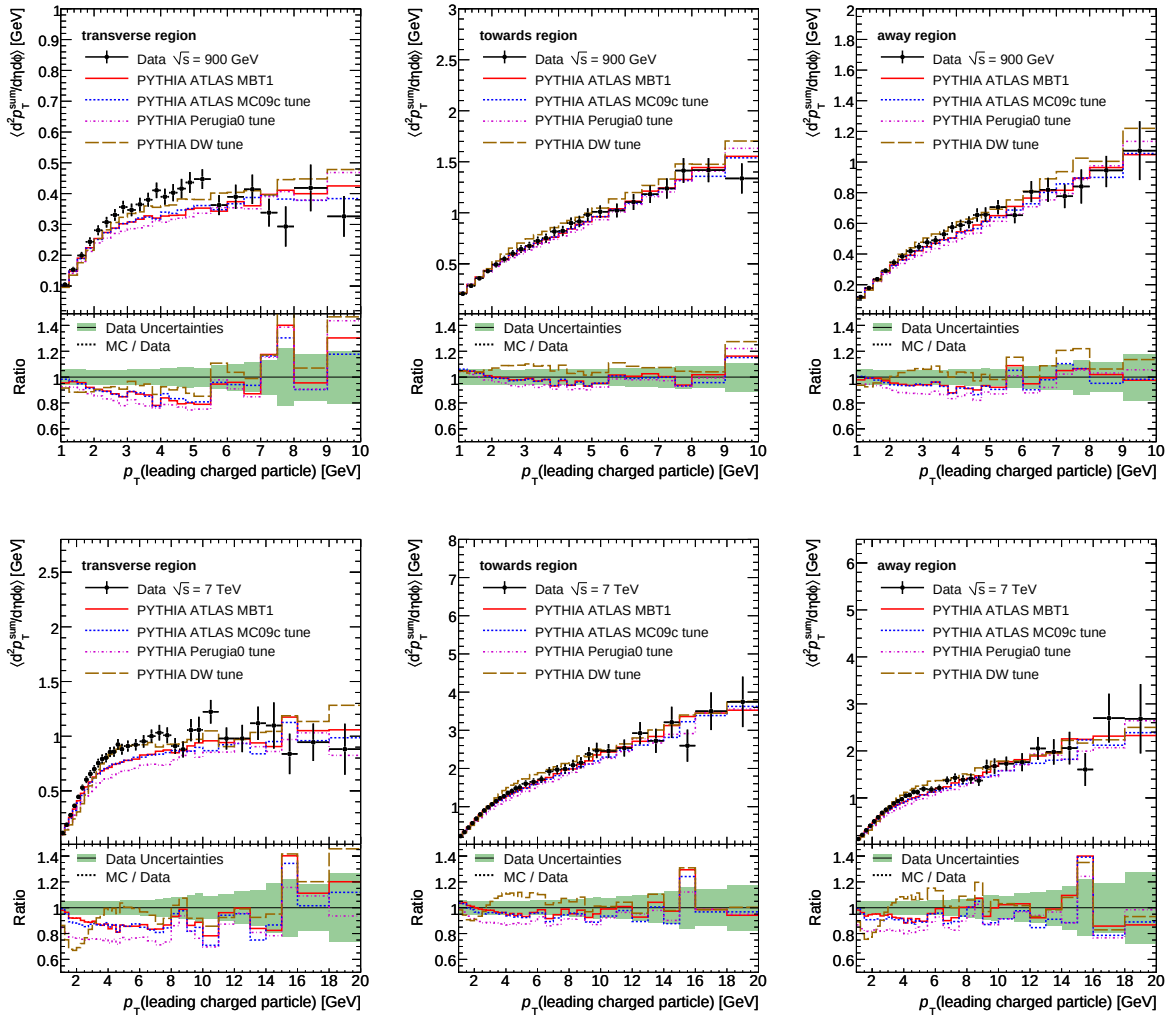

Figure 7.6: ATLAS Underlying event analysis: Charged particle transverse momentum sum density in the region transverse to, towards to and away from the leading track at $\sqrt{s} = 900$ GeV and $\sqrt{s} = 7$ TeV.

7.3.2 Comparison to Tevatron data used in the tuning

In this section the generator output of the derived AMBT1 tune is compared to the various Tevatron datasets that were used at the tuning stage. The results are in each case compared to the MC09c and the Perugia0 tune.

CDF Run 1 Leading Jets

Details of this analysis by the CDF collaboration can be found in [28]. It uses both low-$p_\perp$ and high-$p_\perp$ QCD multijet events, which are based on two different trigger conditions (minimum bias and JET20 respectively). Reconstructed charged particles are used to reconstruct track-jets, based on a cone algorithm with $\Delta R = 0.7$, within $|\eta| < 1$. This pseudorapidity region is then divided into three regions in azimuthal angle of equal total size: the *towards* region, within 60° of the leading track-jet axis, the *transverse* region, between 60° and 120°, and the *away* region with more than 120° from the leading track-jet. It is expected that the toward region is dominated by the hard interaction. The away region should also receive large contributions from the recoil activity against the leading jet. The transverse region is expected to be very sensitive to the underlying event properties, since it is well separated from the hard interaction, due to kinematic reasons.

The observables published in [28] are the density of charged particles and the mean of the sum of the transverse momentum carried by these in the three regions described. These are measured as a function of the $p_\perp$ of the leading track-jet. The data is corrected for K_S and Λ decays and also for the CDF tracking efficiency. The results of a MC generator based analysis can thus be directly compared to the published data.

The comparison of the tunes are shown in Figures 7.7 to 7.10. All tunes describe the data sufficiently well, the AMBT1 tune slightly overestimates the multiplicity in the towards region, but not by much.

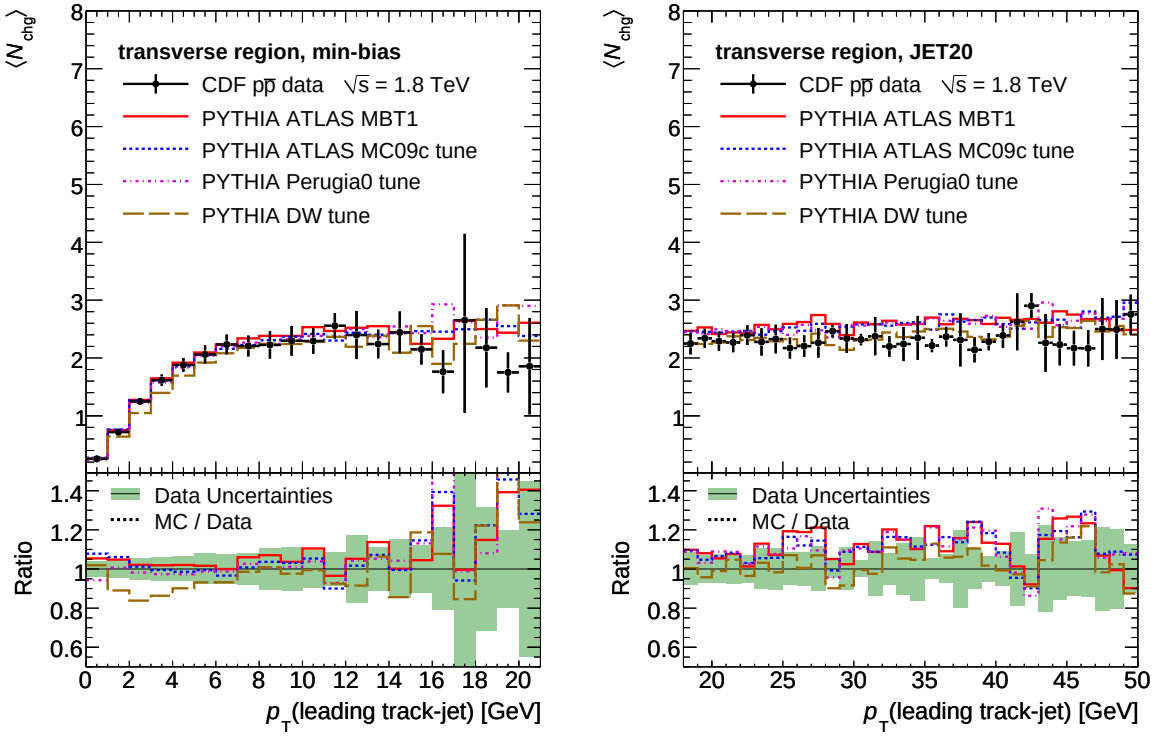

(a) Mean charged multiplicity in the transverse region vs. $p_\perp$ of the leading track-jet.

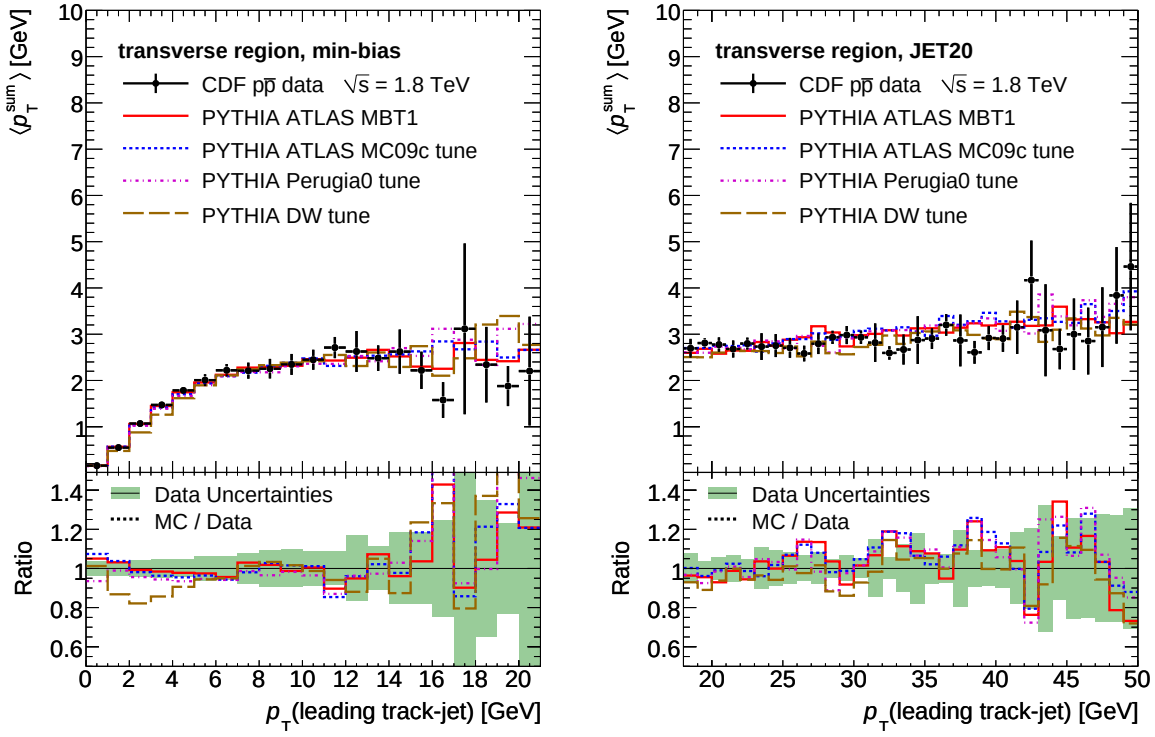

(b) Mean transverse momentum sum in the transverse region vs. $p_\perp$ of the leading track-jet.

Figure 7.7: Comparison of tunes to data from the CDF experiment [28].

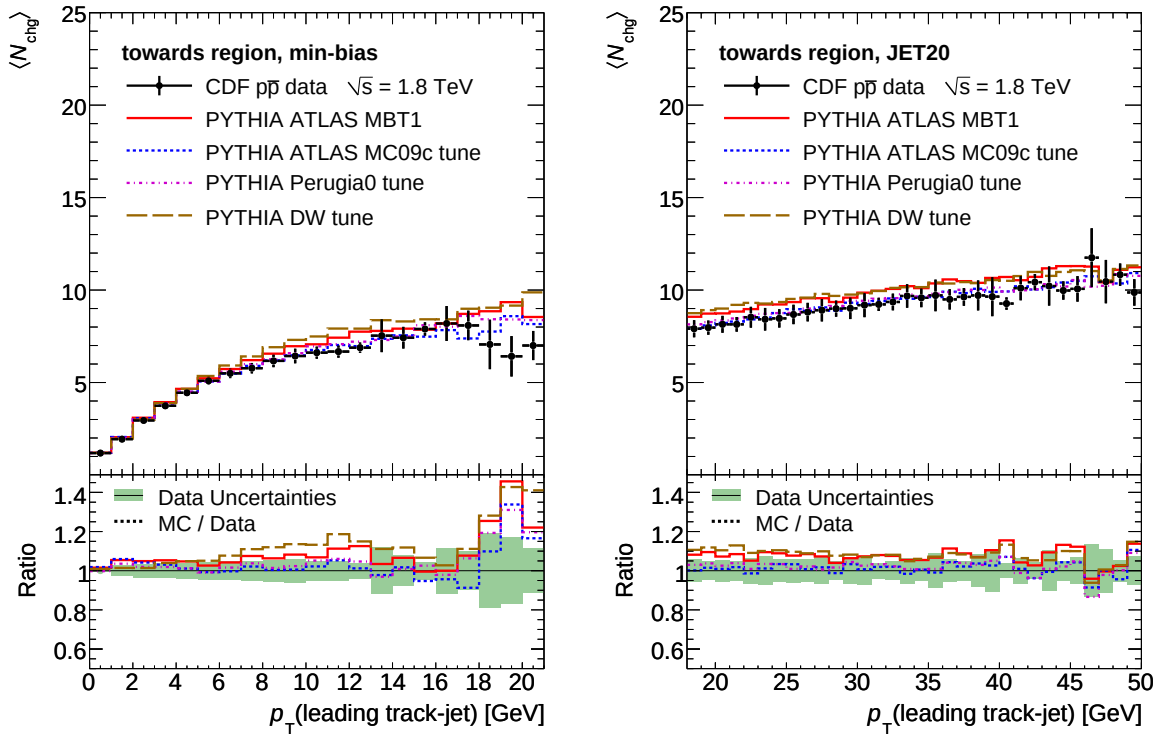

(a) Mean charged multiplicity in the toward region vs. $p_\perp$ of the leading track-jet.

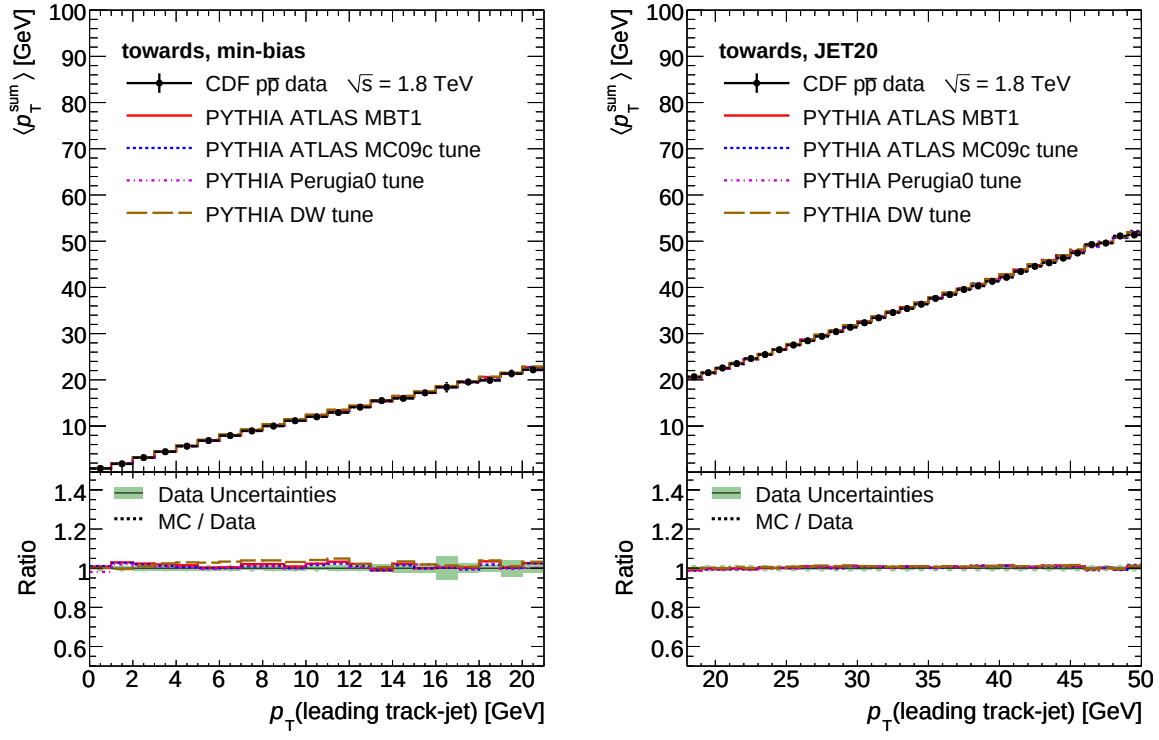

(b) Mean transverse momentum sum in the toward region vs. $p_\perp$ of the leading track-jet.

Figure 7.8: Comparison of tunes to data for the towards region of the leading jet analysis.

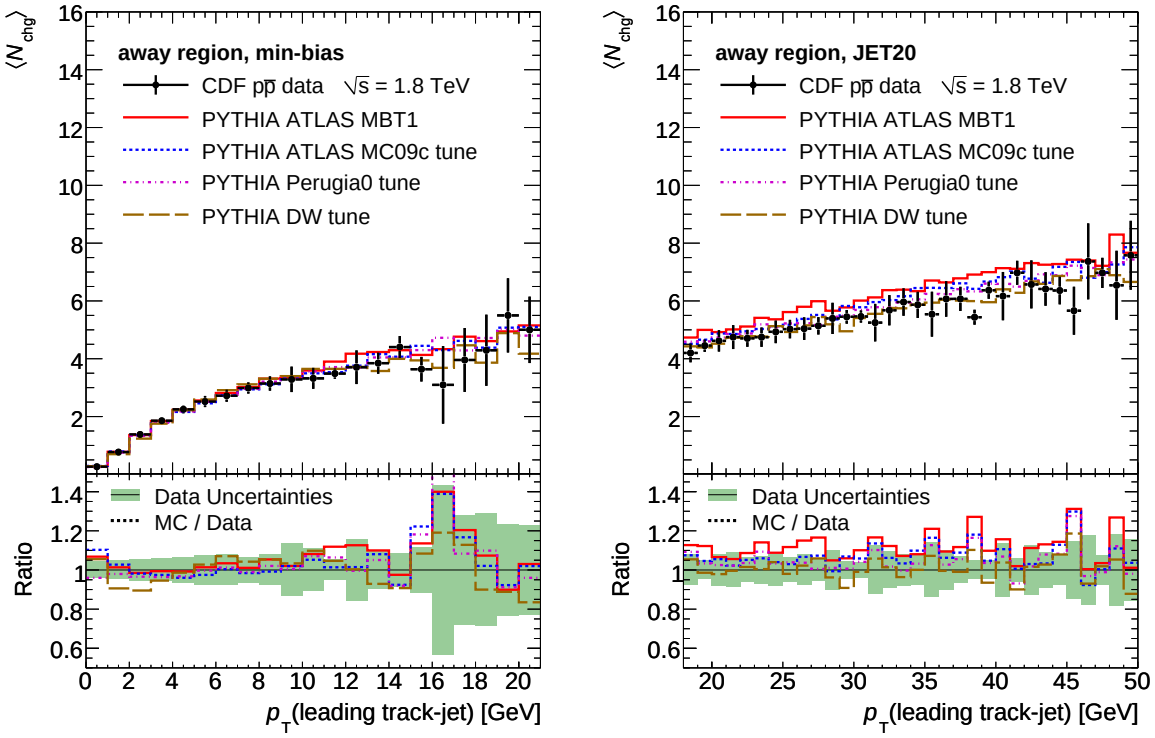

(a) Mean charged multiplicity in the away region vs. $p_\perp$ of the leading track-jet.

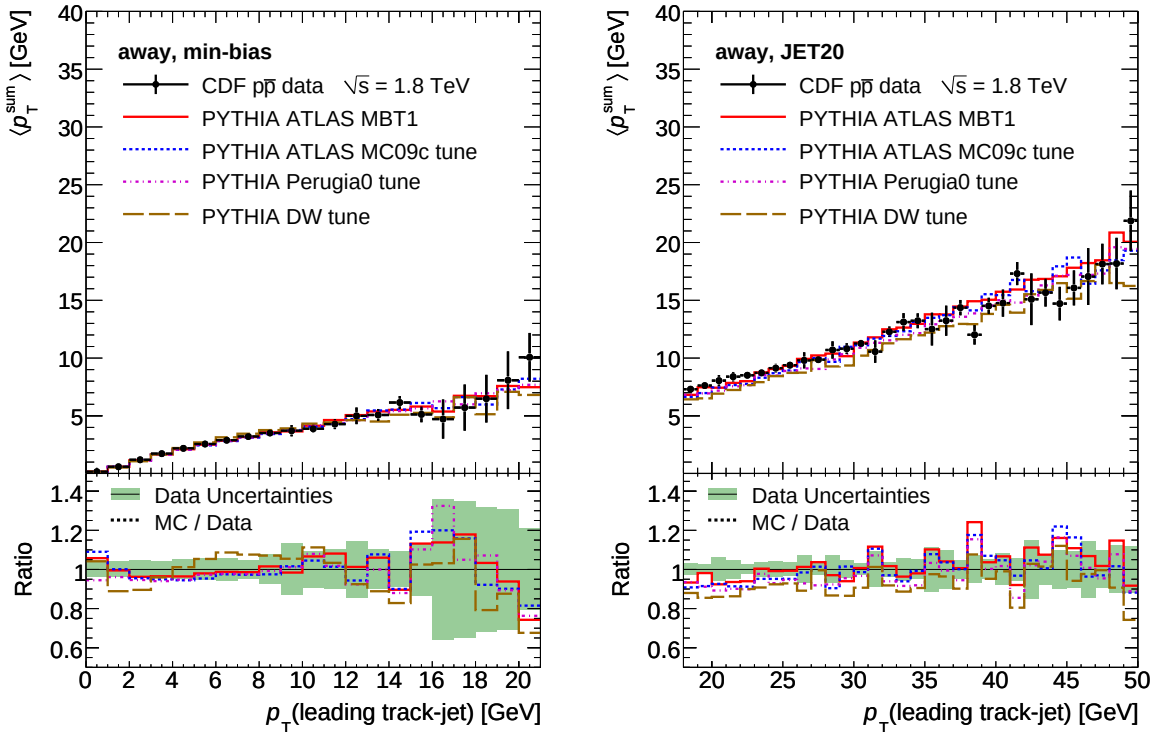

(b) Mean transverse momentum sum in the away region vs. $p_\perp$ of the leading track-jet.

Figure 7.9: Comparison of tunes to data for the away region of the leading jet analysis.

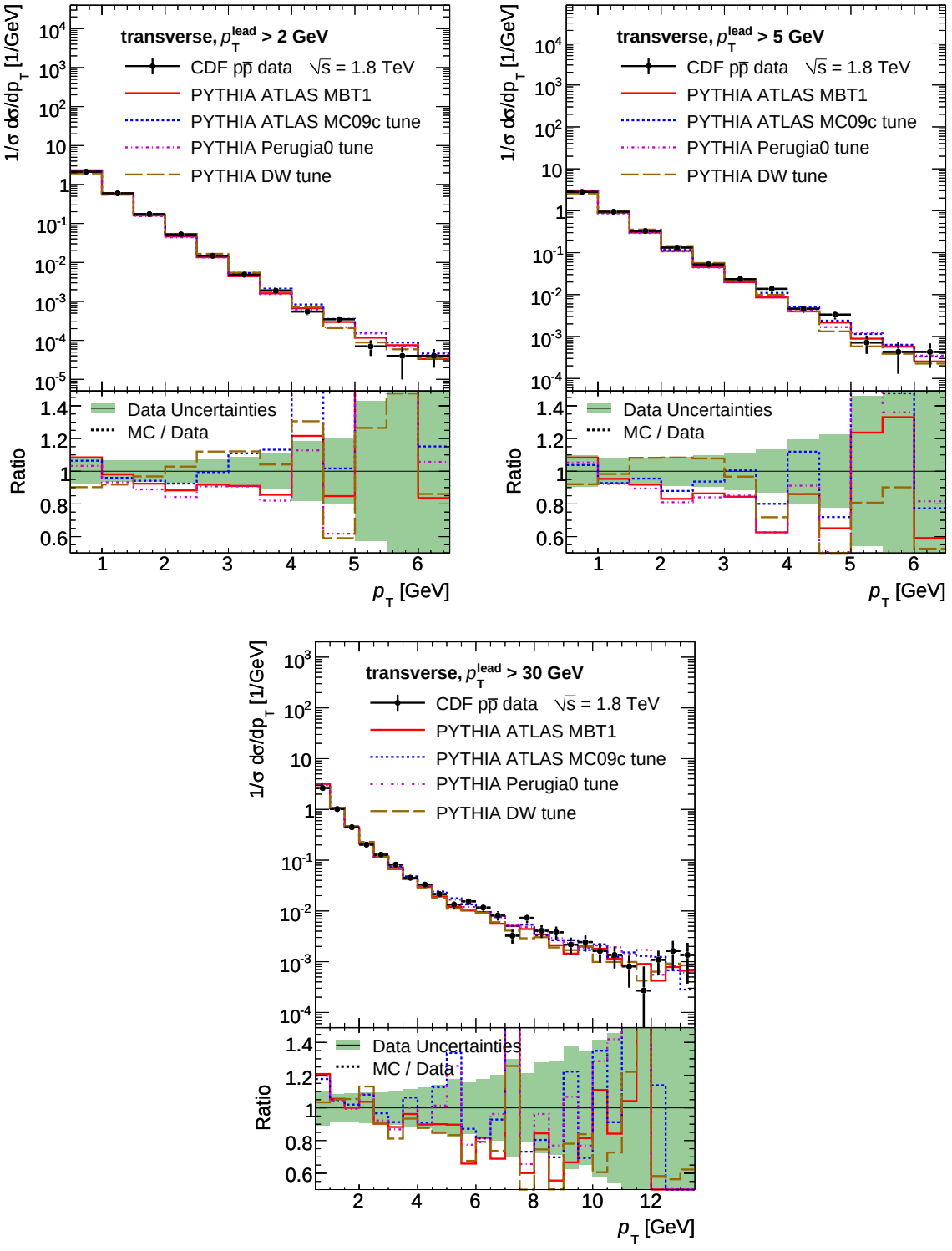

Figure 7.10: Comparison of tunes to data for the transverse momentum spectrum of charged particles in the transverse region, if requiring the leading track-jet to have different minimal transverse momenta.

CDF MIN-MAX analysis

The "MAX-MIN" analysis, published in [27], uses a similar approach to the leading jet analysis. In this case the leading jet is reconstructed as a calorimeter jet (cone 0.7), thus taking also the neutral particles into account. The transverse region is then defined by means of two cones ($\Delta R = 0.7$) perpendicular to the leading jet, but at the same pseudorapidity. The two cones are divided into a MAX cone and a MIN cone according to the scalar sum of transverse momenta of reconstructed charged particles in each cone. The observables that can be used for tuning are the mean number of charged particles in the two cones and the mean transverse momentum sum in the cones, and also the mean difference between the transverse momenta sums of the two cones. These observables are measured as function of the E_{T} of the leading jet and are available at $\sqrt{s} = 1800\,\mathrm{GeV}$ and $630\,\mathrm{GeV}$, but at the lower center-of-mass energy, the charged multiplicity in the MAX and MIN cone is not included in [27].

Comparisons between the tunes and the used observables from this analysis are shown in Figures 7.12 to 7.14. The description of the data is overall satisfactory for all three tunes.

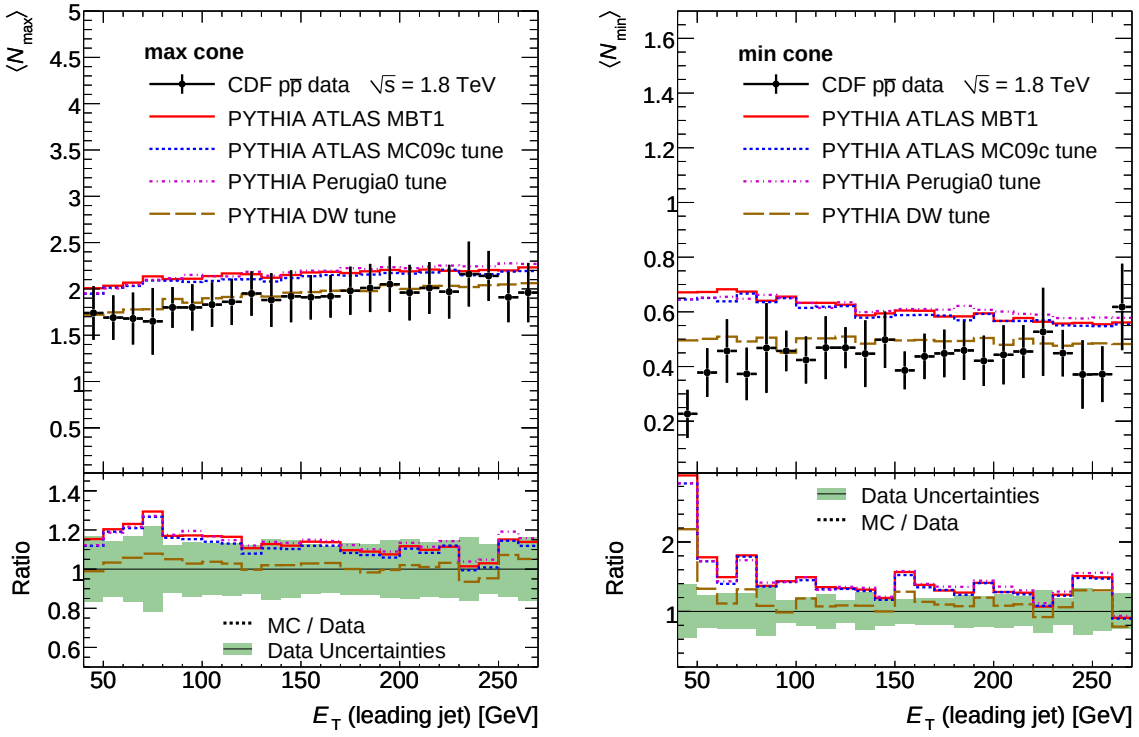

Figure 7.11: Mean charged particle density vs. E_{T} of the leading jet in $p\bar{p}$ collisions at $\sqrt{s} = 1.8\,\mathrm{TeV}$ as described in the text and in [27]. Left: max cone, right: min cone.

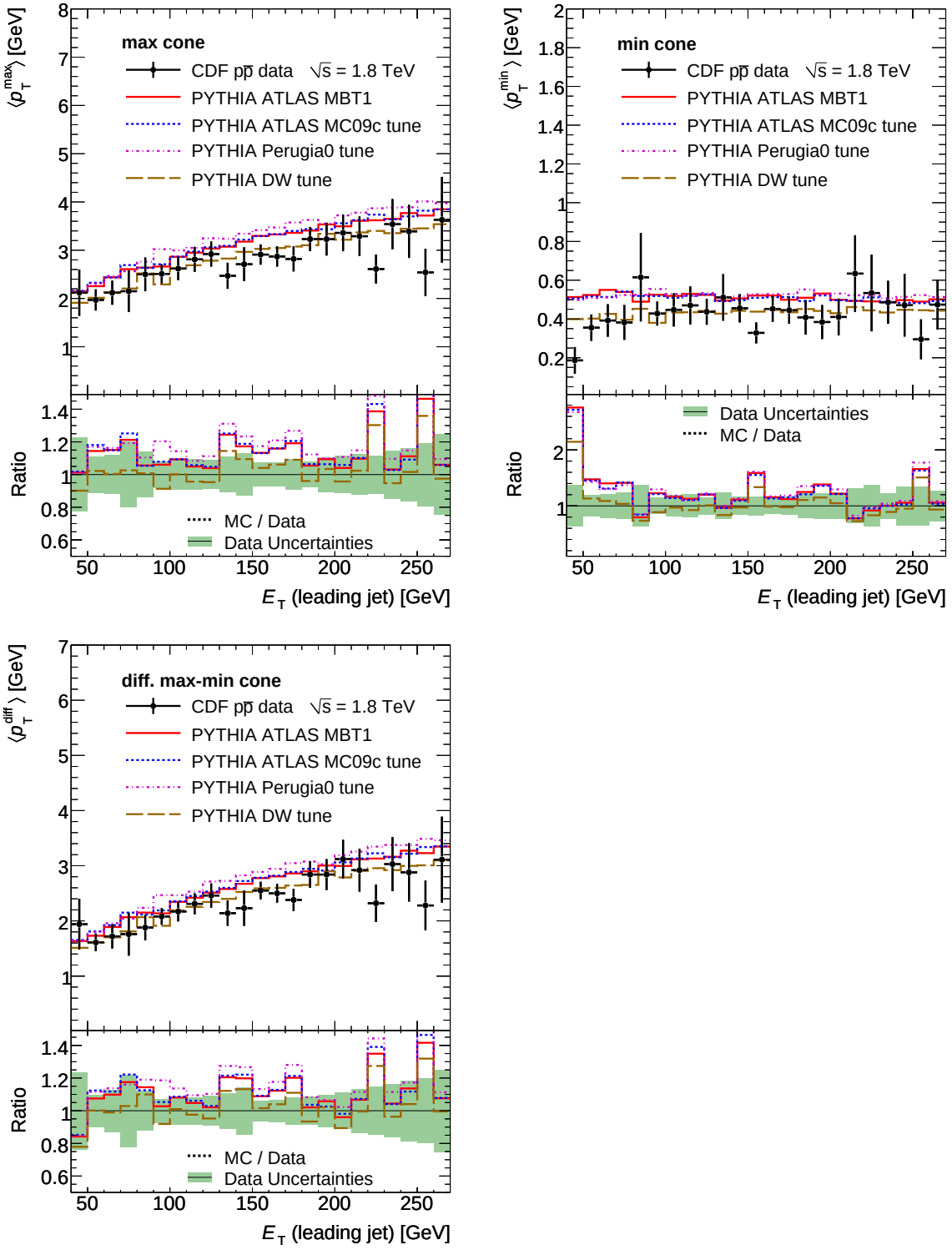

Figure 7.12: Mean charged particle transverse momentum sum vs. E_{T} of the leading jet in $p\bar{p}$ collisions at $\sqrt{s} = 1.8\,\mathrm{TeV}$ as described in the text and in [27]. These data were not used for the MC09 tune. Top left: max cone, top right: min cone, bottom: difference between max and min cone.

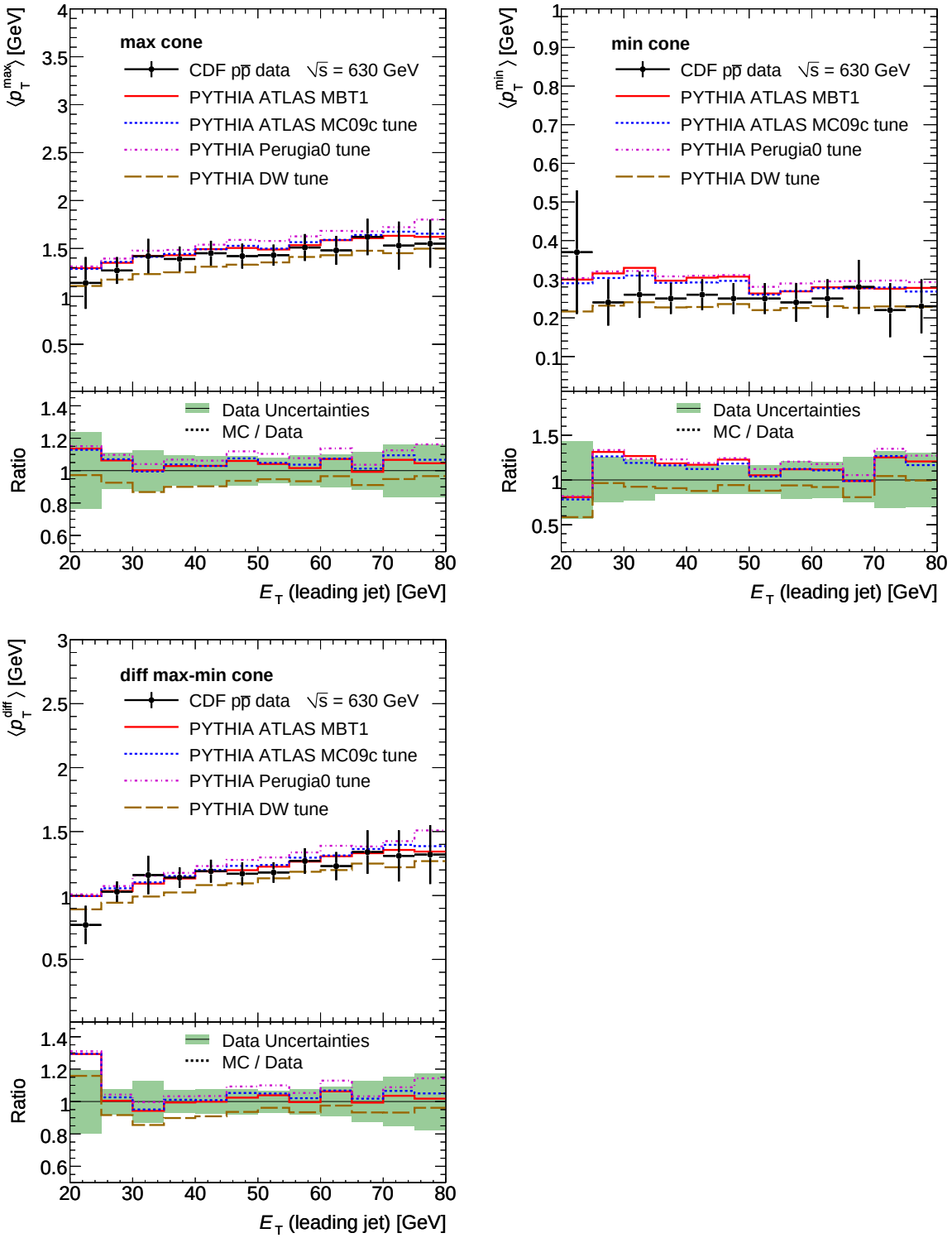

Figure 7.13: Mean charged particle transverse momentum sum vs. E_{T} of the leading jet in $p\bar{p}$ collisions at $\sqrt{s} = 0.63\,\mathrm{TeV}$ as described in the text and in [27]. Top left: max cone, top right: min cone, bottom: difference between max and min cone.

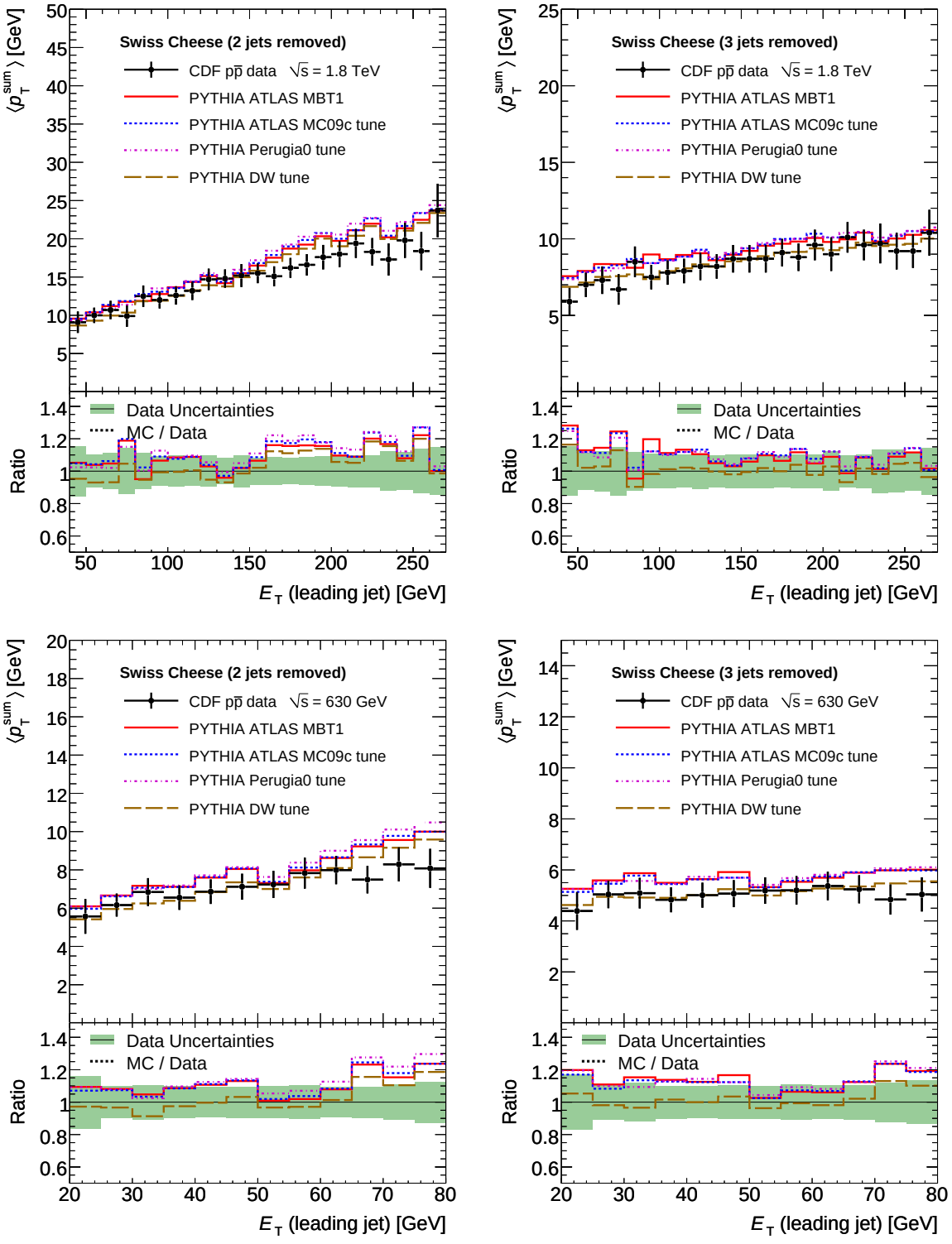

Figure 7.14: "Swiss cheese": Transverse momentum sum when removing 2 jets (left column), and 3 jets (right column) in $p\bar{p}$ collisions at $\sqrt{s} = 0.63\,\text{TeV}$ (bottom row) and 1.8 TeV (top row) as described in [27].

D0 Dijet Angular De-correlations

The DØ collaboration has published a measurement of the azimuthal angle distribution between leading jets in QCD multijet events in [149]. This distribution is very sensitive to extra gluon emissions as they appear in initial state radiation.

A comparison between the tunes and the data is shown in Figure 7.15. It should be noted that no parameters of the initial state parton shower were tuned for the AMBT1 tune.

CDF Z $p_\perp$

This measurement is published by the CDF collaboration in [150] and consists of a measurement of the transverse momentum distribution of Z bosons in Drell-Yan events. The decay mode $Z \to ee$ is used. The low $p_\perp$ part of this distribution is sensitive to the description of the primordial k_T in the proton.

The comparison with the tunes is shown in Figure 7.16. The Perugia0 tune describes the data for small $p_\perp$ slightly better, since the primordial k_T model was tuned there, but not in MC09c or AMBT1.

CDF Minimum Bias Data Run 2

A measurement of minimum bias events by the CDF collaboration has been published in [138]. In particular, the mean track $p_\perp$ is measured as a function of the track multiplicity. This observable is highly sensitive to the colour structure of the event as emphasised e.g. in [151]. As this observable is also included in the ATLAS measurements, it was down-weighted by a factor of 5 in order to ensure that the smaller uncertainties of the CDF measurement do not bias the result of the tune towards the CDF measurement.

The comparison between the tunes and the data is shown in Figure 7.17. AMBT1 is slightly below the CDF measurement, but only by about 2%. As AMBT1 can describe the ATLAS data well, this points to a small tension between the CDF and ATLAS measurements of this observable.

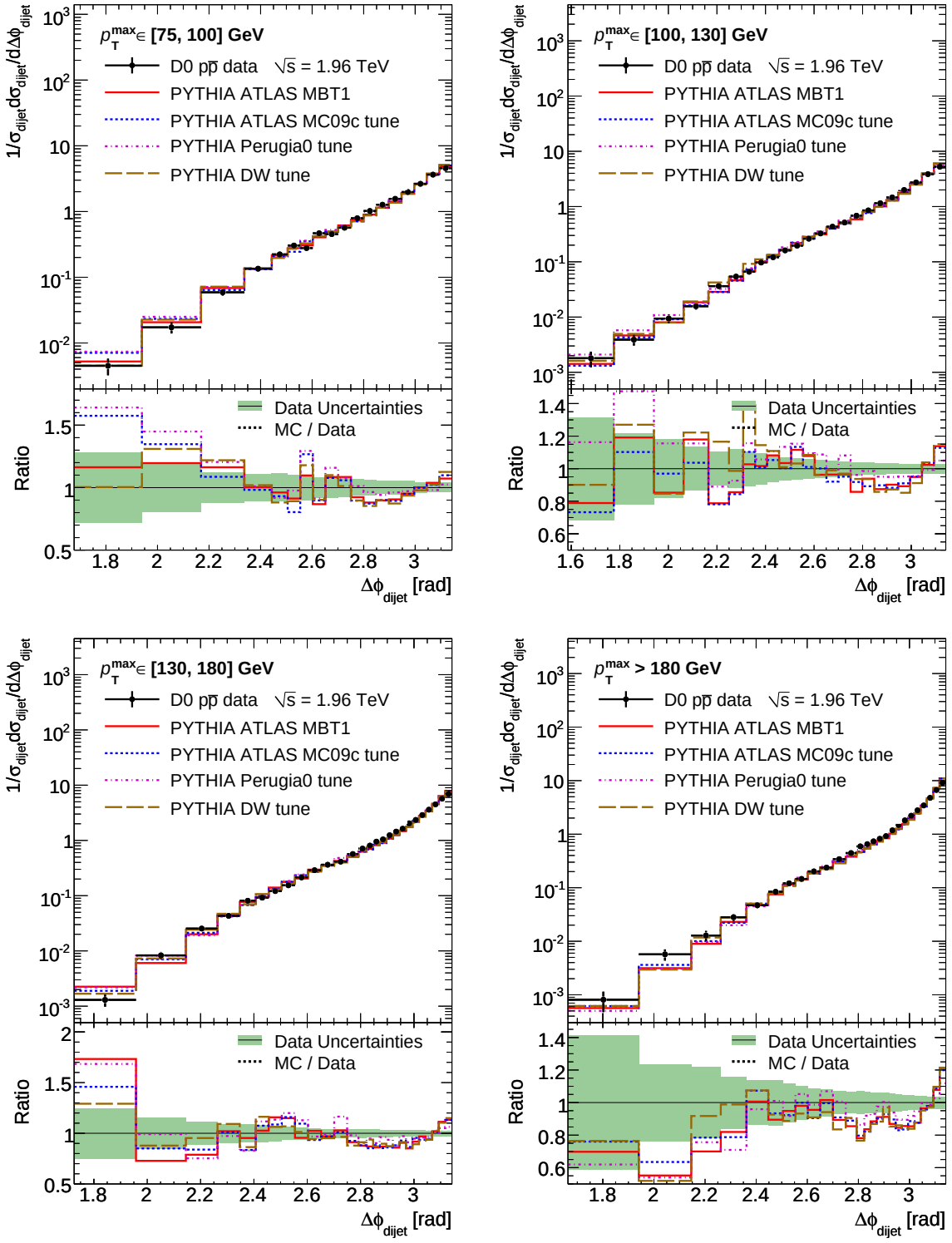

Figure 7.15: Azimuthal angle between the two leading jets in $p\bar{p}$ collisions at $\sqrt{s} = 1.96\,\text{TeV}$. Top left: $p_\perp$ of the leading jet between 75 and 100 GeV, top right: 100 to 130 GeV, bottom left: 130 to 180 GeV, bottom right: more than 180 GeV. The data points show the measurement by the DØ collaboration [149]. These distributions were not used in the MC09 tune.

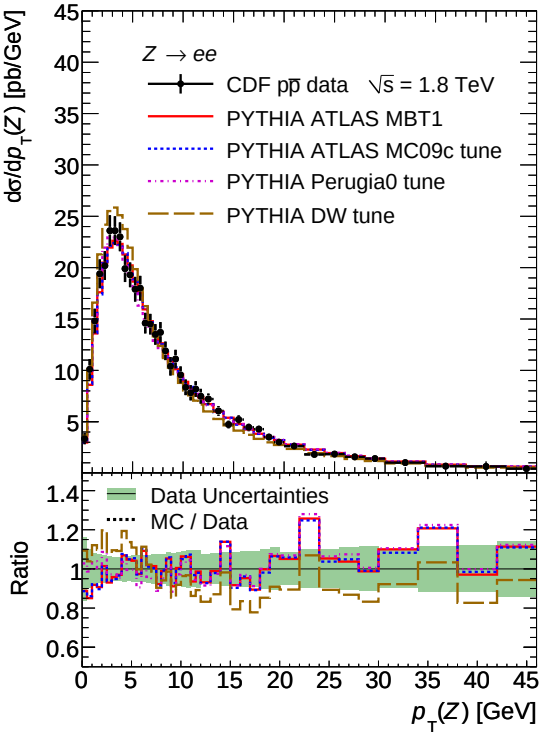

Figure 7.16: Transverse momentum distribution of Z bosons normalised to the measured cross section in Drell-Yan events in $p\bar{p}$ collisions at $\sqrt{s} = 1.8\,\text{TeV}$ as described in the text and in [150]. This distribution was not used in the MC09 tune.

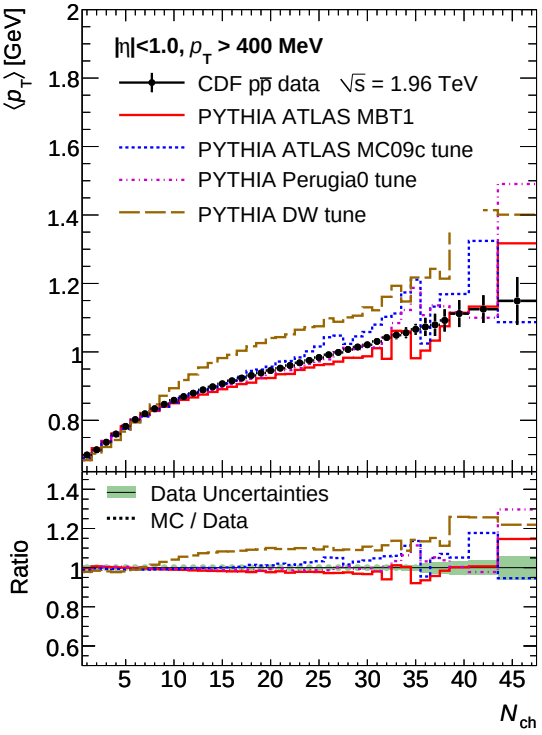

Figure 7.17: Mean charged particle transverse momentum vs. the charged multiplicity in $p\bar{p}$ collisions at $\sqrt{s} = 1.96\,\text{TeV}$. The data points show the measurement by the CDF collaboration [138].

7.3.3 Comparison to CDF Minimum Bias Run 1 (not used in the tuning)

This analysis was published by the CDF collaboration in [152]. It consists of a dataset of minimum bias events, as defined by the CDF trigger system. The observables are the charged multiplicities with $|\eta| < 1$ and $p_\perp > 0.4\,\text{GeV}$ for $\sqrt{s} = 1800\,\text{GeV}$ and 630 GeV. The same corrections as for the leading jet analysis, see Section 7.3.2 are applied. This analysis is very important for the tuning procedure, as it provides data at a significantly different center-of-mass energy compared to 1.8 TeV.

A comparison between the different tunes and the data is shown in Figure 7.18. The AMBT1 tune overestimates the high multiplicity tail. It should be noted that this distribution was not used in the tuning of AMBT1 because of the obvious tension between the CDF and ATLAS datasets. The ATLAS data prefer a tune predicting a higher multiplicity tail than the CDF data. Currently no tune describing both distributions simultaneously was achieved, the source of this discrepancy is under investigation. It should be mentioned that it is not clear, whether the normalisation of the Monte Carlo is correct in this analysis, as the data has been corrected for diffractive processes present after event selection. However, this should only affect the lowest few multiplicity bins and the overall normalisation. But the discrepancy is also present at large multiplicities. This might be due to the differences in the matter overlap distributions between AMBT1 and MC09c, but this change was necessary to describe the ATLAS data.

This behaviour was explored further by performing a second tune using PROFESSOR, where the two observables shown in Figure 7.18 were included in the calculation of the χ^2. For both multiplicity distributions only the part with $N_{ch} \geq 10$ was used. The data at 630 GeV were given a weight of 10, the one at 1800 GeV a weight of 100. The influence on this is shown in Figure 7.19 for the CDF and ATLAS multiplicity measurements.

Clearly including the CDF data in the tune gives a better description of these data, but at the same time the ATLAS data is described worse. This shows that at least for the chosen tuning setup, there is a tension between these two data-sets. Whether this can be solved with other parameter settings has to be explored in the future.

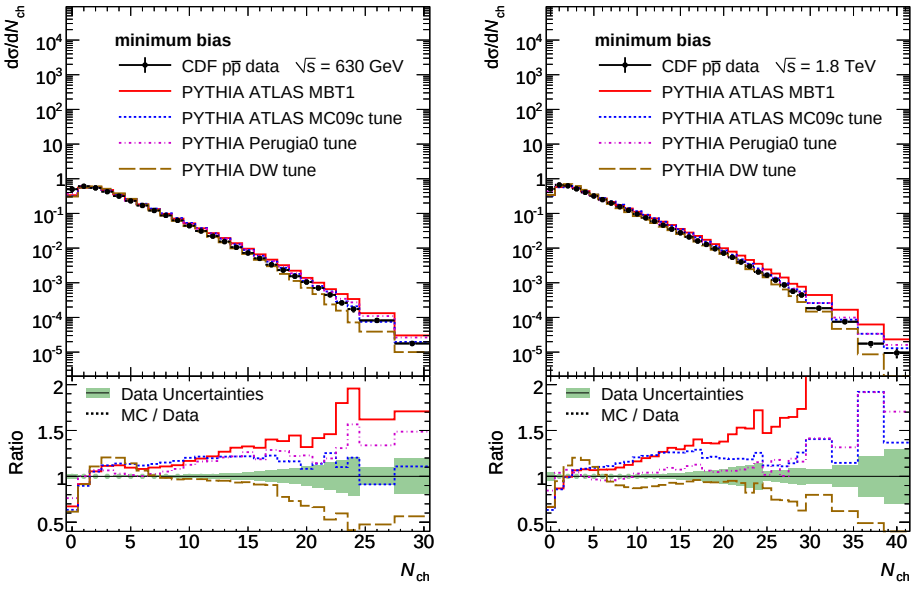

Figure 7.18: Charged multiplicity in minimum bias events [152]. Left: $\sqrt{s} = 630\,\text{GeV}$, right: $\sqrt{s} = 1800\,\text{GeV}$.

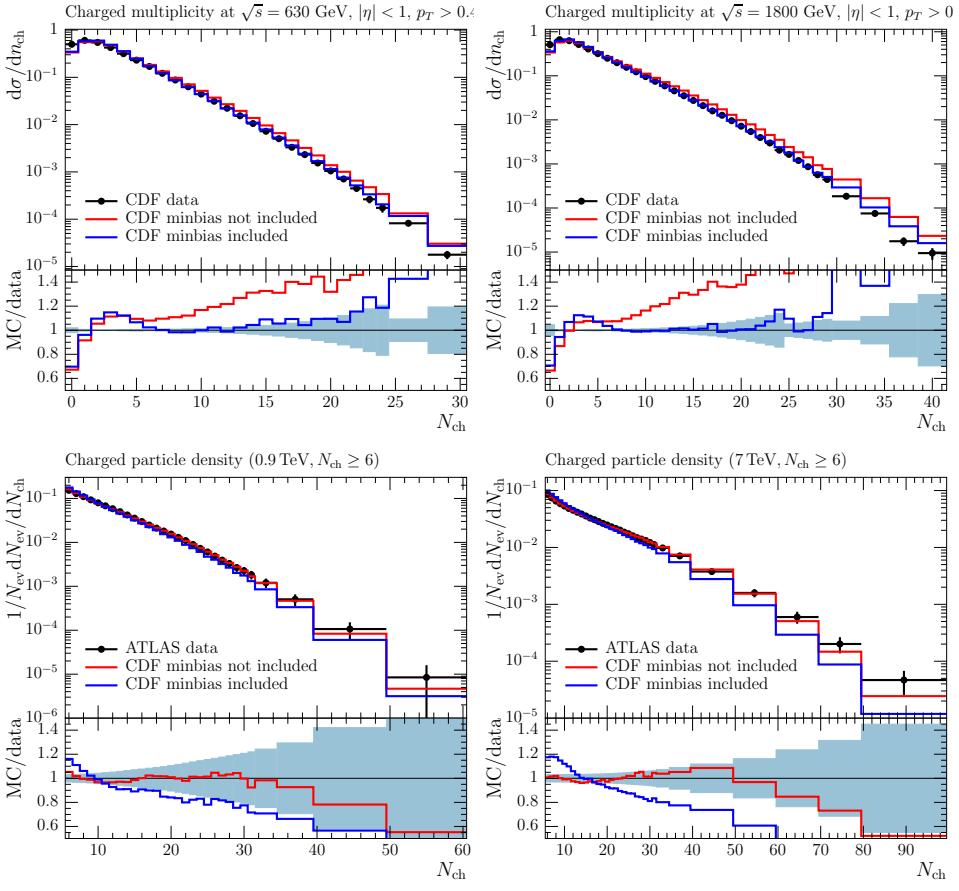

Figure 7.19: Tension in the charged multiplicity in minimum bias events at ATLAS and CDF.

8 Conclusions

The second part of this thesis was concerned with the application of Monte-Carlo event generators in the ATLAS experiment, and in particular with the improvement of non-perturbative models using early ATLAS data. It resulted in the first comprehensive tuning of an event generator to minimum bias measurements at LHC energies.

ATLAS was the first experiment to publish measurements in minimum-bias events at the hadron level with minimal model dependence. By defining the event selection purely through hadron level cuts instead of subtracting any less well understood components using Monte-Carlo models, the measurement is fit to be used for improving Monte-Carlo models.

The foundation that made this work possible is the surprisingly accurate understanding of the ATLAS detector right from the first day of data taking. Especially for the correction back to hadron level it was crucial that various parts of the detector worked well and could be described by the ATLAS detector simulation. The detector components of particular relevance for the measurements employed in the tuning have been briefly summarised together with a short overview of the current status of LHC running.

All ATLAS measurements which have been used in the tuning are explained in enough detail and in particular features not present in analyses of other experiments were pointed out. A slight variation of the event selection criterion in an otherwise unmodified second analysis was motivated by the suppression of events dominated by diffractive reactions. Due to this suppression it became possible to tune e.g. models for multiple parton interactions without suffering from the large uncertainty introduced by a parallel application of diffraction models.

The PROFESSOR program was used in the tuning procedure to determine an optimal set of parameters in an automatic and reproducible way. The parameter space was sampled by running the Monte-Carlo program, and PROFESSOR was then used to interpolate the MC to data deviations between the sample points, selecting the point with minimal deviations as optimal parameter set.

In this specific case, the PYTHIA 6 generator has been tuned including parameters

related to multiple parton interactions, colour reconnection and primordial k_T. Significantly improved agreement with ATLAS measurements was observed, while Tevatron data was still described well. In fact the tune has been successful enough to serve as a basis for further tuning efforts outside the ATLAS experiment [153].

In the future it will be important to continue this effort including more data from the LHC and also for other Monte-Carlo programs. One such example is the Herwig event generator, which plays an important role in ATLAS as a systematic cross check for PYTHIA in the unfolding procedure. A corresponding tuning of the HERWIG generator including the JIMMY MPI model has already been done within the ATLAS MC group [154]. Tunes of the SHERPA event generator are planned in the near future.

Bibliography

[1] G. Corcella et al., *HERWIG 6.5 Release Note*, hep-ph/0210213.

[2] T. Sjöstrand, S. Mrenna and P. Skands, *PYTHIA 6.4 physics and manual*, JHEP **05** (2006), 026, [hep-ph/0603175].

[3] M. Bähr et al., *Herwig++ Physics and Manual*, Eur. Phys. J. **C58** (2008), 639–707, [arXiv:0803.0883 [hep-ph]].

[4] T. Sjöstrand, S. Mrenna and P. Skands, *A brief introduction to PYTHIA 8.1*, Comput. Phys. Commun. **178** (2008), 852–867, [arXiv:0710.3820 [hep-ph]].

[5] T. Gleisberg, S. Höche, F. Krauss, A. Schälicke, S. Schumann and J. Winter, *SHERPA 1.α, a proof-of-concept version*, JHEP **02** (2004), 056, [hep-ph/0311263]; T. Gleisberg, S. Höche, F. Krauss, M. Schönherr, S. Schumann, F. Siegert and J. Winter, *Event generation with SHERPA 1.1*, JHEP **02** (2009), 007, [arXiv:0811.4622 [hep-ph]].

[6] T. Kinoshita, *Mass singularities of Feynman amplitudes*, J.Math.Phys. **3** (1962), 650–677; T. Lee and M. Nauenberg, *Degenerate Systems and Mass Singularities*, Phys.Rev. **133** (1964), B1549–B1562.

[7] R. K. Ellis, W. J. Stirling and B. R. Webber, *QCD and collider physics*, ed. 1, vol. 8, Cambridge Monogr. Part. Phys. Nucl. Phys. Cosmol., 1996.

[8] V. N. Gribov and L. N. Lipatov, *Deep inelastic e-p scattering in perturbation theory*, Sov. J. Nucl. Phys. **15** (1972), 438–450; L. N. Lipatov, *The parton model and perturbation theory*, Sov. J. Nucl. Phys. **20** (1975), 94–102; Y. L. Dokshitzer, *Calculation of the structure functions for deep inelastic scattering and e^+e^- annihilation by perturbation theory in quantum chromodynamics*, Sov. Phys. JETP **46** (1977), 641–653; G. Altarelli and G. Parisi, *Asymptotic freedom in parton language*, Nucl. Phys. **B126** (1977), 298–318.

[9] T. Sjöstrand, *A model for initial state parton showers*, Phys. Lett. **B157** (1985), 321.

[10] V. V. Sudakov, *Vertex parts at very high-energies in quantum electrodynamics*, Sov. Phys. JETP **3** (1956), 65–71; G. P. Korchemsky, *Sudakov form-factor in QCD*, Phys. Lett. **B220** (1989), 629.

[11] S. Höche, F. Krauss, S. Schumann and F. Siegert, *QCD matrix elements and truncated showers*, JHEP **05** (2009), 053, [arXiv:0903.1219 [hep-ph]].

[12] S. Catani and M. H. Seymour, *A general algorithm for calculating jet cross sections in NLO QCD*, Nucl. Phys. **B485** (1997), 291–419, [hep-ph/9605323]; S. Catani, S. Dittmaier, M. H. Seymour and Z. Trocsanyi, *The dipole formalism for next-to-leading order QCD calculations with massive partons*, Nucl. Phys. **B627** (2002), 189–265, [hep-ph/0201036].

[13] S. Schumann and F. Krauss, *A parton shower algorithm based on Catani-Seymour dipole factorisation*, JHEP **03** (2008), 038, [arXiv:0709.1027 [hep-ph]].

[14] T. Carli, T. Gehrmann and S. Höche, *Hadronic final states in deep-inelastic scattering with SHERPA*, Eur. Phys. J. **C67** (2010), 73, [arXiv:0912.3715 [hep-ph]].

[15] G. Corcella et al., *HERWIG 6: an event generator for hadron emission reactions with interfering gluons (including supersymmetric processes)*, JHEP **01** (2001), 010, [hep-ph/0011363].

[16] L. Lönnblad, *Ariadne version 4: A program for simulation of QCD cascades implementing the colour dipole model*, Comput. Phys. Commun. **71** (1992), 15–31.

[17] E. W. N. Glover and A. G. Morgan, *Measuring the photon fragmentation function at LEP*, Z. Phys. **C62** (1994), 311–322.

[18] D. Buskulic et al., ALEPH collaboration, *First measurement of the quark-to-photon fragmentation function*, Z. Phys. **C69** (1996), 365–378.

[19] A. D. Martin, R. G. Roberts, W. J. Stirling and R. S. Thorne, *Parton distributions incorporating QED contributions*, Eur. Phys. J. **C39** (2005), 155–161, [hep-ph/0411040].

[20] K. Hamacher and M. Weierstall, *The Next Round of Hadronic Generator Tuning Heavily Based on Identified Particle Data*, hep-ex/9511011.

[21] P. Abreu et al., DELPHI collaboration, *Tuning and test of fragmentation models based on identified particles and precision event shape data*, Z. Phys. **C73** (1996), 11–60.

[22] B. Andersson, G. Gustafson, G. Ingelman and T. Sjöstrand, *Parton Fragmentation and String Dynamics*, Phys. Rept. **97** (1983), 31–145; B. Andersson, *The Lund model*, vol. 7, Camb. Monogr. Part. Phys. Nucl. Phys. Cosmol., 1997.

[23] T. D. Gottschalk, *A realistic model for e^+e^- annihilation including parton bremsstrahlung effects*, Nucl. Phys. **B214** (1983), 201; T. D. Gottschalk, *An improved description of hadronization in the QCD cluster model for e^+e^- annihilation*, Nucl. Phys. **B239** (1984), 349; B. R. Webber, *A QCD model for jet fragmentation including soft gluon interference*, Nucl. Phys. **B238** (1984), 492; T. D. Gottschalk and D. A. Morris, *A new model for hadronization and e^+e^- annihilation*, Nucl. Phys. **B288** (1987), 729; J.-C. Winter, F. Krauss and G. Soff, *A modified cluster-hadronisation model*, Eur. Phys. J. **C36** (2004), 381–395, [hep-ph/0311085].

[24] C. Amsler et al., Particle Data Group collaboration, *Review of particle physics*, Phys. Lett. **B667** (2008), 1.

[25] P. Richardson, *Spin correlations in Monte Carlo simulations*, JHEP **11** (2001), 029, [hep-ph/0110108].

[26] F. Abe et al., CDF collaboration, *Measurement of Double Parton Scattering in $\bar{p}p$ collisions at $\sqrt{s} = 1.8\,\mathrm{TeV}$*, Phys. Rev. Lett. **79** (1997), 584–589; F. Abe et al., CDF collaboration, *Double parton scattering in $\bar{p}p$ collisions at $\sqrt{s} = 1.8\,\mathrm{TeV}$*, Phys. Rev. **D56** (1997), 3811–3832.

[27] D. E. Acosta et al., CDF collaboration, *Underlying event in hard interactions at the Fermilab Tevatron $\bar{p}p$ collider*, Phys. Rev. **D70** (2004), 072002, [hep-ex/0404004].

[28] T. Affolder et al., CDF collaboration, *Charged jet evolution and the underlying event in proton-antiproton collisions at 1.8 TeV*, Phys. Rev. **D65** (2002), 092002.

[29] T. Sjöstrand and M. van Zijl, *A multiple-interaction model for the event structure in hadron collisions*, Phys. Rev. **D36** (1987), 2019.

[30] J. M. Butterworth, J. R. Forshaw and M. H. Seymour, *Multiparton Interactions in Photoproduction at HERA*, Z. Phys. **C72** (1996), 637–646, [hep-ph/9601371].

[31] A. Donnachie and P. V. Landshoff, *Total cross sections*, Phys. Lett. **B296** (1992), 227–232, [hep-ph/9209205].

[32] G. A. Schuler and T. Sjöstrand, *A scenario for high-energy $\gamma\gamma$ interactions*, Z. Phys. **C73** (1997), 677–688, [hep-ph/9605240].

[33] M. H. Seymour, *Matrix-element corrections to parton shower algorithms*, Comp. Phys. Commun. **90** (1995), 95–101, [hep-ph/9410414]; M. H. Seymour, *A simple prescription for first-order corrections to quark scattering and annihilation processes*, Nucl. Phys. **B436** (1995), 443–460, [hep-ph/9410244]; G. Corcella and M. H. Seymour, *Matrix element corrections to parton shower simulations of heavy quark decay*, Phys. Lett. **B442** (1998), 417–426, [hep-ph/9809451]; G. Miu and T. Sjöstrand, *W production in an improved parton-shower approach*, Phys. Lett. **B449** (1999), 313–320, [hep-ph/9812455]; G. Corcella and M. H. Seymour, *Initial state radiation in simulations of vector boson production at hadron colliders*, Nucl. Phys. **B565** (2000), 227–244, [hep-ph/9908388]; E. Norrbin and T. Sjöstrand, *QCD radiation off heavy particles*, Nucl. Phys. **B603** (2001), 297–342, [hep-ph/0010012].

[34] J. André and T. Sjöstrand, *Matching of matrix elements and parton showers*, Phys. Rev. **D57** (1998), 5767–5772, [hep-ph/9708390].

[35] S. Catani, F. Krauss, R. Kuhn and B. R. Webber, *QCD matrix elements + parton showers*, JHEP **11** (2001), 063, [hep-ph/0109231]; F. Krauss, *Matrix elements and parton showers in hadronic interactions*, JHEP **0208** (2002), 015, [hep-ph/0205283].

[36] N. Brown and W. J. Stirling, *Finding Jets and Summing Soft Gluons: a New Algorithm*, Z. Phys. **C53** (1992), 629–636; S. Catani, Y. L. Dokshitzer, M. Olsson, G. Turnock and B. R. Webber, *New clustering algorithm for multijet cross sections in e^+e^- annihilation*, Phys. Lett. **B269** (1991), 432–438.

[37] S. Catani, Y. L. Dokshitzer and B. R. Webber, *The $k_\perp$ clustering algorithm for jets in deep inelastic scattering and hadron collisions*, Phys. Lett. **B285** (1992), 291–299; S. Catani, Y. L. Dokshitzer, M. H. Seymour and B. R. Webber, *Longitudinally-invariant $k_\perp$-clustering algorithms for hadron–hadron collisions*, Nucl. Phys. **B406** (1993), 187–224.

[38] L. Lönnblad, *Correcting the colour-dipole cascade model with fixed order matrix elements*, JHEP **05** (2002), 046, [hep-ph/0112284]; N. Lavesson and L. Lönnblad, *W+jets matrix elements and the dipole cascade*, JHEP **07** (2005), 054, [hep-ph/0503293].

[39] M. L. Mangano, M. Moretti and R. Pittau, *Multijet matrix elements and shower evolution in hadronic collisions: $Wb\bar{b}+n$-jets as a case study*, Nucl. Phys. **B632** (2002), 343–362, [hep-ph/0108069].

[40] S. Höche et al., *Matching Parton Showers and Matrix Elements*,

hep-ph/0602031; J. Alwall et al., *Comparative study of various algorithms for the merging of parton showers and matrix elements in hadronic collisions*, Eur. Phys. J. **C53** (2008), 473–500, [arXiv:0706.2569 [hep-ph]].

[41] N. Lavesson and L. Lönnblad, *Merging parton showers and matrix elements – back to basics*, JHEP **04** (2008), 085, [arXiv:0712.2966 [hep-ph]].

[42] Z. Nagy and D. E. Soper, *Parton showers with quantum interference*, JHEP **09** (2007), 114, [arXiv:0706.0017 [hep-ph]]; Z. Nagy and D. E. Soper, *Parton showers with quantum interference: leading color, spin averaged*, JHEP **03** (2008), 030, [arXiv:0801.1917 [hep-ph]]; Z. Nagy and D. E. Soper, *Parton showers with quantum interference: leading color, with spin*, JHEP **07** (2008), 025, [arXiv:0805.0216 [hep-ph]].

[43] P. Nason, *A new method for combining NLO QCD with shower Monte Carlo algorithms*, JHEP **11** (2004), 040, [hep-ph/0409146]; S. Frixione, P. Nason and C. Oleari, *Matching NLO QCD computations with parton shower simulations: the POWHEG method*, JHEP **11** (2007), 070, [arXiv:0709.2092 [hep-ph]].

[44] F. Maltoni, K. Paul, T. Stelzer and S. Willenbrock, *Color-flow decomposition of QCD amplitudes*, Phys. Rev. **D67** (2003), 014026, [hep-ph/0209271].

[45] C. Duhr, S. Höche and F. Maltoni, *Color-dressed recursive relations for multi-parton amplitudes*, JHEP **08** (2006), 062, [hep-ph/0607057].

[46] M. L. Mangano, S. J. Parke and Z. Xu, *Duality and multi-gluon scattering*, Nucl. Phys. **B298** (1988), 653.

[47] F. Caravaglios, M. L. Mangano, M. Moretti and R. Pittau, *A new approach to multi-jet calculations in hadron collisions*, Nucl. Phys. **B539** (1999), 215–232, [hep-ph/9807570].

[48] F. Krauss, A. Schälicke, S. Schumann and G. Soff, *Simulating W / Z + jets production at the Tevatron*, Phys. Rev. **D70** (2004), 114009, [hep-ph/0409106].

[49] S. Gieseke, *Uncertainties of Sudakov form factors*, JHEP **01** (2005), 058, [hep-ph/0412342].

[50] A. Banfi, G. P. Salam and G. Zanderighi, *Infrared-safe definition of jet flavour*, Eur. Phys. J. **C47** (2006), 113–124, [hep-ph/0601139].

[51] R. Pittau, *A simple method for multi-leg loop calculations*, Comput. Phys. Commun. **104** (1997), 23–36, [hep-ph/9607309]; R. Pittau, *A simple method for*

multi-leg loop calculations 2: a general algorithm, Comput. Phys. Commun. **111** (1998), 48–52, [hep-ph/9712418].

[52] S. Catani, S. Dittmaier and Z. Trocsanyi, *One-loop singular behaviour of QCD and SUSY QCD amplitudes with massive partons*, Phys. Lett. **B500** (2001), 149–160, [hep-ph/0011222].

[53] V. M. Abazov et al., DØ collaboration, *Search for Decay of a Fermiophobic Higgs Boson $h_f \to \gamma\gamma$ with the DØ Detector at $\sqrt{s} = 1.96$ TeV*, Phys. Rev. Lett. **101** (2008), 051801, [arXiv:0803.1514 [hep-ex]]; T. Aaltonen et al., CDF collaboration, *Search for a Fermiophobic Higgs Boson Decaying into Diphotons in $p\bar{p}$ Collisions at $\sqrt{s} = 1.96$ TeV*, Phys. Rev. Lett. **103** (2009), 061803, [arXiv:0905.0413 [hep-ex]]; G. Aad et al., The ATLAS collaboration, *Expected Performance of the ATLAS Experiment - Detector, Trigger and Physics*, arXiv:0901.0512 [hep-ex]; G. L. Bayatian et al., CMS collaboration, *CMS technical design report, volume II: Physics performance*, J. Phys. **G34** (2007), 995–1579; D. L. Rainwater and D. Zeppenfeld, *Searching for $H \to \gamma\gamma$ in weak boson fusion at the LHC*, JHEP **12** (1997), 005, [hep-ph/9712271]; S. Abdullin et al., *Higgs boson discovery potential of LHC in the channel $pp \to \gamma\gamma + jet$*, Phys. Lett. **B431** (1998), 410–419, [hep-ph/9805341].

[54] I. Hinchliffe and F. E. Paige, *Measurements in gauge mediated SUSY breaking models at LHC*, Phys. Rev. **D60** (1999), 095002, [hep-ph/9812233]; G. F. Giudice, R. Rattazzi and J. D. Wells, *Quantum gravity and extra dimensions at high-energy colliders*, Nucl. Phys. **B544** (1999), 3–38, [hep-ph/9811291]; H. Davoudiasl, J. L. Hewett and T. G. Rizzo, *Experimental probes of localized gravity: On and off the wall*, Phys. Rev. **D63** (2001), 075004, [hep-ph/0006041]; C. Macesanu, C. D. McMullen and S. Nandi, *New signal for universal extra dimensions*, Phys. Lett. **B546** (2002), 253–260, [hep-ph/0207269].

[55] A. Bhatti et al., *Determination of the jet energy scale at the Collider Detector at Fermilab*, Nucl. Instrum. Meth. **A566** (2006), 375–412, [hep-ex/0510047]; B. Abbott et al., DØ collaboration, *Determination of the absolute jet energy scale in the DØ calorimeters*, Nucl. Instrum. Meth. **A424** (1999), 352–394, [hep-ex/9805009]; I. A. Golutvin et al., *Setting the Jet Energy Scale in the CMS Calorimeter using Events with Direct Photons*, Phys. Part. Nucl. Lett. **5** (2008), 447–455.

[56] P. Aurenche, R. Baier, M. Fontannaz, J. F. Owens and M. Werlen, *Gluon content of the nucleon probed with real and virtual photons*, Phys. Rev. **D39** (1989), 3275; W. Vogelsang and A. Vogt, *Constraints on the proton's gluon distribution from*

prompt photon production, Nucl. Phys. **B453** (1995), 334–354, [hep-ph/9505404]; M. Fontannaz and G. Heinrich, *Isolated photon plus jet photoproduction as a tool to constrain the gluon distribution in the proton and the photon*, Eur. Phys. J. **C34** (2004), 191–199, [hep-ph/0312009].

[57] C. H. Llewellyn Smith, *QCD predictions for processes involving real photons*, Phys. Lett. **B79** (1978), 83.

[58] H. Baer, J. Ohnemus and J. F. Owens, *Next-to-leading-logarithm calculation of direct photon production*, Phys. Rev. **D42** (1990), 61–71.

[59] P. Aurenche, R. Baier and M. Fontannaz, *Prompt photon production at colliders*, Phys. Rev. **D42** (1990), 1440–1449.

[60] A. Gehrmann-De Ridder, T. Gehrmann and E. W. N. Glover, *Radiative corrections to the photon + 1 jet rate at LEP*, Phys. Lett. **B414** (1997), 354–361, [hep-ph/9705305]; A. Gehrmann-De Ridder and E. W. N. Glover, *Final state photon production at LEP*, Eur. Phys. J. **C7** (1999), 29–48, [hep-ph/9806316].

[61] S. Frixione, *Isolated photons in perturbative QCD*, Phys. Lett. **B429** (1998), 369–374, [hep-ph/9801442]; S. Frixione and W. Vogelsang, *Isolated-photon production in polarized pp collisions*, Nucl. Phys. **B568** (2000), 60–92, [hep-ph/9908387].

[62] P. Aurenche, R. Baier, M. Fontannaz and D. Schiff, *Prompt photon production at large p_T Scheme invariant QCD predictions and comparison with experiment*, Nucl. Phys. **B297** (1988), 661.

[63] L. E. Gordon and W. Vogelsang, *Polarized and unpolarized isolated prompt photon production beyond the leading order*, Phys. Rev. **D50** (1994), 1901–1916.

[64] P. Aurenche, A. Douiri, R. Baier, M. Fontannaz and D. Schiff, *Large p_T Double Photon Production in Hadronic Collisions — Beyond Leading Logarithm QCD Calculation*, Z. Phys. **C29** (1985), 459–475.

[65] B. Bailey, J. F. Owens and J. Ohnemus, *Order α_s Monte Carlo calculation of hadronic double-photon production*, Phys. Rev. **D46** (1992), 2018–2027.

[66] S. Catani, M. Fontannaz, J. P. Guillet and E. Pilon, *Cross section of isolated prompt photons in hadron-hadron collisions*, JHEP **05** (2002), 028, [hep-ph/0204023]; P. Aurenche, M. Fontannaz, J.-P. Guillet, E. Pilon and M. Werlen, *Recent critical study of photon production in hadronic collisions*, Phys. Rev. **D73** (2006), 094007, [hep-ph/0602133]; Z. Belghobsi et al., *Photon-jet correlations and constraints on fragmentation functions*, Phys. Rev. **D79** (2009), 114024, [arXiv:0903.4834 [hep-ph]].

[67] T. Binoth, J. P. Guillet, E. Pilon and M. Werlen, *A full next-to-leading order study of direct photon pair production in hadronic collisions*, Eur. Phys. J. **C16** (2000), 311–330, [hep-ph/9911340]; T. Binoth, J. P. Guillet, E. Pilon and M. Werlen, *Beyond leading order effects in photon pair production at the Fermilab Tevatron*, Phys. Rev. **D63** (2001), 114016, [hep-ph/0012191].

[68] V. Del Duca, F. Maltoni, Z. Nagy and Z. Trocsanyi, *QCD radiative corrections to prompt diphoton production in association with a jet at hadron colliders*, JHEP **04** (2003), 059, [hep-ph/0303012].

[69] E. L. Berger, E. Braaten and R. D. Field, *Large-p_{T} Production of Single and Double Photons in Proton-Proton and Pion-Proton Collisions*, Nucl. Phys. **B239** (1984), 52.

[70] D. de Florian and Z. Kunszt, *Two photons plus jet at LHC: The NNLO contribution from the gg initiated process*, Phys. Lett. **B460** (1999), 184–188, [hep-ph/9905283]; T. Binoth, J. P. Guillet and F. Mahmoudi, *A compact representation of the $\gamma\gamma ggg \to 0$ amplitude*, JHEP **02** (2004), 057, [hep-ph/0312334].

[71] C. Balazs, P. M. Nadolsky, C. Schmidt and C. P. Yuan, *Diphoton background to Higgs boson production at the LHC with soft gluon effects*, Phys. Lett. **B489** (2000), 157–162, [hep-ph/9905551].

[72] C. Balazs, E. L. Berger, S. Mrenna and C. P. Yuan, *Photon pair production with soft gluon resummation in hadronic interactions*, Phys. Rev. **D57** (1998), 6934–6947, [hep-ph/9712471]; C. Balazs, E. L. Berger, P. M. Nadolsky and C. P. Yuan, *All-orders resummation for diphoton production at hadron colliders*, Phys. Lett. **B637** (2006), 235–240, [hep-ph/0603037]; C. Balazs, E. L. Berger, P. M. Nadolsky and C. P. Yuan, *Calculation of prompt diphoton production cross sections at Fermilab Tevatron and CERN LHC energies*, Phys. Rev. **D76** (2007), 013009, [arXiv:0704.0001 [hep-ph]].

[73] N. Kidonakis and J. F. Owens, *Soft-gluon resummation and NNLO corrections for direct photon production*, Phys. Rev. **D61** (2000), 094004, [hep-ph/9912388]; D. de Florian and W. Vogelsang, *Threshold resummation for the prompt-photon cross section revisited*, Phys. Rev. **D72** (2005), 014014, [hep-ph/0506150].

[74] G. Diana, *High-energy resummation in direct photon production*, Nucl. Phys. **B824** (2010), 154–167, [arXiv:0906.4159 [hep-ph]].

[75] T. Becher and M. D. Schwartz, *Direct photon production with effective field theory*, JHEP **02** (2010), 040, [arXiv:0911.0681 [hep-ph]].

[76] D. R. Yennie, S. C. Frautschi and H. Suura, *The Infrared Divergence Phenomena and High-Energy Processes*, Ann. Phys. **13** (1961), 379–452.

[77] D. J. Summers, *Exponentiation of soft photons in a process involving hard photons*, Phys. Rev. **D53** (1996), 2430–2441, [hep-ph/9405430].

[78] M. H. Seymour, *Photon radiation in final state parton showering*, Z. Phys. **C56** (1992), 161–170; M. H. Seymour, *Soft isolated photon production as a probe of the parton shower mechanism*, Z. Phys. **C64** (1994), 445–452.

[79] A. Buckley et al., *Rivet user manual*, arXiv:1003.0694 [hep-ph].

[80] P. Pfeifenschneider et al., JADE and OPAL collaboration, *QCD analyses and determinations of α_s in e^+ e^- annihilation at energies between 35-GeV and 189-GeV*, Eur. Phys. J. **C17** (2000), 19–51, [hep-ex/0001055].

[81] T. Aaltonen, CDF collaboration, *Measurement of the inclusive isolated prompt photon cross section in $p\bar{p}$ collisions at $\sqrt{s} = 1.96$ TeV using the CDF detector*, Phys. Rev. **D80** (2009), 111106, [arXiv:0910.3623 [hep-ex]].

[82] V. M. Abazov et al., DØ collaboration, *Measurement of the isolated photon cross section in $p\bar{p}$ collisions at $\sqrt{s} = 1.96$ TeV*, Phys. Lett. **B639** (2006), 151–158, [hep-ex/0511054].

[83] V. M. Abazov et al., DØ collaboration, *Measurement of the differential cross section for the production of an isolated photon with associated jet in $p\bar{p}$ collisions at $\sqrt{s} = 1.96$ TeV*, Phys. Lett. **B666** (2008), 435–445, [arXiv:0804.1107 [hep-ex]].

[84] D. E. Acosta et al., CDF collaboration, *Measurement of the Cross Section for Prompt Diphoton Production in $p\bar{p}$ Collisions at $\sqrt{s} = 1.96$ TeV*, Phys. Rev. Lett. **95** (2005), 022003, [hep-ex/0412050].

[85] V. Abazov et al., The DØ collaboration, *Measurement of direct photon pair production cross sections in $p\bar{p}$ collisions at $\sqrt{s} = 1.96$ TeV*, Phys. Lett. **B690** (2010), 108–117, [arXiv:1002.4917 [hep-ex]].

[86] S. Höche, S. Schumann and F. Siegert, *Hard photon production and matrix-element parton-shower merging*, Phys. Rev. **D81** (2010), 034026, [arXiv:0912.3501 [hep-ph]].

[87] S. Frixione and B. R. Webber, *Matching NLO QCD computations and parton shower simulations*, JHEP **06** (2002), 029, [hep-ph/0204244]; S. Frixione and B. R. Webber, *The MC@NLO 3.3 Event Generator*, hep-ph/0612272.

[88] S. Frixione, P. Nason and B. R. Webber, *Matching NLO QCD and parton showers in heavy flavour production*, JHEP **08** (2003), 007, [hep-ph/0305252]; S. Frixione, E. Laenen, P. Motylinski and B. R. Webber, *Single-top production in MC@NLO*, JHEP **03** (2006), 092, [hep-ph/0512250]; S. Frixione, E. Laenen, P. Motylinski, B. R. Webber and C. D. White, *Single-top hadroproduction in association with a W boson*, JHEP **07** (2008), 029, [arXiv:0805.3067 [hep-ph]]; C. Weydert et al., *Charged Higgs boson production in association with a top quark in MC@NLO*, Eur. Phys. J. **C67** (2010), 617–636, [arXiv:0912.3430 [hep-ph]]; P. Torrielli and S. Frixione, *Matching NLO QCD computations with PYTHIA using MC@NLO*, JHEP **04** (2010), 110, [arXiv:1002.4293 [hep-ph]].

[89] P. Nason and G. Ridolfi, *A positive-weight next-to-leading-order Monte Carlo for Z pair hadroproduction*, JHEP **08** (2006), 077, [hep-ph/0606275]; S. Frixione, P. Nason and G. Ridolfi, *A positive-weight next-to-leading-order Monte Carlo for heavy flavour hadroproduction*, JHEP **09** (2007), 126, [arXiv:0707.3088 [hep-ph]]; S. Frixione, P. Nason and G. Ridolfi, *The POWHEG-hvq manual version 1.0*, arXiv:0707.3081 [hep-ph]; S. Alioli, P. Nason, C. Oleari and E. Re, *NLO Higgs boson production via gluon fusion matched with shower in POWHEG*, JHEP **04** (2009), 002, [arXiv:0812.0578 [hep-ph]]; K. Hamilton, P. Richardson and J. Tully, *A positive-weight next-to-leading order Monte Carlo simulation of Drell-Yan vector boson production*, JHEP **10** (2008), 015, [arXiv:0806.0290 [hep-ph]]; S. Alioli, P. Nason, C. Oleari and E. Re, *NLO single-top production matched with shower in POWHEG: s- and t-channel contributions*, JHEP **09** (2009), 111, [arXiv:0907.4076 [hep-ph]]; P. Nason and C. Oleari, *NLO Higgs boson production via vector-boson fusion matched with shower in POWHEG*, JHEP **02** (2010), 037, [arXiv:0911.5299 [hep-ph]]; K. Hamilton, P. Richardson and J. Tully, *A positive-weight Next-to-Leading Order Monte Carlo Simulation for Higgs boson production*, JHEP **04** (2009), 116, [arXiv:0903.4345 [hep-ph]].

[90] S. Alioli, P. Nason, C. Oleari and E. Re, *NLO vector-boson production matched with shower in POWHEG*, JHEP **07** (2008), 060, [arXiv:0805.4802 [hep-ph]].

[91] S. Alioli, P. Nason, C. Oleari and E. Re, *A general framework for implementing NLO calculations in shower Monte Carlo programs: the POWHEG BOX*, JHEP **06** (2010), 043, [arXiv:1002.2581 [hep-ph]].

[92] K. Hamilton and P. Nason, *Improving NLO-parton shower matched simulations with higher order matrix elements*, JHEP **06** (2010), 039, [arXiv:1004.1764 [hep-ph]].

[93] D. A. Kosower, *Antenna factorization of gauge-theory amplitudes*, Phys.

Rev. **D57** (1998), 5410–5416, [hep-ph/9710213]; D. A. Kosower, *Antenna factorization in strongly-ordered limits*, Phys. Rev. **D71** (2005), 045016, [hep-ph/0311272]; A. Gehrmann-De Ridder, T. Gehrmann and E. W. N. Glover, *Antenna subtraction at NNLO*, JHEP **09** (2005), 056, [hep-ph/0505111]; A. Daleo, T. Gehrmann and D. Maître, *Antenna subtraction with hadronic initial states*, JHEP **04** (2007), 016, [hep-ph/0612257].

[94] S. Frixione, Z. Kunszt and A. Signer, *Three-jet cross-sections to next-to-leading order*, Nucl. Phys. **B467** (1996), 399–442, [hep-ph/9512328]; S. Frixione, *A general approach to jet cross sections in QCD*, Nucl. Phys. **B507** (1997), 295–314, [hep-ph/9706545].

[95] T. Gleisberg and F. Krauss, *Automating dipole subtraction for QCD NLO calculations*, Eur. Phys. J. **C53** (2008), 501–523, [arXiv:0709.2881 [hep-ph]].

[96] T. Binoth et al., *A proposal for a standard interface between Monte Carlo tools and one-loop programs*, Comput. Phys. Commun. **181** (2010), 1612–1622, [arXiv:1001.1307 [hep-ph]].

[97] R. D. Field, *Applications of perturbative QCD*, Addison-Wesley, Redwood City, USA, 1989, Frontiers in physics, 77.

[98] S. Plätzer and S. Gieseke, *Coherent Parton Showers with Local Recoils*, arXiv:0909.5593 [hep-ph].

[99] R. Kleiss and R. Pittau, *Weight optimization in multichannel Monte Carlo*, Comput. Phys. Commun. **83** (1994), 141–146, [hep-ph/9405257].

[100] G. P. Lepage, *A New Algorithm for Adaptive Multidimensional Integration*, J. Comput. Phys. **27** (1978), 192; G. P. Lepage, *VEGAS - An Adaptive Multidimensional Integration Program*, CLNS-80/447.

[101] D. Maître, private communication; C. F. Berger et al., *Precise Predictions for W + 3 Jet Production at Hadron Colliders*, Phys. Rev. Lett. **102** (2009), 222001, [arXiv:0902.2760 [hep-ph]]; C. F. Berger et al., *Next-to-leading order QCD predictions for W+3-Jet distributions at hadron colliders*, Phys.Rev. **D80** (2009), 074036, [arXiv:0907.1984 [hep-ph]]; C. F. Berger et al., *Next-to-leading order QCD predictions for Z, γ^*+3-Jet distributions at the Tevatron*, Phys. Rev. **D82** (2010), 074002, [arXiv:1004.1659 [hep-ph]].

[102] P. M. Nadolsky et al., *Implications of CTEQ global analysis for collider observables*, Phys. Rev. **D78** (2008), 013004, [arXiv:0802.0007 [hep-ph]].

[103] M. Schönherr and F. Krauss, *Soft photon radiation in particle decays in SHERPA*, JHEP **12** (2008), 018, [arXiv:0810.5071 [hep-ph]].

[104] S. Dawson, *Radiative corrections to Higgs boson production*, Nucl. Phys. **B359** (1991), 283–300; A. Djouadi, M. Spira and P. Zerwas, *Production of Higgs bosons in proton colliders: QCD corrections*, Phys.Lett. **B264** (1991), 440–446.

[105] C. Anastasiou, K. Melnikov and F. Petriello, *Fully differential Higgs boson production and the di-photon signal through next-to-next-to-leading order*, Nucl. Phys. **B724** (2005), 197–246, [hep-ph/0501130]; C. Anastasiou, G. Dissertori and F. Stöckli, *NNLO QCD predictions for the $H \to WW \to l\nu l\nu$ signal at the LHC*, JHEP **09** (2007), 018, [arXiv:0707.2373 [hep-ph]]; C. Anastasiou, R. Boughezal and F. Petriello, *Mixed QCD-electroweak corrections to Higgs boson production in gluon fusion*, JHEP **04** (2009), 003, [arXiv:0811.3458 [hep-ph]].

[106] S. Catani, D. de Florian, M. Grazzini and P. Nason, *Soft-gluon resummation for Higgs boson production at hadron colliders*, JHEP **07** (2003), 028, [hep-ph/0306211]; G. Bozzi, S. Catani, D. de Florian and M. Grazzini, *Transverse-momentum resummation and the spectrum of the Higgs boson at the LHC*, Nucl. Phys. **B737** (2006), 73–120, [hep-ph/0508068].

[107] J. Campbell and R. K. Ellis, *MCFM – Monte Carlo for FeMtobarn processes*.

[108] J. M. Campbell and R. K. Ellis, *Update on vector boson pair production at hadron colliders*, Phys. Rev. **D60** (1999), 113006, [hep-ph/9905386]; L. J. Dixon, Z. Kunszt and A. Signer, *Helicity amplitudes for $\mathcal{O}(\alpha_s)$ production of W^+W^-, $W^\pm Z$, ZZ, $W^\pm\gamma$, or $Z\gamma$ pairs at hadron colliders*, Nucl. Phys. **B531** (1998), 3–23, [hep-ph/9803250].

[109] C. Adloff et al., H1 collaboration, *Measurement and QCD analysis of jet cross sections in deep-inelastic positron-proton collisions at $\sqrt{s}$ of 300 GeV*, Eur. Phys. J. **C19** (2001), 289–311, [hep-ex/0010054], DESY-00-145.

[110] C. Adloff et al., H1 collaboration, *Three-jet production in deep-inelastic scattering at HERA*, Phys. Lett. **B515** (2001), 17–29, [hep-ex/0106078], DESY-01-073.

[111] B. Abbott et al., DØ collaboration, *Differential cross section for W boson production as a function of transverse momentum in $p\bar{p}$ collisions at $\sqrt{s} = 1.8$ TeV*, Phys. Lett. **B513** (2001), 292–300, [hep-ex/0010026].

[112] A. Heister et al., ALEPH collaboration, *Studies of QCD at e^+e^- centre-of-mass energies between 91 and 209 GeV*, Eur. Phys. J. **C35** (2004), 457–486.

[113] V. M. Abazov et al., DØ collaboration, *Measurement of the normalized $Z/\gamma^* \to \mu^+\mu^-$ transverse momentum distribution in $p\bar{p}$ collisions at $\sqrt{s} = 1.96$ TeV*, arXiv:1006.0618 [hep-ex].

[114] V. M. Abazov et al., DØ collaboration, *Measurement of the shape of the boson rapidity distribution for $p\bar{p} \to Z/\gamma^* \to e^+e^- + X$ events produced at $\sqrt{s}$ of 1.96 TeV*, Phys. Rev. **D76** (2007), 012003, [hep-ex/0702025].

[115] G. Abbiendi et al., OPAL collaboration, *A simultaneous measurement of the QCD colour factors and the strong coupling*, Eur. Phys. J. **C20** (2001), 601–615, [hep-ex/0101044].

[116] C. Adloff et al., H1 collaboration, *Measurement of inclusive jet cross-sections in deep-inelastic ep scattering at HERA*, Phys. Lett. **B542** (2002), 193–206, [hep-ex/0206029], DESY-02-079.

[117] S. D. Ellis and D. E. Soper, *Successive combination jet algorithm for hadron collisions*, Phys. Rev. **D48** (1993), 3160–3166, [hep-ph/9305266].

[118] S. Frixione and G. Ridolfi, *Jet photoproduction at HERA*, Nucl. Phys. **B507** (1997), 315–333, [hep-ph/9707345].

[119] F. Krauss, R. Kuhn and G. Soff, *AMEGIC++ 1.0: A Matrix Element Generator In C++*, JHEP **02** (2002), 044, [hep-ph/0109036].

[120] V. M. Abazov et al., DØ collaboration, *Measurement of the shape of the boson transverse momentum distribution in $p\bar{p} \to Z/\gamma^* \to ee + X$ events produced at $\sqrt{s} = 1.96$ TeV*, Phys. Rev. Lett. **100** (2008), 102002, [arXiv:0712.0803 [hep-ex]].

[121] V. M. Abazov et al., DØ collaboration, *Measurement of Z/γ^*+jet+X angular distributions in $p\bar{p}$ collisions at $\sqrt{s} = 1.96$ TeV*, Phys. Lett. **B682** (2010), 370–380, [arXiv:0907.4286 [hep-ex]].

[122] V. M. Abazov et al., DØ collaboration, *Measurement of the ratios of the $Z/\gamma^* + \geq n$ jet production cross sections to the total inclusive Z/γ^* cross section in $p\bar{p}$ collisions at $\sqrt{s}$=1.96 TeV*, Phys. Lett. **B658** (2008), 112–119, [hep-ex/0608052].

[123] G. C. Blazey et al., *Run II jet physics*, hep-ex/0005012.

[124] V. Abazov et al., DØ collaboration, *Measurements of differential cross sections of Z/γ^*+jets+X events in proton anti-proton collisions at $\sqrt{s} = 1.96$ TeV*, Phys.Lett. **B678** (2009), 45–54, [arXiv:0903.1748 [hep-ex]].

[125] J. M. Butterworth et al., *The Tools and Monte Carlo working group: Summary report*, arXiv:1003.1643 [hep-ph], Proceedings of the Workshop "Physics at TeV Colliders", Les Houches, France, 8-26 June, 2009.

[126] T. Gleisberg, F. Krauss, A. Schälicke, S. Schumann and J.-C. Winter, *Studying W^+W^- production at the Fermilab Tevatron with SHERPA*, Phys. Rev. **D72** (2005), 034028, [hep-ph/0504032].

[127] T. Binoth, T. Gleisberg, S. Karg, N. Kauer and G. Sanguinetti, *NLO QCD corrections to ZZ+jet production at hadron colliders*, Phys. Lett. **B683** (2010), 154–159, [arXiv:0911.3181 [hep-ph]].

[128] C. Lefèvre, *The CERN accelerator complex. Complexe des accelerateurs du CERN*, Dec 2008.

[129] http://lpc.web.cern.ch/lpc/lumiplots.htm.

[130] G. Aad et al., The ATLAS collaboration, *The ATLAS Experiment at the CERN Large Hadron Collider*, JINST **3** (2008), S08003.

[131] J. Pequenao, *Computer generated image of the whole ATLAS detector*, Mar 2008.

[132] W. H. Bell, D. Berge, J. A. Gray, R. Kwee, B. T. Martin, A. Messina, E. L. Nurse, A. J. Richards and P. A. Steinberg, *MBTS trigger efficiency for the minimum bias analysis using Inner Detector tracks from pp interactions at $\sqrt{s} = 900$ GeV*, Tech. Report ATL-COM-DAQ-2010-003 , CERN, Geneva, Jan 2010.

[133] A. Breakstone et al., Ames-Bologna-CERN-Dortmund-Heidelberg-Warsaw collaboration, *Charged Multiplicity Distribution in pp Interactions at ISR Energies*, Phys.Rev. **D30** (1984), 528.

[134] G. Arnison et al., UA1 collaboration, *Transverse Momentum Spectra for Charged Particles at the CERN $p\bar{p}$ Collider*, Phys.Lett. **B118** (1982), 167, Revised version; C. Albajar et al., UA1 collaboration, *A Study of the General Characteristics of $p\bar{p}$ Collisions at $\sqrt{s} = 0.2$ TeV to 0.9 TeV*, Nucl.Phys. **B335** (1990), 261.

[135] R. Ansorge et al., UA5 collaboration, *Diffraction Dissociation at the CERN Pulsed Collider at CM Energies of 900 GeV and 200 GeV*, Z.Phys. **C33** (1986), 175; G. Alner et al., UA5 collaboration, *UA5: A general study of proton-antiproton physics at $\sqrt{s} = 546$ GeV*, Phys.Rept. **154** (1987), 247–383; R. Ansorge et al., UA5 collaboration, *Charged Particle Correlations in $\bar{p}p$ collisions at C.M. Energies of 200 GeV, 546 GeV and 900 GeV*, Z.Phys. **C37** (1988), 191–213; R. Ansorge et al., UA5 collaboration, *Charged Particle Multiplicity Distributions at 200 GeV and 900 GeV Center-Of-Mass Energy*, Z.Phys. **C43** (1989), 357.

[136] T. Alexopoulos et al., E735 collaboration, *Multiplicity dependence of transverse momentum spectra of centrally produced hadrons in $\bar{p}p$ collisions at 0.3 TeV, 0.54 TeV, 0.9 TeV, and 1.8 TeV center-of-mass energy*, Phys.Lett. **B336** (1994), 599–604.

[137] F. Abe et al., CDF collaboration, *Transverse Momentum Distributions of Charged Particles Produced in $\bar{p}p$ Interactions at $\sqrt{s}$ =630 GeV and 1800 GeV*, Phys.Rev.Lett. **61** (1988), 1819; F. Abe et al., CDF collaboration, *Pseudorapidity Distributions of Charged Particles Produced in $\bar{p}p$ Interactions at $\sqrt{s}$ = 630 GeV and 1800 GeV*, Phys.Rev. **D41** (1990), 2330.

[138] T. Aaltonen et al., CDF collaboration, *Measurement of particle production and inclusive differential cross sections in $p\bar{p}$ collisions at $\sqrt{s} = 1.96$ TeV*, Phys. Rev. **D79** (2009), 112005, [arXiv:0904.1098 [hep-ex]].

[139] K. Aamodt et al., ALICE collaboration, *First proton-proton collisions at the LHC as observed with the ALICE detector: Measurement of the charged particle pseudorapidity density at $\sqrt{s}$ = 900 GeV*, Eur.Phys.J. **C65** (2010), 111–125, [arXiv:0911.5430 [hep-ex]]; K. Aamodt et al., ALICE collaboration, *Charged-particle multiplicity measurement in proton-proton collisions at $\sqrt{s}$ = 0.9 and 2.36 TeV with ALICE at LHC*, Eur.Phys.J. **C68** (2010), 89–108, [arXiv:1004.3034 [hep-ex]], Long author list - awaiting processing; K. Aamodt et al., ALICE collaboration, *Charged-particle multiplicity measurement in proton-proton collisions at $\sqrt{s} = 7$ TeV with ALICE at LHC*, Eur.Phys.J. **C68** (2010), 345–354, [arXiv:1004.3514 [hep-ex]].

[140] V. Khachatryan et al., CMS collaboration, *Transverse momentum and pseudorapidity distributions of charged hadrons in pp collisions at $\sqrt{s}$ = 0.9 and 2.36 TeV*, JHEP **1002** (2010), 041, [arXiv:1002.0621 [hep-ex]]; V. Khachatryan et al., CMS collaboration, *Transverse-momentum and pseudorapidity distributions of charged hadrons in pp collisions at $\sqrt{s} = 7$ TeV*, Phys.Rev.Lett. **105** (2010), 022002, [arXiv:1005.3299 [hep-ex]].

[141] G. Aad et al., ATLAS collaboration, *Charged-particle multiplicities in pp interactions at $\sqrt{s} = 900$ GeV measured with the ATLAS detector at the LHC*, Phys.Lett. **B688** (2010), 21–42, [arXiv:1003.3124 [hep-ex]]; *Charged particle multiplicities in pp interactions at $\sqrt{s} = 7$ TeV measured with the ATLAS detector at the LHC*, Tech. Report ATLAS-CONF-2010-024 , CERN, Geneva, Jul 2010.

[142] *Charged particle multiplicities in pp interactions at $\sqrt{s}$ = 0.9 and 7 TeV in a diffractive limited phase-space measured with the ATLAS detector at the LHC and*

new PYTHIA6 tune, Tech. Report ATLAS-CONF-2010-031 , CERN, Geneva, Jul 2010.

[143] *Track-based underlying event measurements in pp collisions at sqrts = 900 GeV and 7 TeV with the ATLAS Detector at the LHC*, Tech. Report ATLAS-CONF-2010-029 , CERN, Geneva, Jul 2010.

[144] *ATLAS Monte Carlo tunes for MC09*, Tech. Report ATL-PHYS-PUB-2010-002 , CERN, Geneva, Mar 2010.

[145] A. Sherstnev and R. Thorne, *Parton Distributions for LO Generators*, Eur.Phys.J. **C55** (2008), 553–575, [arXiv:0711.2473 [hep-ph]].

[146] P. Z. Skands, *The Perugia Tunes*, arXiv:0905.3418 [hep-ph].

[147] *Pythia6 Update Notes*, http://www.hepforge.org/archive/pythia6/update_notes-6.4.22.txt.

[148] A. Buckley, H. Hoeth, H. Lacker, H. Schulz and J. E. von Seggern, *Systematic event generator tuning for the LHC*, Eur. Phys. J. **C65** (2010), 331–357, [arXiv:0907.2973 [hep-ph]].

[149] V. M. Abazov et al., DØ collaboration, *Measurement of Dijet Azimuthal Decorrelations at Central Rapidities in $p\bar{p}$ Collisions at $\sqrt{s} = 1.96$ TeV*, Phys. Rev. Lett. **94** (2005), 221801, [hep-ex/0409040].

[150] A. A. Affolder et al., CDF collaboration, *The transverse momentum and total cross section of e^+e^- pairs in the Z boson region from $p\bar{p}$ collisions at $\sqrt{s} = 1.8$ TeV*, Phys.Rev.Lett. **84** (2000), 845–850, [arXiv:hep-ex/0001021 [hep-ex]].

[151] M. Sandhoff and P. Z. Skands, *Colour annealing - a toy model of colour reconnections*, In Les Houches Physics at TeV Colliders 2005 SM and Higgs Working Group Summary Report hep-ph/0604120.

[152] D. E. Acosta et al., CDF collaboration, *Soft and hard interactions in $p\bar{p}$ collisions at $\sqrt{s} = 1800$-GeV and 630-GeV*, Phys.Rev. **D65** (2002), 072005.

[153] R. D. Field, *CMS UE Data and the New Tune Z1*, talk presented at the MB and UE WG Meeting, LPCC, Sep 2010.

[154] A. G. Buckley and H. Schulz, *First tuning of HERWIG/JIMMY to ATLAS data*, Tech. Report ATL-COM-PHYS-2010-620 , CERN, Geneva, Aug 2010.